Development of the TRISTAN Silicon Drift Detector Modules for the keV sterile Neutrino Search with the KATRIN Experiment

Daniel Siegmann

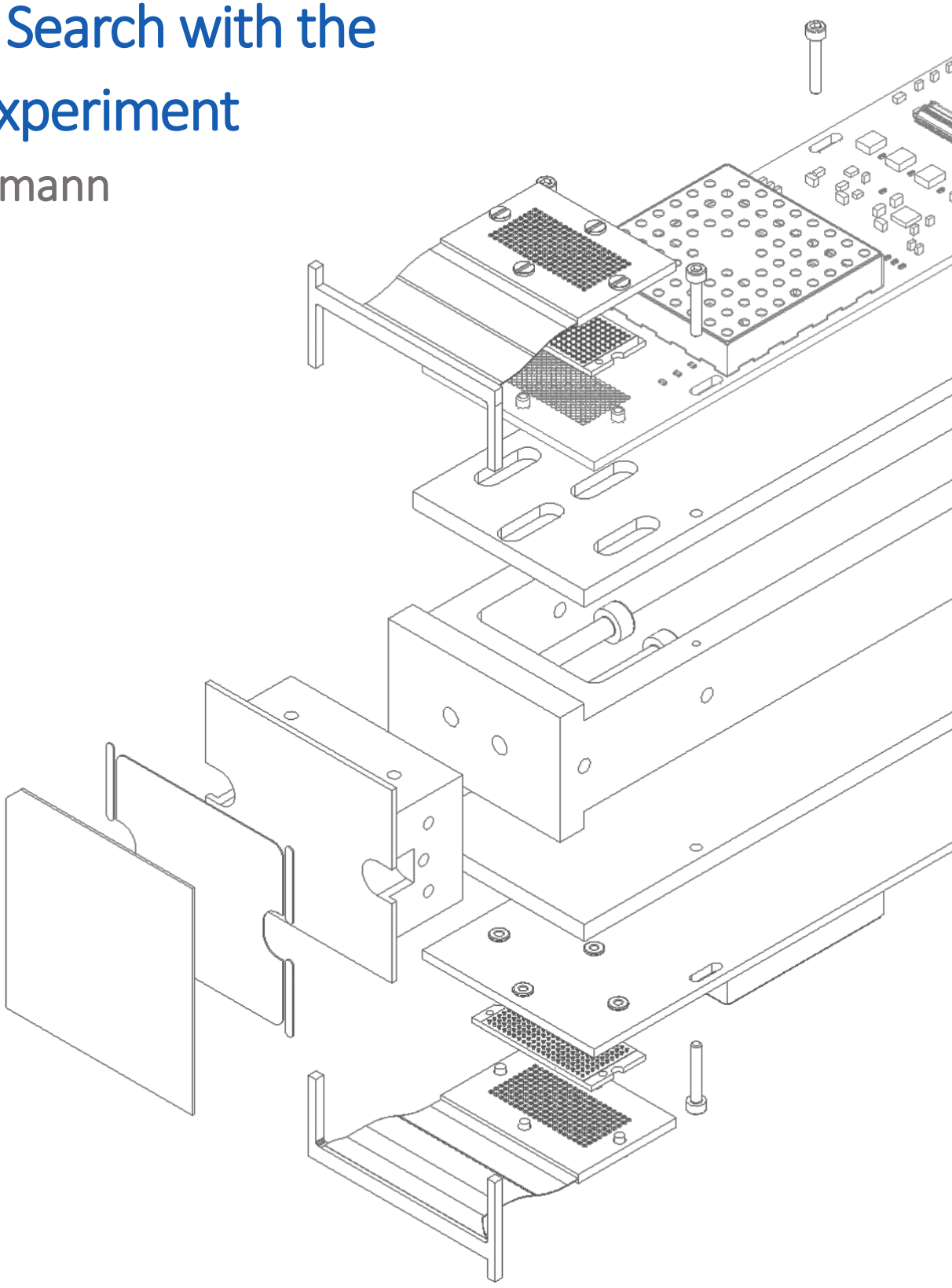

MAX PLANCK INSTITUTE FOR PHYSICS

TUM School of Natural Sciences

Development of the TRISTAN Silicon Drift Detector Modules for the keV sterile Neutrino Search with the KATRIN Experiment

Daniel Benedikt Siegmann

Vollständiger Abdruck der von der
TUM School of Natural Sciences
der Technischen Universität München
zur Erlangung des akademischen Grades eines
Doktors der Naturwissenschaften (Dr. rer. nat.)
genehmigten Dissertation.

Vorsitz:
apl. Prof. Dr. Norbert Kaiser

Prüfende der Dissertation:
1. Prof. Dr. Susanne Mertens
2. Prof. Dr. Bastian Märkisch

Die Dissertation wurde am 19.08.2024 bei der Technischen Universität München eingereicht und durch die TUM School of Natural Sciences am 10.09.2024 angenommen.

ABSTRACT

Right-handed neutrinos, also known as sterile neutrinos, could solve multiple open questions in modern particle physics and cosmology, such as the lightness of the active neutrinos and the content and origin of Dark Matter. If their mass is in the keV range, they pose a suitable dark matter candidate.

One way to experimentally access keV sterile neutrinos is via the kinematics of the β decay. A sterile neutrino with a mass smaller than the kinematic endpoint would lead to a spectral distortion with a kink-like signature proportional to the mixing amplitude with the three light neutrinos. To search for such a spectral distortion on the parts per million (ppm) level, the Karlsruhe Tritium Neutrino (KATRIN) experiment plans to extend its measurement range to probe the entire tritium spectrum with a kinematic endpoint energy of 18.6 keV. This search is planned after the neutrino mass measurements have been completed at the end of 2025. To this end, a new multi-pixel silicon drift detector (SDD) system, called TRISTAN, is currently being developed. The TRISTAN detector system consists of nine identical detector modules, with a targeted energy resolution of 300 eV FWHM at 20 keV.

One of the main goals of this work is the commissioning and characterization of the first detector modules. In particular, the mechanical design and assembly procedure of the detector modules was developed, and multiple detector modules have been built successfully. One of the detector modules has been thoroughly characterized with X-rays in a custom-designed vacuum setup. Important parameters, such as the detector operating voltages, have been optimized. Moreover, the energy resolution, calibration linearity, time stability, and temperature dependence have been investigated. In addition, the trade-off between the signal pile-up probability and energy resolution has been quantified.

To investigate the detector performance in a more realistic environment comparable to the KATRIN experiment (ultra-high vacuum conditions and MAC-E filter environment), one of the detector modules has been installed in the KATRIN Monitor Spectrometer (MoS) and was operated successfully over multiple weeks. Measurements of the electronic noise inside the MoS are in good agreement with the measurements carried out in the laboratory vacuum setup, showing the system's robustness against external noise sources. Furthermore, the energy resolution for mono-energetic electrons from a ^{83m}Kr source and electrons from the spectrometer wall have been measured in the MoS. An average energy resolution of 266 eV at 20 keV could be achieved, which fulfills the target for the keV sterile neutrino search. The developed assembly procedure and characterization measurements performed in this work serve as a basis for the construction and characterization of the final TRISTAN detector system.

ZUSAMMENFASSUNG

Rechtshändige Neutrinos, die auch als sterile Neutrinos bezeichnet werden, könnten mehrere offene Fragen der modernen Teilchenphysik und Kosmologie lösen, wie etwa die Leichtigkeit der aktiven Neutrinos und den Inhalt und Ursprung der Dunklen Materie. Wenn ihre Masse im keV-Bereich liegt, sind sie ein geeigneter Kandidat für dunkle Materie.

Eine Möglichkeit um experimentell Zugang zu sterilen Neutrinos im keV-Bereich zu erhalten, ist die duch die genaue Vermessung des β-Zerfalls. Ein steriles Neutrino mit einer Masse, die kleiner ist als der kinematische Endpunkt, würde zu einer spektralen Verzerrung mit einer Knick-ähnlichen Signatur führen, die proportional zur Mischungsamplitude mit den drei leichten activen Neutrinos ist. Um nach einer solchen spektralen Verzerrung im ppm-Bereich zu suchen, plant das Karlsruhe Tritium Neutrino (KATRIN) experiment, seinen Messbereich auf das gesamte Tritiumspektrum, mit einer kinematischen Endpunktenergie von 18.6 keV zu erweitern. Diese Suche ist geplant, nachdem die Neutrinomassenmessungen Ende 2025 abgeschlossen sind. Zu diesem Zweck wird derzeit ein neues Multi-Pixel-Silizium-Drift-Detektorsystem (SDD) mit der Bezeichnung TRISTAN entwickelt. Das TRISTAN-Detektorsystem besteht aus neun identischen Detektormodulen, mit einer angestrebten Energieauflösung von 300 eV FWHM bei einer Energie von 20 keV.

Eines der Hauptziele dieser Arbeit ist die Inbetriebnahme und Charakterisierung der ersten Detektormodule. Insbesondere wurde das mechanische Design und das Montageverfahren der Detektormodule entwickelt, und es wurden mehrere Detektormodule erfolgreich hergestellt. Eines der Detektormodule wurde in einem speziell entwickelten Vakuumaufbau mit Röntgenstrahlen gründlich charakterisiert. Wichtige Parameter, wie die Betriebsspannungen des Detektors, wurden optimiert. Außerdem wurden die Energieauflösung, die Kalibrierungslinearität, die Zeitstabilität und die Temperaturabhängigkeit untersucht. Darüber hinaus wurde der Kompromiss zwischen der Wahrscheinlichkeit von Signal Pile-Up und der Energieauflösung quantifiziert.

Um die Leistung des Detektormodul in einer realistischeren Umgebung zu untersuchen, die mit dem KATRIN-Experiment vergleichbar ist (ultra-hoch Vacuum und MAC-E-Filterumgebung), wurde eines der Detektormodule in das KATRIN-Monitorspektrometer (MoS) eingebaut und über mehrere Wochen erfolgreich betrieben. Die Messungen des elektronischen Rauschens im MoS stimmen gut mit den im Laborteststand durchgeführten Messungen überein, was die Robustheit des Systems gegenüber externen Rauschquellen zeigt. Außerdem wurde die Energieauflösung für monoenergetische Elektronen aus einer $^{83\mathrm{m}}$Kr Quelle und Elektronen aus der Spektrometerwand im MoS gemessen. Es konnte eine durchschnittliche Energieauflösung von 266 eV bei 20 keV erreicht werden, was die Zielvorgabe für die Suche nach sterilen Neutrinos bei keV erfüllt. Das entwickelte Montageverfahren und die in dieser Arbeit durchgeführten Charakterisierungsmessungen dienen als Grundlage für den Bau und die Charakterisierung des endgültigen TRISTAN-Detektorsystems.

CONTENTS

1

INTRODUCTION AND OBJECTIVES

Many different observables like, e.g., the motion of hydrogen and stars in galaxies and galaxy clusters, indicated that the behavior of our Universe can not be explained by Newtonian mechanics and visible matter alone. Especially the observations of stronger anisotropies in the cosmic microwave background (CMB) show that the structure formation on cosmologically large scales started long before the decoupling of the photons from the primordial plasma. To explain these observations, the existence of a gravitational-acting, matter-like substance that is distributed across the entire universe is required. This new substance, commonly known as dark matter, contributes to around 26.4 % of the total energy density in our universe[1] [1, Ch. 27]. However, the Standard Model of particle physics (SM) does not provide a suitable candidate to explain all the dark matter content. In addition, the observations of neutrino oscillations and the consequence that they need to have a non-vanishing mass, show that there must be physics beyond the SM.

With the extension of the SM by three additional right-handed neutrinos, also known as sterile neutrinos, both of these problems could be explained. In the framework of the neutrino minimal Standard Model (νMSM), two sterile neutrinos in the mass range above GeV are introduced to motivate the lightness of the active neutrinos in the SM [2, 3]. To explain the observed dark matter density in the universe the third sterile neutrino mass would need to be in the keV range or slightly above [4]. As sterile neutrinos are right-handed and carry no color and electrical charge, they do not participate in the weak, strong, and electromagnetic interaction. However, due to their mixing with the (active) left-handed neutrinos, their impact can be detected in laboratory-based experiments apart from their gravitational effect as dark matter.

With the detector upgrade, called TRISTAN, the Karlsruhe Tritium Neutrino (KATRIN) experiment [5] plans to search for such a keV sterile neutrino in the β-decay of tritium after its neutrino mass measurement is completed [6, 7]. Any neutrino mass m_i (active or sterile) smaller than the endpoint energy of tritium with a value of $E_0 \approx 18.6\,\text{keV}$, would lead to a distortion of the electron spectrum at energies[2] below $E_0 - m_i$. Right now, the KATRIN experiment performs a high-precision measurement of the region near the endpoint energy E_0 to determine the effective electron anti-neutrino mass m_β of the active neutrinos in the SM with a final sensitivity better than 300 meV. After the neutrino mass measurement campaign is completed at the end of 2025, the KATRIN beamline will be upgraded with the TRISTAN detector system to search for keV sterile neutrinos up to masses of $m_s \lesssim 18.6\,\text{keV}$, with a targeted sensitivity on the mixing amplitude in the order of $\sin^2(\theta_s) \lesssim 10^{-6}$ [7]. This

[1] For comparison, all ordinary (luminous) mass only contribute to around 5 % of the total energy density in the universe.

[2] In this work, the natural units where the speed of light is set to $c = 1$ is being used.

sensitivity would improve the current laboratory limits by three orders of magnitude.

To reach such a sensitivity in a reasonable amount of time, the entire tritium electron spectrum needs to be measured precisely at count rates of around 10^8 cps. This exceeds the capabilities of the current focal plane detector (FPD) in the KATRIN experiment. To cope with these challenges, the new TRISTAN detector system is based on the SDD technology, which provides excellent spectroscopic properties at the envisioned count rates of 100 kcps per pixel. The TRISTAN detector system will feature more than 1000 active pixels with a targeted energy resolution better than 300 eV at 20 keV. It consists of nine identical detector modules that can be mounted next to each other.

The main goals of this work are the development of the assembly procedure and the characterization of the first TRISTAN detector module in a realistic experimental environment. To this end, this work is divided into four main parts:

Preamble In Chapter 2, an introduction to sterile neutrino dark matter is given. Here, the most important properties of dark matter and neutrinos, as well as the constraints on the sterile neutrino dark matter parameter space (m_s, θ_s), are briefly summarized. The KATRIN experiment and the effect of the active and sterile neutrino mass on the tritium spectrum are described in Chapter 3. In addition, the TRISTAN detector system and the required modifications to the KATRIN beamline for the keV sterile neutrino search, are introduced. Furthermore, the SDD technology and the architecture of the required charge sensitive amplifier (CSA) circuit to read out the signals are discussed in the case of the TRISTAN detector system in Chapter 4. Here, also the difference in the detector response for X-rays and electrons is highlighted.

Development of the TRISTAN Detector Module The technical details of the TRISTAN detector module are given in Chapter 5. First, the general design considerations are being discussed. Then the technical details of the SDD chip and the on-module electronics are provided. Lastly, the TRISTAN detector module assembly procedure developed within this work is described.

Characterization of TRISTAN Detector Modules The commissioning and characterization measurements of the first TRISTAN detector modules with X-ray sources are detailed in Chapter 6. The integration and characterization of the detector module S0-166-4 with electrons in the KATRIN-like environment of the MoS are described in Chapter 7. Here, an inhomogeneity of the energy resolution for electrons has been observed, which can be explained by an additional cleanable substance deposited on the entrance window. The investigations to validate this hypothesis and the tests of the cleaning procedure are given in Chapter 8.

Summary and Conclusion In the end, the most relevant results obtained in the scope of this work are summarized in Chapter 9.

The main outcomes obtained within this work are also published in the peer-reviewed Journal of Physics G in [8].

2

STERILE NEUTRINO AND DARK MATTER PHYSICS

One of the big open questions in physics right now is the origin and nature of dark matter in our Universe. However, the SM does not provide any suitable candidate for it. The introduction of right-handed neutrinos, also known as sterile neutrinos, in the context of the νMSM, could provide a suitable dark matter candidate while at the same time explaining the lightness of the neutrinos in the SM.
As an introduction, the properties of dark matter and neutrinos are briefly highlighted in Chapter 2.1 and Chapter 2.2, respectively. From the observations of neutrino oscillations, we know that neutrinos must have a non-vanishing mass. However, since only left-handed neutrinos are predicted by the SM, they can not receive their mass via the Higgs mechanism. A possible solution to this problem is the introduction of (three) right-handed neutrinos as described in Chapter 2.3. In the context of the νMSM framework, two very heavy sterile neutrinos ($\mathcal{O}(\text{GeV})$) are introduced to explain the lightness of the active[1] neutrinos. In addition, a third sterile neutrino in the keV mass range is introduced since it would provide a suitable dark matter candidate. The constraints of the keV sterile neutrino parameter space (m_s,θ_s) from its production mechanism in the early universe and cosmological and earthbound observations are described in Chapter 2.4. For a more detailed discussion of the different topics, refer to, e.g., [2–4].

2.1 Properties of Dark Matter

Under the assumption of the lambda cold dark matter (ΛCDM) model, dark matter contributes to 26.4 % of the total energy density of our Universe. The presence of it is observed in all gravitationally collapsed structures ranging from the size of the smallest known galaxies up to the size of galaxy clusters. One of the most famous observations of dark matter is the rotation velocity curve of spiral galaxies as a function of the distance to the gravitational center shown in Figure 2.1. If the mass distribution in the galaxy is calculated using the (luminous) contributions of the stellar disk and gas, one expects a decreasing rotational velocity v for larger distances R. However, the measured rotational velocities v can not be explained by this luminous matter alone, and the introduction of a large amount of dark matter is necessary. For more detailed information on the different observable that motivate dark matter, refer to, e.g., [1, Ch. 27].
From the different cosmological observations, a range of conditions can be extracted that dark matter has to fulfill:

- It needs to be **massive** such that it can gravitationally affect the motion and formation on the scales of galaxies and galaxy clusters in our universe.

[1] For better clarity, the three left-handed, light neutrinos of the SM are denoted as active to better distinguish them from the right-handed sterile neutrinos.

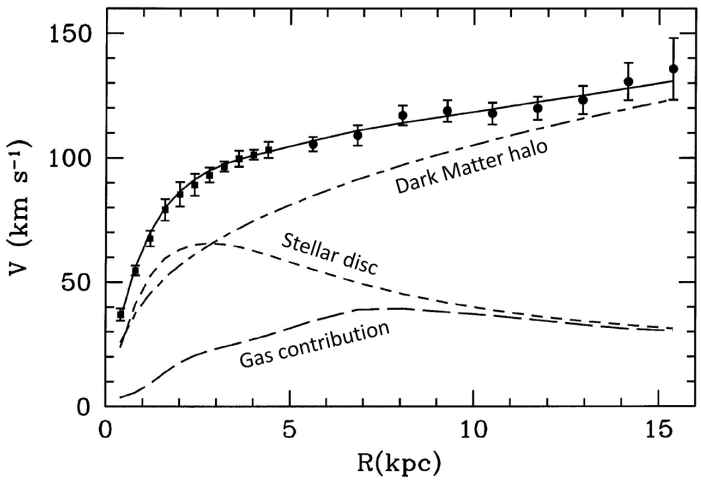

Figure 2.1: Velocity rotation curve of the M33 spiral galaxy
Measured rotation curve (points) compared to the best-fitting model including the contributions of the visible stellar disk and gas as well as the non-visible dark matter contribution in the halo of the Messier 33 (M33) spiral galaxy. If no dark matter existed, the measurements would need to follow the distribution of the visible stellar disk and gas only. The measured velocity of the stars and gas is denoted as V and their corresponding distance to the gravitational center as R. Figure adapted from [9].

- Since it could not be observed by the emission, absorption, or reflection of electromagnetic radiation, it is **non-luminous** and therefore also (at least mostly) **electrically neutral**.
- In addition to the gravitational force, it can only **interact very weakly** with the ordinary matter of the SM. Otherwise, the interaction would have been observed. At most, it can interact at a strength comparable to the weak nuclear force.
- To explain the formation of structures like galaxies and galaxy clusters, it has to create gravitational wells and **clump up**. Therefore, it needs to be relatively slow-moving to not stream out of the gravitational wells, which means in most cases **non-relativistic**.
- Since its effect has been observed on any timescales in the history of the Universe, and is still seen today, it should be **stable** on the scale of the age of the Universe. If it would (quickly) decay into other particles, its density distribution would change differently over time, which is not observed.
- It needs to be (mostly) **non-baryonic** matter as the anisotropies seen in the CMB require that the observed (dark) matter over-densities have to be formed before the decoupling of the photons at $t < 380\,000$ yrs ($E < 0.02$ eV). These over-densities can not be explained by baryonic matter alone, which is produced in the of nucleosynthesis at a time of $t \approx 3$ min to 20 min ($E \approx 0.1$ MeV to 0.05 MeV) after the big bang.

The only possible candidate in the SM that could fulfill (most) of these requirements are (massive) neutrinos. They interact only via the weak interaction and decouple from the thermal equilibrium of the primordial plasma at a time of $t \approx 1$ s ($E \approx 1$ MeV) before the photon decoupling. As the weak interaction strength of the neutrinos is known, the temperature and number density of the relic cosmic neutrino background (CνB) can be estimated to a value of $T_\nu \approx 1.96\,\mathrm{K} \approx 10^{-4}$ eV (today) and $n_\alpha \approx 336/\mathrm{cm}^3$, respectively [2, 10]. Assuming

the case that the relic CνB contributes to the entire observed dark matter density ρ_{DM}, the required sum of the neutrino masses m_Σ can be estimated as shown in Equation (2.2) [2, 11].

$$\rho_{\mathrm{DM}} \stackrel{!}{=} \rho_\nu = n_\alpha \sum_{i=1}^{3} m_i \tag{2.1}$$

$$\Rightarrow m_\Sigma = \sum_{i=1}^{3} m_i \stackrel{!}{\approx} 11.5\,\mathrm{eV} \tag{2.2}$$

This large value is however in strong contradiction with the measurements of the effective neutrino mass $m_\beta \leq 0.45\,\mathrm{eV}\,(95\,\%\ \text{C.L.})$ [12] from β-decay and cosmological limits in the order of $m_\Sigma \leq 0.13\,\mathrm{eV}$ to $0.54\,\mathrm{eV}\,(95\,\%\ \text{C.L.})$ [1, Ch. 27].
As a consequence, physics beyond the SM is likely required to explain the observation of dark matter. This adds to other observations like the neutrino oscillations, the baryon asymmetry in the early universe, and the cosmic inflation, which also strongly indicate physics beyond the SM. These problems could, in principle, be explained by additional (heavy) sterile neutrinos[2] introduced as an expansion of the SM as shown in Chapter 2.3.

2.2 Neutrinos in the Standard Model and Beyond

Even though neutrinos are the most abundant massive elementary particles in the universe, studying them is rather challenging due to their elusive nature. However, with the observation of neutrino oscillations and, as a consequence, the non-zero neutrino mass, they pose one of the first evidence for physics beyond the SM. First, a (semi-historical) introduction to the properties of neutrinos in the SM is given in Chapter 2.2.1. Then, the discovery and formalism of neutrino oscillations are depicted in Chapter 2.2.2.

2.2.1 *Discovery and Properties of Neutrinos*

In the following chapter, a (semi-historical) summary of the most important discoveries related to neutrinos in the SM is given. For more details on this topic, refer to, e.g., [10, 13].

Postulation of the Electron Anti-Neutrino $\overline{\nu}_e$ The measurement of the continuous β-decay spectrum by J. Chadwick was the first hint that neutrinos exist [14]. At the time, this observation was surprising since all other decays (α- an γ-decays) were monoenergetic and conserved energy. Due to its feeble interaction with matter, only the electron could be observed, and the neutrino escaped undetected, seemingly violating the energy conservation. A solution to this problem was postulated by W. Pauli in his famous letter from 1930:
"Namely, the possibility that there could exist in the nuclei electrically neutral particles, that I wish to call [neutrino][3], which have spin 1/2 and obey the exclusion principle and which further differ from light quanta in that they do not travel with the velocity of light." [15]

[2] In this work, the term sterile neutrino describes a singlet fermion that mixes with the left-handed neutrinos ν_L from the SM. The terms sterile neutrino, right-handed neutrino, heavy neutral lepton, and singlet fermion are often used interchangeably, in literature.
[3] In his letter, Pauli actually named this particle neutron. However, since the neutron as we know it today was discovered at a similar time and got this name before Pauli's idea gained popularity, he later renamed it to neutrino - the little neutral one.

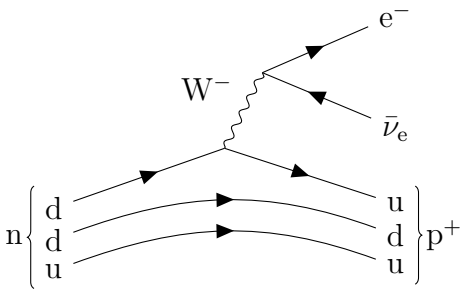

Figure 2.2: Feynman diagram of β-decay
First order Feynman diagram of the β-decay from a neutron n to a proton p^+ releasing an electron e^- and an electron anti-neutrino $\bar{\nu}_\mathrm{e}$ under the emission of a virtual W^--boson. The time axis is from left to right. Figure adapted from [10].

Based on this suggestion and the increasing knowledge about atomic nuclei E. Fermi formulated his theory of β-decay in 1934 [16] which is given in Equation (2.3).

$$ {}^{A}_{Z}\mathrm{X} \rightarrow {}^{A}_{Z+1}\mathrm{Y} + e^- + \bar{\nu}_e + Q \tag{2.3} $$

This process is also known as β^--decay, in which an element X decays to an element Y. As illustrated by the atomic number Z and the mass number A in the process, a neutron n is converted to a proton p^+, releasing an electron e^- and an electron anti-neutrino $\bar{\nu}_e$. The corresponding Feynman diagram of this process is given in Figure 2.2. During the process, the decay energy Q is released, which originates from the mass difference between the initial and final state particles. As a consequence, the decay energy is distributed as kinetic energy across the three particles in the final state. One important quantity of the β^--decay is the kinematic endpoint energy $E_0 = Q - E_\mathrm{rec}$ of the electron. It describes the case where the released electron e^- receives the maximum energy and the electron anti-neutrino $\bar{\nu}_e$ is nearly at rest. To conserve momentum, the remaining recoil energy E_rec is given to the nucleus. As already mentioned by Fermi at this time, the influence of the (potential) neutrino mass would be seen in the decay spectrum near the endpoint energy E_0. More details on measuring the electron anti-neutrino mass and its impact on the β^--decay spectrum are given in Chapter 3.1.1.

Discovery of the Electron Anti-Neutrino $\bar{\nu}_e$ The first direct detection of the electron anti-neutrino $\bar{\nu}_e$ happened in 1956 within the project poltergeist by the team around C. Cowan and F. Reines [17]. They captured anti-neutrinos $\bar{\nu}_e$ emitted from fission processes in a nuclear reactor ($E_\nu \approx \mathcal{O}(\mathrm{MeV})$) on two large water targets. The electron anti-neutrinos $\bar{\nu}_e$ interact via the inverse β-decay with the weakly bound protons of the hydrogen atoms in the water molecules as described in Equation (2.4).

$$ \bar{\nu}_e + p^+ \rightarrow n + e^+ \tag{2.4} $$

The emitted positron e^+ annihilates quickly with an electron e^-, releasing two prompt γ-rays back-to-back with an energy of 511 keV. In addition, the free neutron is detected after a few milliseconds via its absorption on cadmium atoms (dissolved as cadmium chloride ($CdCl_2$) in the water), which emits an additional γ-ray. This distinct coincidence signal can be easily distinguished from the background and was detected via liquid scintillation detectors surrounding the two water tanks.

Discovery of the Electron Neutrino ν_e Experimental evidence for the existence of electron neutrinos ν_e was found in the neutrino-induced recoil following the electron capture (EC) of an orbital electron from argon [18]. The corresponding nuclear reaction is given in Equation (2.5).

$$^{37}\mathrm{Ar} + e^- \rightarrow ^{37}\mathrm{Cl} + \nu_e + Q \tag{2.5}$$

Since only two particles are emitted in the final state with a total energy of $Q = 816\,\mathrm{keV}$, the recoil energy $T_{\mathrm{Cl}} = 9.67\,\mathrm{eV}$ of the nucleus is fixed by energy and momentum conservation and can be predicted. Consequently, the nuclear recoil energy has been measured in multiple experiments by its corresponding velocity, confirming the existence of the electron neutrino ν_e [10, 18, 19].

Discovery of the Muon (Anti-)Neutrino $\overline{\nu}_\mu$ The second neutrino flavor has been found at the high-energy accelerator (15 GeV) in Brookhaven by the team around M. Schwarz in 1962 [20]. They could show that the today-known muon neutrino flavor ν_μ is different from the electron neutrino flavor ν_e emitted from, e.g., β-decay. For their investigations, they observed an almost pure muon neutrino beam ν_μ generated by the decay of pions π^+ as described in Equation (2.6).

$$\pi^+ \rightarrow \mu^+ + \nu_\mu \tag{2.6}$$

The resulting muon neutrino beam ν_μ was measured in a spark chamber placed behind a 11.5 m thick shielding, which stopped all other particles. If all neutrinos were the same, the interactions described in Equation (2.7) and Equation (2.8) would be equally likely.

$$\nu_\mu + n \rightarrow \mu^- + p^+ \tag{2.7}$$

$$\nu_\mu + n \overset{!}{\rightarrow} e^- + p^+ \tag{2.8}$$

However, only six electron-like[4] and 29 muon-like interactions have been observed, clearly showing that at least two neutrino flavors exist.

Discovery of the Tau (Anti-)Neutrino $\overline{\nu}_\tau$ With the discovery of the tau lepton τ in 1975 [21], the search for the corresponding tau neutrino ν_τ started. It was discovered in the year 2001 by the Direct Observation of Nu Tau (DONUT) experiment at Fermilab. Further details on the experimental setup and the creation of the tau neutrino beam ν_τ can be found in [22].

Measurement of the Number of (active) Neutrinos via Z^0-Boson Decay In addition to the discovery of the three neutrino flavors, the corresponding number N_ν of light neutrinos ($m_\nu < m_Z/2$) has also been determined at the large electron-positron collider (LEP) [23]. To this end, the total decay width Γ_Z of the Z^0 resonance with a rest mass of $m_Z \approx 91\,\mathrm{GeV}$ has been measured precisely. Due to its large rest mass, it can decay into all pairs of fermions and anti-fermions in the SM except the top quark. As a consequence, the total decay width Γ_Z is given by Equation (2.9).

$$\Gamma_Z = N_\nu \Gamma_\nu + 3\Gamma_l + \Gamma_h \tag{2.9}$$

Here, Γ_l denotes the decay width of the charged lepton pairs and Γ_h the decay width of hadronic processes, which can be measured precisely in other decay channels. The partial decay width of the neutrino-anti-neutrino pairs Γ_ν can be calculated, leaving only the

[4] A low rate of electron events were expected since the beam was contaminated with electron neutrinos ν_e originating from the also present Kaon decay (e.g., $K^+ \rightarrow e^+ + \nu_e + \pi^0$).

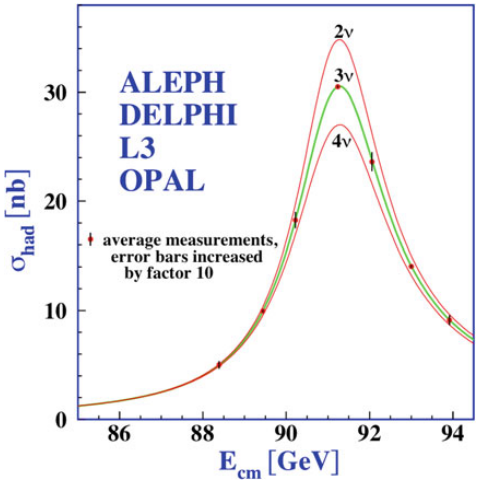

Figure 2.3: Measurement of the Z^0 resonance at the LEP
Measured hadronic cross-section of the e^+e^- collision near the Z^0 resonance. The different lines illustrate the expected cross-sections for different numbers of neutrino families N_ν. The data perfectly matches the case for three neutrino families. Figure taken from [23].

number of neutrino families N_ν as a free parameter. The measured Z^0 resonance as a function of energy is shown together with the expected cross-section for different numbers of neutrino families N_ν in Figure 2.3. The best agreement with the data has been found for $N_\nu = (2.984 \pm 0.008)$ neutrino families [23]. A consequence of this measurement is that every additional neutrino must have a mass larger than $m_z/2 \approx 46\,\text{GeV}$ or does not couple to the Z^0-boson, i.e. is of right-handed chirality, which is also often called sterile.

Parity Violation and Helicity of Neutrinos Until the 1950s, it had been assumed that all physical processes would conserve parity $P(\vec{x}) = P(-\vec{x})$. Or put in other words, every process happens with the same probability P, even if the spatial coordinates $\vec{x}$ are mirrored. To test this hypothesis, an (pseudoscalar) observable like helicity $\mathcal{H}$ can be investigated. It is defined as the normalized scalar product between the spin $\vec{s}$ and momentum $\vec{p}$ of a particle as shown in Equation (2.10) and changes its sign under parity transformation.

$$\mathcal{H} = \frac{\vec{s} \cdot \vec{p}}{|\vec{s}| \cdot |\vec{p}|} \tag{2.10}$$

In fact, for the strong and electromagnetic interaction, it could be shown that the parity is conserved [24]. However, a maximal parity violation has been measured in the case of the weak interaction to which the neutrinos couple. The first experimental proof for parity violation has been found in the experiment performed by C. S. Wu, where the β-decay of polarized ^{60}Co atoms has been investigated [25]. In the experiment, a paramagnetic salt containing ^{60}Co atoms has been placed inside a strong magnetic field to align their spin with the magnetic field direction z. Since the spin of the nucleus changes from $J_{\text{Co}} = +5$ to $J_{\text{Ni}} = +4$, the spins of the electron e^- ($S_e = +1/2$) and electron anti-neutrino $\bar{\nu}_e$ ($S_\nu = +1/2$) have to be aligned with the nuclear spin as illustrated by the arrows above Equation (2.11) and Equation (2.12). The momentum of the electron $\vec{p_e}$ is illustrated by the lower arrows.

$$\overset{\Rightarrow}{{}^{60}_{27}\text{Co}} \longrightarrow {}^{60}_{28}\text{Ni} + \overset{\Rightarrow}{\underset{\rightarrow}{e^-}} + \overset{\Rightarrow}{\bar{\nu}_e} \tag{2.11}$$

$$\overset{\Rightarrow}{{}^{60}_{27}\text{Co}} \longrightarrow {}^{60}_{28}\text{Ni} + \overset{\Rightarrow}{\underset{\leftarrow}{e^-}} + \overset{\Rightarrow}{\bar{\nu}_e} \tag{2.12}$$

If the parity would be conserved, the electron rate measured in the direction of the magnetic field z ($\mathcal{H} = +1$) in which the momentum of the electron $\vec{p_e}$ and its spin $\vec{s_e}$ are fully aligned and in the other direction $-\vec{z}$ where it's fully anti-aligned ($\mathcal{H} = -1$) would be identical. However, an around 40 % higher electron rate has been measured for the emission of electrons e^- with negative helicity $\mathcal{H} = -1$, proving that the weak interaction violates (maximally) parity. Another experiment that confirmed this observation is the pion p^+ decay at rest [26]. A direct measurement of the expected positive helicity of the neutrinos $\mathcal{H}_\nu = +1$ has been performed in, e.g., the Goldhaber experiment [27].

One consequence of these experiments is that the weak interaction only couples to particles with left-handed chirality and antiparticles with right-handed chirality. For a massless particle (like neutrinos in the SM), the positive helicity $\mathcal{H} = +1$ is equivalent to a right-handed chirality, and the negative helicity $\mathcal{H} = -1$ to the left-handed chirality. Since neutrinos are electrically neutral (do not couple to electromagnetic force), colorless (do not couple to strong interaction), and at least in the SM massless (do not couple to gravitational force), the only way how they can be detected is via the weak interaction. As a result, in the SM only left-handed neutrinos and right-handed anti-neutrinos are predicted.

2.2.2 *Neutrino Oscillations*

As neutrinos only appear as left-handed particles in the SM and all other fermions obtain their mass via the Higgs mechanism (see Chapter 2.3), which also requires a right-handed particle to function, they have been assumed massless. However, from the observation of neutrino oscillations, it is clear that at least two neutrinos do have a small non-vanishing mass. This is one of the first pieces of evidence for physics beyond the SM and points towards a new mass generation mechanism. In this chapter, the Solar Neutrino Problem and the discovery of neutrino oscillations are described briefly. In addition, the mathematical framework of neutrino oscillations is explained briefly. For more details, refer to [1, Ch. 14].

Solar Neutrino Problem The search for neutrino oscillations was sparked by the investigations of the solar neutrino flux. Inside the sun many fusion and decay reactions create a large flux of electron neutrinos ν_e with an energy range between 0.1 MeV up to around 20 MeV (mean $\bar{E}_\nu \approx 0.53$ MeV) [28]. In the Homestake experiment by R. Davids and colleagues, the solar electron neutrino flux was measured via the neutrino capture on chlorine (threshold $E_\nu \geq 0.814$ MeV) as shown in Equation (2.13).

$$\nu_e + {}^{37}\mathrm{Cl} \rightarrow {}^{37}\mathrm{Ar} + e^- \tag{2.13}$$

The interaction itself could not be observed in the radiochemical detector. But, the created radioactive Argon isotope ^{37}Ar ($T_{1/2} \approx 35$ d) could be extracted from the detector and its decay rate was measured [29]. In contrast to the predicted interaction rate of (7.5 ± 1.0) SNU the experiment only observed $(2.5600 \pm 0.0016\ (\mathrm{stat}) \pm 0.0015\ (\mathrm{sys}))$ SNU [30]. This discrepancy by almost a factor 3 was confirmed by many subsequent experiments [1, 31] and is known as the Solar Neutrino Problem [32].

Discovery of Neutrino Oscillations The solution to this problem are neutrino oscillations, in which a neutrino produced in a particular flavor, e.g., ν_e, transforms into another flavor on its propagation over very long distances to, e.g., ν_μ. Since the Homestake experiment was only sensitive to the electron neutrino flavor ν_e the other flavors could not be detected. To overcome this problem, the Sudbury Neutrino Observatory (SNO) experiment [33] was built

to measure the total solar neutrino flux independent of its flavor. Similar to other experiments, the electron neutrino flux was measured using the Cherenkov light of the emitted electron e^- in the charge current (CC) interaction with the heavy water (using deuterium D) shown in Equation (2.14).

$$\nu_e + D \rightarrow e^- + p + p \tag{2.14}$$

The total neutrino flux Φ_{NC} was determined using the neutral current (NC) interaction with the heavy water shown in Equation (2.15).

$$\nu_x + D \rightarrow \nu + p + n \tag{2.15}$$

The emitted neutron n is captured (in the first phase of the experiment) on the deuterium (later on NaCl) which produces tritium and emits a detectable γ-ray. The obtained electron neutrino flux $\Phi(\nu_e)$ and the total neutrino $\Phi(\text{NC})$ for the first run on pure D_2O are given in Equation (2.16) and Equation (2.17), respectively [34].

$$\Phi(\nu_e) = (1.7600 \pm 0.0006\ (\text{stat}) \pm 0.0009\ (\text{sys})) \cdot 10^6/(\text{cm}^3\,\text{s}) \tag{2.16}$$
$$\Phi(\text{NC}) = (5.0900 \pm 0.0044\ (\text{stat}) \pm 0.0046\ (\text{sys})) \cdot 10^6/(\text{cm}^3\,\text{s}) \tag{2.17}$$

The measurement of the total neutrino flux $\Phi(\text{NC})$ agrees with the expected neutrino rate from the sun, confirming the flavor change due to neutrino oscillations.

Neutrino Oscillation Formalism To describe this flavor change, the eigenstates of the weak interaction, also known as flavor eigenstates, $|\nu_\alpha\rangle$ ($\alpha = e, \mu, \tau$) are not equal to the eigenstates of their propagation in vacuum denoted as $|\nu_i\rangle$ ($i = 1, 2, 3$). These propagation eigenstates $|\nu_i\rangle$ are also often called mass eigenstates. The correlation between the two sets of eigenstates is given as a linear superposition in Equation (2.18) and Equation (2.19).

$$|\nu_\alpha\rangle = \sum_i U_{\alpha i}\,|\nu_i\rangle \tag{2.18}$$
$$|\nu_i\rangle = \sum_i U^*_{\alpha i}\,|\nu_\alpha\rangle \tag{2.19}$$

The corresponding mixing amplitudes $U_{\alpha i}$ are given by the unitary 3×3 Pontecorvo-Maki-Nakagawa-Sakata (PMNS) matrix shown in Equation (2.20).

$$U_{\text{PMNS}} = \begin{pmatrix} U_{e1} & U_{e2} & U_{e3} \\ U_{\mu 1} & U_{\mu 2} & U_{\mu 3} \\ U_{\tau 1} & U_{\tau 2} & U_{\tau 3} \end{pmatrix} \tag{2.20}$$

It can be parametrized by three mixing angles θ_{12}, θ_{23}, and θ_{13}, which are interpreted as the rotation angle between the eigenstates. The imaginary Dirac Charge-Parity (CP)-phase δ_{CP} quantifies if and to which extent the CP-parity is violated if neutrinos are Dirac-particles. For values of $\delta_{\text{CP}} \neq 0$ or π, the CP symmetry is violated, leading to different behaviors of neutrinos and anti-neutrinos, which possibly explains the matter anti-matter asymmetry in the universe. For the case that neutrinos are Majorana particles, which means they are their own anti-particle, two additional Majorana phases η_1 and η_2 can be introduced. They have no observable effect on the neutrino oscillation but have a CP-conserving influence in neutrinoless double β-decay $\nu 0\beta\beta$. If neutrinos are Dirac particles, these phases are non-physical and can therefore be set to 0 [35]. To better understand the different free parameters, the PMNS matrix U_{PMNS} can be split into four parts as shown in Equation (2.21), where $s_{ij} = \sin\theta_{ij}$

and $c_{ij} = \cos\theta_{ij}$. These parts historically correspond to the different neutrino sources that have been used to measure the corresponding oscillation parameters.

$$U_{\text{PMNS}} = \underbrace{\begin{pmatrix} c_{12} & s_{12} & 0 \\ -s_{12} & c_{12} & 0 \\ 0 & 0 & 1 \end{pmatrix}}_{\text{Solar } e\to\mu} \underbrace{\begin{pmatrix} c_{13} & 0 & s_{13}e^{-i\delta_{\text{CP}}} \\ 0 & 1 & 0 \\ -s_{13}e^{i\delta_{\text{CP}}} & 0 & c_{13} \end{pmatrix}}_{\text{Reactor } \mu\leftrightarrow e} \underbrace{\begin{pmatrix} 1 & 0 & 0 \\ 0 & c_{23} & s_{23} \\ 0 & -s_{23} & c_{23} \end{pmatrix}}_{\text{Atmospheric } \mu\to\tau} \underbrace{\begin{pmatrix} e^{i\eta_1} & 0 & 0 \\ 0 & e^{i\eta_2} & 0 \\ 0 & 0 & 1 \end{pmatrix}}_{\text{Majorana Phase}} \tag{2.21}$$

The propagation of the neutrinos in space is given by the Schrödinger equation using the neutrino energy $E_i = \sqrt{p_i^2 + m_i^2}$ with momentum p_i and a mass m_i given in Equation (2.22).

$$|\nu_\alpha(t)\rangle = \sum_i U_{\alpha i} e^{-iE_i t} |\nu_i\rangle \tag{2.22}$$

Since the neutrinos can only be measured in the flavor eigenstate, the probability of a neutrino in the flavor $|\nu_\alpha\rangle$ to oscillate to another eigenstate $|\nu_\beta\rangle$ is given by Equation (2.23).

$$P(\alpha \to \beta) = |\langle \nu_\beta | \nu_\alpha(t) | \nu_\beta | \nu_\alpha(t) \rangle|^2 = \sum_{ij} U_{\alpha i} U^*_{\alpha i} U^*_{\beta j} U_{\beta j} e^{-i(E_i - E_j)t} \tag{2.23}$$

It can be assumed that in all practical measurements, neutrinos are ultra-relativistic with neglect-able mass ($p \simeq E$) and have the same momentum ($p_i \simeq p_j \simeq p$) such that the energy can be rewritten as $E_i \simeq p + m_i^2/(2E)$ [1, Ch. 14]. This results in the oscillation probability formula given in Equation (2.24).

$$P(\alpha \to \beta) = \left| \delta_{\alpha\beta} - \sin^2(\theta_{ij}) \sin^2\left(1.27 \cdot \Delta m^2_{ij}[\text{eV}^2] \frac{L[\text{km}]}{E[\text{GeV}]}\right) \right| \tag{2.24}$$

As seen in the formula, neutrino oscillations can only be observed if the mass differences $\Delta m^2_{ij} = m_j^2 - m_i^2$ and the mixing angles θ_{ij} are different from zero. An overview on the current parameters can be found in the global analysis [36]. As a consequence of the observation of neutrino oscillations, at least two neutrinos must have non-vanishing masses, showing that there must be physics beyond the SM. However, since the oscillation probability is only sensitive to the squared mass difference Δm^2_{ij}, the absolute mass of the neutrino eigenstates can not be measured with this phenomenon.

2.2.3 *Experimental Limits on the Neutrino Masses*

As noted in Chapter 2.2.2, the oscillation experiments are only sensitive to the squared mass difference Δm^2_{ij} and not at all to the absolute mass of the eigenstates m_i. Since the mass of the neutrinos is expected to be at least five orders of magnitude smaller than the mass of the electron, the experimental determination of it is rather challenging. At the time of writing, the best limits are set by three major experimental approaches from cosmology, neutrinoless double β-decay ($0\nu\beta\beta$-decay) and the kinematics of the β-decay.

Cosmology Since neutrinos are the most abundant particle in the universe with a total number density of around $336/\text{cm}^3$ originating from the CνB, they have a significant influence on the structure formation in the early universe [10]. At a time of around 1 s ($E \approx 1\,\text{MeV}$) after the big bang, they decouple from the primordial plasma and form the relic CνB. When decoupling (known as freeze-out), the neutrinos are ultra-relativistic, acting as hot dark matter

(HDM), carrying energy over large distances. Depending on their energy and mass, they smear out the gravitationally formed small-scale density fluctuations. Assuming the ΛCDM model and combining the measurements of the CMB (photon freezeout at $t \approx 380\,000$ year), gravitational lensing effects, as well as information of large-scale structure formation via the baryonic acoustic oscillations (BAO) stringent upper limits on the sum of the neutrino masses m_Σ can be obtained. Depending on the exact cosmological models applied and the amount of data sets included, different upper limits are derived. The range of the different surveys summarized in [1, Ch. 26] is shown in Equation (2.25).

$$m_\Sigma = \sum_{i=1}^{3} m_i \leq 0.13\,\text{eV to } 0.54\,\text{eV (95 \% C.L.)} \tag{2.25}$$

Neutrinoless Double Beta Decay The search for the $0\nu\beta\beta$-decay is the most sensitive approach to answer the question if neutrinos are Majorana fermions, i.e., their own anti-particle [1, Ch. 14]. In addition, if it is discovered, also the effective neutrino Majorana mass $m_{\beta\beta}$ can be calculated. The general double β-decay ($2\nu\beta\beta$-decay) can occur in neutron-rich elements where the single β-decay is energetically forbidden or at least highly suppressed. In the process, two β-decays happen simultaneously as shown in Equation (2.26) and Figure 2.4a, emitting two electrons e^- and two electron anti-neutrinos $\bar{\nu}_e$.

$${}^{A}_{Z}\mathrm{X} \rightarrow {}^{A}_{Z+2}\mathrm{Y} + 2e^- + 2\bar{\nu}_e + Q \tag{2.26}$$

If neutrinos are Majorana particles, also the lepton-number violating $0\nu\beta\beta$-decay shown in Equation (2.27) and Figure 2.4b can occur.

$${}^{A}_{Z}\mathrm{X} \rightarrow {}^{A}_{Z+2}\mathrm{Y} + 2e^- + Q \tag{2.27}$$

In this case, the virtually emitted electron (anti-)neutrino of one of the vertices is absorbed as an electron neutrino in the other vertex. As a result, the total decay energy $E_{\beta\beta} = Q - E_{rec}$ is given to the two emitted electrons, leading to a mono-energetic peak with an energy above the continues $2\nu\beta\beta$-decay spectrum. At the time of writing, the neutrinoless double β-decay ($0\nu\beta\beta$-decay) has not been observed and therefore a lower limit on the half-life time $T^{0\nu}_{1/2}$ is given by the leading experiments shown in Equation (2.28) [37], and Equation (2.29) [38].

$$T^{0\nu}_{1/2}({}^{76}\mathrm{Ge}) > 1.8 \cdot 10^{26}\,\text{yrs} \tag{2.28}$$

$$T^{0\nu}_{1/2}({}^{136}\mathrm{Xe}) > 2.3 \cdot 10^{26}\,\text{yrs} \tag{2.29}$$

Since the half-life time $T^{0\nu}_{1/2}$ depends on the effective Majorana electron neutrino mass $m_{\beta\beta}$ as shown in Equation (2.30), also a limit on the neutrino mass can be derived from it[5].

$$\left(T^{0\nu}_{1/2}\right)^{-1} = G_{0\nu} \left|M_{0\nu}\right|^2 \left|m_{\beta\beta}\right|^2 \tag{2.30}$$

Here, $G_{0\nu}$ describes the phase space factor and $M_{0\nu}$ the nuclear matrix element of the corresponding nuclei [1]. The correlation between the observable effective Majorana mass (of the electron neutrino ν_e) $m_{\beta\beta}$ and the neutrino mass eigenstates ν_i is given in Equation (2.31).

$$m_{\beta\beta} = \left|\sum_i m_i U^2_{ei}\right| = \left|m_1|U_{e1}|^2 + m_2|U_{e2}|^2 e^{i(\eta_2-\eta_1)} + m_3|U_{e3}|^2 e^{i-\eta_1-2\delta_{\mathrm{CP}}}\right| \tag{2.31}$$

[5] This limit only holds if neutrinos are Majorana particle.

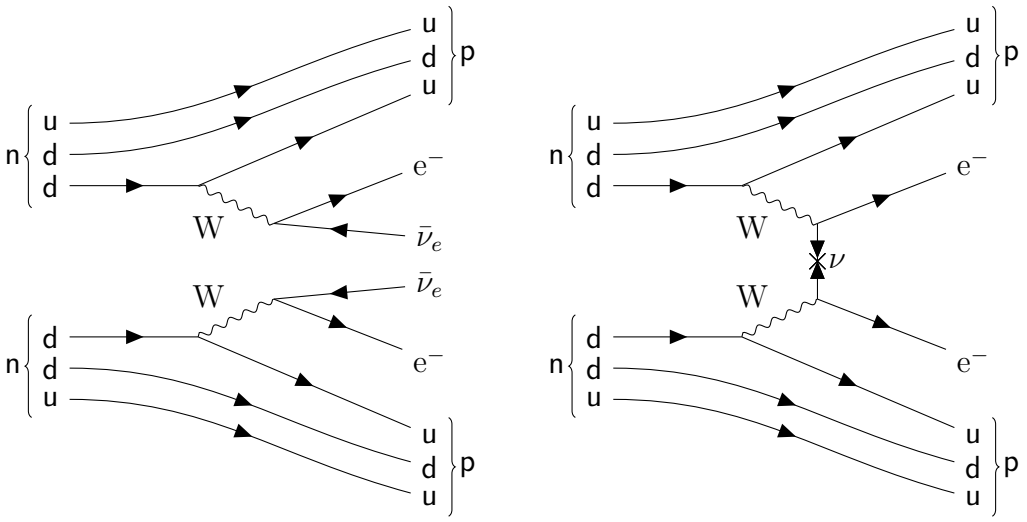

(a) Double β-decay ($2\nu\beta\beta$-decay) **(b)** Neutrinoless double β-decay ($0\nu\beta\beta$-decay)

Figure 2.4: Feynman diagram of the double β-decay
(a) General $2\nu\beta\beta$-decay where two neutrons n decay into two protons p^+ under the emission of two electrons e^- and two electron anti-neutrinos $\bar{\nu}_e$. (b) The $0\nu\beta\beta$-decay is a second order process in with the two neutrinos are virtually exchanged with each other and are therefore not emitted. Figure adopted from [10].

The obtained range of the limits on the Majorana mass $\nu_{\beta\beta}$ for the two experiments are given in Equation (2.32) and Equation (2.33). This range is given since there are larger uncertainties in the calculation of the nuclear matrix element $M_{0\nu}$.

$$m_{\beta\beta}(^{76}\text{Ge}) < 0.079\,\text{eV} \text{ to } 0.180\,\text{eV} \;\; 90\,\% \;\; \text{C.L.} \tag{2.32}$$
$$m_{\beta\beta}(^{136}\text{Xe}) < 0.036\,\text{eV} \text{ to } 0.156\,\text{eV} \;\; 90\,\% \;\; \text{C.L.} \tag{2.33}$$

As a comment, since the effective Majorana mass is the coherent sum, a (partial) cancellation of the terms can be achieved due to the complex CP-violating phase δ_{CP} and the two Majorana phases η_1 and η_2.

Direct Kinematic Measurement One of the most model-independent and direct ways to investigate the absolute neutrino mass scale is via a precise measurement of the kinematics during β-decay. Since some of the decay energy Q has to be used to create the mass of the electron anti-neutrino m_i, the (maximal) kinetic energy of the electron reduces. This leads to spectral distortion of the electron energy spectrum near its endpoint energy E_0. In principle, as the electron anti-neutrino $\bar{\nu}_e$ is an admixture of the different mass eigenstates ν_i, the emitted electron spectrum carries the imprint of all mass eigenstates m_i. However, as the current energy resolution at which the electron energy spectrum can be measured ($\mathcal{O}(1\,\text{eV})$) is much larger than the mass splitting of the (active) neutrinos, only the effective electron anti-neutrino mass m_β shown in Equation (2.34) can be observed.

$$m_\beta = \sqrt{\sum_{i=1}^{3} |U_{ei}|^2 m_i^2} \tag{2.34}$$

In contrast to the Majorana mass term $m_{\beta\beta}$, it is the incoherent sum, which means that the contributions of the individual mass eigenstates m_i are positive and can not cancel each other. As a consequence, together with the measured oscillation parameters, a lower limit

on the effective neutrino mass of $m_\beta > 8.5\,\text{meV}$ for normal neutrino mass ordering (NO) and $m_\beta > 48\,\text{meV}$ for inverted neutrino mass ordering (IO) can be calculated. The current world-leading upper limit given in Equation (2.35) is set by the KATRIN experiment [12].

$$m_\beta = 0.45\,\text{eV} \;\; 90\,\%\;\text{C.L.} \tag{2.35}$$

It uses the principle of a magnetic adiabatic collimation with electrostatic (MAC-E) filter to precisely investigate the electron energy near the tritium endpoint energy E_0. Further details on the tritium decay and the experimental setup are given in Chapter 3.1.

2.3 Why is the Neutrino Mass so Particular?

All charged fermions in the SM are Dirac particles and acquire their mass via the Higgs mechanism. The Higgs field Φ is a scalar field (i.e., it has no spin) with an electric charge and an electrically neutral component $\Phi = (\Phi^+, \Phi^0)^T$ which allows writing down the corresponding Dirac mass term m_D involving both the left-handed l_L and right handed l_R doublets of the leptons l. Following the derivation in [3, 10] the Dirac mass term is given by Equation (2.36).

$$\mathcal{L}_D = -\underbrace{\frac{yv}{\sqrt{2}}}_{m_D}(\bar{l}_L l_R + \bar{l}_R l_L) \tag{2.36}$$

Here, $v \approx 246\,\text{GeV}$ is the non-vanishing vacuum expectation value of the Higgs field Φ, and y is the Yukawa coupling constant that generates the Dirac mass term $m_D \equiv yv/\sqrt{2}$. This mechanism works for all fermions in the SM with the exceptions of neutrinos, since they do not have their corresponding right-handed particles and left-handed antiparticles.

One simple solution to this problem is the addition of three additional right-handed neutrino eigenstates as an extension to the SM. Since they are neutral, colorless, and carry no weak charge, they do not interact with any SM force and are often called sterile. However, they do participate in the mixing of the neutrino flavors, and therefore, the PMNS matrix extends to a 6×6 matrix. With the addition of these three additional neutrinos, it is possible to construct the neutrino Dirac mass term via the Higgs mechanism as shown in Equation (2.36). Consequently, the masses are generated via the Yukawa interactions identical to the other fermions in the SM. However, since the neutrino masses ($m_\nu \leq 0.45\,\text{eV}$ [12]) are tiny compared to the vacuum expectation energy $v = 246\,\text{GeV}$ an unnatural small Yukawa coupling of $y_\nu \leq 10^{-12}$ would be necessary to explain the lightness of the neutrinos.

Yet, since neutrinos are neutral, they could be in principle their own anti-particle, also known as Majorana particles. Therefore, a more general Euler-Lagrangian $\mathcal{L}_{\nu,\,\text{mass}} = \mathcal{L}_D + \mathcal{L}_M$ can be constructed. The additional Majorana coupling is shown in Equation (2.37). For more details on the derivation, refer to, e.g., [10].

$$\mathcal{L}_M = -\frac{1}{2}m_L(\bar{\nu}_L^c \nu_L + \bar{\nu}_L \nu_L^c) - \frac{1}{2}m_R(\bar{\nu}_R^c \nu_R + \bar{\nu}_R \nu_R^c) \tag{2.37}$$

Here, the terms m_L and m_R denote the additional Majorana mass terms related to the left-handed (active) neutrinos ν_L and the right-handed (sterile) neutrinos ν_R. This equation also indicates that the eigenstates ν_L (ν_R) couple to their charge conjugate ν_L^c (ν_R^c) via the

corresponding Majorana mass term m_L (m_R). The combination of the Dirac mass therm and Majorana mass term is given in Equation (2.38).

$$\mathcal{L}_{\nu,\,\text{mass}} = \mathcal{L}_D + \mathcal{L}_M = -\frac{1}{2}(\bar{\nu}_L, \bar{\nu}_L^c) \begin{pmatrix} m_L & m_D \\ m_D & m_R \end{pmatrix} \begin{pmatrix} \nu_R^c \\ \nu_R \end{pmatrix} + \text{ h.c.} \tag{2.38}$$

As a reminder, for the derivation of Equation (2.38), three additional right-handed neutrino fields ν_R have been assumed, leading to a 6×6 mass matrix. To obtain the corresponding six mass eigenvalues, the matrix has to be diagonalized. For the simplest case[6] in which $m_L = 0$ the described Dirac case (see above) and the Seesaw mechanism[7] type I:

Seesaw Type I Under the assumption that $m_R >> m_D$, the matrix can be block-diagonalize [3] and the mass eigenstates are then given by Equation (2.39) and Equation (2.40).

$$m_a = \frac{m_D^2}{m_R} << m_D \tag{2.39}$$

$$m_s = m_R \left(1 + \frac{m_D^2}{m_R^2}\right) \approx m_R \tag{2.40}$$

Commonly, the small masess m_a are associated with the three active neutrinos in the SM to fulfill the above-mentioned boundaries due to the Yukawa coupling constants. The large Majorana mass terms m_s are associated with the added sterile neutrino flavor and effectively suppress the active neutrino masses m_i. Without any further assumptions, no limit is set to the Majorana mass terms m_s, such that it can explain the lightness of the neutrino mass on the sub-eV scale. An important consequence of the Seesaw mechanism type I is that for every non-vanishing (active) neutrino mass m_i, one sterile neutrino with a non-vanishing active-sterile mixing θ_{is} and a large Majorana mass $m_R \geq \mathcal{O}(\text{GeV})$ is needed [4]. It is important to note that for a heavy sterile neutrino N_1 which would act like dark matter, its active-sterile mixing θ_{is} must be tiny to ensure its stability on the timescale of the universe [2, 39]. Therefore, a dark matter sterile neutrino can not simultaneously explain the lightness of the active neutrinos.

The Neutrino Minimal Standard Model Using the principle of Ockham's razor, which tries to minimize the number of new particles while maximizing the number of problems in physics it solves, one can construct the neutrino minimal Standard Model (νMSM). In this framework, three right-handed neutrinos are introduced, with their corresponding masses and couplings tuned to explain the lightness of the active neutrinos, generate the baryon asymmetry via leptogenesis in the early universe, and provide a suitable dark matter candidate [2, 3]. Two very heavy sterile neutrinos ($\mathcal{O}(\text{GeV})$) are introduced to explain the lightness of (two) active neutrinos and create a baryon asymmetry via the leptogenesis. The other sterile neutrino has a mass in the order of keV to be a good dark matter candidate [2]. If it were lighter, the free streaming length would be too large, smearing out small-scale structures, which is not observed. If it were much larger (like the other two introduced sterile neutrinos), it would decay quickly, and none of it would be left today. An illustration of the influence of different sterile neutrino masses on different physics questions is given in Figure 2.5.

[6] The more complex models with $m_L \neq 0$ like, e.g., the seesaw type II mechanism, can be found in [3].

[7] The name seesaw originates from the fact that the heavier the (sterile) neutrino mass m_S, the lighter the (active) neutrino mass m_a, which would be an explanation for the lightness of the (active) neutrinos.

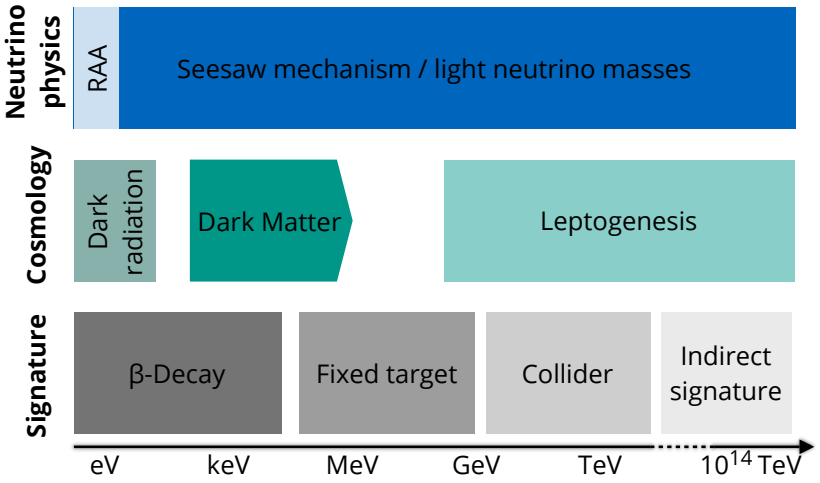

Figure 2.5: Illustration of the influence of sterile neutrino mass ranges on physics
Depending on the mass of a sterile neutrino it has different effects on neutrino physics, cosmology and accessible experiments in the laboratory. The abbreviation RAA stands for reactor anti-neutrino anomaly described in, e.g., [4]. Figure adapted from [2].

2.4 Sterile Neutrinos as Dark Matter

As sterile neutrinos must be produced in the early Universe at high temperatures to be dark matter, the available parameter space (m_s, θ_s) can be constrained by their possible production mechanism. The Dodelson-Widrow and Shi-Fuller mechanisms are introduced in Chapter 2.4.1. In addition, the consideration of the available phase space for dark matter and the limits derived form the (non-)observation of a potential sterile neutrino decay signal are discussed in Chapter 2.4.2. The laboratory limits from the kinematic investigation of a potential sterile neutrino production in β-decay and EC are being discussed at the end in Chapter 2.4.3.

2.4.1 *Sterile Neutrino Production Mechanism*

To create the right abundance of dark matter while being stable on the timescale of the universe, the interaction and mixing of the keV sterile neutrino need to be feeble. Consequently, it is never in thermal equilibrium with the primordial plasma, and the production happens via the active-sterile mixing θ_{is}. In this chapter, different possible production mechanisms (freeze-in) and their constraints on the keV sterile neutrinos parameter space are summarized. For a more detailed discussion, refer to, e.g., [2–4]. To simplify the discussion, only one active neutrino flavor ν_a and one sterile neutrino flavor ν_s are being considered. Analog to Equation (2.24) the mixing between the two mass eigenstates $|\nu_1\rangle$ and $|\nu_4\rangle$ is denoted as θ_s.

Non-Resonant Production (Dodelson-Widrow) The simplest and most robust form of keV sterile neutrino production in the early universe is via the Dodelson-Widrow mechanism [40]. While the active neutrinos $|\nu_a\rangle$ are in thermal equilibrium with the primordial plasma of SM particles, the sterile neutrino $|\nu_s\rangle$ are out of thermal equilibrium and have a negligible initial abundance. However, the constantly produced active neutrino eigenstates $|\nu_a\rangle$ can oscillate into a tiny fraction of sterile neutrinos $|\nu_s\rangle$ via the coherent oscillation, suppressed by its mixing amplitude $|U_{e4}|^2 = \sin^2(\theta_s)$. In addition, sterile neutrinos $|\nu_s\rangle$ can be produced via scattering, with the primordial plasma mediated by the weak interaction. This destroys the coherence of the mass eigenstates $|\nu_i\rangle$ and projects them into one of the flavor eigenstate $|\nu_a\rangle$

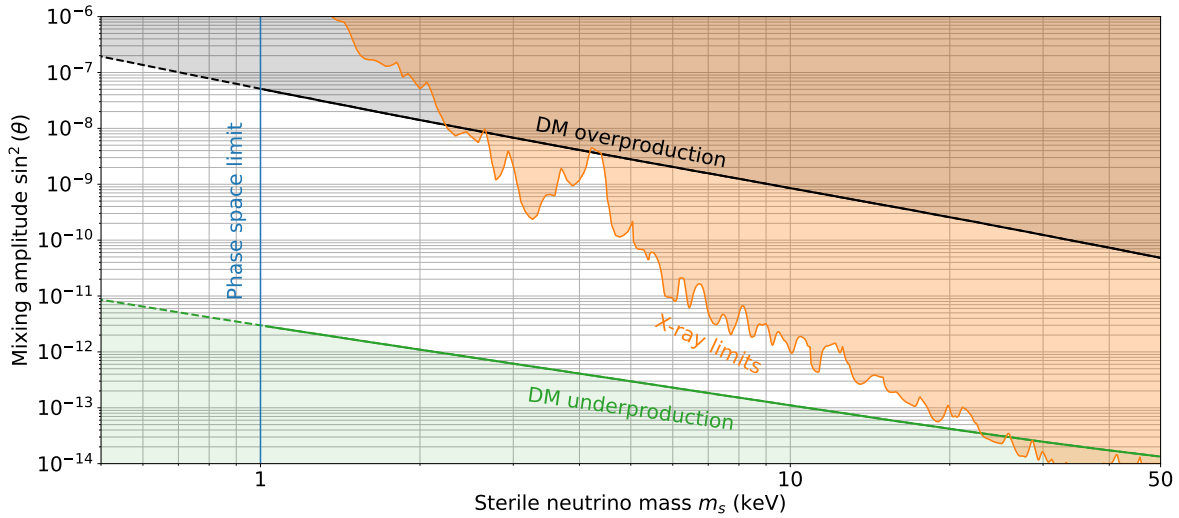

Figure 2.6: Cosmological bounds on keV sterile neutrinos
The upper straight line corresponds to the non-resonant production of sterile neutrino dark matter using the Dodelson-Widrow mechanism [40]. The lower straight line corresponds to the dark matter underproduction limit using the Shi-Fuller production mechanism [41]. The X-ray limits at 95 % C.L. are extracted from [2, 42–46]. Figure adapted from [47].

or $|\nu_s\rangle$. Since the active neutrinos $|\nu_a\rangle$ start oscillating again into a small fraction of sterile neutrinos $|\nu_s\rangle$ after many collisions, a sizable abundance of sterile neutrinos $|\nu_s\rangle$ is produced. The amount of dark matter produced depends in this mechanism only on the sterile neutrino mass m_s and the active-sterile mixing angle θ_s and leads to the solid black line in Figure 2.6 if one assumes that all dark matter is made of keV sterile neutrinos. For larger mixing angles θ_s, too much dark matter would be produced, effectively creating an upper bound.

Resonant Production (Shi-Fuller) The next simplest mechanism is the Shi-Fuller mechanism [41], which includes the possibility of a resonant production due to a Mikheyev-Smirnow-Wolfenstein (MSW) effect caused by a lepton asymmetrie present in the early universe. Similar to the MSW effect in the Sun, the transition between the active and sterile neutrino flavor eigenstate is enhanced, resulting in a larger production rate compared to the Dodelson-Widrow mechanism. Its effect scales with the amount of lepton asymmetry present at the time before the decoupling of neutrinos and allows the creation of the correct amount of dark matter with a smaller sterile mixing θ_s. However, observations of the Big Bang nucleosynthesis (BBN) constrain the value of the maximal possible lepton asymmetry, creating a lower bound in the sterile neutrino parameter space [4]. This lower bound is denoted as DM underproduction in Figure 2.6.

2.4.2 *Cosmological Constrains*

From observations of the dark matter density and emitted X-ray spectrum of cosmological objects, different limits on the sterile neutrino parameter space (m_s, θ_s) can be derived. The most important ones are summarized below. For more details, refer to, e.g., [2–4].

Phase Space Considerations A very robust lower limit on the mass of any fermionic dark matter, therefore also sterile neutrinos, is given by the Termaine-Gunn bound [48]. It assumes that the total phase-space density of a fermionic dark matter particle must follow the Pauli principle and, consequently, can not exceed the density of a degenerated Fermi gas. Using this assumption, bounds on the sterile neutrino mass m_s can be derived from observations

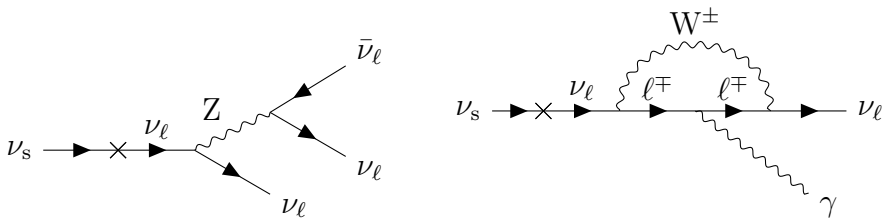

(a) Primary decay channel **(b)** Secondary decay channel

Figure 2.7: Leading Feynman diagram of sterile neutrino decay channels
(a) Primary decay channel of a sterile neutrino ν_s to three (active) neutrinos. (b) Secondary decay channel of a sterile neutrino ν_s to a ligher (active) neutrino flavor under the emission of a X-ray. Figures adapted from [4] and [35].

of the dark matter content in dwarf spheroidal satellites of our Milky Way. Depending on the assumptions taken into account, the limits range from 0.2 keV up to 6 keV [4]. A recent study which uses more robust assumptions independent of the dark matter formation model finds a lower limit of $m_s \gtrsim 0.1$ keV.

Decay of Sterile Neutrinos The decay of a sterile neutrino with a mass m_s smaller than twice the electron mass (1022 keV) is dominated by its decay into the three lighter neutrinos as shown in Figure 2.7a. If one requires that the corresponding process is (much) longer than the age of the Universe, an upper limit on the mixing amplitude $\sin^2(\theta_s)$ can be derived as depicted in Equation (2.41) [4].

$$\sin^2(\theta_s) < 3.3 \cdot 10^{-4} \left(\frac{10\,\text{keV}}{m_s} \right) \tag{2.41}$$

Suppressed by a factor of $1/128$, the radioactive decay to a light neutrino and a photon is possible as shown in Figure 2.7b. Due to energy and momentum conservation (assuming the emitted neutrino has only a tiny mass), the photon is created with an energy of $E_\gamma = 1/2 \cdot m_s$. As a result, the decay of the sterile neutrino would create a mono-energetic signal emitted from regions with a large dark matter density proportional to $\sin^2(\theta_s) \cdot m_s^5$ [4]. Even though the decay rate is tiny, modern X-ray telescopes see about $10 \cdot 10^{78}$ dark matter particles inside their line of sight to nearby galaxy clusters. A potential signal may be detectable as an unexplained line that cannot be emitted by the cosmological objects in their field of view. An overview of the different X-ray searches is given in [2]. The derived exclusion limits shown in Figure 2.6 also include more recent observations in [42–46, 49]. In 2014, the XMM-Newton data observed an unidentified X-Ray line at around 3.55 keV, which would potentially correspond to a sterile neutrino with a mass of $m_s \approx 7.1$ keV [50]. However, recent reviews of this line seem to rule out the dark matter interpretation [4, 51]. Alternative detection mechanisms of earth-bound detectors via the scattering or neutrino capture of dark matter sterile neutrinos are discussed in [2].

2.4.3 *Laboratory Based Constrains*

On the laboratory scale on Earth, keV sterile neutrinos can be investigated through their production mechanism in β-decay or EC. In the case of β-decay, the measured electron spectrum is a superposition containing all neutrino mass eigenstates m_i, including a sterile mass eigenstates m_s that are smaller than the decay energy Q. The existence of a sterile neutrino would lead to a spectral distortion with a kink-like signature at an energy

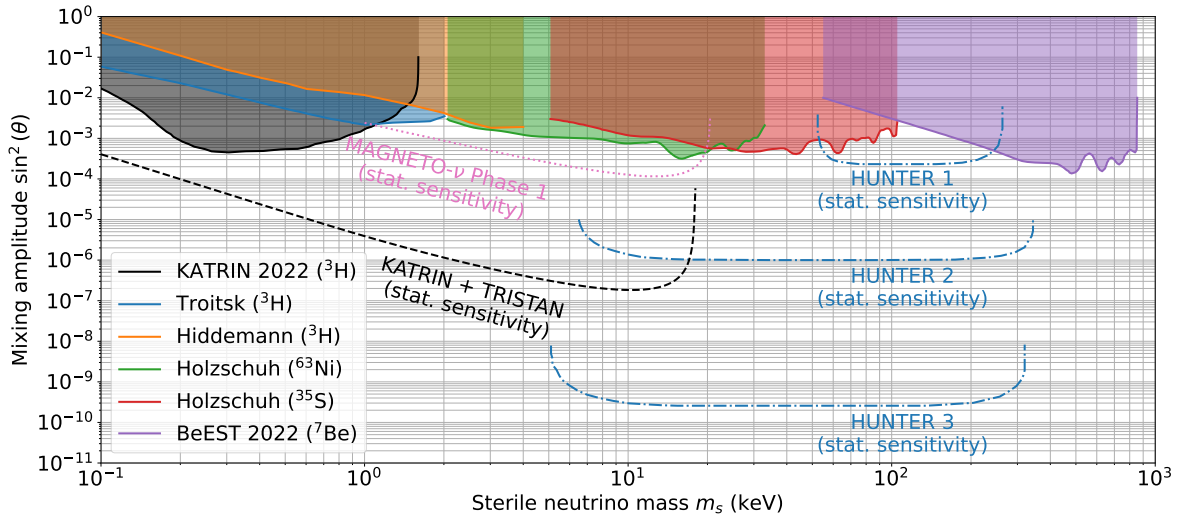

Figure 2.8: Laboratory limits on the keV sterile neutrino parameter space
The excluded regions are illustrated by the semi-transparent areas with a 95 % C.L. [52–54, 56]. They include the KATRIN limit derived from the low activity tritium data set acquired in the commissioning run in 2018 [56]. The projected statistical sensitivity of the keV sterile neutrino search of the KATRIN experiment with its upcoming detector upgrade TRISTAN is shown as the dashed black line. In addition, the statistical sensitivity of the first phase of the MAGNETO-ν experiment (pink dotted) [57] and the HUNTER phases (dashed dotted blue) [58] are shown. Figure adapted from [47].

below $E_0 - m_s$ (see Chapter 3.2). In the case of the EC, the same information is contained in the energy spectrum of the atomic recoil instead. The current laboratory limits derived from high-precision spectroscopy measurements of different β-decaying isotopes and the EC of ^{7}Be are illustrated in Figure 2.8 [52–56]. The limits include the investigations of the commissioning run of the KATRIN experiment at a low source activity of around 0.5 % compared to the nominal settings [56]. In the near future, the KATRIN experiment will be upgraded with the TRISTAN detector system to perform a keV sterile neutrino search over the entire tritium spectrum. The expected statistical sensitivity is illustrated by the dotted black line [47]. More details on the KATRIN experiment and the TRISTAN detector upgrade are given in Chapter 3.

Apart from the keV sterile neutrino search with KATRIN, multiple experiments are upgraded and constructed to extend the limits on keV sterile neutrinos. In the case of the BeEST experiment, the upcoming phases, III and IV, will improve their statistics by more than two orders of magnitude, significantly improving their sensitivity in the on the sub-MeV scale [55]. Furthermore, the MAGNETO-ν experiment is currently investigating the β-decay of ^{241}Pu ($Q \approx 20.8\,\text{keV}$) implanted in magnetic microcalorimeter [57]. An alternative approach is preceded by the heavy unseen neutrinos from total energy-momentum reconstruction (HUNTER) experiment, which plans to investigate the EC of ^{137}Cs ($\tilde{Q} \approx 320\,\text{keV}$) in a magento-optical trap where they can measure the atomic recoil energy by time of flight [58]. Due to the larger decay energy, the projected sensitivities are complementary to the keV sterile neutrino search with KATRIN.

In comparison to the limits obtained from cosmological observations shown in Figure 2.6, the laboratory limits are much weaker. However, since the sterile neutrino ν_s is directly produced in the laboratory measurements, they do not rely on any cosmological model or assumption like the dark matter production or interaction. In a study by C. Benso [59], different influences on the production and decay of keV sterile neutrinos

have been investigated that could lead to a (large) reduction of the limits set by X-ray observations. One of the simplest examples would be the case that sterile neutrinos only contribute to about 1 % to 10 % of the dark matter content in the universe. In this scenario, the X-ray constraints in the mass range of $m_s \lesssim 10\,\text{keV}$ reduces down to the accessible region of the keV sterile neutrino search with KATRIN.

3

THE KATRIN EXPERIMENT AND THE TRISTAN DETECTOR UPGRADE

The Karlsruhe Tritium Neutrino (KATRIN) experiment is designed to measure the spectral distortion of the tritium β-decay spectrum near its endpoint energy E_0, to determine the effective electron anti-neutrino mass m_β with a sensitivity better than 300 meV [5, 60]. The data taking for the neutrino mass measurement campaign is foreseen to continue until the end of 2025. Subsequently, a high-statistic measurement of the full tritium β-decay spectrum will be performed to search for a keV-scale sterile neutrino with a sensitivity on the mixing amplitude $\sin^2(\theta)$ on the ppm level [7, 61]. To this end, the KATRIN experiment will be modified, and the new TRISTAN detector system will be installed. It is capable of handling the necessary high rates in the order of 10^8 cps while maintaining a good energy resolution of better than 300 eV at 20 keV.

First, the KATRIN experiment is introduced in the context of the neutrino mass measurement, in Chapter 3.1. Then, the TRISTAN detector upgrade for the keV sterile neutrino search with the KATRIN experiment is being discussed in Chapter 3.2.

3.1 Neutrino Mass Measurement with the KATRIN Experiment

In this chapter, the KATRIN experiment is detailed in the context of the currently ongoing neutrino mass measurement campaigns. An introduction to the tritium β-decay and its imprint of the neutrino masses is given in Chapter 3.1.1. The MAC-E filter principle used in the KATRIN experiment to measure the tritium β-decay spectrum in an integral way is described in Chapter 3.1.2. A summary of the technical realization and the most important parts of the KATRIN experiment is given in Chapter 3.1.3. At the end, the most recent neutrino mass limits are given in Chapter 3.1.4.

3.1.1 *Tritium β-Decay Spectrum*

The tritium β-decay is well-suited for the investigations of the effective electron anti-neutrino mass m_β since it is a supper-allowed decay ($T_{1/2} \approx 12.33$ yrs) with a comparably low kinematic endpoint energy $E_0 \approx 18.6$ keV [62]. It decays to ^{3}He under the emission of an electron e^- and an electron anti-neutrino $\bar{\nu}_e$ as shown in Equation (3.1).

$$T \rightarrow {}^3\mathrm{He}^+ + e^- + \bar{\nu}_e + Q \tag{3.1}$$

The decay energy Q is given by the mass difference between the mother nucleus m_T and the daughter nucleus m_He plus the electron mass m_e. This energy Q is shared between the kinetic energy E of the electron, the involved masses m_i and kinetic energy E_ν of the neutrino, and

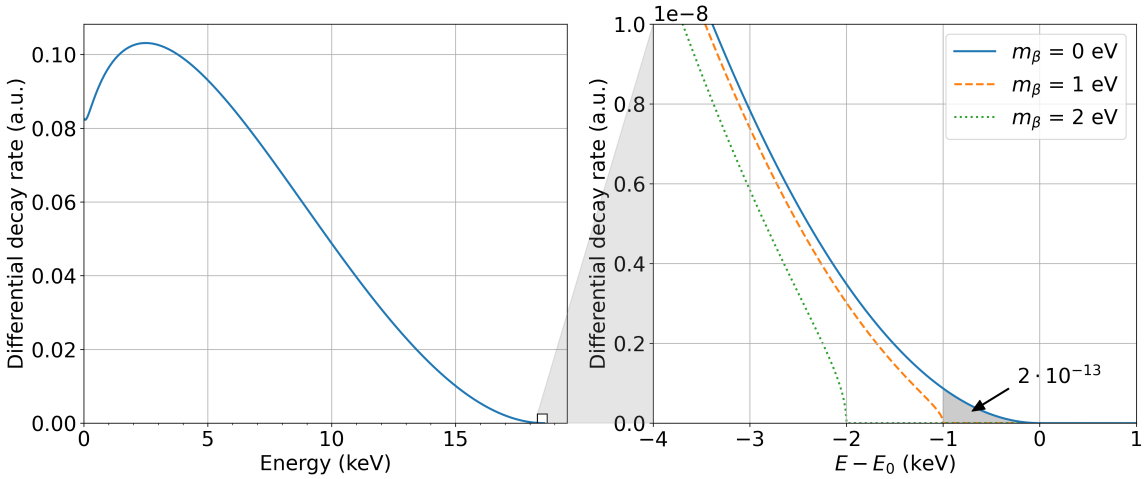

Figure 3.1: Entire tritium β-decay spectrum and zoom on endpoint region
In the figure on the left-hand side the entire β-decay spectrum of the measured electron is shown. On the right-hand side, a zoom is provided on the endpoint region. The lines illustrate the effect of different neutrino masses m_β on the kinetic endpoint region E_0. In comparison to the entire energy spectrum, only around $2 \cdot 10^{-13}$ electrons have an in the region between E_0 and $E_0 - 1\,\text{eV}$. Figure adapted from [63].

the nuclear recoil energy E_{rec} of the ^{3}He atom. Consequently, the maximal energy of the electron, also known as the kinematic endpoint energy E_0, is given by Equation (3.2).

$$E_0 = Q - E_{\text{rec}} - m_i \tag{3.2}$$

From this relation, it is clear that the region near the kinematic endpoint E_0 is affected by the (small) value of the active neutrino masses. The simplest case assuming only one effective electron neutrino mass m_β involved in the β-decay is depicted in Figure 3.1. The spectral shape near the endpoint and the absolute value of the endpoint energy E_0 shift depending on the value of the effective electron neutrino mass m_β. This effect can also be seen in the formula for the tritium β-decay probability using Fermi's golden rule as shown in Equation (3.3) [16, 62].

$$\frac{\mathrm{d}\Gamma(E; m_i)}{\mathrm{d}E} = \frac{G_F^2 |V_{ud}|^2}{2\pi^2} |M_{\text{nuc}}|^2 \cdot F(Z, E) \cdot E_e p_e E_\nu \sum_i |U_{ei}|^2 \underbrace{\sqrt{E_\nu^2 - m_i^2}}_{p_{\nu,i}} \tag{3.3}$$

Here, G_F denotes the Fermi constant and $F(Z, E)$ the energy-dependent Fermi function. The Cabibbo-Kobayashi-Maskawa (CKM)-matrix element between the up u and down d quark is denoted as V_{ud} and the energy independent nuclear matrix element as M_{nuc}. Furthermore, the total energy and momenta of the electron and neutrino are given as $E_{e/\nu}$ and $p_{e/\nu}$, respectively. Since Equation (3.3) depends on the sum of the different mass eigenstates m_i weighted by the PMNS-mixing amplitudes $|U_{ei}|$, the resulting electron energy spectrum is a superposition of them. This means that, in theory, each individual neutrino mass m_i creates spectral distortion and shift of the kinematic endpoint energy E_0, depending on its value and mixing. However, since the neutrino mass differences $\Delta m_{ij}^2 \lesssim 25 \cdot 10^{-4}\,\text{eV}^2$ [1, Ch. 14] measured via oscillation experiments are much smaller than the currently possible energy resolution of around 1 eV, they can not be resolved experimentally. Therefore, commonly,

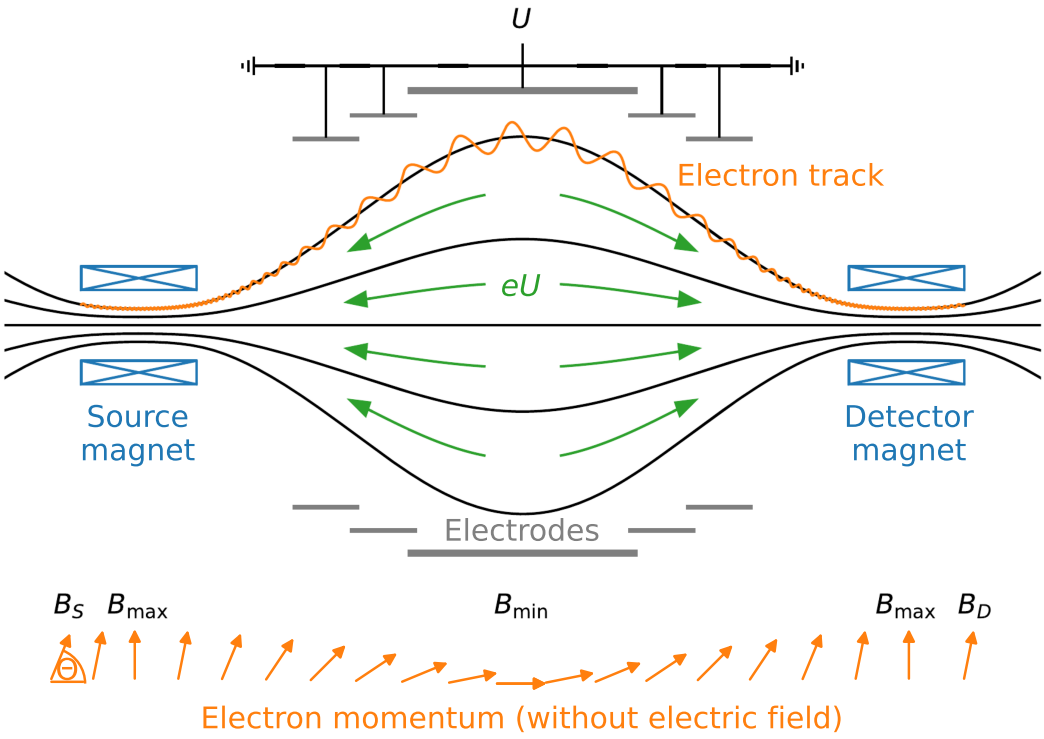

Figure 3.2: Illustration of the MAC-E filter principle
Cross-section of a MAC-E filter along its radial symmetry axis. Two cylindrical superconducting magnets (blue) form the magnetic field (black). The orange curve along the magnetic field lines depicts the electron cyclotron motion, and its momentum direction is illustrated by the arrows at the bottom of the graphic. The electron starts in the source section at a magnetic field B_s and travels towards the analyzing plane at the magnetic field B_min. A set of cylindrical retarding electrodes (grey) form the electric retarding potential eU illustrated by the green arrows. Electrons with a high enough momentum surpass the electric retarding potential and are counted at the detector behind the superconducting magnet. The magnetic field strength at the detector is denoted as B_D. Adopted from [66].

the effective electron neutrino mass m_β (see Equation (2.34)) is assumed. In this case, Equation (3.3) simplifies to Equation (3.4), which was also used to generate Figure 3.1.

$$\frac{\mathrm{d}\Gamma(E;m_\beta)}{\mathrm{d}E} \propto C \cdot F(Z,E) \cdot (E+m_e) \cdot p \cdot (E_0-E) \cdot \sqrt{(E_0-E)^2-m_\beta^2} \tag{3.4}$$

3.1.2 *MAC-E Filter Measurement Principle*

In the KATRIN experiment, the principle of a magnetic adiabatic collimation with electrostatic (MAC-E) filter [64, 65] is used to determine the effective electron neutrino mass with a final sensitivity $m_\beta \leq 300\,\mathrm{meV}$ [5, 12]. The general principle of a MAC-E filter is illustrated in Figure 3.2. It acts as a high-pass filter for electrons and only transmits them if their energy E is higher than the applied retarding potential eU. Here, e denotes the elementary charge of an electron, and U the applied voltage to the electrode system. Two superconducting solenoid

magnets located on each side of the spectrometer form an axial symmetrical magnetic field[1]. The so-called analyzing plane is located in the center between the two magnets, where the minimal magnetic field B_{min} and the maximal (negative) retarding potential eU is present. The magnetic field strength B_{min} is many orders of magnitude smaller than the magnetic field strength B_{max} inside the two magnets and the source section B_{S}. If an electron is emitted from the source section towards the analyzing plane, they are guided by the magnetic field into the spectrometer between the two magnets. It performs a cyclotron motion on its path due to the Lorentz force. Hence, its momentum can be separated into a transversal (perpendicular) component $p_{\perp}$ and a longitudinal (parallel) component $p_{\parallel}$ with respect to the magnetic field. Under the assumption that the electron's motion is adiabatic[2], its orbital magnetic momentum μ given in Equation (3.5) stays constant. Here, the radius of the cyclotron motion is denoted as r, the electron velocity perpendicular to the magnetic field as v, and the magnetic field strength as B. Due to the decrease in magnetic field strength from B_{max} to B_{min}, the transversal momentum $p_{\perp}$ decreases as shown in Equation (3.6). Since the total energy of the electron is conserved its transversal momentum $p_{\perp}$ is transformed into a longitudinal momentum $p_{\parallel}$, reaching the maximal longitudinal momentum in the analyzing plane at B_{min}.

$$\mu = \frac{1}{2} erv = \frac{p_{\perp}^2}{2m_e B} = \frac{E_{\perp}}{B} = \mathrm{const}, \text{ using } E_{\perp} = \frac{p_{\perp}^2}{2m_e} \tag{3.5}$$

$$\Leftrightarrow \frac{E_{\perp}^{\mathrm{max}}}{B_{\mathrm{max}}} = \frac{E_{\perp}^{\mathrm{min}}}{B_{\mathrm{min}}} \tag{3.6}$$

The retarding potential eU is applied by a set of cylindrical electrodes, which form an electrostatic barrier for (only) the longitudinal momentum component $p_{\parallel}$ of the electrons. Therefore, only electrons with longitudinal kinetic energy $E_{\parallel} = p_{\parallel}^2/(2m_e)$ larger than the retarding potential eU can surpass this barrier and get re-accelerated and focused onto the detector behind the analyzing plane. By varying the retarding potential eU in small steps dE and counting the number of electrons arriving at the detector $d\Gamma(E)$, the integral energy spectrum $\Gamma(eU)$ of the electrons emitted in the source can be measured as shown in Equation (3.7).

$$\Gamma(eU) = \int_{eU}^{E_0} \frac{\mathrm{d}\Gamma(E)}{\mathrm{d}E} \mathrm{d}E \tag{3.7}$$

The energy resolution ΔE of this MAC-E filter principle is given by the fraction between the minimal and maximal magnetic field strength B_{min} and B_{max}, respectively as shown in Equation (3.8). Loosely speaking, the energy resolution ΔE is created by the remaining transversal energy $E_{\perp}^{\mathrm{min}}$ in the analyzing plane, which is not seen by the electric potential eU. The exact derivation for this formula can be found in [62].

$$\frac{\Delta E}{E} = \frac{B_{\mathrm{min}}}{B_{\mathrm{max}}} \tag{3.8}$$

[1] In a real experiment like KATRIN, additional solenoid magnets are placed round the spectrometer to further shape the magnetic field and compensate for the Earth's magnetic field. Here, they are omitted for simplicity reasons.

[2] The adiabatic approximation holds if the change in magnetic field strength $\frac{d\hat{B}}{dt}$ on its path into the spectrometer is small compared to the parallel momentum $p_{\parallel}$ of the electron: $\left|\frac{1}{B}\frac{d\hat{B}}{dt}\right| << \omega_c = \frac{eB}{\gamma m_e}$, where $\hat{B}$ describes the magnetic field vector and ω_c the electron cyclotron frequency. The charge and mass of the electron are denoted as e and m_e, respectively. The relativistic factor of the electron is given as γ. [62]

The ratio between the transversal and longitudinal momentum component $p_\perp$ and $p_\parallel$ of the electron is described by the angle θ shown in the bottom of Figure 3.2. If an isotropic electron source would be placed at the position of the maximal magnetic field B_{max}, half of the electrons would be emitted towards the analyzing plane and could be measured. In this case, the acceptance angle Θ_{max}, defined as the largest angle under which an electron can be emitted to still enter the spectrometer, is $\pi/2$. In practice, this acceptance angle Θ_{max} is chosen to be smaller since it increases its longitudinal momentum and reduces the traveled distance of the electrons in the source section. On their path through the source, they scatter with the residual gas of the source and lose part of their energy. Lowering the magnetic field in the source section to $B_{\mathrm{S}} < B_{\mathrm{max}}$ leads to a reduction of the maximal acceptance angel Θ_{max} as shown in Equation (3.9). An electron that is emitted in the source with an angle below the maximal acceptance angel Θ_{max} passes through the maximal magnetic field B_{max} with (almost) only transversal energy, while any electron emitted under a larger angle is reflected at the position of the maximal magnetic field B_{max}.

$$\theta_{\mathrm{max}} = \arcsin\left(\sqrt{\frac{B_{\mathrm{S}}}{B_{\mathrm{max}}}}\right) \tag{3.9}$$

Using the KATRIN design values of $B_{\mathrm{max}} = 6\,\mathrm{T}$, $B_{\mathrm{min}} = 0.3\,\mathrm{mT}$, and $B_{\mathrm{S}} = 3.6\,\mathrm{T}$ [60] an energy resolution of $\Delta E \approx 0.93\,\mathrm{eV}$ at the tritium endpoint energy of $E_0 \approx 18.6\,\mathrm{keV}$ and a maximal acceptance angle of $\Theta_{\mathrm{max}} \approx 51°$ can be calculated. At the time of writing, the applied settings in the KATRIN experiment are set to $B_{\mathrm{max}} = 4.2\,\mathrm{T}$, $B_{\mathrm{min}} = 0.6\,\mathrm{mT}$ and $B_{\mathrm{S}} = 2.53\,\mathrm{T}$ [5]. The energy resolution is therefore higher at $\Delta E = 2.77\,\mathrm{eV}$ [5]. In comparison, the energy resolution of the MoS, which is used in this thesis, is $\Delta E \approx 1.08\,\mathrm{eV}$ at the tritium endpoint and has a larger acceptance angle of $\Theta_{\mathrm{max}} \approx 65°$. The magnetic field strength in the MoS are approximately $B_{\mathrm{max}} = 6\,\mathrm{T}$, $B_{\mathrm{min}} = 0.35\,\mathrm{mT}$, and $B_{\mathrm{S}} = 2.5\,\mathrm{T}$. Here it is important to note, that the energy resolution in the order of a few eV is not the limiting factor for a neutrino search with a sensitivity on the neutrino mass $m_\beta \approx 300\,\mathrm{meV}$ but rather the collected signal statistics in the endpoint region [60].

To transport the electrons generated in the source section towards the detector, their path must be free of any obstacles. To estimate the required sizes of the different parts of the experiment the conservation of magnetic flux Φ can be used. Assuming the electrons are generated over a cross-section area A_{S} in a homogeneous magnetic field B_{S} in the source section, the mapped area of electrons traveling through the analyzing plane with a magnetic field strength of B_{min} can be calculated as shown in Equation (3.10).

$$\Phi = \int B\,\mathrm{d}A = B_{\mathrm{S}} \cdot A_{\mathrm{S}} = B_{\mathrm{min}} \cdot A_{\mathrm{max}} = \mathrm{const.} \tag{3.10}$$

The design value for the transported magnetic flux in the KATRIN experiment is $\Phi = 191\,\mathrm{T\,cm^2}$ [60], which is mainly driven by the magnetic field strength B_{S} and diameter of the source section. Using the magnetic field strength of $B_{\mathrm{min}} = 0.3\,\mathrm{mT}$, the electron flux tube has a diameter of 9 m at the position of the analyzing plane. For an experiment like KATRIN the signal statistic and therefore its sensitivity to the neutrino mass m_β is directly proportional to its source strength. Increasing the source strength to some extent requires an increase in source diameter (to reduce scattering with the residual gas molecules),

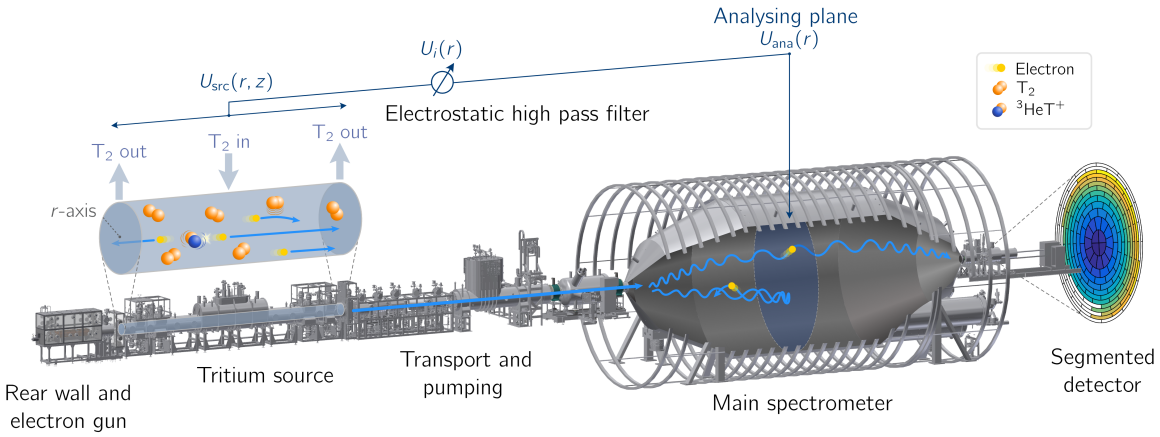

Figure 3.3: Illustration of the KATRIN beamline
The β-electrons generated in the WGTS are magnetically guided through the pumping section to the main spectrometer. The main spectrometer uses the MAC-E filter principle and acts like a high-pass filter on the electrons. The electrons with an energy larger than the applied retarding potential eU at the analyzing plane are then magnetically guided to the FPD and counted. Figure provided by L. Köllenberger.

which increases the size of the magnetic flux tube Φ. This is one of the reasons why the spectrometer of the KATRIN experiment is much larger than its predecessors [60].

3.1.3 *The KATRIN Beamline*

The 70 m long beamline of the KATRIN experiment is illustrated in Figure 3.3. The two main regions of the experiment are the source and transport section (STS), which provides a pure electron flux of 10^{11} cps from the tritium β-decay, and the source and detector section (SDS), which measures the electron energy via the MAC-E filter principle. Inside the STS are the windowless gaseous tritium source (WGTS), and the transport section. The SDS mainly consists of the MAC-E filter spectrometer and the detector section with the FPD. In the following, these components are briefly described. For more details, refer to, e.g., [5].

Windowless Gaseous Tritium Source One of the key parts of the KATRIN experiment is the WGTS, which provides a high and stable electron flux (10^{11} Bq $\pm 0.1\,\%$/h) from the β-decay of tritium. In the neutrino mass measurement, the extremely high rate is required since only a tiny fraction of the electrons end up in the region of interest (ROI) near the kinematic endpoint E_0. The achieved high stability of the decay rate is beneficial to drastically reduce the systematic uncertainty in the integral measurement with the MAC-E filter principle. The WGTS consists of a 10 m long stainless steel tube with a diameter of 90 cm, which is continuously filled with molecular tritium gas T_2 ($p \approx 3 \cdot 10^{-3}$ mbar) through small capillaries placed in the length-wise center. While the injected tritium freely streams to either end of the WGTS, a fraction of it decays. The created β-electrons are guided magnetically ($B_S = 2.53$ T) to either end of the WGTS. Since any material in the path of the electron would alter its energy, no physical window can be placed on the ends of the WGTS to constrain the gas. Instead, the first differential pumping section on either end of the WGTS reduces the tritium density by a factor of 1000 [67]. The removed tritium is purified and re-injected again through the capillaries in the center, creating a closed loop with a stable (nominal) column density of $\rho d = 5 \cdot 10^{17}$ molecules/cm^2 and a tritium purity of $\epsilon_T > 95\,\%$. To ensure the stability of

tritium column density, the entire WGTS is enclosed by a cryostat, keeping the temperature at 30 K in nominal operation.

Transport Section Since any residual tritium inside the spectrometer section would lead to an undesired background, the gas flow from the WGTS is reduced by 14 orders of magnitude inside the transport section. To achieve this reduction, the differential pumping section (DPS) and a cryogenic pumping section (CPS) are located between the WGTS and the spectrometer section. Inside the DPS, five superconducting magnets are placed under an angle of 20° with respect to each other, effectively blocking the direct line of sight between the WGTS and the spectrometer section. Since the electrons are charged, they follow the magnetic chicane. At the same time, the (mostly) neutral gas molecules collide with the wall, thus increasing their likelihood of getting pumped away by the turbo-molecular pumps. In this section, the gas flow is reduced by at least seven orders of magnitude. However, the turbo-molecular pumps are no longer efficient for even lower pressures, and the remaining tritium is removed in the CPS. The same arrangement of the magnets is also applied in the CPS to create the chicane path for the electrons. In addition, the inner surfaces of the beam tube are cooled to 3 K, acting as a cold trap for the remaining gas molecules. To increase the effectiveness of the cold trap, the entire surface is covered with small gold-plated fins, drastically increasing the surface area. Additionally, a small layer of argon frost is condensed on the surfaces, increasing the sticking coefficient. To maintain efficient trapping and remove the frozen tritium, the CPS has to be regenerated periodically by heating it. Furthermore, the small amount of positive tritium ion also emitted from the source is blocked by ring electrodes with a positive electrostatic potential between 5 V to 200 V.

Spectrometer Section The integral measurement of the β-electron energy is done with the Main Spectrometer using the MAC-E filter principle described in Chapter 3.1.2. The main vacuum vessel has a diameter of around 10 m and a length of around 24 m to ensure the adiabatic transport of the electrons while providing a good energy resolution of $\Delta E = 0.93$ eV using the design settings [5]. It is operated at an ultra-high vacuum better than 10^{-11} mbar to guarantee that the electrons do not scatter with the remaining gas molecules and, more importantly, reduce the production of background events. This ultra-low pressure is achieved using a combination of non-evaporable getter pumps and cascades of turbo-molecular pumps. The retarding potential eU at the analyzing plane is created by the vessel potential in combination with the fine wire-electrode system. As any fluctuation of the retarding potential eU leads to an uncertainty on the (integral) electron energy, the sophisticated high-voltage system is designed to be stable on the ppm level [68]. In addition, the applied retarding voltage eU is monitored with a custom build high-precision voltage divider [69].

Detector Section All electrons that overcome the retarding potential eU are magnetically guided to the detector section and are measured on the FPD. The most important parts of the detector section are illustrated in Figure 3.4. Before the electrons reach the FPD, their energy is boosted by 10 keV inside the post acceleration electrode (PAE) to reduce detector systematics like back-scattering, and the energy loss due to the reduced charge collection efficiency (CCE) at the entrance window. The FPD itself is a monolithic silicon positive-intrinsic-negative detector (PIN detector) with a diameter of 125 mm. It consists of 148 pixels with equal surface area arranged in a ring-wise pattern. The main task of the FPD is to count the electron rate. However, using its intrinsic energy resolution of around 2 keV FWHM, different quality cuts to remove background events are being performed. The total rate limit of the FPD is approximates 10^6 cps, which is more than sufficient for the neutrino mass measurement with KATRIN, however, two orders of magnitude below the targeted

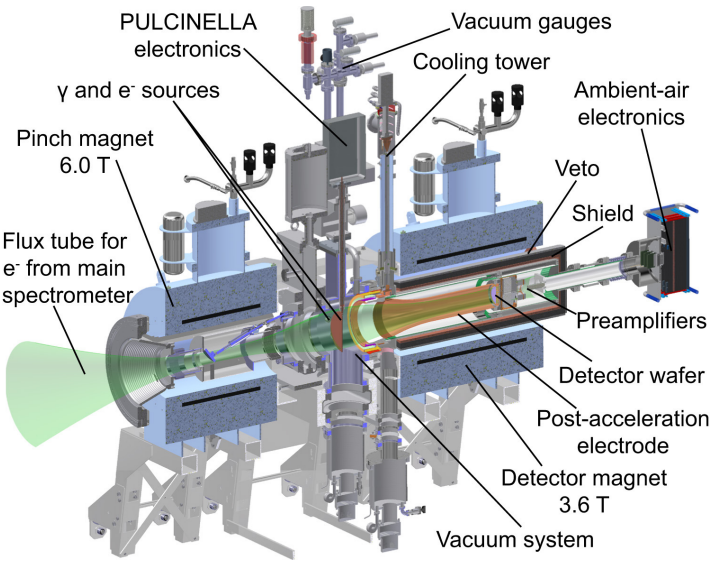

Figure 3.4: Illustration of the KATRIN detector section
Mechanical computer aided design (CAD) cross-section of the main components in the detector section of the KATRIN beamline. The detector section is directly connected to the Main Spectrometer, which would be situated on the left-hand side of this illustration. Under nominal settings, the FPD wafer is situated at a magnetic field strength with a value of $B_{\mathrm{D}} \approx 2.52\,\mathrm{T}$. The figure is taken from [70].

rate for the keV sterile neutrino search. To calibrate the detector with X-rays, an ^{241}Am source can be moved in front of the detector between the two superconducting magnets. In addition, photoelectric electrons can be generated from a titanium disk (called PULCINELLA) illuminated with UV light. Depending on the negative potential applied to the disk, a large-area electron beam with an energy of up to 25 keV can be produced [5].

3.1.4 *Resent Results of the KATRIN Experiment*

The measured integral tritium spectrum is compared to the spectral model given in Equation (3.11) to extract the square of the effective electron anti-neutrino mass m_β^2 and the kinematic endpoint energy E_0 [5].

$$R(eU; E_0, m_\beta^2) = A_{\mathrm{S}} \cdot N_{\mathrm{T,\,eff}} \int_{eU}^{E_0} \frac{\mathrm{d}\Gamma(m_\beta^2, E_0)}{\mathrm{d}E} \cdot f(E, eU)\mathrm{d}E + R_{\mathrm{bg}}(eU) \tag{3.11}$$

The detection rate R is given by the convolution of the differential β-spectrum $\frac{\mathrm{d}\Gamma}{\mathrm{d}E}$ with the experimental response function $f(E-eU)$. Here, A_{S} describes the normalization factor, $N_{\mathrm{T,\,eff}}$ the effective number density of the tritium atoms in the source, and R_{bg} the background rate. More details on the additional systematic parameters, which are included in the experimental response f and the differential β-spectrum $\frac{\mathrm{d}\Gamma}{\mathrm{d}E}$ are given in [71]. In the case that the best-fit of the model to the experimental data is compatible with $m_\beta^2 = 0$, the obtained result is converted to an upper limit on the neutrino mass m_β using the Feldman-Cousins or the Lokhov-Tkachov method [71]. Using the data from the first five measurement campaigns, the KATRIN experiment stets the current world-leading limit on the effective electron anti-neutrino mass m_β shown in Equation (3.12) [12].

$$m_\beta \leq 0.45\,\mathrm{eV}\ (90\,\%\ \ \mathrm{C.L.}) \tag{3.12}$$

The final sensitivity is targeted to be better than $m_\beta \leq 300\,\text{meV}$ after 1000 days of live measurements at the end of 2025.

Since for the measurements of the neutrino mass, the energy spectrum is analyzed down to an energy of 40 eV below the kinematic endpoint energy E_0, the data can also be used to search for a sterile neutrino on the eV mass scale. Up to now, the data from the first two measurement campaigns have been analyzed, and the resulting exclusion limits can be found in [72]. Furthermore, in the commissioning run of the KATRIN experiment at around 0.5 % of the nominal column density, the tritium spectrum has been measured 1.6 keV below the kinematic endpoint energy E_0. The resulting limits of the analysis of the integral tritium spectrum are shown in Figure 2.8 [56].

3.2 keV Sterile Neutrino Search using the TRISTAN Detector Upgrade

In this chapter, the TRISTAN detector upgrade for the keV sterile neutrino search with the KATRIN experiment is being discussed. First, the signature of a keV sterile neutrino and the resulting spectral distortion of the tritium β-decay spectrum are described in Chapter 3.2.1. Then, the technical realization of the TRISTAN detector system is given in Chapter 3.2.2.

3.2.1 *keV Sterile Neutrino Signature in Tritium β-Decay*

As shown in Equation (3.3), the tritium β-decay spectrum is a superposition of all neutrino mass eigenstats m_i weighted by their mixing $|U_{ei}|^2$ with the electron flavor $|\nu_e\rangle$. Consequently, also a keV scale sterile neutrino with a mass smaller than the kinematic endpoint $m_i < Q \approx 18.6\,\text{keV}$ would lead to a spectral distortion deeper inside the tritium β-decay spectrum. Since the mass eigenstates of the light-active neutrinos are tiny compared to a neutrino mass on the keV scale, and their effect deeper inside the spectrum becomes negligible, the superposition of the sterile neutrino mass m_s and the effective (active) neutrino mass m_β is given by Equation (3.13) [4, 6].

$$\frac{\mathrm{d}\Gamma(m_s,\theta_s)}{\mathrm{d}E} = \cos^2(\theta_s)\frac{\mathrm{d}\Gamma(m_\beta)}{\mathrm{d}E} + \sin^2(\theta_s)\frac{\mathrm{d}\Gamma(m_s)}{\mathrm{d}E} \tag{3.13}$$

Here, the keV scale sterile neutrino mass is denoted as m_s and the active-sterile mixing amplitude as $|U_{e4}|^2 = \sin^2(\theta_s)$. An illustration of the effect for a sterile neutrino mass $m_s = 10\,\text{keV}$ with a very large (nonphysical) mixing amplitude of $\sin^2(\theta) = 0.2$ is given in Figure 3.5. Due to the keV sterile neutrino, a distinct spectral distortion with a kink-like feature is introduced at energies below $E_0 - m_s$.

Using the ultra-luminous tritium source of the KATRIN experiment (10^{11} Bq) and a measurement time of three years, in principle a statistical sensitivity in the order of $\sin^2(\theta_s) < 10^{-8}$ would be possible with a differential measurement (assuming $\Delta E \lesssim 500\,\text{eV}$ FWHM) [6]. Even though the energy resolution of a MAC-E filter is much better ($\mathcal{O}(1\,\text{eV})$), the additive nature of the integral measurement reduces the sensitivity by more than one order of magnitude compared to a differential measurement [6, 47]. As the precise spectroscopic measurement at the full source strength of KATRIN is technically very challenging, the keV sterile neutrino search will be performed at a source strength of around 1 % or 10^8 cps. This reduces the sensitivity to around 10^{-6} after one year of measurement time. Since the FPD was never designed for such high rates and has an energy resolution in

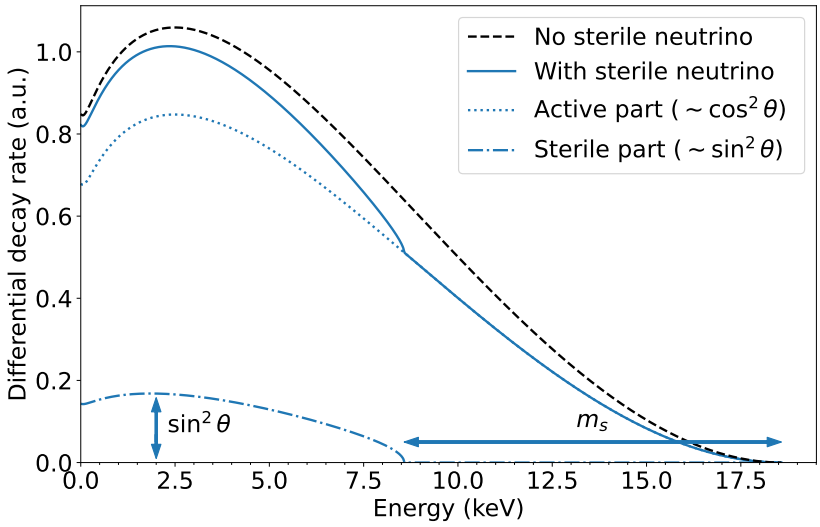

Figure 3.5: Effect of a keV sterile neutrino on the tritium β-decay spectrum
The imprint of a keV sterile neutrino mass of $m_s = 10\,\text{keV}$ with an unphysically large mixing amplitude of $\sin^2\theta = 0.2$ is shown in comparison to the β-decay spectrum without any sterile neutrino mass m_s.

the order of 2 keV FWHM, it will be replaced with the TRISTAN detector system currently in development [7].

3.2.2 *The TRISTAN Detector System*

To achieve a sensitivity on the ppm level, the statistical and systematic uncertainties need to be in the same order of magnitude. The statistical sensitivity can be achieved with a count rate of 10^8 cps for one year of measurement time. To reduce the rate to a technically manageable level of around 10^5 cps, while maintaining a good energy resolution, the TRISTAN detector will consist of around 1000 pixels. Each pixel has a diameter of around 3 mm to optimize and minimize the effects of charge-sharing, detector backscattering, and electric and magnetic back reflection, which influence the detector response [47, 73]. A precise understanding of the detector response is crucial to minimize the systematic effects and maintain the measured spectral shape of the keV sterile neutrino imprint. To this end, an energy resolution of 300 eV at 20 keV is targeted, which necessitates a low level of electronic noise and a thin entrance window in the order of 50 nm. The detector technology that can fulfill these requirements and is used for the TRISTAN detector system are SDDs. More details on the working principe are given in Chapter 4.

In the baseline design, the TRISTAN detector system will consist of nine identical detector modules, each hosting 166 pixels, as shown in Figure 3.6. They are placed next to each other to form the TRISTAN detector system with around 1500 pixels. However, due to the circular geometry of the electron flux tube and the KATRIN beamline, only around 1260 pixels will be illuminated. In this configuration, the TRISTAN detector system can be installed at the position of the FPD with smaller modifications required to the detector section. The integration into the KATRIN beamline is planned after the neutrino mass measurements are completed at the end of 2025. The first physics measurements to search for keV sterile neutrinos are expected to start in 2026. More details on the detector modules themselves and the assembly procedure developed within this work are given in Chapter 5. The first characterization measurements with X-rays and electrons in

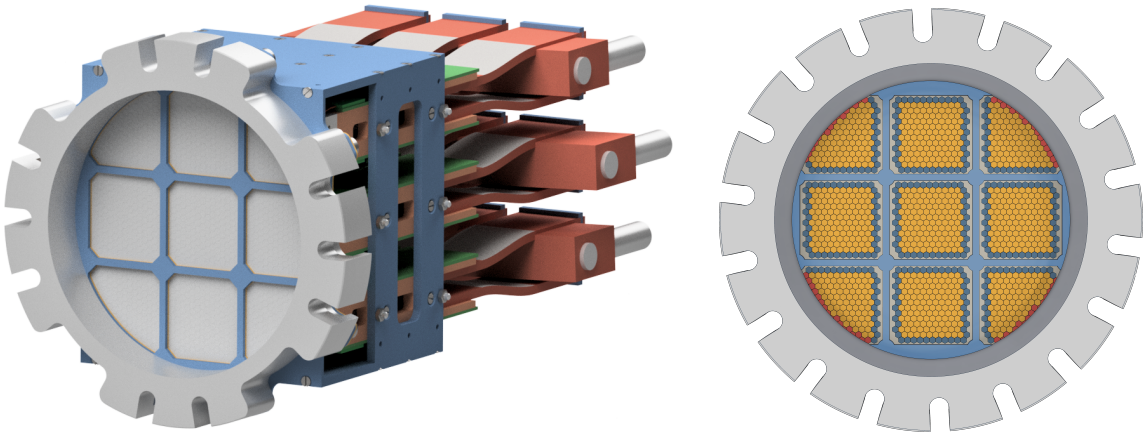

(a) Isometric projection **(b)** Front view

Figure 3.6: Rendering of the TRISTAN detector system with nine modules
The TRISTAN detector system consists of nine identical detector modules which are positioned in a 3×3 grid next to each other. The circular stainless steel flange in front of the SDD chips is installed at the position of the FPD directly connected to the PAE. The blue grid-like structure in front of the detector illustrates the vacuum shield. It covers the gaps between individual detector modules and reduces the conductance between detector sections (with the outgassing electronics) and the Main Spectrometer section. Figure adopted from [47].

the semi-realistic MAC-E filter environment of the MoS are described in Chapter 6 and Chapter 7, respectively.

In addition to the TRISTAN detector system, also the KATRIN beamline configuration has to be optimized for the keV sterile neutrino search. Since the retarding potential eU is turned off or at least set to a very low value in the order of 500 V [47], the electrons have a much higher surplus energy than in the case of the neutrino mass measurement. To ensure the adiabatic transport, the magnetic field configuration along the entire beamline has to be optimized [74]. Furthermore, the effects of back-scattered electrons emitted from the rear wall in the WGTS and electrically or magnetically back-reflected electrons must be minimized. These optimizations to the KATRIN beamline are the topic of currently ongoing studies [47].

4

SILICON DRIFT DETECTOR TECHNOLOGY AND CHARGE SENSITIVE AMPLIFIER

To fulfill the requirements resulting from the keV sterile neutrino search with the KATRIN experiment, described in Chapter 3.2.2, the TRISTAN detector system is based on the SDD technology. The general working principle of semiconductor detectors and the technique of sidewards depletion, which is used to create SDD are described in Chapter 4.1 and Chapter 4.2, respectively. A more detailed description of the working principle for semiconductor particle detectors can be found in, e.g., [75–78]. One key feature of the TRISTAN SDD chips is the integrated nJFET in every anode. Together with the ETTORE ASIC amplifier, they make up the CSA circuit as shown in Chapter 4.3. Details on the different types of electronic noise apparent in the SDD and their effect on the measured energy resolution are given in Chapter 4.4. Furthermore, the energy deposition profiles of electrons and X-rays are discussed in Chapter 4.5. Due to the slightly different interaction mechanism, electrons deposit their energy much closer to the surface of the SDD in the region with a reduced CCE. As a result, the detector response of X-rays and electrons differ, especially for lower energies. An empirical model to describe the detector response for X-rays and electrons is given in Chapter 4.6 and Chapter 4.7, respectively.

4.1 Basic Working Principle of a Semiconductor Detector

Silicon semiconductor detectors have been used in spectroscopic applications since the early 1960s. One of their main advantages is their good intrinsic energy resolution due to the small ionization energy $w = 3.63\,\text{eV}$ [79] required to create, on average, one electron-hole pair. In general, semiconductor detectors are operated as reversed bias diodes to create a region without any free charge carriers in which the ionizing radiation can be detected.

Properties of an Intrinsic Semiconductor To better understand the working principle of semiconductor detectors, the energy band structure in the crystal lattice can be considered. Semiconductor materials like silicon have a forbidden region between the conductance and valance bands of the crystal energy structure as illustrated in Figure 4.1a. The difference between the energy of the conduction band's lower edge and the valence band's upper edge is defined as band gap energy E_g. At absolute zero temperatures and without impurities, electrons occupy only the valence band, while the conductance band is completely empty. In this case, silicon would be a perfect insulator since no free charge carriers are available to conduct an electrical current. However, since the band gap energy $E_\text{g} = 1.124\,\text{eV}$ $(300\,\text{K})$ of silicon is relatively small, electrons can be thermally excited from the valence band to the conductance band at room temperature. If such an excitation happens, it leaves a vacancy inside the valence band, which is called a hole. Both the electrons and holes act like free

charge carriers in the crystal lattice with a negative and positive charge, respectively, and contribute to the conductance of the material. The number density of free electrons n in the conductance band and the number density of free holes p in the valence band in a semiconductor is given by Equation (4.1) and Equation (4.2), respectively.

$$n = 2 \underbrace{\left(\frac{2\pi m_n k_b T}{h^2} \right)^{3/2}}_{N_C} \cdot \underbrace{e^{-(E_C - E_F)/k_b T}}_{\approx F(E_C)} \tag{4.1}$$

$$p = 2 \underbrace{\left(\frac{2\pi m_p k_b T}{h^2} \right)^{3/2}}_{N_V} \cdot \underbrace{e^{-(E_F - E_V)/k_b T}}_{\approx F(E_V)} \tag{4.2}$$

They are derived from the temperature-dependent Fermi-Dirac function $F(E)$ and the effective density of states in the conductance N_C and valence bands N_V. Here, the energy level of the conductance (valence) band is denoted as E_C (E_V), the effective mass of electrons (holes) is denoted as m_e (m_p), the Planck constant as h, the Boltzmann constant as k_b, and the temperature as T. A summary of the material properties of ultra-pure silicon, which is commonly used for detector applications, is given in Table 4.1. Further details on the derivation can be found in, e.g., [76, 77].

The concentration of electrons n and holes p are equal for a semiconductor with a negligible concentration of impurities. Such a semiconductor is commonly also called intrinsic. The intrinsic charge carrier concentration n_i is given as the square root of the product of electron and hole concentration[1] as shown in Equation (4.3) [76]. It is independent of the Fermi level and, therefore, also independent of the doping concentration.

$$n_i = \sqrt{n \cdot p} = \sqrt{N_C N_V} \cdot e^{-E_g/2k_b T} \approx 1.45 \cdot 10^{10}/\mathrm{cm}^3 \tag{4.3}$$

To put this number in perspective, an X-ray of the Mn-K$_\alpha$ line of ^{55}Fe at 5.9 keV [81] generates approximately $n_{5.9\mathrm{keV}} = 1625$ electron-hole pairs at complete absorption. In comparison to the intrinsic charge carrier density of silicon at room temperature n_i, the signal electrons number $n_{5.9\mathrm{keV}}$ is many orders of magnitudes smaller and could not be measured.

Semiconductor Doping To alter the conductive behavior of semiconductors and, e.g., build a detector out of it, additional energy levels inside the forbidden region between the valence and conductance band can be introduced by impurities. These additional energy levels increase the probability in the Fermi-Dirac formalism to excite electrons or holes to the corresponding conductance or valence band, respectively. If impurities are introduced on purpose, it is also called doping. Since silicon is a type IV material of the periodic table with four valence electrons, it can be doped with type III or type V impurities to alter its free charge carrier concentration. Doping can be achieved by, e.g., ion implantation, diffusion of dopants, or epitaxy. In the case of a type V doping with five valence electrons (e.g., phosphorus), an additional shallow energy band is introduced slightly below the conductance band. It acts as an electron donator and releases a free electron charge carrier into the conductance band. This type of doping, also called n-type doping, is illustrated in Figure 4.1b. At room temperature, the free electron density n is equal to the doping concentration N_D

[1] To the total number density of silicon atoms is in the order of $10^{22}/\mathrm{cm}^3$, only every 10^{12} atom is ionized due to thermal excitation.

Table 4.1: Material properties of ultra-pure silicon used for detector applications
The content of this table is taken from [76, 79, 80] and provided by P. Lechner from the Semiconductor laboratory of the Max Planck Society (HLL).

Characteristics	Value
Atomic number	14
Structure	Diamond
Lattice orientation	$\langle 100 \rangle$
Density	$2.328\,\mathrm{g/cm^3}$
Coefficient of thermal expansion (CTE) α	$2.56 \cdot 10^{-6}/\mathrm{K}$
Band gap energy E_g at 300 K	1.124 eV
Band gap energy E_g at 0 K	1.170 eV
Intrinsic carrier density n_i	$1.45 \cdot 10^{10}/\mathrm{cm^3}$
Electron mobility μ_e	$1350\,\mathrm{cm^2/(V\,s)}$
Hole mobility μ_h	$450\,\mathrm{cm^2/(V\,s)}$
Effective valence band density N_V	$1.83 \cdot 10^{19}/\mathrm{cm^3}$
Effective conductance band density N_C	$3.22 \cdot 10^{19}/\mathrm{cm^3}$
Average electron-hole pair energy w	3.63 eV
Fano factor F	0.115
Relative permittivity ϵ_r	11.7
Maximal electric field E_{max}	$30\,\mathrm{V/\mu m}$
Intrinsic resistivity ρ (typical)	$235\,\mathrm{k\Omega\,cm}$
Intrinsic resistivity ρ (TRISTAN)	$4\,\mathrm{k\Omega\,cm}$
n-type base material doping concentration N_D (TRISTAN)	$\approx 1.06 \cdot 10^{12}/\mathrm{cm^3}$
p-doping concentration N_A (TRISTAN)	$\gtrsim 10^{18}/\mathrm{cm^3}$

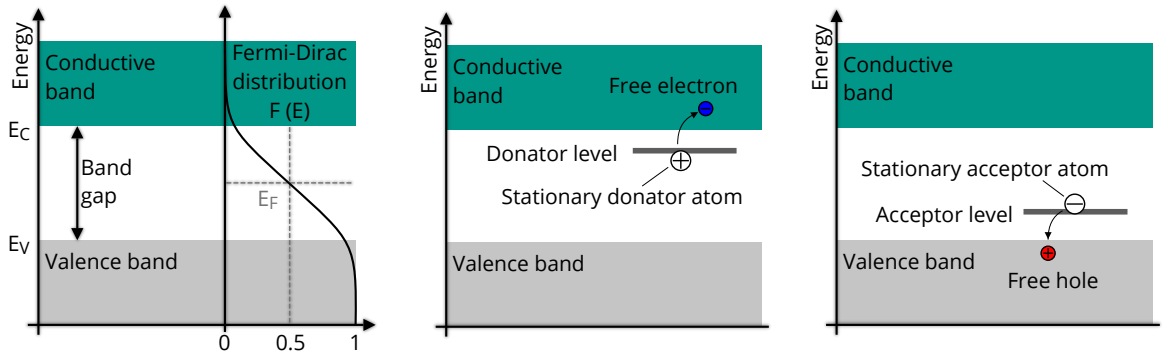

(a) Intrinsic semiconductor **(b)** n-type semiconductor **(c)** p-type semiconductor

Figure 4.1: Concept of semiconductor band structure and doping types
(a) Illustration of the band gap structure in an intrinsic semiconductor. The electron occupancy following the Fermi-Dirac distribution is shown in the right half. (b) Illustration of the energy level in a semiconductor for doping with a type V electron donator element, also known as n-type doping. (c) Illustration of the energy level in a semiconductor for doping with a type III electron acceptor element, also known as p-type doping. Adapted from [82].

of the donator atoms[2] as all atoms are ionized. Inside an n-type doped semiconductor, the electron density is increased. Hence, the electrons are called majority charge carriers, while holes are called minority charge carriers. Similarly, by introducing materials of type III of the periodic table with only three valence electrons (e.g., boron), an additional energy level just above the valence band can be introduced. This additional level acts as an electron acceptor, creating an additional free hole inside the valence band. The energy band structure of p-type doping is shown in Figure 4.1c. The acceptor doping density is commonly denoted as N_A, and here, the holes are called the majority charge carriers, while the electrons are called minority charge carriers.

pn-Junction and PIN-Detector A pn-junction describes the transition between a p-doped and an n-doped semiconductor region. Due to the difference in electron density n and hole density p, the majority charge carriers diffuse thermally into the oppositely doped regions. Since the acceptor and donator atoms are stationary in the lattice, the n-doped region becomes positively charged and the p-doped region negatively charged. The created electric field between the two regions counteracts the movement of the majority charge carriers, reducing their drift until an equilibrium is reached at the so-called diffusion or build-in voltage $U_{\text{diffusion}}$. It is described in Equation (4.4) and mainly depends on the ratio of the doping concentration N_A and N_D, and the intrinsic charge carrier density n_i.

$$U_{\text{diffusion}} \approx \frac{k_b T}{e} \ln\left(\frac{N_A \cdot N_D}{n_i^2}\right) \tag{4.4}$$

Due to the electric field inside this region, any charge carriers that are created (e.g., via thermal ionization, at impurities, or due to ionizing radiation) are forced outside, creating a region basically free of any charge carriers. This region is called the depletion zone or sometimes the space charge region. Here, electrons drift to the positively charged n-doped region and holes to the negatively charged p-doped region. If now ionizing radiation enters the material, it creates many electron-hole pairs in a short amount of time (less than 1 ps [75])

[2] Typical doping concentrations are in the order of $10^{16}/\text{cm}^3$ for light doping and $10^{19}/\text{cm}^3$ for heavy doping concentrations [76].

inside the depletion zone. The increase in electron-hole pairs is many orders of magnitude larger than the continuously generated electron-hole pairs due to the leakage I_{leak} current[3] and can be, in principle, measured as the detector signal at the electrical contacts with the depletion layer, e.g., the detector anode.

Reverse Biased Diode To increase the width of the depletion zone W, an additional voltage rectified with the diffusion voltage $U_{\text{diffusion}}$ can be applied. This configuration is often called a reverse biased diode, and its depletion width W can be estimated using Equation (4.5).

$$W = \sqrt{\frac{2\epsilon_0\epsilon_r}{e}\left(\frac{1}{N_A}+\frac{1}{N_D}\right)(U_{\text{diffusion}}+U_{\text{bias}})} \approx \sqrt{\frac{2\epsilon_0\epsilon_r}{eN_D}U_{\text{bias}}} \tag{4.5}$$

Here, the permittivity in vacuum is denoted as ϵ_0 and the one in silicon as ϵ_r [77]. To simplify the equation in the context of a detector application, it can be assumed that $N_D \ll N_A$ and $U_{\text{bias}} \gg U_{\text{diffusion}}$. A detailed derivation can be found in [76].

As an example, in semiconductor detectors like the TRISTAN SDD chip, the p-doped region is heavily doped ($N_A \leq 10^{18}/\text{cm}^3$) while the bulk material is only lightly n-doped ($N_D = 1.05 \cdot 10^{12}/\text{cm}^3$). This way, the depletion region extends over a larger distance than for a symmetric doping concentration. For this example, the diffusion voltage is $U_{\text{diffusion}} \approx 0.58\,\text{V}$ and the depletion zone extends over $W \approx 25\,\mu\text{m}$ at room temperature. By applying an external voltage U_{bias} in reverse bias mode, the depletion zone increases and, therefore, also the sensitive volume of the detector increases. For the TRISTAN SDD chips, typically a bias voltage $U_{\text{bias}} \approx 100\,\text{V}$ is applied, leading to a depletion width of $W_{100\,\text{V}} \approx 352\,\mu\text{m}$. If the detectors were not an SDD, which further includes a sideward depletion, a more negative biasing voltage U_{bias} would be necessary to fully deplete the detector over the entire wafer thickness of 450 µm.

Lifetime of Electron-Hole Pairs and Leakage Current For the recombination of an excited electron or hole, an additional phonon is necessary to conserve energy and momentum. However, in actual detector devices, this process is dominated by second-order effects. As a result, the effective lifetime τ_L of the excited electrons and holes is entirely dominated by the impurity (or trap) concentration N_t, as shown in Equation (4.6).

$$\tau_L = \frac{1}{\sigma v_{th} N_t} \tag{4.6}$$

Here, the thermal velocity is denoted as v_{th} ($\approx 10^7\,\text{cm/s}$) and the charge carrier cross-section as $\sigma(\approx 10^{-15}\,\text{cm}^2)$. Different energy levels for doping atoms can be seen in Figure 4.2. An important message from the Shockley-Read-Hall theorem [83] is that the impurities not only act as traps for charge carriers (which influence the 1/f noise in the detector) but also as a center of electron-hole pair creation [76]. Especially metal impurities like copper (Cu), gold (Au), and iron (Fe), which introduce an energy level in the center of the band gap (called deep energy levels), can act as a 'stepping stone' for both electrons and holes. This effect can strongly increase the leakage current in the device. As shown in Equation (4.7), the leakage current I_{leak} is proportional to the effective lifetime τ_L and scales with the depletion

[3] A rough estimation of the rate of electron-hole pairs generated due to leakage current is given in Chapter C.1.

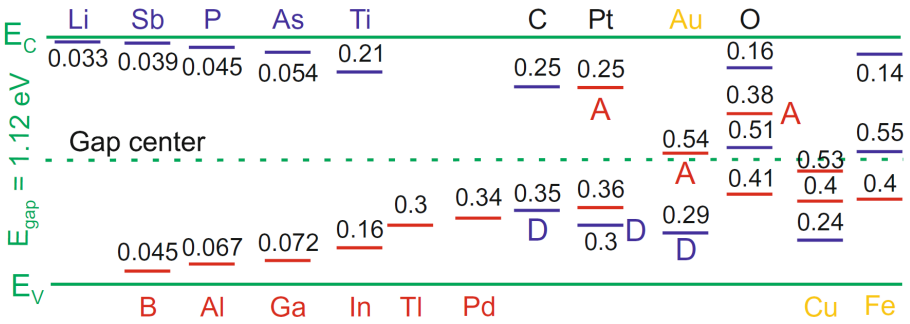

Figure 4.2: Energy levels of various impurities in silicon
Various additional energy levels in the band gap of silicon from acceptor (red or denoted with A) and donator (blue or denoted with D) elements are shown. The upper and lower boundaries of the valence and conductance bands are illustrated in green. The corresponding numbers to every energy level denote the required excitation energy in electron volt (eV). Useful dopants add levels near the conductance or valence band. Impurities with energy levels in the center, like gold or copper, are undesired and only increase the leakage current without any other helpful effect. The illustration and information is taken from [76].

width W and the detector area A. Additionally, since it depends on the intrinsic charge carrier density n_i, it increases with the temperature T.

$$I_{\text{leak}} = \frac{en_i}{2\tau_L} W \cdot A \propto N_t \sqrt{U_{\text{bias}}} T^{3/2} \exp\left(-\frac{E_G}{2k_b T}\right) \tag{4.7}$$

4.2 Working Principle of Silicon Drift Detectors

To illustrate the working principle of an SDD illustrated in Figure 4.3 and better understand the idea behind the sideward depletion [84], one can start with a simple PIN detector shown in Figure 4.4a. It is similar to the structure of a pn-junction, with the difference that there is a lightly n^--doped[4] region between the heavily n^+-doped anode and p^+-doped back implantation (cathode). Here, the side of the wafer on which the anode is placed is called the readout side. The entrance window side is the opposite side with the p^+-doped implantation for the so-called back contact (BC). To fully deplete the detector volume, a biasing voltage U_{bias} following equation Equation (4.5) has to be applied between the two implantations. Since both implantations cover the entire surface of the detector, the capacitance of the anode can be estimated with the formula for a plate capacitor shown in Equation (4.8).

$$C_{\text{A}} = \epsilon_0 \epsilon_r \frac{A}{W} \tag{4.8}$$

The width is given by the depletion depth W, and the area A is determined by the surface area of the anode. As shown later in Equation (4.21), the electronic noise n_{ENC} and, therefore, the detector energy resolution is proportional to the anode capacity C_{A}.

$$n_{\text{ENC}} \propto C_{\text{A}} \tag{4.9}$$

[4] The signs in the doping names (e.g., n^- and n^+) illustrate light and heavy doping, respectively.

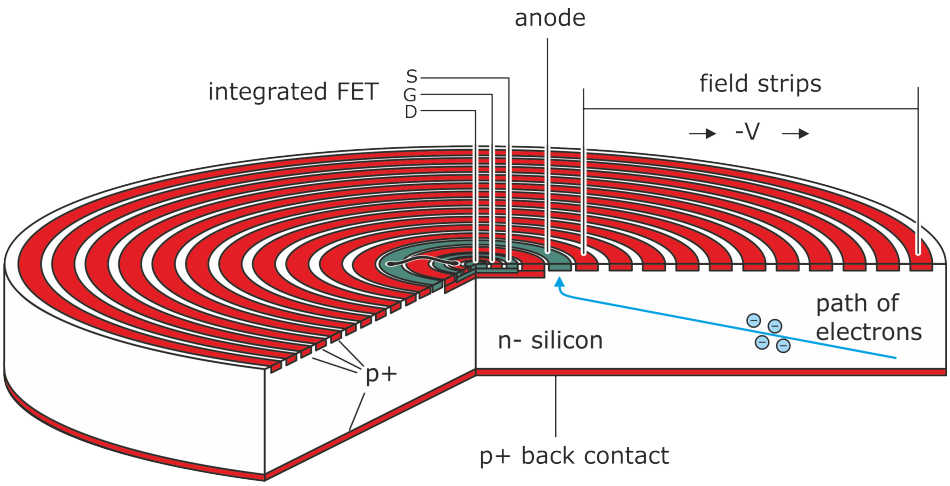

Figure 4.3: Cross-section of a silicon drift detector
Cross-section of a circular SDD detector with an integrated nJFET enclosed by the anode. The lightly n^--doped silicon substrate is shown in white. The p^+-doped implantation for the back contact, drift rings, and nJFET are depicted in red. The n^+-doped implantation for the anode and nJFET are illustrated in green. Adapted from [85], courtesy of P. Lecher.

Assuming a detector or pixel with a diameter of 3 mm and a wafer thickness of $w = 450\,\mu\text{m}$ the detector capacity would be at least 1600 fF. However, the anode size can be drastically reduced using the concept of sideward depletion [84]. In the case of the TRISTAN SDD, the capacity of the detector anode is $C_\text{A} = 112\,\text{fF}$, which is an improvement by one order of magnitude. To achieve this reduction of the anode size while still depleting the entire detector volume, not only the entrance window is p^+-doped, but also parts of the opposite readout side as shown in Figure 4.4b. Due to this p^+-doping, the depletion zone extends from each side of the wafer. In the simple, fully depleted example shown in Figure 4.4c, the potential between the two p^+-doped sides would form a well in which the electrons would be trapped and could only escape via diffusion processes. To place only a small anode on the detector's backside, an additional electric potential gradient is needed to guide the electrons to the center of the device. This gradient is achieved by separating the p^+ implantation into smaller drift rings. A potential gradient between the inner most ring (R1) and the outer most ring (RX) can now be applied by, e.g., connecting the individual drift rings in a chain via a resistance between them. This concept is illustrated in Figure 4.4d and a cross-section of a circular SDD (with an integrated n-channel junction gate field-effect transistor (nJFET)) is shown in Figure 4.3. Due to this technique, a tiny anode capacity almost independent of the detector size can be achieved, which is the key to an energy resolution close to the Fano limit [85, 86].

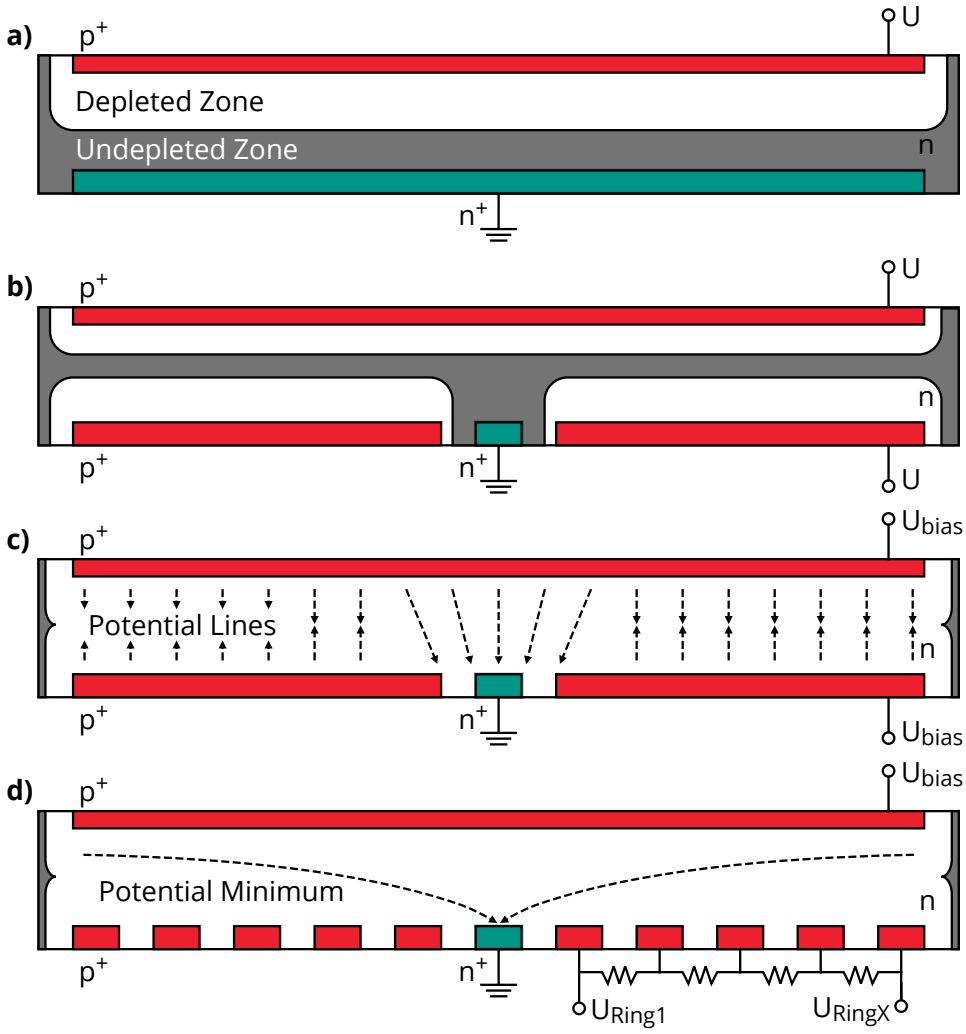

Figure 4.4: Illustration of sideward depletion
Illustration of the steps between a pn-junction or PIN detector (a) towards an SDD (d). In (b) and (c) the intermediate steps of the principle of sideward depletion without any drift rings are shown. The heavily doped p-implantations p^+ are illustrated in red, and the n-doped anode implantation n^+ is shown in green. The depletion zone in the lightly doped silicon base material n is illustrated in white, while the not-depleted region is colored in grey. In (a) and (b) the case where the applied voltage U is small, and the detector is not fully depleted are illustrated, respectively. A more negative voltage U_{bias} is applied in (c) and (d) to fully deplete the detector. Due to the p^+ implantation on both sides of the silicon wafer, the entire volume of the detector can be depleted, and the anode size can be largely reduced. A potential difference through resistances between the RX and R1 is applied to shape the electric field lines inside the SDD as illustrated in (d). With this additional radial field, the electrons are guided from every point in the detector to the anode. Adapted from [82].

4.3 Closed-Loop Negative Feedback Charge Sensitive Amplifier

A charge sensitive amplifier (CSA) circuit is typically used for silicon semiconductor detectors to read the signals from the anode. It integrates the collected charge $\Delta Q = Q \cdot \delta t$ at the anode and converts it into a voltage step ΔV proportional to the incoming energy E. Here, δt denotes a short time interval in which the charge is collected[5]. The working principle of a CSA is explained in this chapter with the example of the TRISTAN SDD. Here, the preamplification is performed with a negative feedback loop CSA circuit which consists of the integrated nJFET and the 1$^{\text{st}}$ stage of the ETTORE application-specific integrated circuit (ASIC) amplifier [88] as shown in Figure 4.5. A second amplification can be enabled via the ETTORE ASIC 2$^{\text{nd}}$ stage, which amplifies the signal by another factor of ten[6] and introduces a decay constant of $\tau_{\text{decay}} = 15\,\mu\text{s}$.

First Stage Amplification By design, the potential at the gate of the transistor U_G, which is connected to the anode, does not change in a closed-loop negative feedback CSA (in the source follower mode). Any electron charge Q collected at the gate of the transistor (which is connected to the anode of the detector) leads to an amplified current which charges the capacitance C_{AC}. This, in turn, introduces a potential difference between the negative and positive input of the amplifier. The collected electron charge Q results in a positive voltage change at the output of the amplifier. Since the feedback capacitance C_{FB} is directly connected to the amplifier output, the (negative) feedback pulls the electrons away from the gate into the capacitor until an equilibrium is reached between the amplifier inputs. This equilibrium occurs if no charge is left at the gate. For an operational closed-loop negative feedback CSA, the measured change in output voltage ΔV is therefore given by Equation (4.10) [89, 90]. This equation holds for the case that the amplification A of the amplifier is large ($A >> \frac{C_{\text{Tot}}+C_{\text{FB}}}{C_{\text{FB}}}$).

$$\Delta V_{\text{1st}} = \frac{\Delta Q}{C_{\text{FB}}} \tag{4.10}$$

It is important to note that the output voltage ΔV_{1st} of the negative feedback CSA is independent of the amplification A and only depends on the feedback capacitance C_{FB}. From a technological point of view, it is much easier to manufacture capacitors with low variety than amplifiers. An exemplary output of the ETTORE ASIC 1$^{\text{st}}$ stage is shown in Figure 4.6a.

Second Stage Amplification The ETTORE 2$^{\text{nd}}$ stage amplifier repeats the principle of a closed-loop negative feedback CSA with an additional feedback resistor R_{decay} and AC-coupling. Due to the additional feedback resistor R_{decay}, the capacitor C_{decay} continuously discharges over time, adding a decay constant of $\tau_{\text{decay}} = C_{\text{decay}} \cdot R_{\text{decay}} = 15\,\mu\text{s}$ to the signal output. The amplification of the voltage change of the 1$^{\text{st}}$ stage output is then given by Equation (4.11).

$$\Delta V_{\text{Out}} = \frac{nC_{\text{decay}}}{C_{\text{decay}}} \cdot \Delta V_{\text{1st}} = n \cdot \Delta V_{\text{1st}} \tag{4.11}$$

[5] For the TRISTAN SDD, it is in the order of 100 ns. More details can be found in [87].
[6] In low gain operation the second amplification can also be set to five instead of ten.

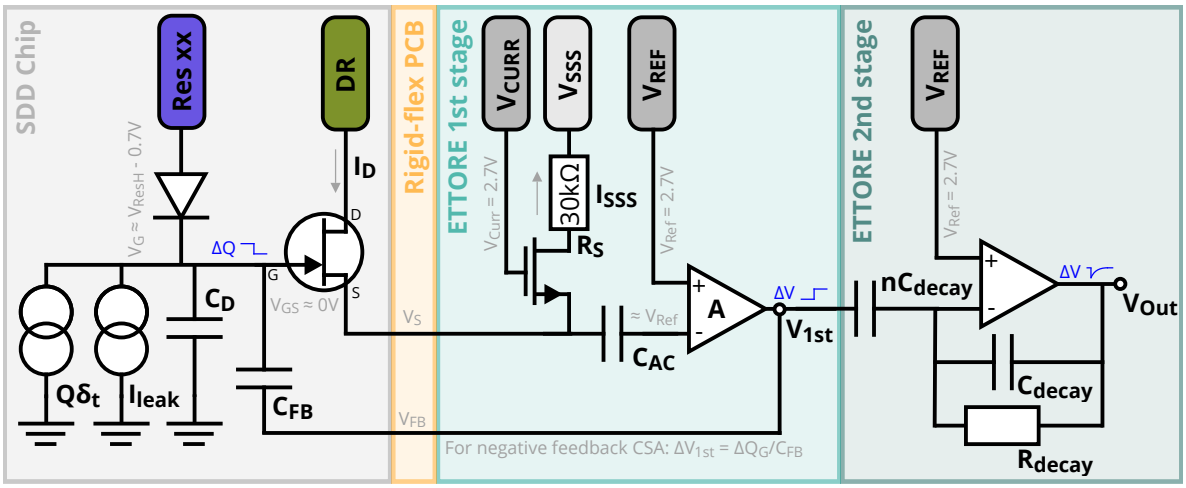

Figure 4.5: Illustration of a CSA circuit with integrated nJFET
Simplified on module signal amplification chain of the TRISTAN SDD and ETTORE ASIC amplifier. The signal is amplified in a closed-loop negative feedback CSA circuit with two stages. A signal is illustrated as a constant current source, which induces a charge $\Delta Q = Q \cdot \delta t$ in a short amount of time δt at the anode of the detector. V_{1st} denotes the output after the ETTORE 1st stage amplification and V_{Out} the one after the ETTORE ASIC 2nd stage. The important parameters of the circuit are summarized in Table 5.2. The figure is adapted from [88, 89].

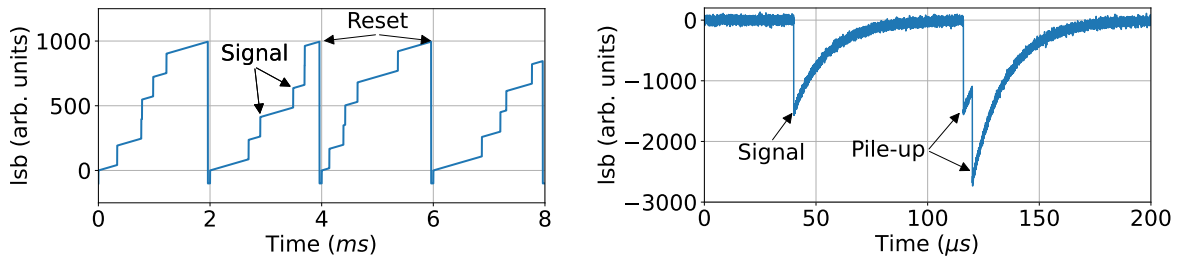

(a) First stage waveform **(b)** Second stage waveform

Figure 4.6: Illustration of the output signal for both ETTORE stages
The waveforms are a simple simulation for illustration only, where the deposited energy in the detector is proportional to voltage change measured in, e.g., least significant bit (lsb) of a connected DAQ. (a) Signal of the 1st stage ETTORE ASIC output. Each steep increase in lsb corresponds to a signal event. The slope between the signal events depicts the leakage current in the detector. The steep decrease in lsb every 2 ms corresponds to the reset of the detector anode to drain its accumulated charge. (b) Zoom on the AC-coupled signal output of the 2nd stage ETTORE ASIC amplifier. It introduces an additional gain of $n = 10$ in normal operation and inverts the pulse direction with a decay constant of $\tau_{decay} = 15\,\mu s$. For (pile-up) events that happen in a short period, the second event can lie on the decaying shoulder of the first event.

Here, n denotes the selectable ETTORE ASIC gain modes with a normal gain ($n = 10$) and a low gain ($n = 5$) mode. The typical output of this stage is depicted in Figure 4.6b. The AC-coupled ETTORE 2$^{\text{nd}}$ stage can be turned off for, e.g., debugging reasons.

Using the example of the Mn-K$_\alpha$ line of ^{55}Fe a voltage step of $\Delta V_{1\text{st}} = \frac{1625 \cdot e}{25\,\text{fF}} = 10\,\text{mV}$ is measured after the ETTORE 1$^{\text{st}}$ stage amplification. Together with the ten times amplification (normal mode) of the ETTORE 2$^{\text{nd}}$ stage the output voltage step is then $\Delta V_{\text{Out}} = 100\,\text{mV}$. For completeness, the XGLab[7] bias and buffer boards add another amplification of the signal by a factor two at their outputs.

4.4 Energy Resolution and Electronic Noise in SDD

When ionizing radiation like X-rays and β-electrons enter a semiconductor detector, energetic electrons are generated, which interact and scatter with the detector material in a cascade-like form. If the deposited energy per interaction is greater than the band gap energy $E_g = 1.124\,\text{eV}$ of silicon, an electron-hole pair can be created. Here, an electron is lifted from the valence band to the conductance band. In reality, other phenomena, such as scattering on the nucleus and phonon emission, introduce additional energy losses in interactions with the detector material, resulting in the average energy of $w = 3.63\,\text{eV}$ to create an electron-hole pair. The average number of created electron-hole pairs n due to the ionization is proportional to the incoming energy E of the incoming radiation as shown in Equation (4.12).

$$E = w \cdot n \tag{4.12}$$

By separating the electron-hole pairs and collecting the electrons on the anode, the signal charge $Q = n \cdot e$ can be measured. It is the product of the created charge carriers n and the elementary charge e.

Fano Statistics Due to unavoidable fluctuations in the interaction processes with the detector material, the number of generated electron-hole pairs n varies. This variation in the number of generated charge carriers n ultimately defines the minimal (best) energy resolution σ_{Fano} that can be achieved with a silicon semiconductor detector. Since the generation of the charge carriers does not follow a purely statistical random process, the Fano factor F [91] is introduced as shown in Equation (4.13).

$$F = \frac{\sigma_{\text{Fano}}^2}{\mu} \tag{4.13}$$

$$\Rightarrow \sigma_{\text{E,Fano}} = \sqrt{Fnw^2} = \sqrt{FEw} \tag{4.14}$$

It describes the correlation between the mean μ of an observable (here the number of charge carriers n) and its variance σ_{Fano}. For a process that follows a Poisson distribution, the Fano factor is defined as $F = 1$. In general, the Fano factor depends on the material and slightly on the temperature. An overview of different materials and temperatures can be found, e.g., in [75]. For silicon semiconductor detectors, a much smaller Fano factor $F = 0.115$ [79] is observed at room temperature, which improves the minimal achievable energy resolution σ_{Fano} as shown in Equation (4.14). The energy resolution for semiconductor detectors is commonly

[7] XGLab Srl, Bruker Nano Analytics, Via Conte Rosso 23, 20134 Milano, Italy.

measured as the full width half maximum (FWHM) ΔE, which is correlated to the width σ_E of a Gaussian distribution as shown in Equation (4.15).

$$\Delta E = 2\sqrt{2\ln 2} \cdot \sigma_E \tag{4.15}$$

As an example, the theoretically minimal energy resolution, free of any electronic noise, is $\Delta E_{5.9\,\mathrm{keV,Fano}} = 2\sqrt{2\ln 2} \cdot \sigma_{5.9\,\mathrm{keV,Fano}} \approx 119\,\mathrm{eV}$ FWHM for the Mn-K_α line due to the intrinsic broadening correlated with the Fano statistics.

4.4.1 *Electronic Noise*

In addition to the Fano statistics, the energy resolution σ_E measured in a semiconductor detector is influenced by different noise sources from the detector itself and its connected CSA. This increases the minimal energy resolution $\sigma_{\mathrm{E,Fano}}$ given by Fano statistics as shown in Equation (4.16). Here, σ_{el} denotes the standard deviation of the electronic noise.

$$\sigma_E = \sqrt{\sigma_{\mathrm{E,Fano}}^2 + \sigma_{\mathrm{el}}^2} = \sqrt{FEw + (n_{\mathrm{ENC}} w)^2} \tag{4.16}$$

In general, noise is denoted as an (unpredictable) variation of currents $\langle I \rangle$ or voltage $\langle U \rangle$ over time in a detector system. Commonly, it is quantified as equivalent noise charge (ENC) n_{ENC} for semiconductor detectors. It describes the number of the equivalent charge carriers, e.g., electrons collected in the anode of an SDD, which would lead to a signal at the amplifier output with the same height as the root mean square of the electronic noise [75].

Electronic noise can be divided into three main categories: series noise (e.g., thermal noise), 1/f noise (e.g., flicker noise), and parallel noise (e.g., leakage current). A more detailed description can be found in, e.g., [75, 78], and the derivations of the different terms are described in [92].

Series Noise (Thermal Noise) Series noise is also sometimes referred to as thermal, Johnson, voltage, or white[8] noise. It describes the electronic noise component that occurs due to the random thermal motion of charge carriers inside a conductor [93]. A real resistor R behaves like an ideal (noiseless) resistor with an additional thermal noise source $\langle U_{\mathrm{series}}^2 \rangle$ connected in series. The spectral thermal noise density $\frac{d\langle U_{\mathrm{thermal,resistor}}^2 \rangle}{df}$ is given in Equation (4.17) and is independent of the frequency f. In the case of an SDD with an integrated nJFET, the thermal noise mainly originates from the transistor in the CSA. As shown in Equation (4.18), the spectral thermal noise density for a transistor depends on its transconductance g_m. This type of noise is most dominant for short energy filter times τ.

$$\frac{d\langle U_{\mathrm{series,resistor}}^2 \rangle}{df} = 4 k_b T R \tag{4.17}$$

$$\frac{d\langle U_{\mathrm{series,transistor}}^2 \rangle}{df} = \frac{8}{3} \frac{k_b T}{g_m} \tag{4.18}$$

[8] Since it is independent of the frequency, it is often referred to as white noise.

1/f Noise (Flicker Noise) $1/f$ noise or sometimes called flicker noise describes the statistical variation of the charge carrier density n and their mobility μ which is anti-proportional to the frequency f as shown in Equation (4.19).

$$\frac{d\langle U_{1/\mathrm{f}}^2\rangle}{df} = \frac{A_f}{f} \tag{4.19}$$

In a semiconductor detector, it can originate from the trapping-detrapping effect at crystal defects in the lattice. Such traps in, e.g., the n-channel of the nJFET lead to a modulation of the transistor current and depend on the trapping lifetime τ_L. Since this lifetime is not statistically independent, it does not create a flat white noise density spectrum like the series noise but rather a $1/f$ dependence. Due to the irregular change in current, this effect is also called random telegraph noise or popcorn noise [94]. This $1/f$ noise affects all energy filter times τ with approximately the same strength.

Parallel Noise (Leakage Current) Parallel noise, sometimes called shot or current noise, describes the effect in the variation of currents $\langle I^2\rangle$ flowing through a diode or detector. In SDD, it is mainly created by the leakage currents I_{leak} and is also independent of the frequency f as shown in Equation (4.20). In contrast to the $1/f$ noise the current variation of the leakage current is statistical and not correlated. A nice overview of the different types of leakage current can be found in [75, 92]. It mainly effects the energy resolution for longer energy filter times τ and scales with the temperature as shown in Equation (4.7).

$$\frac{d\langle I_{\mathrm{parallel}}^2\rangle}{df} = 2I_{\mathrm{leak}}e \tag{4.20}$$

4.4.2 *Electronic Noise Curve*

In a physical measurement of signal events in a semiconductor detector, an energy filter is applied to reconstruct the energy E of an event. Since the electronic noise is frequency-dependent, the shape and length of the energy filter τ influence the magnitude in which the reconstructed energy is affected. For a trapezoidal energy filter with a rise time of τ_{rise} the level of noise in ENC is given by Equation (4.21).

$$n_{\mathrm{ENC}}^2 = \frac{\sigma_{\mathrm{el}}^2}{w^2} = \underbrace{\frac{A_1}{w^2}C_{\mathrm{A}}^2 4k_bT\left(\frac{2}{3g_m} + \frac{1}{g_m^2 R_s}\right)\cdot\frac{1}{\tau_{\mathrm{rise}}}}_{\text{series}} + \underbrace{\frac{A_2}{w^2}C_{\mathrm{A}}^2 A_f}_{1/f} + \underbrace{\frac{A_3}{w^2}\frac{2eI_{\mathrm{leak}}}{(2\pi)^2}\cdot\tau_{\mathrm{rise}}}_{\text{parallel}} \tag{4.21}$$

Here, the capacitance at the anode is given as $C_{\mathrm{A}} = C_D + C_{\mathrm{FB}} + C_{\mathrm{stray}}$, where C_{stray} denotes all stray capacitances. To receive this formula, each individual noise component $\frac{d\langle U^2\rangle}{df}$ is multiplied by its transfer function $|H(f)|^2$ and the energy filter response $A(f)$ and integrated over the frequency f. The coefficients A_1, A_2, and A_3 are energy filter-dependent parameters. For a derivation of this formula, refer to [95]. An illustration of an electronic noise curve is shown in Figure 4.7. At shorter energy filter rise times τ_{rise}, the electronic noise and, therefore, the energy resolution is mainly defined by the series noise. In contrast, at larger energy filter rise times τ_{rise}, the main contribution to the ENC originates from parallel noise sources, like, e.g., the leakage current.

To emphasize the temperature dependence of the electronic noise, Equation (4.21)

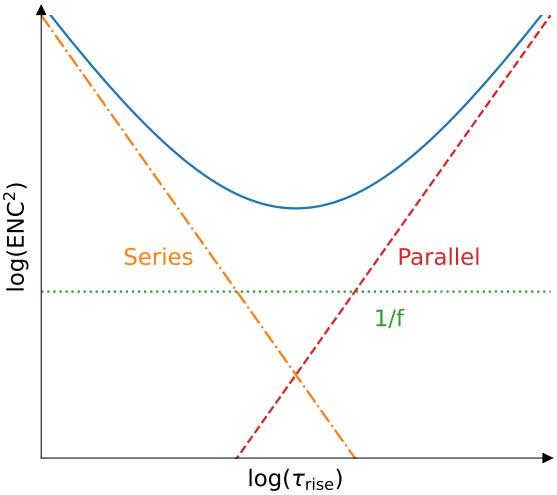

Figure 4.7: Illustration of noise curve and its contributions
The level of noise in ENC^2 is illustrated as the solid blue line as a function of the energy filter rise time τ_{rise}. The dotted lines illustrate the different contributions of the series, 1/f, and parallel noise that contribute to the total noise curve. The formula for the ENC is given in Equation (4.21).

can be simplified[9] to Equation (4.22). All other temperature-independent constants are summarised in the parameters a_0, a_1, and a_2.

$$n_{\text{ENC}}^2 = a_0 \frac{T}{\tau_{\text{rise}}} + a_1 + a_2 T^{3/2} \exp\left(-\frac{E_G}{2k_b T}\right) \tau_{\text{rise}} \tag{4.22}$$

4.5 Energy Deposition Profile and Entrance Window Effects

For X-rays in the energy range of a few ten keV, the dominant interaction with the detector material is via the photoelectric effect. The photon is completely absorbed, and its energy is transferred to an atomically bound electron. This electron is sometimes called a primary electron, and its kinetic energy is the initial X-ray energy minus its atomic binding energy. The created vacancy in the inner electron shell of the atom is highly unstable and quickly filled by an electron from a higher shell. An additional (fluorescence) X-ray or an Auger electron can be created in this process. The emitted X-ray is usually absorbed in secondary photoelectric interactions, again creating electrons that ionize the detector material. This behavior is illustrated in the upper half of Figure 4.8. The absorption or interaction probability of X-rays in silicon is shown in Figure 4.9a as a function of depth. It is important to note that the energy deposition in the detector material starts at the position of creating the (primary) electron via the photoelectric effect. As an example, less than 0.5 % of the X-rays with an energy higher than 5 keV interact on the first 100 nm in which the CCE of the detector is reduced [96]. Consequently, most of the X-rays interact in the fully sensitive region of the detector, and the shape of the main peak is mostly defined by the Gaussian variation due to the Fano Statistics σ_{Fano} and the electronic noise σ_{el}.

For incoming β-electrons, the critical difference to incoming X-rays is the missing first photoelectric effect. The β-electron directly interacts and scatters with the detector material, ionizing it on its path as illustrated in the lower part of Figure 4.8. Compared to

[9] As noted in [92] also the resistance of the transistor channel creates a shot noise, which has to be taken into account. This part is proportional $n_{\text{ENC}}^2 \propto \frac{T}{R_{\text{ch}}} \tau_{\text{rise}}$ and is not taken into account in this thesis since it is absorbed in the different constants a_0 and A_3.

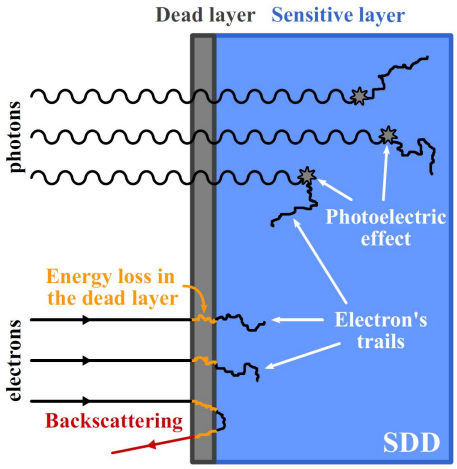

Figure 4.8: Comparison of the interaction of X-rays and β-electrons
In the upper half of the graphic, the interaction of X-rays (photons) via the photoelectric effect is illustrated. In comparison, the interaction of β-electrons is shown in the lower part. The fully sensitive detector volume is illustrated in blue. For the reduced CCE at the entrance window, a completely insensitive dead layer (grey region) on top of the detector material has been assumed for illustration purposes. The energy loss in the entrance window region is illustrated by the yellow part of the electron trail. The figure is taken from [89].

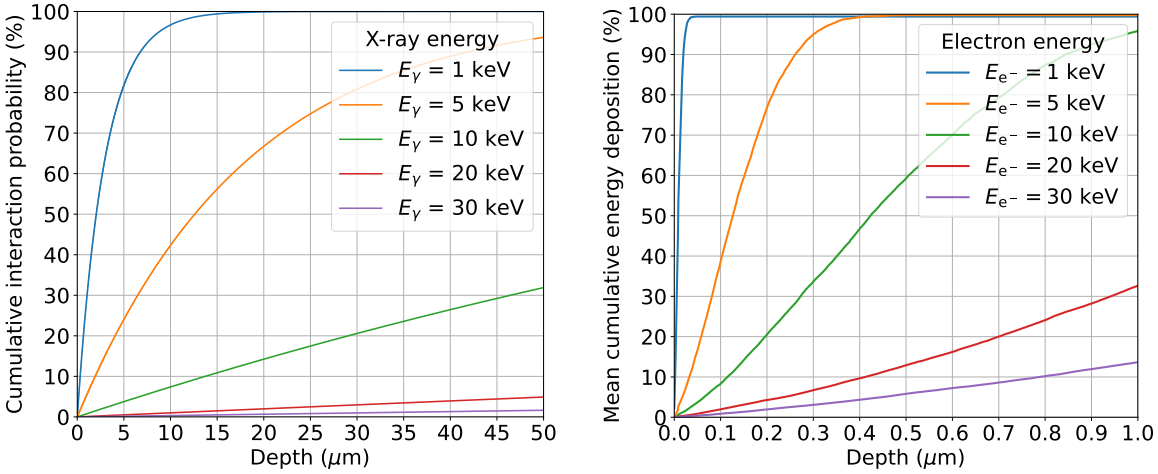

(a) Photon interaction probability

(b) Electron energy deposition

Figure 4.9: Interaction profile for X-rays and electrons in silicon
(a) Cumulative interaction probability for X-rays as a function of interaction depth in silicon. The curves are calculated using $P(z|E_\gamma) = (1 - \exp(-\alpha(E_\gamma) \cdot z))$ motivated by the absorption formula [97]. For energies ≥ 5 keV, less than 0.5 % of all X-rays interact in the first 100 nm. The absorption coefficients $\alpha(E_\gamma)$ are taken from [97]. (b) Normalized cumulative average energy deposition of monoenergetic electrons as a function of interaction depth in silicon. To create the curves 1000 electrons are simulated, and the average energy deposited in 1 nm wide bins are calculated and normalized to the total deposited energy. This simulation is repeated for every incident electron energy. The data has been provided by D. Spreng using the simulation software GEANT4 [98].

the X-ray interaction probability, the cumulative energy deposition profile for β-electrons in silicon is shown in Figure 4.9b. As an example a β-electron with 5 keV deposits already 40 % of its total energy in the first 100 nm. This means that, on average, β-electrons deposit their energy much closer to the detector's surface than X-rays. In this region, the CCE[10] is reduced compared to the rest of the detector volume, and only a fraction of the deposited energy E is measured.

One contribution to the reduction of the CCE originates from a thin layer (approximately 10 nm) of silicon dioxide on the entrance window surface. Since it is an insulator, the created (low energetic) electron-hole pairs are trapped in this layer and create a fully insensitive detector region (also called the dead layer). This layer is unavoidable as it grows when silicon is exposed to air. To avoid inhomogeneities, the silicon dioxide layer is grown under controlled conditions while manufacturing the SDD chips. The second contribution is created by the finite depth of the doping for the BC implantation in the order of several tens of nm [99] inside the SDD chip. Here, the electric fields are much weaker than in the fully sensitive detector material, and the electron-hole pairs mainly travel via diffusion. This movement occurs until they either recombine and are lost or reach a region with stronger electric fields and get collected at the anode. To put this region of reduced CCE into perspective, for the TRISTAN SDD, the reduced CCE at the entrance window extends over the first few 100 nm [96]. Depending on the energy and the reduced CCE in the entrance window region, a significant fraction of the signal charge is lost, influencing and changing the detector response compared to X-rays. Further investigations on the entrance window effects can be found in, e.g., [61, 63, 82].

4.6 Detector Response to X-Rays

To illustrate the measured detector response of a TRISTAN SDD to X-rays, a typical energy spectrum of an ^{55}Fe source is shown in Figure 4.10a. It consists of the two main peaks corresponding to the Mn-K$_\alpha$ and Mn-K$_\beta$ lines at 5.895 keV and 6.490 keV, respectively. The silicon escape peak of the Mn-K$_\alpha$ line is clearly visible, while the silicon escape peak of the Mn-K$_\beta$ line is only slightly visible. They are created via ionization, where the incident radiation kicks out an electron of the K-shell, leaving a vacancy in the silicon detector material. When the created vacancy is filled by an electron from a higher shell, a fluorescence photon with 1.740 keV [100] is created. In the case of the silicon escape peaks, this photon is not reabsorbed in the detector material, leaving it undetected. At around 0.5 keV, the effects of the energy threshold set in the data acquisition system (DAQ) for this measurement are visible. In this energy spectrum measured in the MoS, an additional fluorescence line of aluminum at 1.487 keV is visible. It originates from the fluorescence X-ray emitted by a thin aluminum foil placed between the detector and the source.

In the scope of this thesis, mainly the two dominant peaks of the ^{55}Fe spectrum have been used to quantify the detector performance and its calibration. To this end, only a fit in the region near them is performed as shown in Figure 4.10b. Here, each peak is described by a Gaussian distribution $G(E|\mu, \sigma, N_G)$, with a width σ, a mean position μ and a normalization factor N_G as given in Equation (4.23). To accommodate for the backgrounds and detector effects like charge sharing and backscattering at energies below the peak, a shelf-like distribution $S(E|\mu, \sigma, N_S)$ is assumed as shown in Equation (4.24). To model effects generated by the diffusion of the secondary electrons in, e.g., the entrance

[10] The CCE is sometimes also called quantum efficiency.

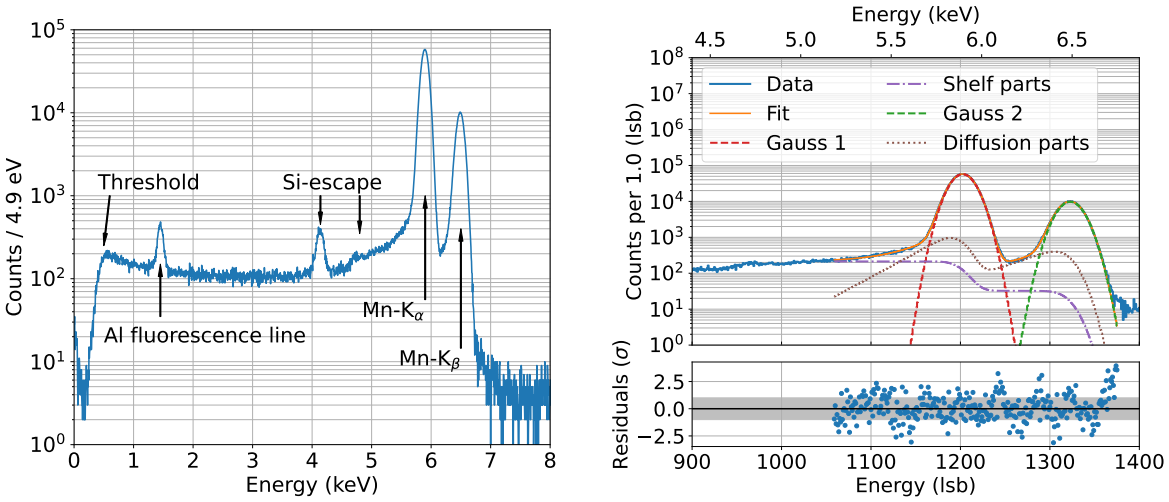

(a) ^{55}Fe spectrum in MoS **(b)** Fit to ^{55}Fe spectrum

Figure 4.10: Typical ^{55}Fe spectrum and fit function for its main peaks
(a) Calibrated energy spectrum measured in pixel 01-02 in the MoS. The energies of the two main peaks are listed in Table 6.1. The two silicon escape peaks are shifted by 1.740 keV [100] towards lower energies. An additional fluorescence line for the aluminum line is visible at 1.487 keV since an additional thin aluminum foil has been installed between the detector and the source. (b) Typical fit of the peak region of an ^{55}Fe spectrum. The fit is illustrated in the solid orange line with a reduced $\chi^2 \approx 1.5$. The different sub-components are shown in the dashed lines.

window region, an exponential step function $D(E|\mu,\sigma,\beta,N_D)$ is assumed as described in Equation (4.25). It models the small asymmetric tail for the lower energies of the main peak. Its strength is given by the normalization N_D and the width by the parameter β. A more detailed description of the detector response to X-rays can be found in [92] with examples of the influence of the different parameters.

$$G(E|\mu,\sigma,N_G) = \frac{N_G}{\sqrt{2\pi}\sigma}\exp\left(-\frac{(E-\mu)^2}{2\sigma^2}\right) \tag{4.23}$$

$$S(E|\mu,\sigma,N_S) = N_S\left(1-\operatorname{erf}\left(\frac{E-\mu}{\sqrt{2}\sigma}\right)\right) \tag{4.24}$$

$$D(E|\mu,\sigma,\beta,N_D) = N_D\exp\left(\frac{E-\mu}{\beta}\right)\left(1-\operatorname{erf}\left(\frac{E-\mu}{\sqrt{2}\sigma}+\frac{\sigma}{\sqrt{2}\beta}\right)\right) \tag{4.25}$$

The entire function for the two peaks in the ^{55}Fe spectrum is given by Equation (4.26). To reduce the complexity of the fit, the normalization parameters of the shelf and diffusion part for the second ^{55}Fe peak (Mn-K$_\beta$ line) are assumed to be proportional to the first peak height N_G (Mn-K$_\alpha$ line). In addition, the parameter β is set equal for the two peaks. The energy resolution in terms of FWHM is extracted using Equation (4.15) since the width of the X-ray peaks is dominated by the Gaussian width σ.

$$\begin{aligned} P_{2\gamma}(E) = {} & G(E|\mu_1,\sigma_1,N_{G1}) + S(E|\mu_1,\sigma_1,N_{S1}) + D(E|\mu_1,\sigma_1,\beta,N_{D1}) \\ & + G(E|\mu_2,\sigma,N_{G2}) + S\left(E|\mu_2,\sigma_2,N_{S1}\frac{N_{G2}}{N_{G1}}\right) + D\left(E|\mu_2,\sigma_2,\beta,N_{D1}\frac{N_{G2}}{N_{G1}}\right) \end{aligned} \tag{4.26}$$

For the measurements with the ^{241}Am source the peaks given in Table 6.3 are fitted individually in a narrow region of approximately one FWHM, since the total spectrum is much more complex. In this narrow region, the spectrum is mostly described by a Gaussian function $G(E|\mu, \sigma, N_G)$. In addition, a flat background is assumed to roughly model the shelf part originating from other lines.

In all measurements with X-rays, the detector is calibrated in situ with the peak positions μ_i of the different lines. The linear calibration curve, given in Equation (4.27), with a slope s and offset o is fitted to the peak positions and used to convert the energy from lsb to eV.

$$E[\mathrm{eV}] = s[\mathrm{eV/lsb}] \cdot E[\mathrm{lsb}] + o[\mathrm{eV}] \tag{4.27}$$

4.7 Detector Response to Electrons

As described in Chapter 4.5, β-electrons in the keV range interact much more strongly with the detector material than X-rays and therefore their energy deposition profile is much closer to the entrance window. This has a large impact on the detector response shown in Figure 4.11. Since they deposit a non-negligible amount of their energy already in the first few 100 nm of the detector[11] they are affected by the reduced CCE near the entrance window. Consequently, the measured main peak for monoenergetic electrons shifts to lower energies (compared to X-rays with the same energy), and the asymmetric low energy tail becomes more pronounced, effectively decreasing the detector energy resolution. To model the main peak of the electron spectrum again, a Gaussian function $G(E|\mu, \sigma, N_G)$ is assumed to describe the electrons that deposit almost their entire energy in the detector. For the asymmetric shoulder, two diffusion functions $D(E|\mu, \sigma, \beta, N_D)$ are assumed to take the electrons into account, which lost more energy in the entrance window region.

Another form of incomplete charge collection are back-scattered electrons. Since the electron undergoes scattering processes that can change the momentum direction, it is possible that it (or other secondary electrons generated in the process) leave the detector material. As a result, only a fraction of its energy is deposited in the (sensitive) detector material, creating a continuous back-scattering tail. For electrons with an incident energy of 20 keV back-scattered electrons account for approximately 20 % and form an important part of the detector response. This back-scatter probability increases with shallower incident angles and lower incident energies up to 40 % [101]. To describe this back-scatter tail, a power function with a free exponent c and a normalization N_B is used as described in Equation (4.28).

$$B(E|\mu, N_B, c) = N_B \left(1 - \frac{E}{\mu}\right)^c \tag{4.28}$$

[11] As an example electrons with 5 keV deposit roughly 40 % on the first 100 nm.

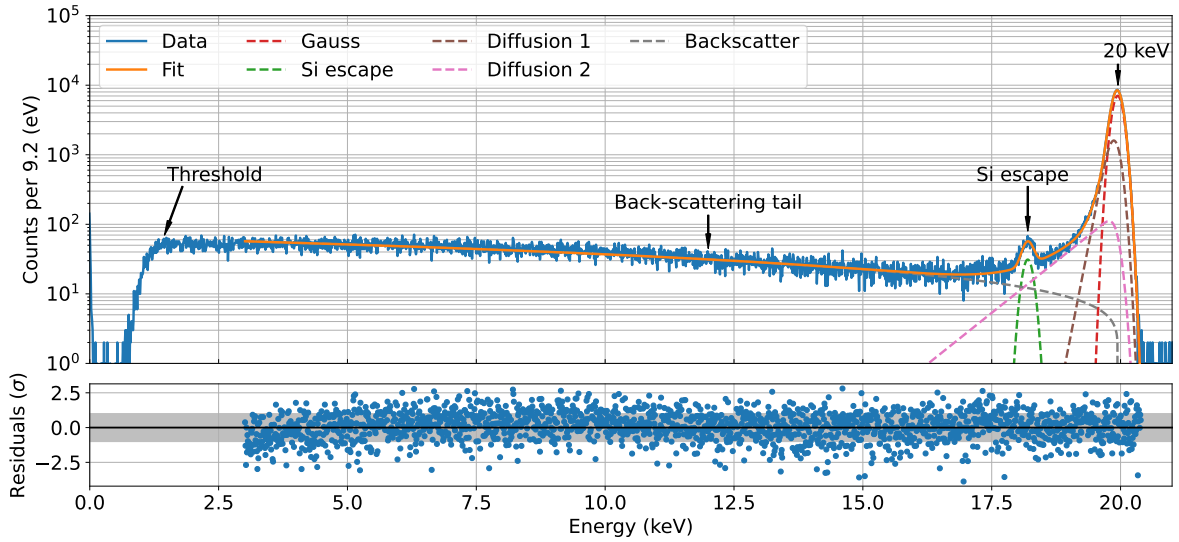

Figure 4.11: Typical 20 keV electron spectrum with fit functions
Calibrated energy spectrum for monoenergetic electrons measured in the E-gun vacuum chamber setup in pixel 01-02 for detector S0-166-4. The data is shown in blue and the fit is illustrated by the solid orange line with a reduced $\chi^2 \approx 1.15$. The different parts of the fit function associated to different detector effects are illustrated by the dashed lines. On the bottom the residuals between data and the fit in terms of standard deviation σ are given. Here, the grey area illustrates the 1σ band.

The entire function for the fit is shown in Equation (4.29), including another Gaussian function to model the silicon escape peak[12].

$$\begin{aligned} P_{\mathrm{e}^-}(E) = {} & G(E|\mu_1, \sigma, N_G) + D(E|\mu, \sigma, \beta_1, N_{D1}) + D(E|\mu, \sigma, \beta_2, N_{D2}) \\ & + G(E|\mu_{\mathrm{Si}}, \sigma_{\mathrm{Si}}, N_{G,\mathrm{Si}}) + B(E|\mu, N_B, c) \end{aligned} \tag{4.29}$$

To extract the energy resolution in terms of FWHM, the fit function shown in orange is used and evaluated at half of the peak height maximum. To simplify the analysis in the different measurements like the MoS, also a reduced fit with only a Gaussian and one diffusion function is performed to extract the FWHM. For these fits, the ROI is limited to a width of approximately two times the expected FWHM.

[12] The Gaussian function G and the diffusion function D are the same as for the X-ray response shown in Equation (4.23) and Equation (4.25), respectively.

5

THE TRISTAN DETECTOR MODULE

In this chapter, the TRISTAN detector module and its assembly procedure are introduced. The general design considerations that define the overall shape and structure of the detector module are given in Chapter 5.1. A description of the resulting mechanical structure, which has been developed in this work, is presented in Chapter 5.2. The 166 pixel TRISTAN SDD chip which is installed at the front of the detector module is described in Chapter 5.3. The on-module electronics that handle the amplification of the signals and filter the detector voltages are outlined in Chapter 5.4. An overview of the different temperature sensors on the detector module and their calibration is given in Chapter 5.5. The assembly and cleaning procedure, which has been developed in this thesis, are described in Chapter 5.6. This chapter also covers the most important observations that affected the yield of functional pixels related to the assembly procedure. The different detector modules that have been assembled in this work are shortly described in the appendix in Chapter B.

5.1 Design Considerations for the Detector Module

Besides the requirements motivated by the physics of the keV mass scale neutrino search discussed in Chapter 3.2.2, the driving design decisions for the TRISTAN detector system are given by

- SDD technology related requirements and limitations
- Compatibility with the KATRIN MAC-E filter environment
- Manufacturing of individual module components

SDD Technology In general, the concept of SDDs is very flexible in size and shape. Nevertheless, the requirements on the detector system in terms of segmentation (number of pixels to keep the pile-up low) and energy resolution (to not smear out the shape distortion of the sterile neutrino) are beyond the current technological possibilities in producing one large monolithic detector with a size of approximately 20 cm in diameter. Thus, the detector system is segmented into smaller multi-pixel detector modules shown in Figure 5.1.

At the front side of the detector module sits a large rectangular (40 mm x 38 mm) monolithic SDD chip consisting of 166 pixels, which is glued to a silicon ceramic composite called Cesic [102]. Additionally, two rigid-flex printed circuit boards (PCBs) are glue to the Cesic interposer which provide the electrical connection between the SDD chip and the on-module electronics. In this work this assembly of SDD chip, Cesic interposer and rigid-flex PCBs is called detector front. It is mounted onto the copper cooling structure which is connected to the cooling system. The on-module electronics for the signal amplification

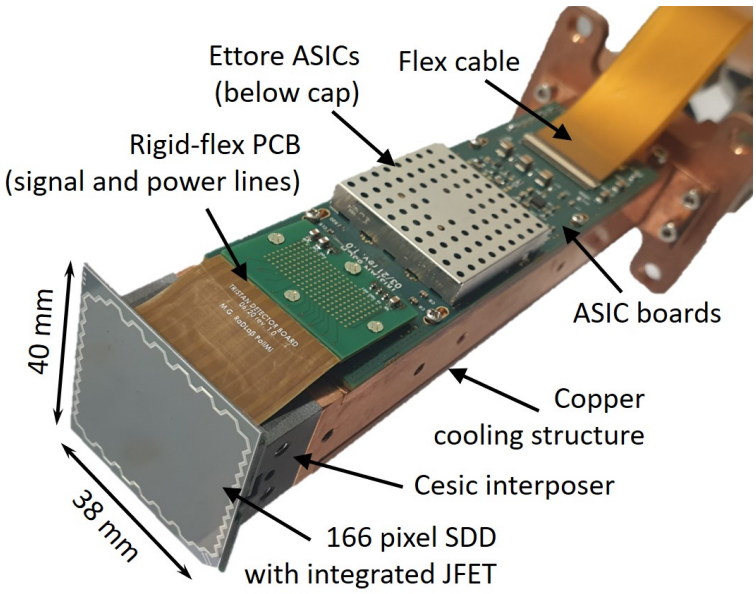

Figure 5.1: Photograph of a TRISTAN detector module
The picture shows a fully equipped 166 pixel detector module connected to a cooling system. The main components of the detector module such as the SDD chip, Cesic interposer, rigid-flex PCB, ASIC board and cooling structure are labeled.

are placed on two identical PCBs, called ASIC boards on the sides of the copper cooling structure. This arrangement makes it possible that the individual detector modules can be placed next to each other, minimizing the insensitive area of the detector system to almost cover the entire electron flux tube of the KATRIN experiment. The segmentation of the detector system into smaller detector modules has the additional benefit that the design can be tested on a smaller scale.

Compatibility with KATRIN Environment The TRISTAN detector system will consist of nine detector modules and will be deployed in the position of the current FPD system. Here, the detector system will experience magnetic fields up to 2.5 T [7, 47, 73]. Furthermore, the detector system needs to be compliant with the ultra-high vacuum conditions in the detector section. In the case of the neutrino mass measurement with KATRIN, a vacuum of 10^{-11} mbar is maintained in the main spectrometer to keep the background rate in the ROI near the retarding potential energy at a low-level of 220 mcps [103]. To achieve such an ultra-high vacuum, the gas load from the detector section towards the main spectrometer has to be in the order of $5 \cdot 10^{-8}$ mbar L/s [7]. A first estimation of the expected gas load due to the detector modules components can be found in the investigations with prototype parts [7, 104]. However, since for the keV sterile neutrino search with KATRIN, the anticipated rates on the detector are more than eight orders of magnitude larger, the vacuum requirements are less stringent, and a vacuum pressure in the order of 10^{-9} mbar can likely be tolerated. Therefore, all materials involved in the detector module have as low as possible outgassing properties. Additionally, all materials are either non-magnetic or at least of low magnetic permeability to reduce the mechanical forces and ensure the electrical functionality in the large magnetic fields.

Manufacturing of the Detector System To reduce the complexity in the manufacturing process an interconnection (mechanically and electrically) between the detector front and the back of the detector module (consisting of ASIC boards and copper cooling structure) was

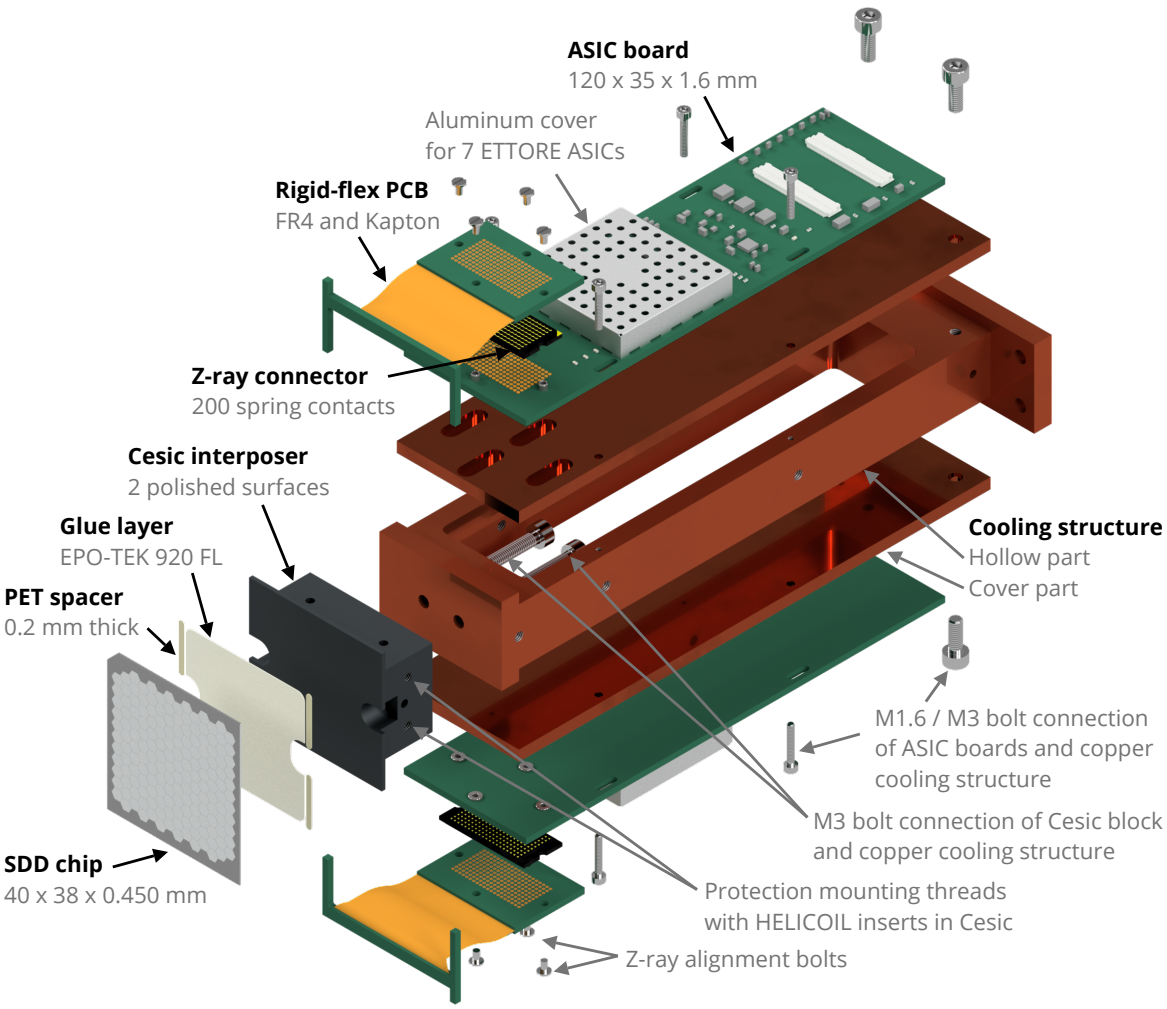

Figure 5.2: Illustration of the detector module components
For reasons of visual clarity, the detector module has been decomposed into the individual components.

introduced. This decision is mainly driven by the gluing and wire bonding of the SDD chip and the high-density PCB design of the ASIC boards.

5.2 Mechanical Design Considerations and Decisions

The mechanical structure of the detector module is based on two basic elements: the Cesic interposer and the cooper cooling structure. Their main purpose are the mechanical support of all components as well as the provision of a good thermal conductivity towards the cooling system. The different mechanical and electrical components of the detector module are illustrated in Figure 5.2. All materials used for the mechanical structure of the detector module have been selected to be very compatible with the environment of the KATRIN detector section in terms of magnetic field compatibility and outgassing properties. The material properties are listed in Table 5.1.

The coupling between the SDD chip and the support structure is a critical point in the detector module design. Since in the KATRIN experiment the detector modules will be placed next to each other, the only possible region for a mechanical connection is the readout side of the SDD chip. The mechanical connection is realized by gluing the SDD chip

Table 5.1: Properties of module materials
Comparison of the mechanical, thermal and electrical properties of the materials used in the detector module. All properties are given for room temperature of 293.15 K. For silicon the data is taken from [78, 80, 105]. The information are taken from: Cesic [102], Copper [106, 107], stainless steal [108, 109].

Material properties	Silicon	Cesic	Copper	Stainless steel
Density (kg/m^3)	2.329	2.96	8.93	8.0
Linear CTE ($10^{-6}/K$)	2.56	2.3	16.4	16.0
Thermal conductivity ($W/(m\,K)$)	156	200	385	16.3
Specific electrical resistance ($\Omega\,m$)	$2.3 \cdot 10^{3}$	$3.5 \cdot 10^{-5}$	$1.7 \cdot 10^{-8}$	$7.4 \cdot 10^{-5}$
Magnetic susceptibility χ_m	$-3.7 \cdot 10^{-6}$		$-8 \cdot 10^{-8}$	0.05 to 0.1 (304L) < 0.01 (316L)
Outgassing rate ($mbar\,L/(cm^2\,s)$)			$< 4 \cdot 10^{-11}$	$< 1 \cdot 10^{-12}$

with an electrically insulating, low outgassing two-component epoxy (EPO-TEC 920-F [110]) on a silicon ceramic composite made of Cesic [102]. The glue was selected since it has been used successfully in various satellite projects in which the HLL was involved [111, 112]. The Cesic material has been chosen since it matches the CTE of the SDD material (silicon) quite well and has a high specific strength and good machinability. The matching of CTE is very important, since the detector module will be exposed to a wide range of temperatures ranging from 60 °C during the bake out in the assembly procedure, down to temperatures of −40 °C during the operation in the experiment. A larger mismatch in the CTE of the materials could result in damages or even cracks in the large SDD chip[1].

Keeping in mind the shape of the detector module and its assembly procedure, the form of the Cesic interposer illustrated in Figure 5.3 arises from the following design considerations:

- A large contact area between the SDD chip and the Cesic is beneficial due to a good thermal conductivity and relatively low mounting pressure on the (active[2]) readout area during the assembly procedure.
- An uneven or rough surface finish on the Cesic interposer can lead to an uneven pressure on the SDD chip, which in the worst case could piercing into the readout structure and damage it. Therefore, a flat and polished surface finish is used.
- Fixing the rigid-flex PCB on the Cesic interposer reduces the parts that mechanically interact directly with the sensitive active readout area of the SDD chip. In the following, this region of the Cesic interposer is referred to as fins.
- The fins on which the rigid-flex PCB is glued, need to be thick enough to mechanically support the PCB. Additionally they need to withstand the tensile forces that can arise when the rigid-flex PCB is mounted to the ASIC boards. On the other hand, to ensure

[1] E.g., a piece of copper with the length of 40 mm expands approx. 60 µm more than the same size SDD chip over the temperature range of 100 °C
[2] The here called active and passive regions of the SDD chip are illustrated in Figure 5.23a.

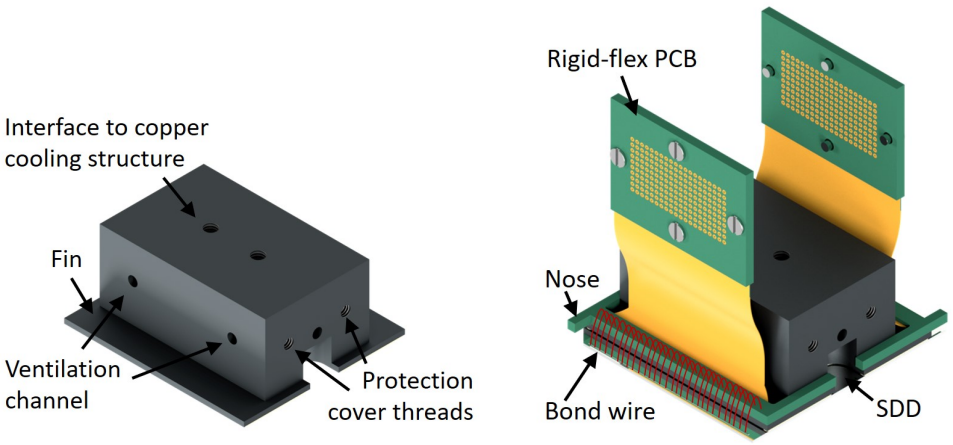

(a) Cesic interposer **(b)** Detector front

Figure 5.3: Illustration of Cesic interposer
(a) CAD illustration of Cesic interposer used in detector modules. (b) Cesic interposer with the rigid-flex PCBs glued to its fins. The SDD chip is visible beneath the Cesic interposer with its entrance window facing downwards. The wire bonds from the SDD chip to the rigid-flex PCB are illustrated in red.

the wire bonds can be placed reliably the total height of the Cesic fin together with the rigid-flex PCB has to be in the order of 3 mm. Therefore, a height of 1 mm for the fins has been chosen in the design.

- The dimensions of the Cesic interposer need to be small enough such that the assembly fits under the bonding machine. Moreover, the interposer needs to have a small mass to minimize the pressure on the SDD chip during the assembly procedure.

In its unprocessed form, Cesis has a comparably rough surface. To ensure a flat surface finish that cannot damage the readout side of the SDD chip, the large contact area of the Cesic interposer is polished by the manufacturer. After polishing, according to the manufacturer, a surface roughness of a few nm is achieved. This is much smaller than the glue layer (190 µm) between the SDD chip and Cesic interposer. The other side of the Cesic interposer, which is connected to the copper cooling structure, is also polished to ensure good thermal contact. Due to the demanding vacuum compatibility requirements no thermal compound is used between mating sides of the Cesic interposer and the copper cooling structure.

Multiple threads are machined into the Cesic interposer to connect it to the copper cooling structure and the protection covers. Since the Cesic material is slightly brittle, the threads could wear down, creating small loose particles inside them. To avoid these small particles and improve the resilience of the threads, stainless steel HELICOIL® threaded inserts are installed inside the threads of the Cesic interposer. To ensure vacuum compatibility, all threaded holes inside the Cesic interposer have an additional ventilation channel to avoid virtual leaks coming from trapped gas beneath the screw.

The mechanical connection between the Cesic interposer and the copper cooling structure is realized by two M3 stainless steel bolts. They are inserted into the hollow part of the cooling structure. Making the copper cooling interface structure hollow reduces the overall mass of the detector module and allows for easier access to the two connecting bolts. Two plates are mounted on the top and bottom surfaces of the main hollow structure. They

serve as a thermal contact area for the two ASIC boards and mechanically fix their position. As for the Cesic interposer, all cavities are equipped with an additional ventilation channel.

5.3 The TRISTAN SDD Chip

An important part of the detector module is the SDD chip with 166 pixels. A photograph of it is shown in Figure 5.4. The chips are produced by the HLL from a high-resistivity n-type silicon material. The wafer itself has a diameter of 6 inch (15.24 cm) and a thickness of 450 µm and provides space for several TRISTAN devices. In Figure 5.5, the wafer layout for two different TRISTAN productions is shown. The detectors used in this thesis are from the production SDD33. The rectangular chip has the outer dimensions of 38 x 40 mm^2. The individual pixels have a hexagonal shape with a diameter of approximately 3 mm^3 and are arranged in a gapless honeycomb structure. The active area of one 166 pixel SDD chip is $A_{\text{active}} = 1172\,\text{mm}^2$, which corresponds to a about 77.1 % of the total chip area. This pixel size has been chosen to minimize detector-related effects such as charge sharing, backscattering, and back-reflection [73]. All structures and traces required for the drift field generation and collecting anodes are placed on the so-called readout side of the device as shown in Figure 5.4a. As can be seen in the photograph, the (vertical) traces connecting the individual pixels are routed to the upper and lower hemisphere H of the SDD chip. In this work, the upper hemisphere (with the cut corner) is denoted as the northern hemisphere N and the other one as the southern hemisphere S. The bond pads for the electrical connection are placed at the upper and lower boundaries of these hemispheres. The geometry of the detector is almost symmetric between the upper and lower part, with the small exceptions of the cut corner for the BC wire bonds in the lower left and the temperature diode in the upper right corner. The other side of the detector on which the incident radiation is impinging is called entrance window side, see Figure 5.4b. It consists of the negatively biased, non-structured p^+-implanted contact (called BC) that extends over the entire active area of the chip and depletes the detector. This implantation is surrounded by another p^+-implantation called back frame (BF). It is set to a slightly more negative voltage and prevents electrons from entering the depleted detector volume from the undepleted region outside the pixels. Two wire bonds are used at the cut corner of the SDD chip to electrically connect the BC and BF contacts to the nose of the rigid-flex PCB.

Every pixel features an integrated nJFET inside the n^+-doped anode and an integrated feedback capacitance of $C_{\text{FB}} = 25\,\text{fF}$. It is operated in a closed-loop negative feedback CSA circuit as described in Chapter 4.3. The feedback (FB) and source (SC) lines connect the anode and nJFET of each pixel to the corresponding bond pads at the outer edges of the SDD chip. These, in turn, are connected with the ETTORE ASIC amplifiers on the ASIC boards via the rigid-flex PCBs. A schematic of the bus system in the anode region is shown in Figure 5.6a. A deep p^+-implantation, called inner guard ring (IGR), is placed around the nJFET to prevent any charge carriers from entering it directly. By applying a negative voltage to the IGR the electric fields in the anode region are shaped such that the signal electrons are guided to the anode. They then enter the gate of the nJFET via a metal connection on the surface of the SDD chip. Reset diodes integrated into each anode are used to drain the collected charges from the anode and feedback capacitor C_{FB} in a pulsed reset mode. As shown in Figure 5.6b, these reset diodes are grouped into 14 stripes,

[3] The inner diameter of the hexagonal pixel is $d_i = 2856\,\text{mm}$ and the outer diameter is $d_o = 3.298\,\text{mm}$. The area of a hexagon is equivalent to the area of a circle with a diameter of 3 mm.

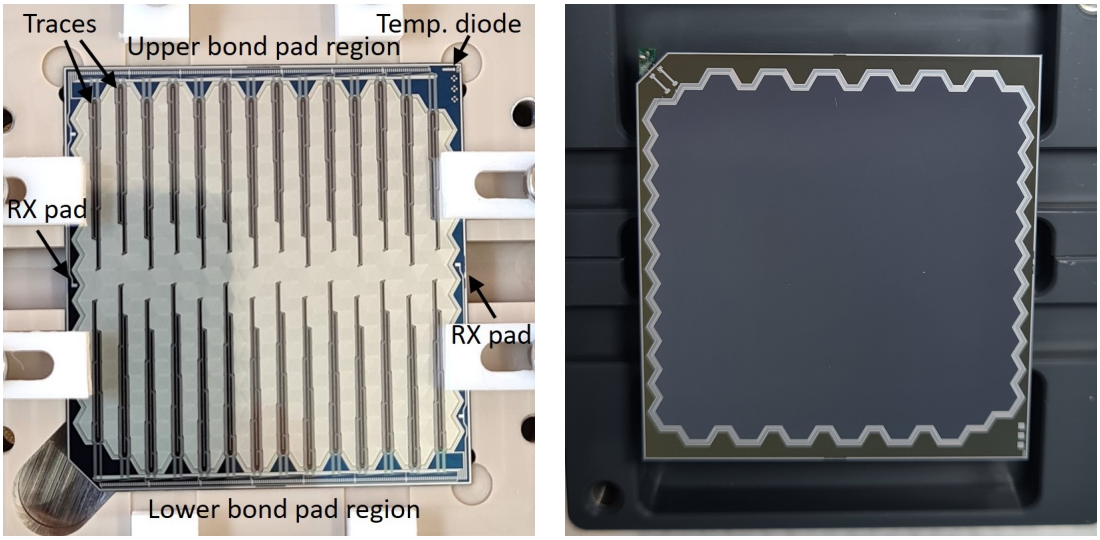

(a) Readout side **(b)** Entrance window side

Figure 5.4: Photographs of a TRISTAN SDD chip with 166 pixels
(a) Readout side of an SDD chip inside the PEEK jig used in the assembly process. (b) Entrance window side of an assembled detector module. In the upper left corner, the two bond wires for the BC and BF implantation can be seen.

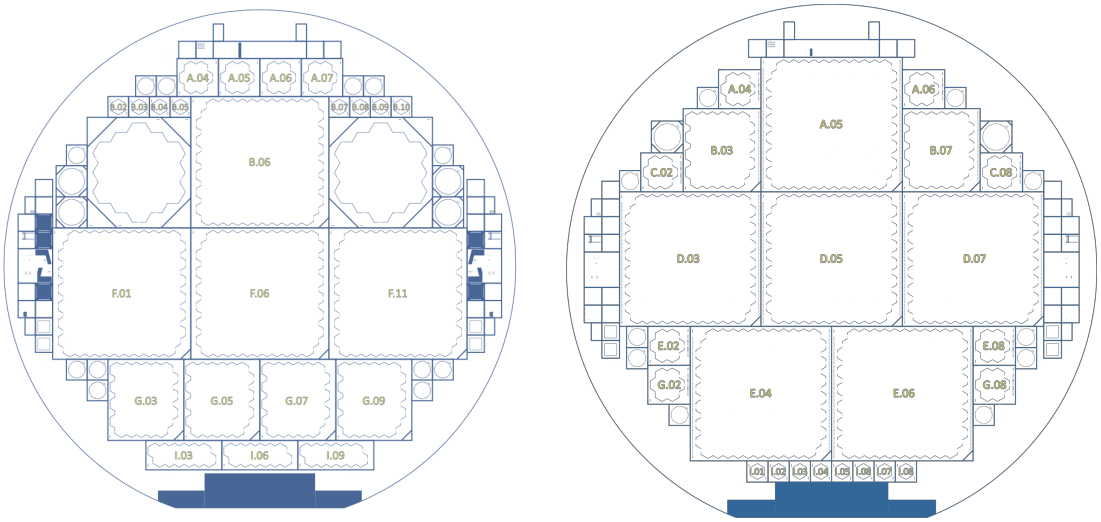

(a) Wafer layout of production SDD33.x **(b)** Wafer layout of production SDD35.x

Figure 5.5: Wafer layout for the TRISTAN SDD chips
Illustration of the wafer layout for different production runs of the TRISTAN SDD chips. The wafers are seen from the readout side. The labels in the center of each chip are the corresponding chip numbers. (a) Layout of the production SDD33 with four 166 pixel SDD chips and multiple 7, 12 and 47 pixel prototype SDD chips. In this work, only SDD chips from this production have been used. (b) Layout of production SDD35 which hosts six 166 pixel SDD chips per wafer. In this production, improvements in the SDD chip layout have been implemented to reduce the crosstalk between pixels.

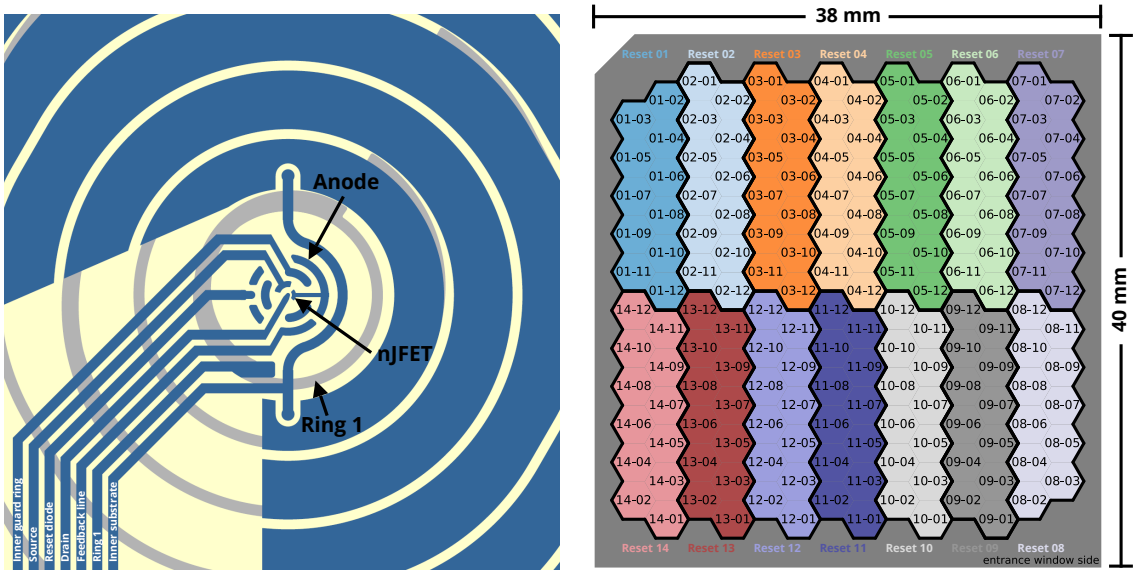

(a) Metal traces in the anode region **(b)** Arrangement of reset groups

Figure 5.6: Electrical bus structure and reset groups in the SDD chip
(a) Illustration of the metal traces (blue) of the different structures in the anode region. Courtesy of P. Lecher. (b) Illustration of the different reset groups of the 166 pixel SDD chip as seen from the entrance window side. Each group consists of 12 pixels, which share one common reset line. All reset groups have been synchronized to minimize crosstalk and reduce the complexity of the on-module electronics.

with each twelve pixels[4]. In theory, each reset group could be drained individually. However, to minimize the risk of potential crosstalk and to reduce the complexity of the electronic ASIC boards, the entire SDD chip is reset with one synchronous signal across the entire SDD chip.

Each pixel has 21 concentric drift rings arranged around the anode, with the innermost and outermost drift rings referred to as R1 and RX, respectively. The individual drift rings of a given pixel are connected in series with a resistance of $R_{\mathrm{C}} \approx 235\,\mathrm{k\Omega}$. The traces of the R1 contacts are connected together to one bond pad for each hemisphere of the SDD chip. The RX is a continuous p^{+}-implantation that extends over the entire SDD chip. It is connected (redundantly) via two bond pads on the sides of the SDD chip. To create the drift field within the detector, a negative voltage of $V_{\mathrm{R1}} \approx -10\,\mathrm{V}$ and $V_{\mathrm{Rx}} \approx -120\,\mathrm{V}$ is applied to the drift ring contacts. Since the other drift rings are connected in series to R1 and RX, their voltage continuously decreases (more negative) from R1 to RX. An equivalent electrical circuit for the voltage divider in the drift ring network is shown in Figure 5.7. The total resistance of the network is $R \approx 28.3\,\mathrm{k\Omega}$ and results in a total current in the order of 4 mA. A measurement of the currents can be found in the appendix in Chapter C.2. A summary of the technical details for the 166 pixel SDD chips is given in Table 5.2.

[4] Compared to other reset groups, the groups 01 and 14 are missing one pixel. They have been removed to allow for the placement of the BC wire bonds and temperature diode.

Table 5.2: Design values for 166 pixel TRISTAN SDD chip and ASIC boards
Overview of the 166 pixel TRISTAN SDD chip properties and ASIC board power consumption. The information was provided by P. Lechner and M. Gugiatti [89].

TRISTAN SDD chip characteristics	Value
Wafer substrate type	n-type Si $\langle 100 \rangle$
Wafer thickness	450 µm
Wafer doping concentrations	$0.9 \cdot 10^{12}\,\mathrm{cm}^{-3}$
Number of pixels	166
Chip size A_{SDD}	$38 \times 40\,\mathrm{mm}^2 \approx 1520\,\mathrm{mm}^2$
Active area A_{active}	$1172.44\,\mathrm{mm}^2$ (77.1 %)
Golden area A_{golden}	$847.55\,\mathrm{mm}^2$ (55.8 %)
Pixel area A_{px}	$\approx 7.06\,\mathrm{mm}^2$
Number of drift rings	21
Resistance between drift rings R_{C}	$\approx 235\,\mathrm{k\Omega}$
Total resistance of drift ring network	$\approx 28.3\,\mathrm{k\Omega}$
Feedback capacitance C_{FB}	25 fF
Anode capacitance C_{D}	112 fF
nJFET gate capacitance C_{G}	56 fF
Stray capacitance C_{stray}	10 fF
Total detector capacitance C_{Tot}	178 fF
nJFET bias current I_{SSS}	300 µA
nJFET transconductance g_{m}	300 µA/V
1/f noise coefficient A_{f}	$5 \cdot 10^{-12}\,\mathrm{V}^2$
nJFET power dissipation P_{JFET}	$\approx 2\,\mathrm{mW}$
Total chip power dissipation P_{Tot}	$\approx 250\,\mathrm{mW}$
ETTORE ASIC power dissipation per channel $P_{\mathrm{ch,\ ETTORE}}$	$\approx 21\,\mathrm{mW}$
Total power dissipation per ASIC board P_{83ch}	$\approx 2000\,\mathrm{mW}$
Back contact bias voltage V_{BC}	−80 V to −120 V
Back frame guard voltage V_{BF}	−90 V to −130 V
Innermost drift ring voltage V_{R1}	−5 V to −15 V
Outermost drift ring voltage V_{RX}	−100 V to −150 V
Anode guard ring voltage V_{IGR}	−15 V to −35 V
Temperature diode guard voltage	−15 V
nJFET drain voltage V_{Dr}	5 V to 10 V
Reset diode low V_{ResLow}	−10 V

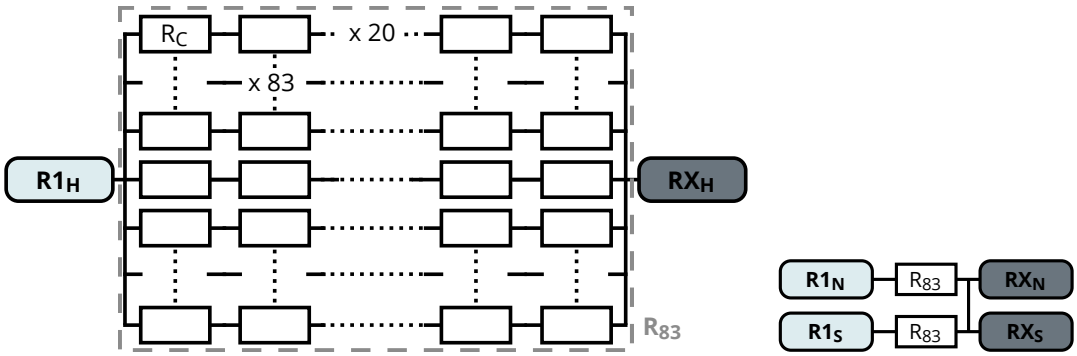

(a) Resistor network for one SDD hemisphere **(b)** Total network

Figure 5.7: Electrical circuit of drift ring resistor network
(a) Resistance network of the voltage divider in one SDD hemisphere H. The network consists of 83 resistors in parallel. Each pixel, in turn, has 20 resistors in series (one between all adjacent drift rings). The resistance between each drift ring is $R_C \approx 235\,\text{k}\Omega$. The equivalent resistance per pixel is approximately 4.7 MΩ and $R_{83} \approx 56.6\,\text{k}\Omega$ per hemisphere H. (b) Global resistance network of the entire SDD chip. The resistor networks of the two hemispheres N and S are connected via the RX p^+-implantation. The equivalent resistance of the entire network is 28.3 kΩ.

5.3.1 *Integrated vs External FET*

For the amplification of the signals detected with the TRISTAN SDD chip, an nJFET integrated into the anode of every pixel in combination with a specifically developed readout ASIC, called ETTORE is used. The electronic circuit of the CSA for one pixel is shown in Figure 4.5. The purpose of the nJFET is to increase the current flowing through the SC and FB lines (and therefore is less sensitive to noise variations). This allows the ETTORE ASIC amplifier to be placed several centimeters away from the pixel anodes. The integrated nJFET minimizes the distance between the anode and gate of the transistor, which reduces the stray capacity C_{stray} at the gate. To better understand the effects of the transistor placement, one can simplify Equation (4.21) to Equation (5.1).

$$n_{\text{ENC}}^2 \propto \underbrace{\frac{(C_D + C_{\text{FB}} + C_{\text{stray}} + C_{\text{G}})^2}{g_m}}_{\text{series}} \propto \underbrace{\frac{(C_D + C_{\text{FB}} + C_{\text{stray}} + C_{\text{G}})^2}{C_{\text{G}}}}_{\text{using } g_m \propto C_{\text{G}}} \tag{5.1}$$

$$C_{\text{A}} = C_D + C_{\text{FB}} + C_{\text{stray}} + C_{\text{G}} \tag{5.2}$$

As shown, the electronic noise and thus the energy resolution scales quadratically with the capacitance of the anode C_{A}. The stray capacitance $C_{\text{stray}} \approx 10\,\text{fF}$ for the TRISTAN SDD chips is much smaller than the detector capacitance with a value of $C_D = 112\,\text{fF}$ since the nJFET is directly integrated into the anode. To put this stray capacitance into perspective, a rough estimation can be performed. As described in Chapter 5.3, the traces of the individual pixels run from the anode to the outer edges of the SDD chip. For a pixel in the center of the SDD chip the trace is approximately $l_{\text{trace}} \approx 20\,\text{mm}$ long with a width of $w_{\text{trace}} \approx 10\,\mu\text{m}$. Between trace and the fixed potential of the drift rings is a silicon oxide layer ($\epsilon_{\text{SiO}_2} = 3.9$) with a thickness of $d_{\text{SIO}_2} \approx 2\,\mu\text{m}$. Assuming a simple model with a plate capacitor between the trace and the drift rings a stray capacitance of $C_{\text{stray,trace}} \approx 3.5\,\text{pF}$ can be estimated using Equation (5.3).

$$C_{\text{stray,trace}} = \epsilon_0 \epsilon_{\text{Si0}_2} \frac{A_{\text{trace}}}{d} = \epsilon_0 \epsilon_{\text{Si0}_2} \frac{l_{\text{trace}} \cdot w_{\text{trace}}}{d} \tag{5.3}$$

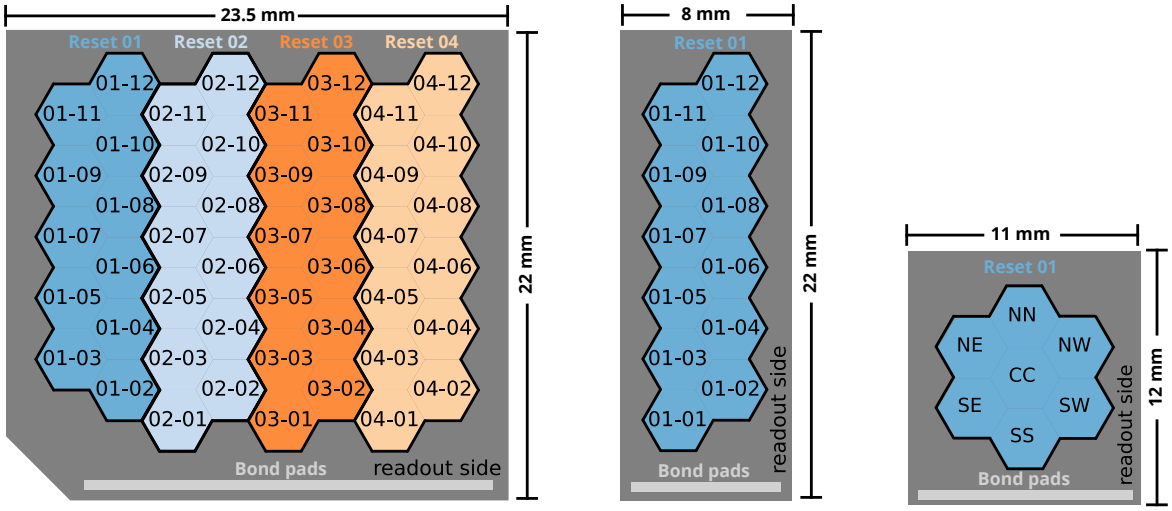

(a) 47 pixel SDD chip **(b)** 12 pixel SDD chip **(c)** 7 pixel SDD chip

Figure 5.8: Illustration of the TRISTAN prototype SDD chips with 7, 12 and 47 pixels
All devices feature the same pixel geometry with a diameter of 3 mm and an integrated nJFET as the 166 pixel SDD chips. (a) Layout of a 47 pixel SDD chip with an active area of 331.82 mm^2. (b) Layout of a 12 pixels SDD chip with an active area of 84.7 mm^2. (a) Layout of a 7 pixels SDD chip with an active area of 49.3 mm^2.

This value is more than one order of magnitude larger than the actual detector capacitance C_D and would strongly increase the noise in the detector. Therefore, for detectors with an external field-effect transistor (FET), the connection to the anode is typically realized using wire bonds. The wire bonds strongly increase the distance d to other lines at a fixed potential, and the stray capacitance C_{stray} is mainly determined by the bond pad region. One example of this implementation are the TRISTAN 7 pixel prototype detectors with external CUBE ASIC amplifiers, whose performance is discussed in [61]. For these smaller 7 pixel prototype devices, this solution is suitable since the CUBE ASICs amplifier could be placed next to the SDD chip. For the detector modules, the placement of amplifiers is technically more challenging due to the geometrical constraints for the almost gapless placement of detector modules. The amplifiers, such as the CUBE ASIC and all corresponding supply lines, would need to be placed on top or in very close proximity to the SDD chip surface to perform the wire bonding. The benefits and drawbacks of the external and internal FET for SDDs are discussed in [89].

5.3.2 *TRISTAN Prototype SDD Chips*

The characterization of the first TRISTAN detectors was performed using prototype devices with a smaller number of pixels. They have the same pixel geometry with integrated nJFET, but with less pixels (7, 12 and 47). The different SDD chips are illustrated in Figure 5.8. The 7 pixel devices have been used to investigate the drift of the charge carriers [87] and the back scattering properties [101]. The 12 and 47 pixel devices mainly have been used to develop the on-module ASIC electronic boards as described in [89]. In the scope of this thesis, the 47 pixel SDD chips have been used to test the feasibility of mounting procedure on the Cesic interposer in which the SDD chip is placed perpendicular to the readout electronics (so-called 3D module design). The measurements with these 47 pixel prototype detectors in the MoS are described in [113].

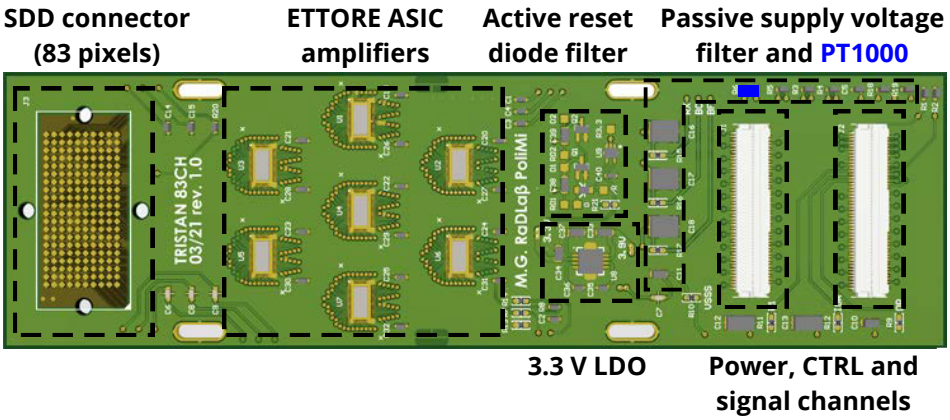

Figure 5.9: Layout of the TRISTAN detector ASIC ASIC board
Overview of the different components on the ASIC board. Each ASIC board can provide the signal amplification for up to 83 pixels via seven ETTORE ASIC amplifiers. The signal, power, and control (CTRL) lines are connected via two 100 pin FPC connectors. In blue, the location of the platinum thermistor (PT1000) is illustrated. Figure adapted from [89].

5.4 On-Module Electronics

The on-module electronics consists of two identical high-density twelve-layer PCBs, which host the ETTORE ASIC amplifiers and provide the filtering for the detector voltages. These boards are called ASIC boards, and each of them is connected to one hemisphere of the SDD chip via a rigid-flex PCB. They are manufactured from the standard PCB material FR4. The boards have the outer dimensions of $120 \times 35\,\mathrm{mm}^2$. To enable an almost gapless side-by-side installation of the modules, the width of the ASIC broads is slightly smaller than the outer dimensions of the SDD chip. The most important building blocks are illustrated Figure 5.9.

SDD Connector for 83 Pixels Each hemisphere of the SDD chip is electrically connected to a rigid-flex PCB using wire bonds. These PCBs consist of two rigid parts as well as one flexible part in the center. The latter one makes it possible to perform the 90° bent to mount the ASIC boards perpendicular to the SDD chip. The schematic and a photograph of the rigid-flex PCB is shown in Figure 5.10. To connect a rigid-flex PCB to the ASIC board, a 200-pins dual-compression interposer[5] with a 1 mm pitch is used. This compact interposer is placed between the contacts of the rigid-flex PCB and the corresponding contact pads on the ASIC board. The pinout of the contacts on the ASIC boards can be found in the appendix in Figure D.4.

ETTORE ASIC Amplifier Each ASIC board hosts seven ETTORE ASIC amplifiers [88] that form a closed-loop negative feedback CSA circuit with the integrated nJFET in the SDD chip. These ASICs have been designed by the company XGLab[6] in collaboration with the Politecnico di Milano University to specifically meet the requirements of the TRISTAN SDD chips. A simplified version of the CSA circuit is shown in Figure 4.5. Each ETTORE ASIC amplifies up to twelve pixels, which is in accordance with the number of pixels for a given reset group in the SDD chip. Each channel of the ETTORE ASIC hosts a preamplifier with an SC and a FB lines that are connected to the corresponding pixel contacts. The output of this first amplification stage is a linearly increasing ramp (due to the leakage current) with the

[5] Z-Ray dual-compression interposer with 200 pins part (number) ZA1-20-2-1.00-Z-10. Additionally, the mounting hardware is required part (number) ZHSI-01-01.
[6] XGLab Srl, Bruker Nano Analytics, Via Conte Rosso 23, 20134 Milano, Italy.

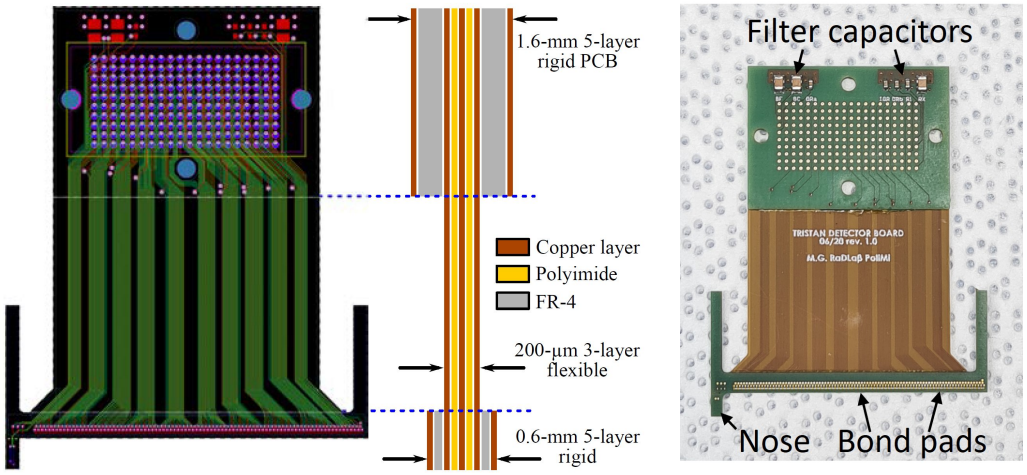

(a) Rigid-flex PCB schematic **(b)** Rigid-flex PCB photograph

Figure 5.10: Schematic and photograph of the rigid-flex PCB
(a) Layout and cross section of the rigid-flex PCB. It is used to connect the SDD chip to the ASIC boards. It consists of a rigid part that hosts the bond pads, a flexible part to enable a 90° bend, and another rigid part that is connected via a z-ray interposer to the ASIC board. Figure taken from [89]. (b) Photograph of rigid-flex PCB.

step-like signal superimposed onto it. In this work, this output is called 1$^{\text{st}}$ stage. In addition, the ETTORE ASIC provides a second AC-coupled readout stage, which can be activated via the biasing system by disabling the SEL_PRE signal. In normal operation[7], the 2$^{\text{nd}}$ stage introduces an additional gain of a factor ten. Moreover, due to the resistive feedback character of this stage, the signals show an exponential decay with a time constant of $\tau_{\text{decay}} = 15\,\mu\text{s}$.

To prevent the 1$^{\text{st}}$ stage ETTORE ASIC output from saturation and drain the collected charges in the anode, the detector has to be rested. For a cooled detector module ($\approx -35\,^{\circ}\text{C}$ at the SDD chip), the frequency at which the detector module has to be reset is mainly driven by the signal count rate, since collected leakage current in the order of a few pA at the anode is much smaller. The reset of the preamplifier can be realized in the following ways:

- The reset of the detector module can be initiated in periodic intervals using an external pulse generator.
- Alternatively, the reset for the detector module can be initiated by a level-sensitive comparator, the ETTORE ASICs that detects the saturation of the preamplifier (1$^{\text{st}}$ stage)[8].

For the measurements performed in this thesis, only the first mode with an externally pulsed reset signal has been used since it has been proven to be more robust in case of pixel failures.

In case one of the detector pixels does not work properly and might negatively affect the performance of other (neighboring) pixels, it can be disabled. To this end, a power-down circuit is integrated into each channel of the ETTORE ASIC amplifier. This circuit detects if the signal output of the ETTORE ASIC channel is shorted to ground and disables it. In this

[7] Alternatively, a low gain mode can be enabled. In this mode, the gain of the 2$^{\text{nd}}$ stage is reduced to a factor of five.
[8] If one of the pixels 1$^{\text{st}}$ stage output exceeds the set saturation voltage V_{th}, a signal (SAT_OUT) is sent to the biasing system, which initiates the reset mechanism for the entire detector module.

way, it is possible to implement the disable feature without any additional (logic) control lines.

Every active channel has a power consumption of about 21 mW. Taking into account the 83 pixels of one detector hemisphere, one entire ASIC board has a power consumption of around 2000 mW. More details on the ETTORE ASIC amplifier and the design considerations for the ASIC boards can be found in [88] and [89].

Passive Supply Voltage Filter Due to the high length (about 2 m) of the supply line cables between the detector and the biasing system, they are susceptible to electronic noise, such as electron electromagnetic interference. In particular, the detector biasing and supply voltages of the CSA are sensitive to noise fluctuations. To minimize this effect and filter all important supply voltages, the ASIC boards are equipped with (passive) low-pass RC filters.

Active Reset Diode Filter Since the supply line of the reset diode is directly connected to the anode of every pixel, it can introduce noise in the CSA and readout chain. To reduce this effect, the reset diode supply line needs to be filtered. During the operation of the detector module, the reset signal is by default set to a negative voltage $V_{\mathrm{ResL}} \approx -10\,\mathrm{V}$. During the reset, the voltage is switched to a positive value $V_{\mathrm{ResH}} \approx 4\,\mathrm{V}$ for a short time period (around 1.5 µs) to drain the collected charges from the anode. As a consequence of the fast voltage change, using a passive RC filter for the other supply voltages would not work. To overcome this problem, an active switch-mode filter is implemented. It disconnects the capacitor (of the RC filter for the reset line) just before the arrival of the reset pulse and reconnects it thereafter. More details on the implementation can be found in [89].

Low-Dropout Regulator for 3.3V ETTORE ASIC Supply Voltage To provide power to the ETTORE ASIC amplifiers independent of the voltage drop in the cables from the biasing system (approximately 0.2 V on the 2 m long cables), a low-dropout regulator (LDO) is placed directly on the ASIC board. It processes the slightly higher input voltage arriving at the ASIC board and regulates it down to the required value of 3.3 V for the ETTORE ASIC amplifiers. In this thesis, a supply voltage of 3.9 V is provided at the biasing system, which gives enough headroom (higher voltage) for the LDO.

Power, Control, and Signal Channel Connection Each ASIC board is connected to the outside vacuum electronics via two 100-pin flexible printed circuit (FPC) cables, which carry the supply voltages and output signals of the ETTORE ASIC amplifiers. They are connected on the ASIC board via two FPC connectors[9]. The upper connector and cable (closer to the ETTORE ASICs) carry 50 single-ended ETTORE ASIC outputs and corresponding ground connection for each of those. The lower connector and cable carry the remaining 33 signal lines as well as the supply and control voltages for the SDD chip and the ETTORE ASICs. The FPC cables are made from the polyamide Kapton. The material has been chosen since it features a low outgass rate[10]. The copper traces for the signals and voltages are distributed across two layers and arranged such that potential crosstalk is minimized [89]. The layouts of the FPC cables and of the 100-pin μ-D connectors are shown in Figure D.6 and Figure D.7 in the appendix. The test points for the different supply and control voltages on the ASIC board are given in the appendix in Chapter D.1.

[9] Connector part (number): Hirose FH29B-100S-0.2SHW.

[10] The outgassing rate of four short FPC cables (length of 30 cm) has been measured to be in the order of 1 mbar L/s [7].

5.5 Detector Module Temperature Sensors

The detector module hosts a total of three temperature sensors. Each ASIC board has one platinum thermistor (PT1000) with a normal resistance of 1000 Ω at 0 °C. The resistivity of the sensors changes linearly with temperature and is a robust method to measure temperatures since no calibration of the sensor is required. It is located in close proximity to the upper FPC connector for the signal outputs as shown in Figure 5.9. A more detailed zoom on the corresponding ASIC board region can be found in the appendix in Figure D.3. For each thermistor, a two-wire measurement of the resistance[11] can be performed. Due to the location of these sensors, they only provide an estimate of the ASIC board temperature but not for the SDD chip temperature. It has been observed that if one of the ASIC boards is not connected properly to the copper block, it heats up much more (temperature difference of more than 40 K) than the other board, due to a poorer thermal connection. Fortunately, as shown in Chapter 6.3, this temperature difference between the ASIC boards does not seem to have an impact on the detector performance. However, due to effects such as outgassing, this should still be avoided.

The third temperature sensor is a silicon bandgap temperature diode. It is directly integrated into one corner of the SDD chip readout side as shown in Figure 5.4a. The sensor measures a voltage drop at the diode and needs to be calibrated. For this two PT100 thermistors[12] are mounted on the entrance window of detector S0-166-1 as shown in Figure 5.11a. The upper left one is in close proximity to the temperature diode and is used for the calibration. It is important to mention that this procedure should not be performed with a fully functional detector (S0-166-1 was already damaged when the calibration measurement was performed), since the placement of any material or mechanical stress acting on the entrance window can severely damage the SDD chip.

To calibrate the temperature diode, the cooling system is first set to a value of 25 °C. The voltage drop ΔU_{SDD} and the temperature of the PT100 thermistor placed near the corner of the SDD chip are monitored over roughly 45 min in thermal equilibrium. The average over this time window for each sensor is calculated to get the first calibration point. Subsequently, the cooling system is set to a value of −50 °C. The measured voltage drop ΔU_{SDD} as well as the PT100 temperature is shown in Figure 5.11b. The average over a time period of approximately 2 h is calculated for the two sensors. To determine the temperature dependence of the temperature diode, a linear relationship with a slope s and an offset o is being used as shown in Equation (5.4).

$$T_{\mathrm{SDD}}[^{\circ}\mathrm{C}] = s[^{\circ}\mathrm{C/V}] \cdot \Delta U_{\mathrm{SDD}}[\mathrm{V}] + o[^{\circ}\mathrm{C}] \tag{5.4}$$

The calibration parameters obtained are listed in Table 5.3. Since this calibration method can potentially damage the detector, it has not been repeated with other devices. The manufacturer of the SDD chips (HLL) expects a similar behavior of the temperature diodes across different devices. Therefore, the obtained temperature calibration parameters are used for all SDD chips utilized in this thesis. To check this hypothesis, it might be useful to repeat the test with more (damaged) detector modules.

[11] This measurement technique does not account for the resistance change of the wires leading to the thermistor resulting in a small systematic uncertainty in the measured resistance and thus the temperature.
[12] The resistance of a PT100 platinum thermistor is 100 Ω at 0 °C.

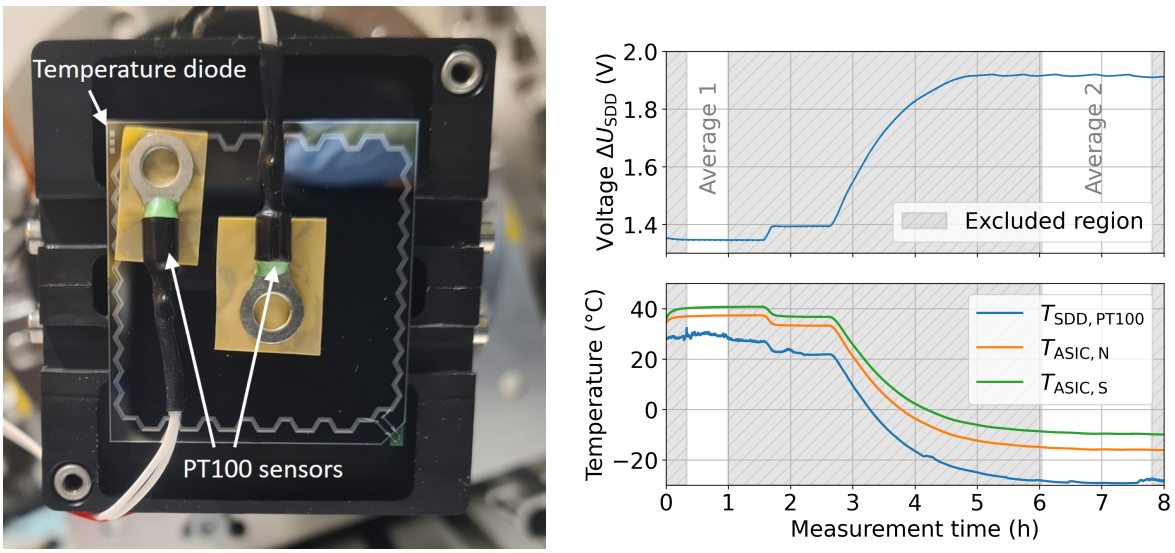

(a) S0-166-1 equipped with PT100 sensors **(b)** Temperature calibration measurement

Figure 5.11: SDD temperature diode calibration
(a) Photograph of the PT100 sensors mounted on the entrance window of detector S0-166-1 (at this time already partially damaged). The resistance of these sensors is measured to correlate it to the voltage drop ΔU_{SDD} measured in the SDD temperature diode. (b) Temperature calibration measurement of the voltage drop ΔU_{SDD} in the SDD temperature diode (top) and temperature of the upper left corner PT100 thermistor glued onto the SDD chip entrance window. In the course of the measurement in the vacuum cross setup, the cooling system has been first set to 25 °C, then shortly to 15 °C and then to −50 °C. The regions where the system changed its temperature are excluded and marked in grey. The average values for each sensor are calculated in the two white regions and used to calibrate the voltage drop in the temperature diode. The calibration parameters are listed in Equation (5.3). As a reference, also the ASIC board temperatures are shown.

Table 5.3: SDD temperature diode calibration parameter
Linear calibration parameters for the rough calibration of the SDD temperature diode using $T_{\mathrm{SDD}}[°\mathrm{C}] = s \cdot U_{\mathrm{SDD}}[\mathrm{V}] + o$. The corresponding measurement is shown in Figure 5.11 using detector S0-166-1 and the XGLab biasing system.

Slope s	Offset o
−102.57 °C/V	162.67 °C

5.6 Module Assembly Procedure

As described in Chapter 5.2, the detector module is subdivided into two main parts: the detector front, consisting of the SDD chip itself, which is glued on the Cesic interposer, and the copper cooling structure together with the on-module electronics (ASIC boards). The assembly of the detector front is performed under clean room conditions in the laboratories of the HLL. In the first step, the SDD chip is electrically tested in a probe station as described in Chapter 5.6.1. Thereupon, the SDD chip is glued on the Cesic interposer, see Chapter 5.6.2. A protection cover is installed on the detector front to ensure secure transportation between institutes. In the second step, the detector front and the on-module electronics are installed on the copper cooling structure, as discussed in Chapter 5.6.4. In the first iterations of the assembly procedure, approximately 10 % of all pixels were malfunctioning. This could be related to the glue that was used to connect the SDD chip with the Cesic interposer. In particular, this glue contained small spacer pills that were intentionally used to ensure a

defined spacing between the two components. After having replaced the glue, the yield was much higher. This will be discussed in more detail in Chapter 5.6.5. Due to the complexity of the on-module electronics, an intermediate prototype ASIC board for up to 47 pixels has been developed before the first tests with the 166 pixel SDD chips have started. The adapted assembly procedure for SDD chips with 47 pixels is described in the appendix in Chapter A.2.

5.6.1 *Electrical Functionality Test of the SDD Chip*

Before a SDD chip is glued on the Cesic interposer, its functionality is tested on a probe station in the clean room of the HLL. A photograph of the setup is shown in Figure 5.12a. The tests can be performed either on the un-diced wafer or using the already diced SDD chips placed inside a jig made from polytetrafluoroethylene (PTFE), as can be seen in Figure 5.12b. For the electrical tests, thin needles are placed with precision manipulators on the bond pads of the SDD chip as shown in Figure 5.12c. The needles are electrically connected to laboratory power supplies, which can precisely apply and measure voltages and currents. With these tests on the probing station, it is possible to exclude malfunctioning SDD chips from the assembly procedure and estimate the operation voltages of the detector. In the following, the most important tests are briefly described. A more detailed overview of the test procedure is given in Chapter A.1.

R1-RX Voltage Divider Network One crucial part of the detector is the R1-RX voltage divider network since it creates the drift fields inside the SDD chip. It is expected to behave like an ohmic resistor with a value of $R_{83} \approx 56.6\,\mathrm{k\Omega}$ (for each detector hemisphere). The corresponding current-voltage curve (I-U curve) can be measured by applying a voltage between the R1 and RX bond pads on each hemisphere. SDD chips that fail this test are excluded from the assembly procedure since it is likely that at least one entire hemisphere will be malfunctioning.

Entrance Window Implantation To get an estimation of the leakage current in the SDD chip, the current between the negatively biased BC implantation on the entrance window side and the outer substrate (OS) is measured. For the TRISTAN SDD chips, a leakage current between $20\,\mathrm{pA/cm^2}$ and $70\,\mathrm{pA/cm^2}$ is expected. Devices with much higher leakage currents are excluded from the assembly procedure.

Integrity of Feedback Capacitors To test the integrity of the feedback capacitor integrated into the anode of each pixel, the current between the FB line of each pixel towards the drain (DR) contact is measured. Since the test is performed for each pixel individually, it is sensitive to the pixel position. For a functional device, a current below 1 pA is expected. If no current is measured at all, a problem with the trace between the anode and the bond pad is likely to result in a non-functional pixel. Pixels with largely increased currents also have a high probability of not working. This can be explained by the fact that the capacitor loses its charge over time, creating a decaying waveform in the CSA circuit. It is important to note that this test is only sensitive to the integrity of the feedback capacitor and not the value of the capacitance.

nJFET Drain and Input Characteristics The drain and input characteristics of the nJFET are important parameters for the operation point of the detector. The two characteristics I-U curves are measured for each pixel individually and are a measure for the functionality of the integrated nJFET.

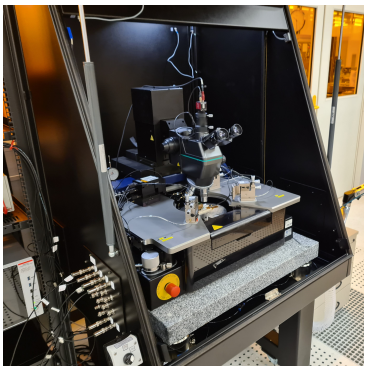

(a) Probe station setup

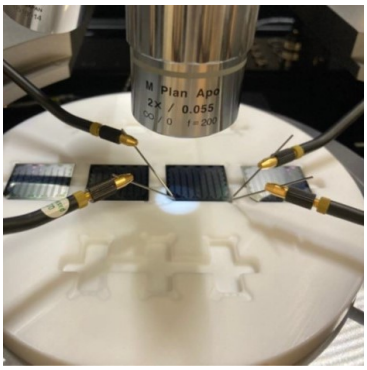

(b) Needles on SDD chip

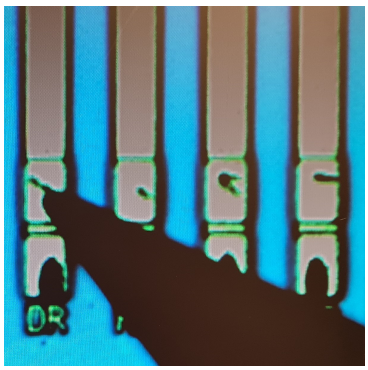

(c) Close-up of needle

Figure 5.12: Probe station for functionality tests of SDD chips
(a) Photograph of the probe station setup with a light-tight enclosure in the clean room of the HLL. (b) Photograph of 47 pixel SDD chips inside the probe station. The chips are placed inside a jig made from PTFE. (c) Microscope picture of the bond pad area with one needle placed on the drain (DR) contact. On this particular chip, wire bonds had already been placed and again removed on the lower pads. On the upper pads, small scratches from the needle can be seen.

5.6.2 *Assembly Procedure of the Module Detector Front*

The assembly procedure of the detector front is a critical step during the fabrication of a detector module. In this step, the SDD chip is glued onto the Cesic interposer and connected electrically via wire bonds to the rigid-flex PCBs. As discussed in Chapter 5.6.5, particles introduced into the glue can heavily damage the SDD chip and must be avoided. Therefore, the entire assembly is performed inside the clean room of the HLL, and all involved parts are cleaned thoroughly directly before they are assembled.

Design of the Mounting Jig For connecting the fragile SDD chip to the Cesic interposer, a dedicated mounting jig made from the thermoplastic polymer polyether ether ketone (PEEK) has been designed, see Figure 5.13a. Its primary purpose is the mechanical support of the bond pad regions of the SDD chip during the bonding process. If these regions are not supported properly, the vibrations caused by the bonding process can lead to loose connections or even cracks in the SDD chip, see Chapter A.3.2. On the one hand, the PEEK material provides sufficient stiffness to support the chip during the bonding. However, the material is also soft enough such that the SDD chip is not damaged. Additionally, it is resistant to all chemicals, like the glue and cleaning solvents, used in the assembly procedure. Moreover, it has been used with success in previous projects by the bonding technicians at the HLL.

To protect the sensitive entrance window region of the SDD chip, a large cut-out is milled into the center of the PEEK jig. A thin frame of material around this cut-out supports the SDD chip on the small passive regions along its outer edges. To keep the SDD chip in place, another frame with its outer dimensions is milled into the jig with small tolerances. Here, the height of the outer frame (400 µm) is slightly lower than the SDD chip (450 µm). This is advantageous since the Cesic interposer can be directly placed on the surface of the SDD chip without touching the PEEK jig. In an earlier iteration of the PEEK jig, the height of the outer frame was higher than the SDD chip in the attempt to better align the Cesic interposer on the SDD chip. Given the tight tolerances, it often happened that the Cesic interposer got canted on one side of the jig, thus touching only a small part of the surface of the SDD chip. To release the Cesic from the jig, it has to be

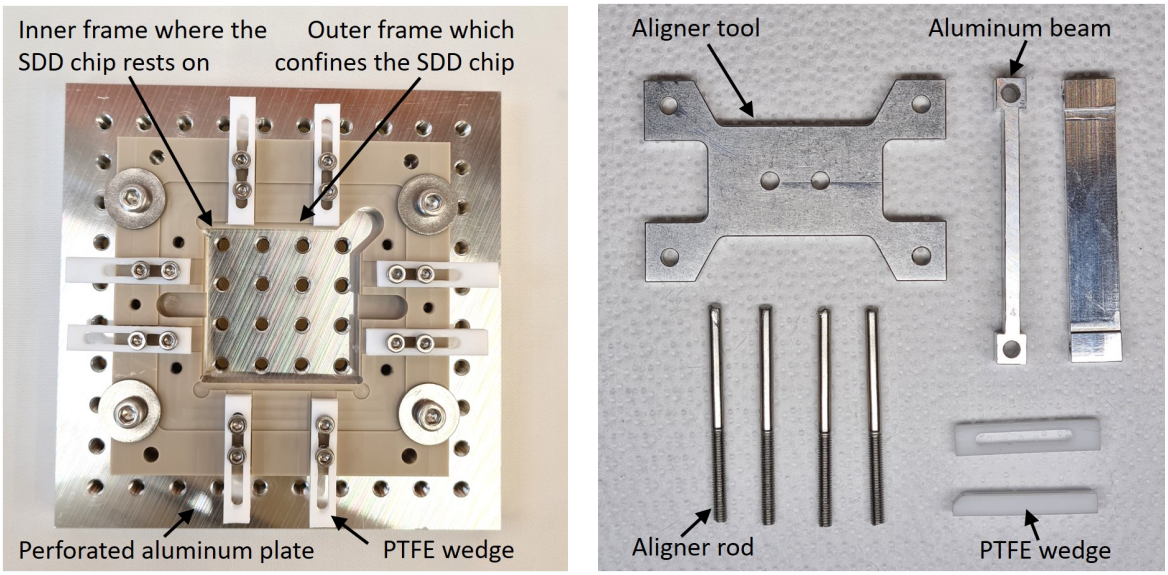

(a) PEEK jig for SDD chip mounting

(b) Alignemt and fixation parts

Figure 5.13: Photographs of detector assembly jig
Photograph of the jig used for mounting the detector front. (a) PEEK assembly jig mounted on a perforated aluminum plate with PTFE wedges installed. (b) Parts used to align and fixate the Cesic interposer and SDD chip during the assembly procedure.

gently pushed to the side, sliding over the SDD chip. This is an unwanted movement that can damage the SDD chip as discussed in Chapter 5.6.5.

During the assembly procedure, the detector, together with the jig, is placed inside an oven for 5.5 h at 60 °C to bake out the glue. To prevent the jig from warping and keep the inner frame where the SDD chip rests as flat as possible, the jig is machined from a 10 mm-tick plate. Furthermore, it is mounted on a perforated aluminum plate. The mechanical drawings can be found in Chapter E.2.3.

During different steps in the assembly procedure, especially during the wire bonding, the SDD chip is gently fixated in the PEEK jig. This fixation is realized using multiple wedges made from the material PTFE (Teflon™) that can be mounted at different positions of the PEEK jig. The material was chosen since it is very soft and cannot damage the SDD chip. Moreover, the glue does not adhere to this material.

Assembly of Rigid-Flex PCB and Cesic Interposer In the first step of the assembly of the detector front, the rigid-flex PCBs are glued onto the fins of the Cesic interposer. Prior to the assembly, all parts are cleaned with acetone, isopropyl, and de-ionized water in an ultrasonic bath. Acetone is used to remove organic substances such as fingerprints or oil residuals. Acetone itself can leave a thin film on the surface, which is removed by applying isopropyl and de-ionized water. To reduce the formation of water stains, all parts are dried using a stream of nitrogen. In particular, the Cesic interposer has to be cleaned thoroughly since it can contain some residual cutting oil from the manufacturing process inside the threaded inserts. These cutting oils can have high outgassing rates, which can deteriorate the vacuum conditions [114] or even contaminate the detector surface.

After having cleaned the parts, the Cesic interposer is placed into the PEEK jig as

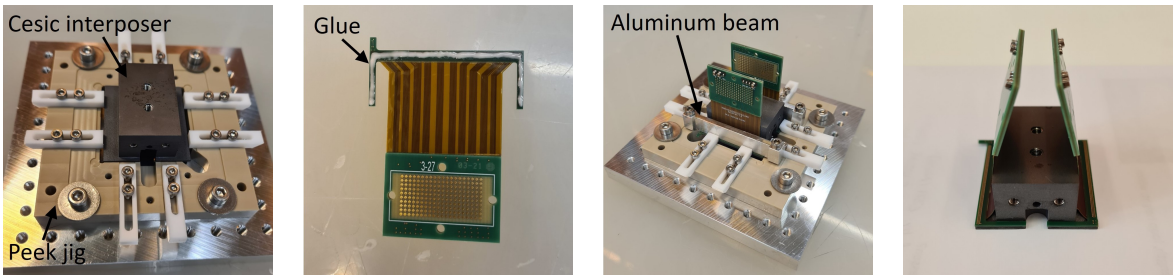

(a) Cesic preparation **(b)** Glue on rigid-flex **(c)** Gluing and fixation **(d)** Finished Cesic

Figure 5.14: Installation of rigid-flex PCBs on the Cesic interposer
Photographs of the different steps for gluing the rigid-flex PCBs to the Cesic interposer. (a) Preparation of the Cesic interposer inside the PEEK jig. (b) Glue pattern on the bottom side of the rigid-flex PCB. Its bond pads are on the opposite side of the glue. (c) Fixation of the rigid-flex PCBs on the Cesic interposer via aluminum beams for the curing the glue in the oven. (d) Finished assembly after the bake-out in the oven for 5.5 h at 60 °C.

shown in Figure 5.14a. The flat sides[13] of the PTFE wedges are pressed against the fins of the Cesic interposer and are used as a mechanical stop for the rigid-flex PCBs. A thin layer of the two-component epoxy (EPO-TEC 920-F [110]) is applied to the bottom side of the rigid-flex PCBs as depicted in Figure 5.14b. Subsequently, the rigid-flex PCBs are placed on top of the fins of the Cesic interposer and gently pressed down. To fix the position of the rigid-flex PCBs, two horizontal aluminum beams are installed across them as illustrated in Figure 5.14c. For curing, the assembly is placed inside an oven for 5.5 h at 60 °C. The finished part consisting of the Cesic interposer and two rigid-flex PCBs can be seen in Figure 5.14d.

Gluing of SDD onto Cesic Interposer In the next step, the prepared Cesic interposer is glued to the SDD chip. This is a critical step during the assembly since any particles introduced into the glue can damage the readout structure of the SDD chip. A detailed investigation of the effect of particles inside the glue and the pressure applied to the SDD chip during the assembly can be found in Chapter 5.6.5. Just as before, all parts are cleaned with acetone, isopropyl, and de-ionized water, respectively. The electrically tested SDD chip (see Chapter 5.6.1) is placed inside the PEEK jig with the entrance window side facing downwards, as shown in in Figure 5.15a. On each hemisphere of the SDD chip, one wire bond has to be placed between the R1/RX network towards an aluminum trace near the outer edge of the detector. For technical reasons, the connection is performed with wire bonds instead of using a direct aluminum trace[14].

In the next step, a thin layer of glue (adhesive bed) with a rectangular shape is applied to the Cesic interposer. To ensure a homogeneous thickness of the adhesive bed, four bands of a 190 µm-thick polyethylene terephthalate (PET) foil [115] are attached to the edges of the polished side of the Cesic interposer. As shown in Figure 5.15c and Figure 5.15d, the glue is first applied in the rectangular region. Afterward, the excess adhesive is removed by scraping it off. This ensures that the glue has the same thickness as the height of the PET foil. Subsequently, the PET bands of the PET foil are removed from

[13] This flat side is the side opposite to the 45° angled chamfer.
[14] The required connection to the R1/RX network crosses another aluminum trace on a much lower potential than the RX voltages. Creating a good insulation between these two aluminum traces on different potentials is technologically much more challenging, and the wire bonds are a good solution to circumnavigate this problem.

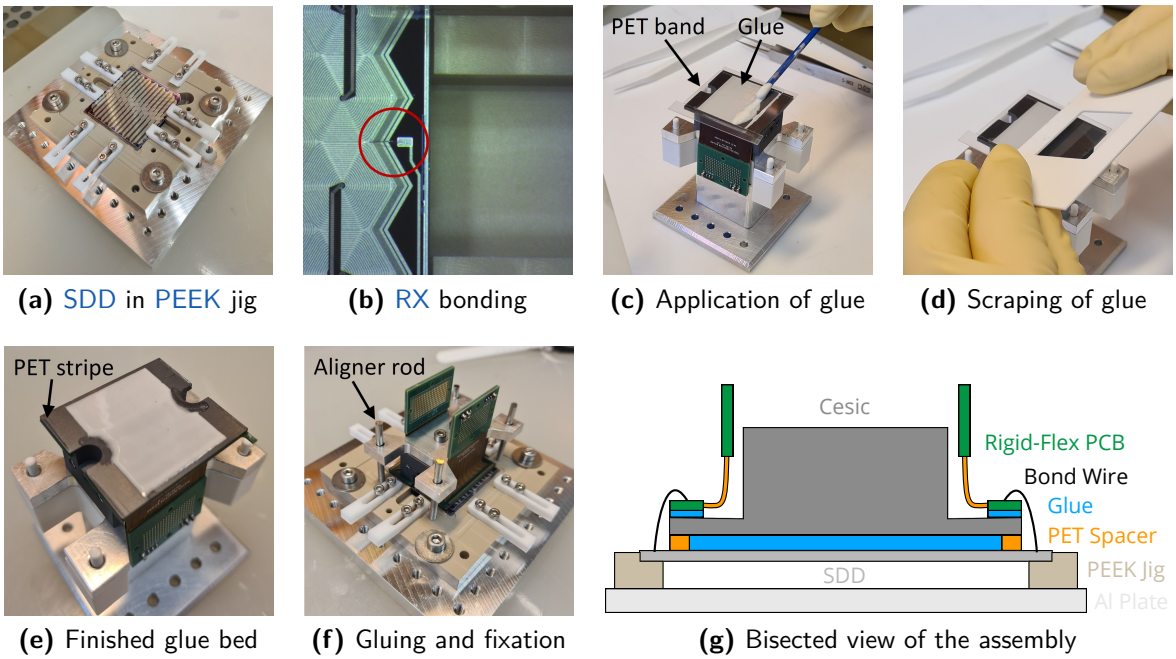

(a) SDD in PEEK jig **(b)** RX bonding **(c)** Application of glue **(d)** Scraping of glue

(e) Finished glue bed **(f)** Gluing and fixation **(g)** Bisected view of the assembly

Figure 5.15: Photographs and schematic of the mounting procedure of the detector front The photographs illustrate the different steps during the mounting procedure. (a) Placement of the SDD chip inside the PEEK jig with the readout side facing up. (b) Wire bond connection of the RX network lines on the electronic side of the SDD chip. (c) Application of glue to the Cesic interposer. (d) Scraping of glue to the same height as the PET stripes. (e) Cesic interposer with glue and PET stripes on the outer sides. (f) Assembly of the Cesic interposer on top of the SDD chip. (g) Bisected view of all parts involved in the assembly. Some of the pictures have already been published in [8].

the Cesic interposer. Four smaller laser-cut PET stripes (0.6 mm x 10 mm) are then attached to the outer edges of the Cesic interposer next to the glue. These stripes only touch the passive area of the SDD chip and are used to have a defined distance between the chip and the Cesic interposer. Additionally, this avoids potential damages that could be caused by residual impurities like small particles in the glue.

Using four aligner rods that are screwed into the PEEK jig, the prepared Cesic interposer is then gently positioned on top of the SDD chip. Since some mechanical play is required for the sliding motion, these rods only roughly fix the relative position between the Cesic interposer and the SDD chip with a precision on the order of a few hundred micrometers. For curing, the glued parts are then placed in an oven (temperature of 60 °C) that is flushed with nitrogen for a time period of 5.5 h. Flushing the oven with nitrogen is done to prevent substances evaporating from the oven, glue, or other parts of the assembly from settling on the entrance window of the SDD chip. Here, mainly the entrance window is at risk since already thin layers of a substrate can worsen the detector performance as shown in Chapter 8. A bisected view of the assembly is shown in Figure 5.15g.

Wire Bonding After the glue has hardened, the aligner rods are removed, and the SDD chip can be electrically connected to the rigid-flex PCBs. To this end, ultrasonic wire bonding is used with aluminum wires with a diameter of 25 µm. As shown in Figure 5.16a, almost 400 wires must be set to fully connect both hemispheres of SDD chip. A close-up of the connections can be seen in Figure 5.16b. The parameters used for the wire bonding process are listed in Table 5.4.

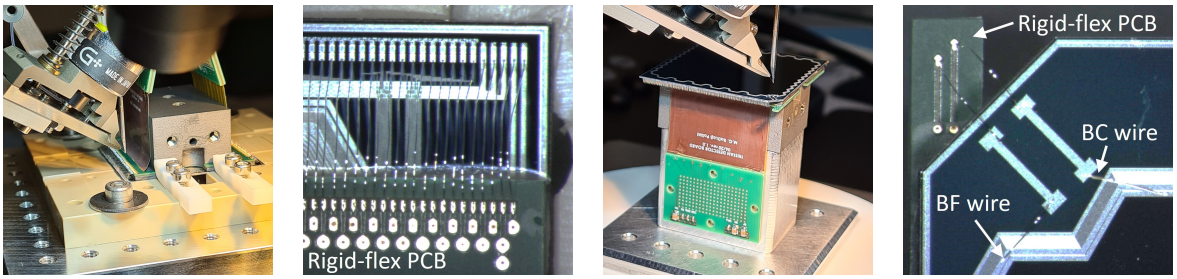

(a) Wire bonding **(b)** Wire bonds **(c)** BC/BF bonding **(d)** BC/BF wire bonds

Figure 5.16: Photographs of the detector wire bonding
(a) Side view of the wire bonding for connecting the SDD chip electrically to the rigid-flex PCB. (b) Close-up view of the wire bond connections from the electronic readout side of the SDD chip to the rigid-flex PCB. (c) Wire bonding of the BF and BC contacts on the entrance window side of the SDD chip to the nose of the rigid-flex PCB. (d) Wires bonds between the BC and BF contacts on the SDD chip towards the nose of rigid-flex PCB. Some of the pictures have already been published in [8].

Table 5.4: Wire bonding parameters between SDD chip and rigid-flex PCB
For the wire bonding a manual wedge bonder (F&S Bontec Series 53X) is used with aluminium wires with a diameter of 25 µm. The first connection of the wire bond is placed on the pads of the rigid-flex PCB and the second one on the bond pads of SDD chip. In this order, the bonds are placed from a higher vertical position to a lower one, which slightly reduces the stress on the wire bonds that are close to their welding point. Additionally, it serves as a safety check for the parameters since the first bond is placed on the rigid-flex PCB, which can handle much higher loads and stress. The loop height used for the bonds is approximately 2000 µm.

Parameter	First bond connection	Second bond connection
Bond Force	26 cN	25 cN
US Power	88 dig	88 dig
US Time	26 ms	25 ms
Td Steps	12 µm	10 µm

For electrically connecting the BC and BF lines, the detector front is removed from the PEEK jig, and the wire bonds towards the nose of the rigid-flex PCB are placed, as shown in Figure 5.16c. These two voltages are applied on the entrance window side to deplete the detector volume. Due to technological limitations, the connection from the electronic side of the SDD chip towards the entrance window side can not be realized with, e.g., silicon-trough via. Therefore, one corner of the SDD chip is cut away to allow the wire bonds to be placed between the nose of the rigid-flex PCB and the entrance window side of the SDD chip, seen Figure 5.16d. Another set of wire bonds is then placed on the aluminized frames that are connected to the implanted regions for the BC and BF.

Detector Entrance Window Cleaning In the first characterization measurements of the 166 pixel detector modules with electrons, an inhomogeneous detector response has been observed between different pixels (see 7.4.5 and Chapter 8.2). This inhomogeneity is most notable for lower energy electrons at around 5 keV, and results in a difference of energy resolution of almost a factor of two. As described in Chapter 8, the origin of this inhomogeneity is related to an additional substance on top of the entrance window, which

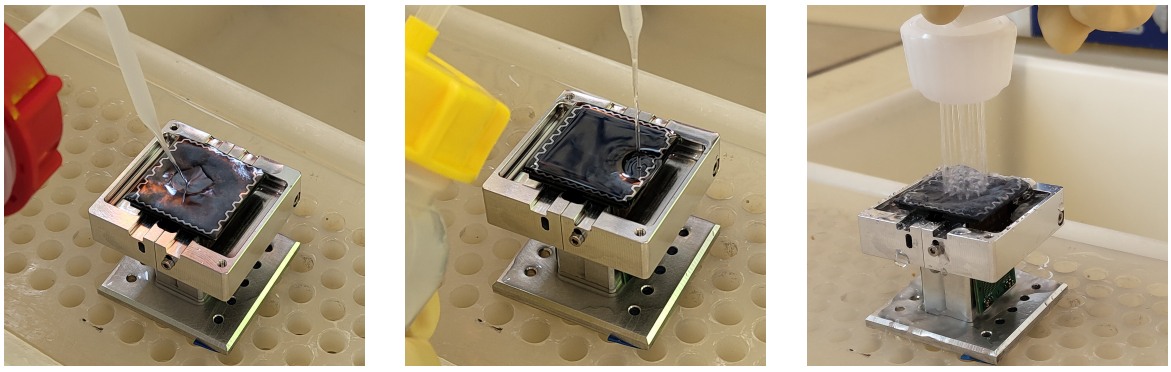

(a) Acetone cleaning **(b)** Isopropyl cleaning **(c)** De-ionized water cleaning

Figure 5.17: Entrance window cleaning procedure of the assembled SDD chip
Photographs of the different steps during the cleaning procedure of the detector entrance window. In each step, the detector entrance window is rinsed with the respective liquid for about 2 min while moving across the entire SDD chip surface. First, to remove organic substances, the surface is rinsed with acetone (a). Then, to remove residuals of the acetone cleaning, the surface is cleaned with isopropyl (b). Finally, the detector is rinsed with de-ionized water (c).

effectively increases the entrance window thickness. Currently, it is assumed that the deposition of this substance occurs during the assembly procedure of the detector front. Fortunately, the investigations have shown that the substance can be removed from the entrance window by deploying a dedicated cleaning procedure, restoring a homogeneous detector response across pixels.

The best detector performance with a much more homogeneous detector response could be achieved by rinsing the detector entrance window with acetone, isopropyl, and de-ionized water, respectively. As illustrated in Figure 5.17, the different liquids (roughly 400 mL) are rinsed successively over the entrance window. During the rinsing, a sweeping motion is performed to cover the entire entrance window surface. After cleaning, the entrance window is first dried with a stream of nitrogen to remove larger water droplets from the entrance window and bond pad region. Then the detector is placed inside an oven under a nitrogen atmosphere at 60 °C for a few hours to remove all remaining water.

As a remark, the three different solvents have been used since they are also utilized in various cleaning steps during the processing of the wafers. In the investigations performed in this thesis, acetone has been the most effective solvent for removing the additional substance on the entrance window. Its drawback is that it leaves a thin film of residual on the entire SDD chip. This film also deposits on the bond pad region and makes the wire bonding much more difficult. To remove this residual film, isopropyl and de-ionized water are used. In this work, the cleaning with acetone and isopropyl could also be applied to already wire-bonded modules with success. However, the final cleaning with de-ionized water led to a deformation of some of the wire bonds due to the adhesion forces. The deformed wire bonds had to be replaced since they created short circuits between them. The effects of the different cleaning steps are described in Chapter 8.3. For the future assembly of the detector modules, it might be useful to clean the detector surface before the wire bonding.

Detector Protection and Transportation After the assembly of the detector front has been finished, a protective cover is installed around the detector front. It protects the detector front from dust and mechanical damage that might occur during transportation or assembly

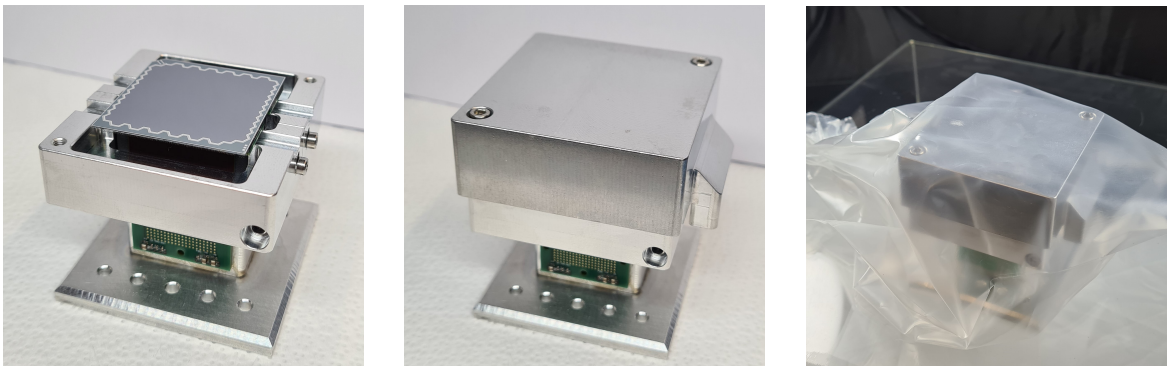

(a) Protection jaws **(b)** Protection hat **(c)** Detector in nitrogen bag

Figure 5.18: Installation of the detector protection cover
(a) Detector front with protection jaws mounted on each side of the Cesic interposer. (b) Protection hat installed on top of the jaws enclosing the SDD chip and protecting the device against mechanical damage and dust depositions. (c) Detector assembly with protection cover installed in a sealed bag filled with nitrogen to protect it against humidity and particles during transportation.

in a measurement setup. First, two protection jaws are installed on each side of the Cesic interposer to protect the wire bond region on the electronic readout side of the SDD chip, see Figure 5.18a. In the next step, the protection hat is mounted on top of the jaws. It fully covers the detector entrance window, see Figure 5.18b. To protect the detector front against humidity, the assembly is placed into a plastic bag that is filled with nitrogen and then sealed. In this configuration, the detector can be transported. The technical drawings of the protection cover can be found in Chapter A.4.

5.6.3 *Assembly and Cleaning of on Module Electronic Boards*

As described in Chapter 5.4, the on-module electronics consist of two identical PCBs that host the ETTORE ASIC amplifiers. The other electronic SMD components are connected to the boards using reflow soldering. To ensure vacuum compatibility, solder with no-clean flux and the composition Sn96.5-Ag3.0-Cu0.5 is used [89, 116]. To remove residuals from the soldering procedure, the PCB is cleaned afterward in an ultrasonic bath with de-ionized water, as illustrated in Figure 5.19. Then, the ETTORE ASIC amplifiers are glued with a thin layer of epoxy onto the PCB for a good thermal contact and cured at 100 °C in an oven. In the last step, the ETTORE ASIC amplifiers are connected via wire bonds (AlSi1%, diameter 25 µm) to the PCB. A more detailed description of the assembly of the on-module electronics can be found in [89] .

5.6.4 *Assembly of the Complete Detector Module*

In the last step, the detector front is connected to the copper cooling structure and to the on-module electronics. Since the detector module is operated in a vacuum, all mechanical parts are cleaned thoroughly to remove any potential contamination that could spoil the vacuum. During the manufacturing of the parts, various cutting greases or oils are used, which typically have high outgassing rates and vapor pressures. Different cleaning procedures are applied to remove these long-chained carbon compounds. The parts made from stainless steel are first roughly wiped with acetone to remove coarse contaminants. Afterward, the parts are cleaned in a heated ultrasonic bath at 60 °C with an alkaline degreaser solution. Finally, the parts are rinsed with de-ionized water and dried at 120 °C for a few hours. For

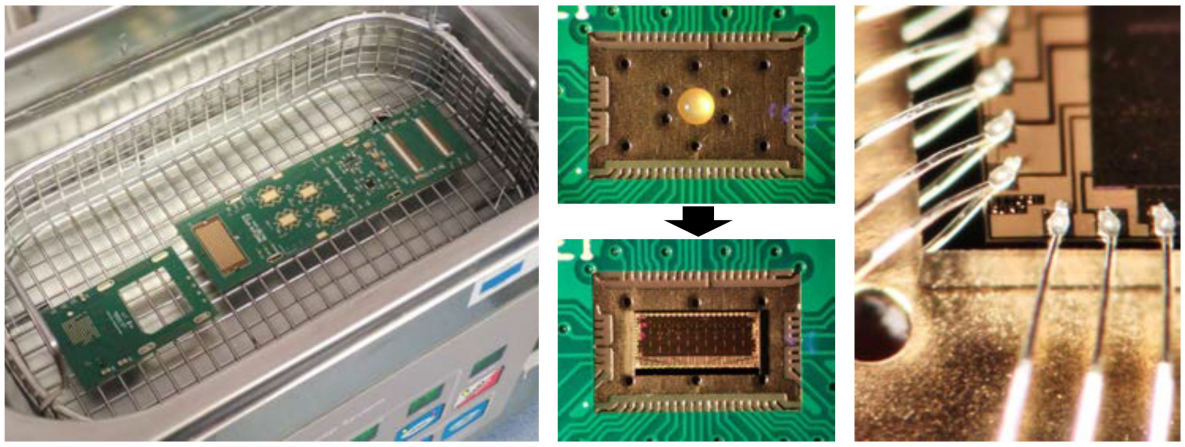

Figure 5.19: ASIC board cleaning and assembly of ETTORE ASIC amplifier
The photograph on the left shows the cleaning of an on-module electronics PCB and a detector PCB (for a 47 pixel prototype detector) in an ultrasonic bath with de-ionized water. The photograph in the center shows the deposition of the epoxy glue on the pad for the ETTORE ASIC amplifiers. In the picture on the right-hand side, a close-up of the bond pad region on the ETTORE ASIC amplifier is shown. Figure taken from [89].

the copper parts, coarse contaminants are also removed manually with acetone. Next, the parts are placed in a water solution with citric acid for a few hours. Finally, the copper parts are cleaned with de-ionized water and dried at room temperature. A more detailed description can be found in [114, 117].

The detector front is connected to the copper cooling structure via several screws as shown in Figure 5.20a. Then, two copper covers and ASIC boards are mounted on each side of the copper cooling structure. To electrically connect the detector front with the ASIC boards, Z-ray compression connectors[15] are placed on the ASIC boards as shown in Figure 5.20b. Here, the golden triangle on the Z-ray connector has to be aligned with the mark on the lower left corner on the ASIC boards. Each Z-ray connector is mounted with four small bolts to ensure a uniform pressure across the connector[16]. A photograph of the final detector module (with the protection jaws still installed) mounted in a test setup is shown in Figure 5.20c.

5.6.5 *Improving the Yield of the Assembly Procedure*

During the first detector assembly tests, approximately 10 % of the pixels were malfunctioning. An overview of the malfunctioning pixels for the different 47 pixel and 166 pixel detectors can be seen in Figure 5.21. The different behaviors of the malfunctioning pixels can be found in the appendix in Chapter B.1. Based on the experience with multiple 47 and 166 pixel detectors featuring a planar design, i.e., a design in which the SDD chip and the ASIC boards are arranged in the same plane, a much higher yield close to 100 % in working pixels is expected [89, 118]. The main differences between the planar design and the detector module are the rigid-flex PCB and the large contact area between the SDD chip and the Cesic interposer. The rest of the experimental setup and electronic readout chain are identical for

[15] Z-Ray dual-compression interposer with 200 pins (part number: ZA1-20-2-1.00-Z-10). In addition to that, the corresponding mounting hardware is required (part number: ZHSI-01-01).
[16] Given by the manufacturer the normal force per pin approximately 30 g/pin. For the entire connector, this corresponds to approximately 59 N.

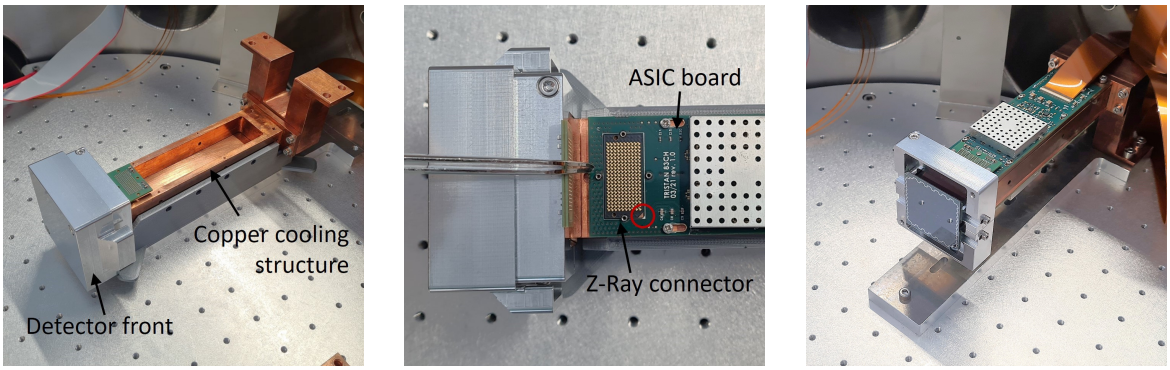

(a) Installation of detector front **(b)** Placement of Z-ray connector **(c)** Assembled detector module

Figure 5.20: Full assembly of detector module
(a) Connecting the detector front to the copper cooling structure. Here, an additional part made from copper is attached at the end of the cooling structure. It is used to connect the detector module to the cooling plate of the vacuum chamber. (b) Placement of the Z-ray connector between the rigid-flex PCB and the ASIC board. (c) Finished detector module with protection jaws still installed.

both detector designs. Therefore, four hypotheses are discussed as potential causes for the malfunctioning pixels:

1. The malfunctioning pixels could originate from damages or design issues in the rigid-flex PCB.
2. The glue could chemically react with the SDD chip surface in such a way that it damages pixels. In principle, this would not affect the planar detector design since here, only the insensitive edges of the SDD chip are glued.
3. The mechanical pressure exerted on the SDD chip during the assembly procedure could create small defects or cracks in the silicon crystal structure, leading to the malfunctioning of the pixels.
4. The additional spacer pills mixed into the EPO-TEC 920-F glue (at this stage of the project) could act like a rough surface and get impinged into the sensitive area of the SDD electronic readout side. Caused by small movements during gluing, the spacer pills would act like sandpaper, damaging or scratching the readout side of the SDD chip.

Hypothesis: Malfunctioning of Pixels caused by the Rigid-Flex PCB To exclude the rigid-flex PCB as a potential cause of the malfunctioning pixels, functional pixels of the assembled detector S0-47-4 have been disconnected and then wire bonded to presumably defective rigid-flex PCB lines. However, these pixels stayed functional after the modification of the wire bond scheme, excluding the rigid-flex PCB as a cause of the problem. A more detailed description of the investigation can be found in Chapter A.3.1.

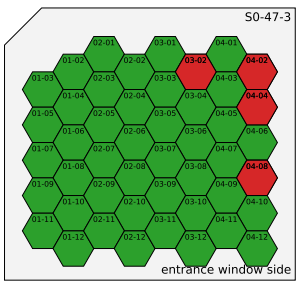

(a) Functionality of S0-47-3

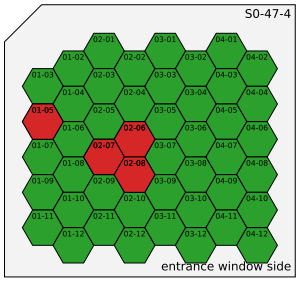

(b) Functionality of S0-47-4

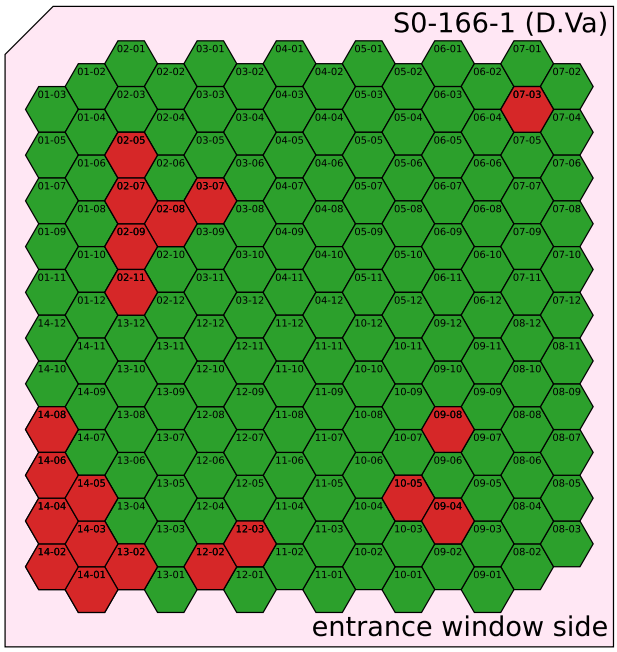

(c) Functionality of S0-166-1

Figure 5.21: Functional pixels for detector fronts assembled with spacer pills in glue
For the shown detector fronts, the EPO-TEC 920-F [110] glue with additional spacer pills inside has been used. The functional pixels are colored in green, while the malfunctioning pixels with distortions on the waveform level are shown in red. A more detailed description of the different distortions seen on the waveform level for detector S0-166-1 can be found in Chapter B.1.

Hypothesis: Damages due to Chemical Reaction with Glue To test whether the EPO-TEC 920-F glue itself can cause the malfunctioning of pixels, it was applied to the entire readout electronic side of a working planar 47 pixel detector. First, the functionality of the detector SDD33.2 W01.G05 was tested without the glue applied with an ^{55}Fe calibration source. In Figure 5.22a, the energy resolution of the Mn-K$_\alpha$ line is shown for a measurement at room temperature. After this measurement, the glue was applied to the entire sensitive area of the readout electronic side of the SDD chip as illustrated in Figure 5.22b. The application and curing of the glue were performed inside the clean room of the HLL. In Figure 5.22c, the measured energy resolution after the application of the glue is shown. Between the two measurements, none of the pixels were damaged, and their measured energy resolution is very compatible. This observation most likely excludes the chemical reactions due to the application of the glue as the possible cause for the malfunctioning of pixels.

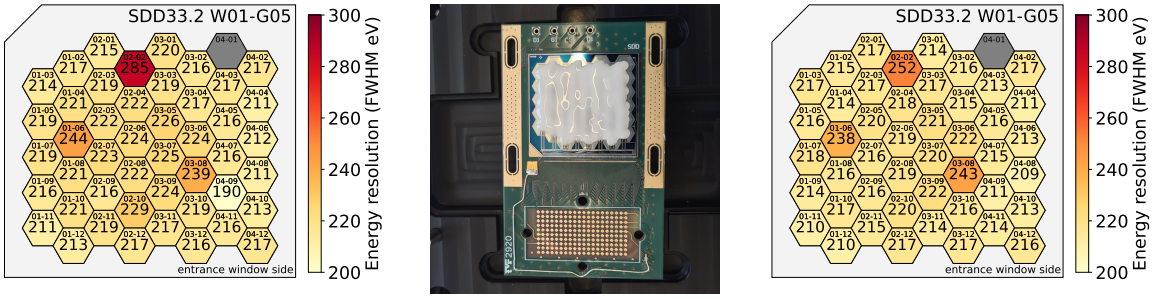

(a) Energy resolution without glue **(b)** Planar 47 pixel detector **(c)** Energy resolution with glue

Figure 5.22: Planar 47 pixel detector with glue applied to the readout side
Investigation of the impact of the glue (EPO-TEC 920-F) on the detector performance when being applied to the readout side. The Mn-K_α line of an ^{55}Fe calibration source is used to determine the energy resolution. Pixel 04-01 (marked grey) has been excluded from the analysis due to a problem already existing before the measurement. (a) Pixel map of the measured energy resolution before the application of the glue. (b) Photograph of the planar detector SDD33.2 W01-G05 after the application of the glue to the sensitive area of the readout side. (c) Pixel map of the measured energy resolution after the application of the glue.

Hypothesis: Damages due to Mechanical Pressure The mechanical pressure applied to the SDD chip during the assembly differs significantly for the planar and the module detector design. For the planar detector design, the glue is applied to the more robust passive region of the entrance window side, see Figure 5.23a. During the curing, the SDD chip is placed on the cutout in the PCB without any external pressure being applied. Figure 5.23b shows a photograph of a fully assembled 166 pixel planar detector as seen from its entrance window side. In contrast, during the assembly of the detector module, the SDD chip rests in the PEEK jig. The contact area is similar to the planar detector design, but additionally, the Cesic interposer and the aluminum aligner jig are placed on top of the much more sensitive area of the electronics readout side. As listed in Table 5.5, this strongly increases the mechanical pressure on the passive region. But more importantly, it creates an additional pressure of 0.048 g/mm^2 to the much more sensitive active area of the SDD chip.

To test if the increased pressure on the active area in the detector module assembly could damage pixels, different weights (masses from 15 g to 103 g) have been placed on the active area of the readout side. For this investigation, the planar 47 pixel detector (SDD33.2 W01.G05) with glue applied to its electronic readout side has been used. The experimental setup is shown in Figure 5.24. It is important to note that since the glue had already hardened, it acts like a protecting layer (against, e.g., mechanical scratches or punctuation) of the readout side. Cylindrical weights from aluminum with a diameter of 20 mm have been placed onto the SDD chip, and measurements with an ^{55}Fe calibration source are being performed in parallel. The weights have been placed in increasing order as indicated by the sequence in Table 5.6. As a reference, the weight of 15 g corresponds to the same amount of pressure on the active area of the SDD chip as during the assembly of a detector module. Performing the test with a weight of 103 g, more than the sixfold pressure has been applied to the active area of the SDD chip. In all measurements, the pixels remained functional. For applied pressures up to 0.194 g/mm^2 on the active area, which is four times the expected pressure during the assembly procedure, the detector performance in terms of the energy resolution is not degraded. As a matter of fact, during the first few measurements, the average energy resolution actually improves (decreases by 11 eV or 5 %) compared to the first measurement without additional weights. This observation might be explained by a

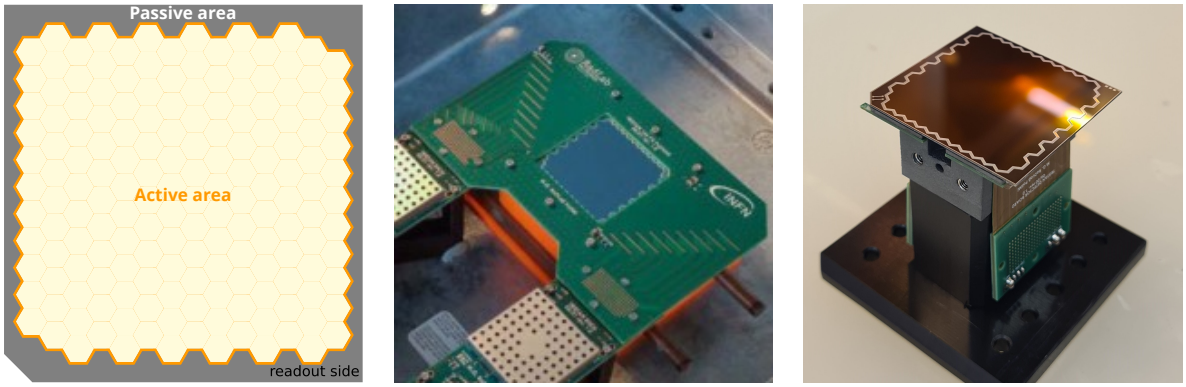

(a) Readout side **(b)** 3D planar detector **(c)** 3D detector module

Figure 5.23: Comparison of planar detector design and detector module
(a) Schematic showing the passive (mainly bare-bone silicon with only some aluminum traces) and the much more sensitive active area (regions with more complex structures for nJFET, IGR, etc.) of the SDD chip. (b) Planar 166 pixel detector as seen from the entrance window side. Figure adapted from [89]. (c) Front of a detector module with a 166 pixel SDD chip glued to Cesic interposer.

Table 5.5: Comparison of pressures applied to different SDD chip areas during assembly
The values listed have been estimated for the assembly of a 166 pixel SDD chip. The interface area corresponds to the region of the SDD chip, which is in contact with the glue and the detector board (planar design) or Cesic interposer (detector module), respectively.

Parameter	Planar detector design	Detector module design
Interface position	Passive area of SDD chip	Active area of SDD chip
Interface side	Entrance window	Readout side
Interface area	$\approx 152\,\mathrm{mm}^2$	$\approx 1230\,\mathrm{mm}^2$
Weight acting on SDD chip	2 g (SDD chip)	59 g (2 g + 39 g + 18 g) (SDD + Cesic + aligner)
Mounting pressure on passive area of entrance window side	$0.013\,\mathrm{g/mm}^2$	$0.338\,\mathrm{g/mm}^2$
Mounting pressure on active area of electronic readout side		$0.048\,\mathrm{g/mm}^2$

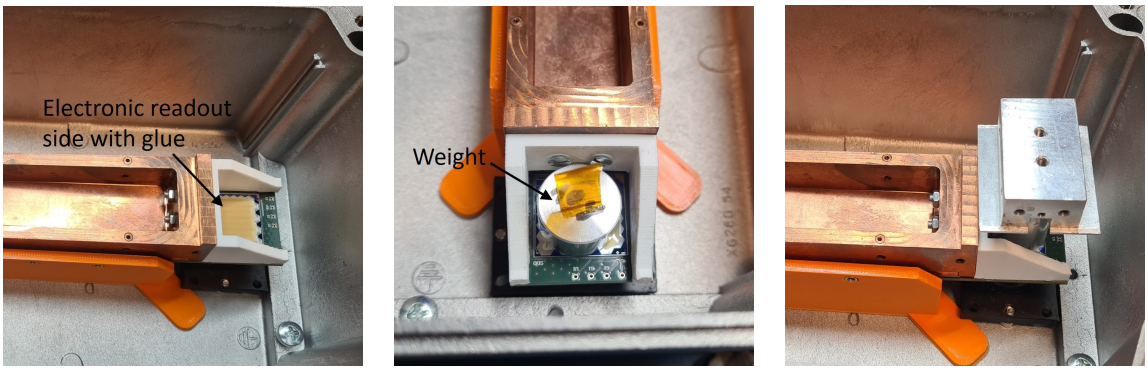

(a) Planar 47 pixel detector **(b)** Weight on active area **(c)** More weight on active area

Figure 5.24: Photographs of weights placed on a 47 pixel planar detector
The pressure and weight test are performed with the planar 47 pixel detector SDD33.2 W01-G05. Its entrance window side is covered with hardened EPO-TEC 920-F glue. (a) Planar 47 pixel detector placed inside an aluminum dark box with the electronic readout side facing upwards. On the other side of the detector (entrance window side, here facing to the bottom side of the box), a ^{55}Fe calibration source has been placed. (b) Weight (10 g) placed on top of the active area of the electronic readout side of the SDD chip (on top of the glue layer). (c) Additional weights (including a dummy Cesic interposer) placed on the readout side of the SDD chip.

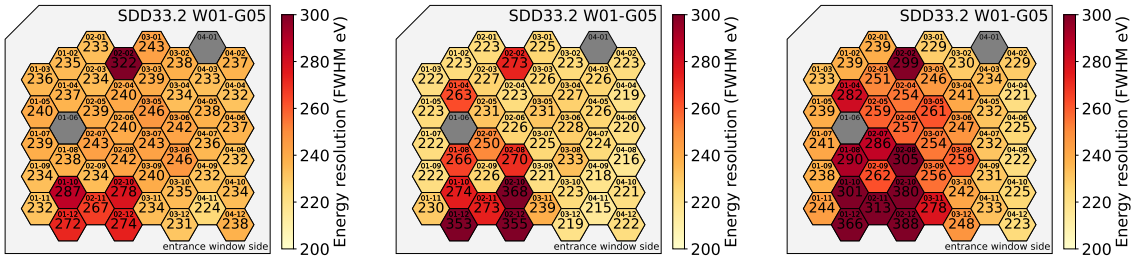

(a) No weight applied **(b)** 100 % relative pressure **(c)** 681 % relative pressure

Figure 5.25: Energy resolution of a planar 47 pixel detector with weights placed on it
Pixel maps showing the energy resolution for the Mn-K$_\alpha$ line in a measurement with an ^{55}Fe calibration source. In the measurements, weights have been placed on the electronic readout side of the detector. The relative pressure describes the applied pressure on the SDD chip with respect to the pressure experienced in the assembly procedure of a 166 pixel detector module.

cooling effect of the weights on the SDD chip. Since all measurements were performed at room temperature (no thermal bath or external cooling), the SDD chip temperature during operation was above 40 °C. At the beginning of the measurement campaign, the weights were placed with a temperature of approximately 20 °C onto the much hotter SDD chip, likely cooling it down. Over the course of the measurements, the weight placed directly onto the SDD chip started heating up, which could be sensed by hand when placing more weights on top. Since none of the pixels got damaged during the measurements, this likely excludes the pressures alone as the cause of the complete malfunctioning of pixels in the module assembly. However, it should still be mentioned that in two measurements with much higher pressures, the overall energy resolution was slightly degraded (around 10 eV). The degradation remained present in a subsequent measurement without weights four days later. This is a hint that for pressures with values higher than 0.194 g/mm^2, a degradation of the detector performance in terms of the energy resolution is possible.

Table 5.6: Overview of weights placed on a 47 pixel planar detector
Overview of the weights placed on top of the readout side of a planar 47 pixel detector (SDD33.2 W01-G05). The contact area of the passive region of the SDD chip with the PCB is approximately 60 mm^2. The diameter of the aluminum weights is 20 mm, resulting in a contact area of 315 mm^2. The relative active (passive) area pressure is taken with respect to the mounting pressure of 0.048 g/mm^2 on the electronic readout side (0.338 g/mm^2) for a 166 pixel detector module as listed in Table 5.5. To extract the average energy resolution $\overline{\Delta E}$, the Mn-K$_\alpha$ line of an ^{55}Fe calibration source has been used. The measurement has been performed at room temperature, and pixels 01-06 and 04-01 have been excluded from the analysis due to an independent connection problem already before the measurement.

Weight	Active area pressure	Relative active pressure	Passive area pressure	Relative passive pressure	$\overline{\Delta E}$ FWHM
0 g	0 g/mm^2	0 %	0.008 g/mm^2	0 %	243 eV
15 g	0.048 g/mm^2	100 %	0.026 g/mm^2	8 %	240 eV
35 g	0.111 g/mm^2	231 %	0.592 g/mm^2	175 %	232 eV
61 g	0.194 g/mm^2	404 %	1.025 g/mm^2	303 %	241 eV
87 g	0.276 g/mm^2	575 %	1.458 g/mm^2	431 %	258 eV
103 g	0.327 g/mm^2	681 %	1.725 g/mm^2	510 %	259 eV
4 days of measurement break with other tests performed in the setup					
0 g	0 g/mm^2	0 %	0.008 g/mm^2	0 %	253 eV

Hypothesis: Damages due to Particles or Rough Surfaces In the early iteration of the detector assembly procedure, spacer pills with a diameter of 70 µm from aluminum oxide were mixed into the glue. The intention was to create a spacing with a well-defined distance between the SDD chip and the Cesic interposer. To test if the particles in the glue can damage the detector, sandpaper with a comparable grain size was carefully placed on the electronic readout side of a planar 47 pixel detector. As shown in Figure 5.26, Kapton tape, as well as the sandpaper, has been attached to one of the cylindrical weights (15 g) from the previous tests. This weight has been chosen since it corresponds to the expected mounting pressure during the assembly of the detector module. To test the detector performance with the sandpaper on the readout side, a measurement with an ^{55}Fe source has been performed. The energy resolution of the Mn-K$_\alpha$ line and the corresponding energy spectra for representative measurements are shown in Figure 5.27. The measured average energy resolution and the number of functional pixels for all measurements are listed in Table 5.7.

For the measurements with particle sizes up to 32 µm, no effect on the detector performance in terms of the energy spectra and energy resolution has been observed. However, when increasing the grain size of the sandpaper, mimicking particles with a diameter of 42 µm, three additional pixels stopped working. Furthermore, several distortions can be observed in the energy spectra of some pixels. When placing a sandpaper with a particle size of 105 µm on top of the detector readout side, another pixel stopped working. After the sandpaper had been removed, the defective pixels and distortion in the energy spectrum remained present, as seen in Figure 5.27d. This is a strong indication that particles inside the glue potentially damage pixels.

During the assembly procedure of the following 166 pixel detector module (S0-166-2), the same glue, just without the spacer pills, has been used. The measurements have shown that

(a) Planar 47 pixel detector

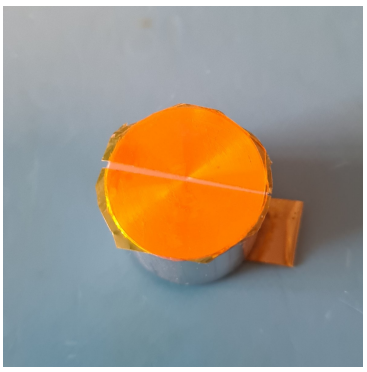

(b) Weight with Kapton tape

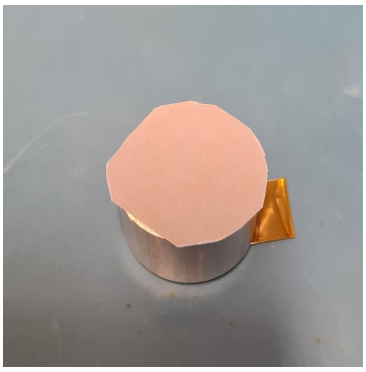

(c) Weight with sand paper

Figure 5.26: Photograph of sandpapers placed on a planar 47 pixel detector
For the investigations the planar 47 pixel detector SDD33.2 W07-G03 has been used. (a) Planar 47 pixel detector placed inside an aluminum dark box with the readout side facing upwards. On the other side of the detector (entrance window side, here facing to the bottom side of the box), a ^{55}Fe calibration source has been placed. (b) Kapton tape applied to 15 g aluminum weight. (c) Sandpaper applied to 15 g aluminum weight.

Table 5.7: Overview of sandpapers placed on a planar 47 pixel detector
Weight (15 g) equipped with sandpaper (different grit sizes) placed on the readout side of a planar 47 pixel detector (SDD33.2 W07-G03). To extract the average energy resolution $\overline{DeltaE}$ in FWHM, the Mn-K$_\alpha$ line of an ^{55}Fe calibration source has been used. Pixels 01-06, 04-04 and 04-08 were excluded from the analysis due to a problem independent of the tests.

Particle size	Grit size	Weight	$\overline{\Delta E}$	Number of working pixel
	Kapton	15 g	219 eV	44
≈ 10 µm	P2500	15 g	220 eV	44
≈ 21 µm	P1200	15 g	223 eV	44
≈ 32 µm	P800	15 g	226 eV	44
≈ 42 µm	P600	15 g	255 eV	40
≈ 105 µm	240	15 g	266 eV	39
Nothing placed on SDD chip		0 g	256 eV	39

Kapton does not damage the SDD chip. As a result, it has been decided to use thin stripes of Kapton (and later PET) attached to the Cesic interposer to create a well-defined spacing between the SDD chip and the Cesic interposer. The assembly of the detector module S0-166-2 shows that these adjustments in the assembly procedure resulted in the production of a fully working 166 pixel detector, see Chapter B.2. Consequently, for the production of all subsequent detector modules the glue without spacer pills has been used.

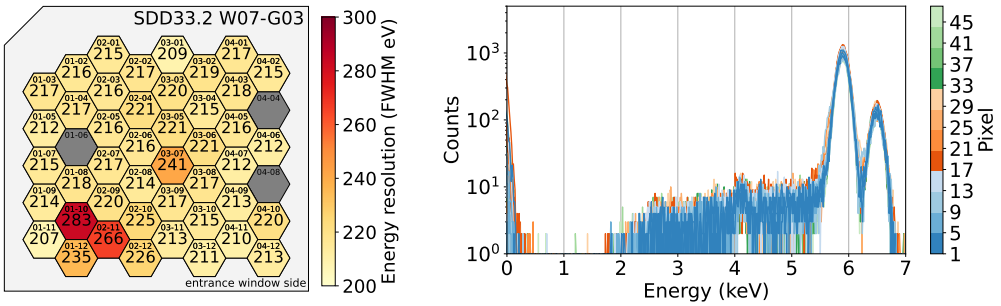

(a) Kapton tape on 15 g weight

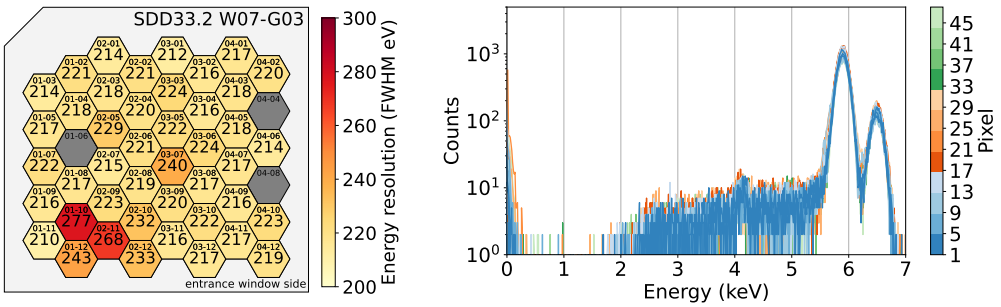

(b) 21 µm particles with P1200 sandpaper on 15 g weight

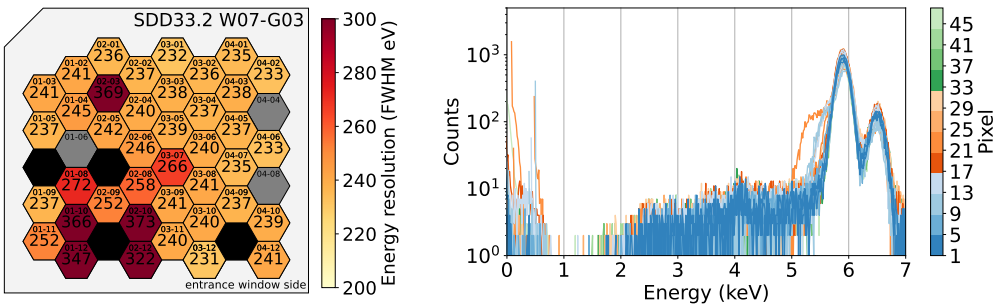

(c) 42 µm particles with P600 sandpaper on 15 g weight

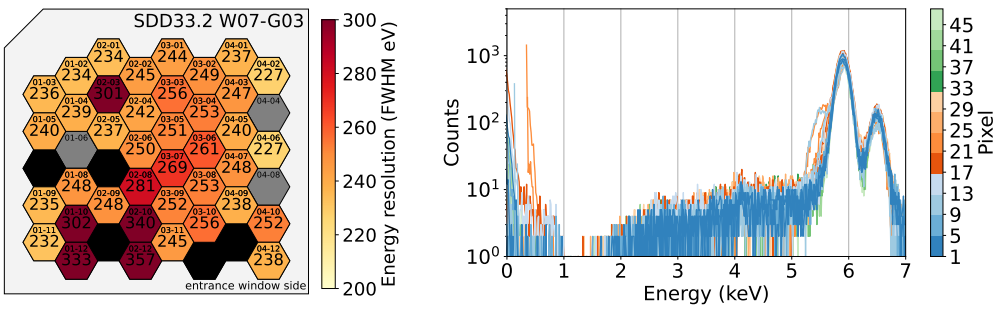

(d) No weights on detector after sandpaper tests

Figure 5.27: Effects of particles on planar 47 pixel detector
Energy resolution pixel maps and energy spectra for measurement with sandpaper placed on the electronic readout side with detector SDD33.2 W07-G03. The pixels in grey have been disabled due to problems before the measurement campaign. The pixels colored in black started malfunctioning due to the performed tests. (a) Measurement with Kapton foil applied to 15 g aluminum weight. (b) and (c) Measurement with P1200 and P600 sandpaper applied to 15 g aluminum weight with a particle size of approximately 21 µm and 42 µm, respectively. (b) Measurement without any weight applied to the detector, after the measurements with different sandpaper grids up to a particle size of 105 µm had been performed.

6

CHARACTERIZATIONS WITH X-RAYS

One goal of this work is the assembly and characterization of a detector module (S0-166-4), which was later installed into the MoS to test its performance with electrons in a more realistic MAC-E filter environment, see Chapter 7. To prepare the detector module for this integration and investigate its performance with X-rays, a dedicated bench test setup has been developed as described in Chapter 6.1. The optimizations of the detector voltage to improve the detector performance in terms of energy resolution and functional pixels are given in Chapter 6.2. Even though SDDs and their connected CSA circuit components can be operated already at room temperature, the energy resolution improves when cooled down. Therefore, the detector module has been operated at different temperatures as described in Chapter 6.3. Furthermore, the linearity of the energy calibration and the energy resolution as a function of X-ray energy are investigated with an ^{241}Am source, as described in Chapter 6.4 and Chapter 6.5, respectively. The stability of the detector module in terms of count rate, energy calibration, and energy resolution are examined in Chapter 6.6.

6.1 Experimental Setup

To commission and test the first detector modules with X-rays, a dedicated bench test setup, has been developed as shown in Figure 6.1. The vacuum chamber consists of a tube-like stainless steel vessel, which roughly reassembles the geometry of the detector section in the MoS. A vacuum pressure of approximately 10^{-6} mbar can be achieved. Additionally, the tube-like vessel can be slid to the side, such that the detector module is easily accessible, as shown in Figure 6.1. The detector module is mounted to the heat exchange block of the cooling interface pipes. These pipes are electrically and thermally insulated from the rest of the vacuum chamber at the position of the feedthrough flange. Using a refrigerated circulator and a silicon-based cooling liquid[1] the detector module can be cooled to temperatures of −35 °C at the SDD chip.

6.1.1 *Electronic Readout Chain*

A simplified schematic of the electronic readout chain for the entire setup is outlined in Figure 6.2. The supply voltages and currents for the detector module are provided by the XGlab biasing and control board[2]. This board also controls the different settings that can be adjusted on the ETTORE ASIC, see Chapter 5.4. The individual signals of the detector

[1] Here, the Julabo F81 refrigerated circulator and the cooling liquid Julabo Thermal HY have been used. Its a working temperature between −80 °C to 55 °C. Part number: 8 940 105.

[2] Some smaller modifications to the factory design of the XGLab biasing and control system are described in Chapter D.5.

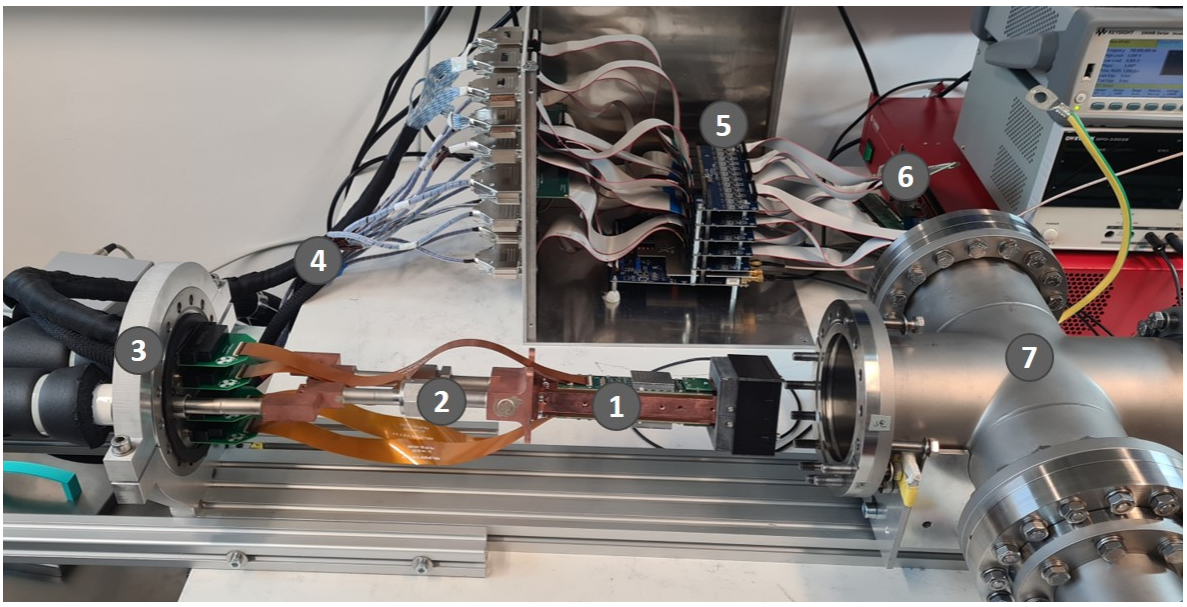

Figure 6.1: Photograph of the detector bench test setup at the MPP
(1) Detector module with a black protection cover, which can hold different calibration sources and protects the detector front mechanically. (2) Pipes and heat exchange block for the liquid cooling circuit connected to an external refrigerated circulator. (3) Feedthrough for the cooling pipes and the 400 electrical connections of the four FPC cables with a length of 30 cm connected to the detector module. (4) Twisted pair cable with a length of approximately 1 m to connect the detector module to the biasing and control system (5) on the air side. (6) DAQ system consisting of three CAEN VX2740B units. (7) The vacuum cross can be pushed over the detector module along the rails on the bottom. Adapted from [8].

module are connected to the XGLab buffer boards, which are installed on top of the XGLab biasing and control board. These buffer boards amplify the signals by another factor of two and allow for the adjustment of the baseline voltage of the signal output[3]. The entire XGlab system is electrically connected to the detector module via four 100 pin micro-D connectors[4] with single wires with a length of 1 m (at ambient air) and four 100 pin FPC cables with a length of 30 cm (in vacuum). For completeness, inside the vacuum, four right angle through-hole 100 pin AirBorn micro-D connectors[5] are used together with a small adapter PCB to connect to the FPC cables.

At the output of the buffer boards, the signals are routed via short ($\approx$ 15 cm) flat ribbon cables to the digital pulse processing (DPP) unit. There, three synchronized CAEN VX2740B digitizers perform a full waveform digitization of the signal with their integrated analog-to-digital converters (ADCs) and form the DAQ system. Each of the units can handle up to 64 channels in parallel [119]. Depending on the application, different data acquisition modes can be selected. They differ in the amount and type of data, which is saved by the CAEN VX2740B digitizer.

Waveform Data Acquisition Mode In this mode, the raw digitized waveform of each channel can be saved every 8 ns at a resolution of 16 bit. Due to the large amount of data created by the 166 pixels of a detector module in the order of 40 GB/s, this acquisition mode can

[3] The output impedance of the buffer boards is 82 Ω.
[4] Micro-D connector 100 pins with 1.0m Kapton wire. Part number: Allectra 380S-MICD-100-1000.
[5] D-Sub Mil-Spec Connectors M Series with 100 pins. Part number: AirBorn MK-452-100-335-620S

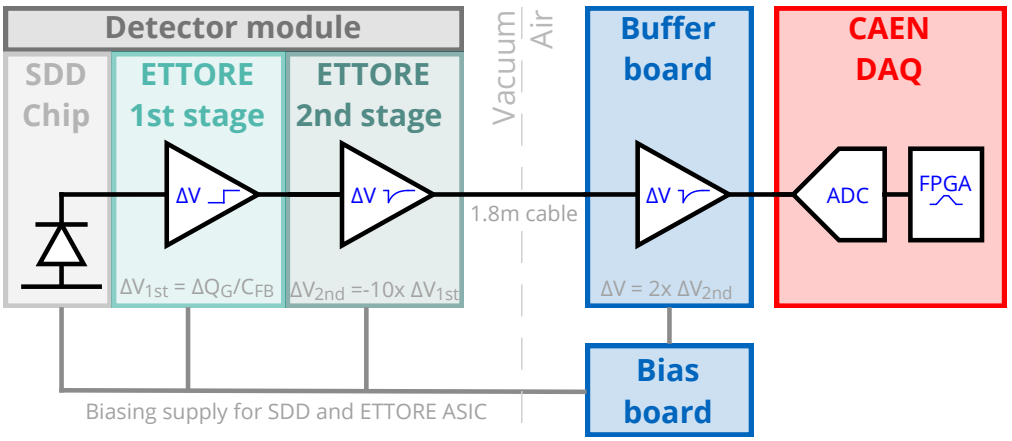

Figure 6.2: Schematic of electronic readout system
Simplified schematic of the electronic readout chain for the detector module. The black lines represent signal connections, and the grey lines depict the power supply connections. The XGLab biasing and control board is illustrated in blue, and the DPP DAQ system consisting of three 64 channel digital signal processor with 16 bit resolution at 125 MS/s (CAEN VX2740B) units is illustrated in red. A more detailed schematic of the on-module electronics can be found in Figure 4.5.

not be operated continuously[6]. Therefore, only shorter data sets in the order of 100 ms can be taken. In this work, it is used, e.g., to measure the leakage current in the detector and perform a noise analysis of the signal.

List Mode Data Acquisition The field programmable array (FPGA) inside the CAEN VX2740B digitizer triggers on any event above a given threshold and extracts its time and energy information, and saves them. For the energy value of each event, a fixed trapezoidal filter with an exponential baseline correction is applied. This acquisition mode strongly reduces the amount of data saved to around 11 GB/h per module and still allows for timing investigations like charge sharing or rate stability measurements[7].

Spectrum Data Acquisition Mode This acquisition mode is similar to the list mode, but it only saves the energy in a cumulative histogram for each pixel. It further reduces the amount of saved information to around 20 MB per detector module and allows for measurements over multiple days or weeks[8]. To still have some time information, for, e.g., rate investigations, the acquisition can be divided into smaller sub-runs, each containing one histogram per channel and sub-run.

List Wave Data Acquisition Mode This acquisition mode is a compromise between the full waveform data acquisition mode and the list mode data acquisition. For every event above a given threshold, not only the time and energy information is saved but also a snippet of the corresponding waveform with a length of up to 20 µs. The saved waveform snipped allows

[6] In a continuous digitization every 8 ns, $125 \cdot 10^6$ Hz $\cdot$ 2 B = 250 MB/s would be generated for each pixel at 16 bit (= 2 B) resolution. An entire detector module at this sampling rate and resolution would create more than 40 GB/s.

[7] For each event roughly 18 B are stored separated in energy (2 B), time stamp (8 B), channel and board ID (4 B), and various flags (4 B). Assuming a count rate of 1 kcps and 166 pixels, this corresponds to roughly 11 GB per hour.

[8] For each pixel, a histogram with 32 768 entries is being saved to a *.txt* file. In this work, the file size per pixel is in the order of 110 kB, independent of the measurement time. For one detector module with 166 pixels, this corresponds to approximately 20 MB.

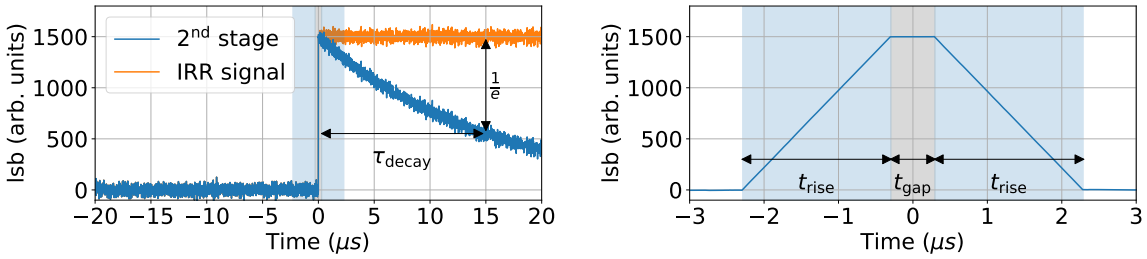

(a) Typical signal waveform

(b) Typical trapezoidal filter

Figure 6.3: Trapezoidal and IIR filter illustration
(a) Waveform of a typical event with a height of 1500 lsb comparable with the ETTORE ASIC amplifier 2nd stage output with a decay time of $\tau_{\text{decay}} = 15\,\mu\text{s}$. To create a step-like signal (orange) that is used in the trapezoidal filter, the waveform is de-convoluted with an IIR filter. The shaded areas illustrate the trapezoidal filter. The waveforms are simple simulations for demonstration purposes. (b) Typical response of a trapezoidal filter output for IIR filtered waveform shown in (a). The trapezoidal filter rise time is set to $t_{\text{rise}} = 2\,\mu\text{s}$ and the gap time to $t_{\text{gap}} = 0.5\,\mu\text{s}$. These values are chosen for the example since they are used for most of the measurements in this thesis.

to perform an offline analysis with, e.g., custom trapezoidal filtering to create noise curves. However, also this mode creates a lot of data in the order of 830 MB/s and can only be used for a limited amount of time[9].

6.1.2 *Energy Reconstruction of Signals in the Detector*

To reconstruct the energy of the signal events, a trapezoidal filter with an exponential baseline correction is applied to the waveform [120]. The working principle of such a filter is illustrated in Figure 6.3. Since this filter can only be used on a step-like signal, a de-convolution is applied to the exponentially decaying output of the 2nd stage of the ETTORE ASIC amplifier. To this end, an infinite impulse response (IIR) filter is applied to the waveform using the transformation described in Equation (6.1).

$$y[n] = y[n-1] + x[n] - \alpha \cdot x[n-1] \tag{6.1}$$

Here, $x[n]$ describes the waveform x at the (sample) position n, and the de-convoluted waveform is denoted as y. The decay of the signal is introduced via the factor $\alpha = \exp(1/\tau_{\text{decay}})$. It is important to note that this formula only works if the baseline of the signal has no offset, which means that the signal decays back to, e.g., 0 lsb. In Figure 6.3a, a typical waveform with a signal and the output after the de-convolution with the IIR filter are shown.

For the energy reconstruction, the average across the waveform is calculated in two windows with the rise time length t_{rise}, which are separated by the gap time t_{gap}. By subtracting the two averages from each other at different positions of the waveform with a step-like signal, its output has the characteristic trapezoidal shape seen in Figure 6.3b. The height of the trapezoid corresponds to the height of the signal in the waveform. In this filter, it is important that the gap time t_{gap} is larger than the pulse rise time of the signal in the waveform, such that the averaging is performed over the flat regions before and after the signal.

[9] The waveform for every event with a length of 20 µs requires 5 kB of storage at 125 MHz and 16 bit resolution. Assuming a detector module with 166 pixels and a typical count rate of 1 kcps per pixel measured in this thesis, this would corresponds to 830 MB/s or approximately 3 TB/h.

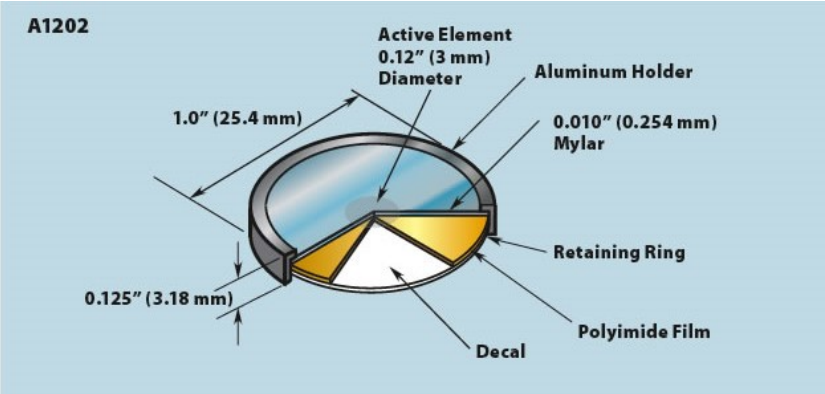

Figure 6.4: Illustration of a standard disk gamma source - Type M
The active element is deposited on aluminized Mylar (polyester) disk which is covered with a Kapton (polymide) foil. The active area spreads over a diameter of 3 mm in the disk's center. The overall diameter of the source is 25.4 mm, with a thickness of 3.18 mm. The illustration is taken from [121].

6.1.3 *X-Ray Calibration Sources*

For the investigations in this work, different X-ray calibration sources are installed in front of the detector module. They are placed in an adapted version of the protection cover at a distance of 12 mm to the SDD chip. For the characterizations of the detector module an ^{55}Fe source and an ^{241}Am source have been used. Both sources are disk-like (type M) with an active area of 3 mm diameter as shown in Figure 6.4.

Encapsulated ^{55}Fe source The radioactive isotope ^{55}Fe decays via EC from the K shell to ^{55}Mn with a half-life of (2.7563 ± 0.0004) yrs [122]. It leaves a vacancy in the K shell, which is filled by an electron from a higher shell. An Auger electron or an X-ray is emitted, which carries the energy difference between the shells. However, since the source used in this work is enclosed with an 254 µm thick Mylar foil, the electrons are completely stopped while X-rays can leave it. The most dominant emitted X-ray lines are shown in Table 6.1. As the energy resolution of the TRISTAN SDDs (approximately 150 eVFWHM at 5.9 keV) is much larger than the separation between the Mn-K$_{\alpha 1}$ and Mn-K$_{\alpha 2}$ (11 eV) line, the average energy weighted by the intensity of both lines is used instead. In the further course of this thesis, this weighted average is denoted as Mn-K$_\alpha$ with an energy of 5.895 keV. A typical energy spectrum of this source is illustrated in Figure 6.5a. The two main peaks of the Mn-K$_\alpha$ and Mn-K$_\beta$ lines are clearly visible. The corresponding silicon escape peaks are apparent at around 4.16 keV and 4.75 keV, respectively. Further details on the energy spectrum and the detector response can be found in Chapter 4.6. The specific ^{55}Fe source used inside the X-ray bench test setup at the Max Planck Institute for Physics (MPP) showed some unintentional

Table 6.1: Dominant X-ray energies for the decay of ^{55}Fe to ^{55}Mn via electron capture
The energies contained in this table are taken from [81]. To calculate the weighted energy, the weighted sum of nearby lines is taken using the relative intensities as weights.

Line	Energy (keV)	Relative intensity	Weighted energy (keV)
Mn-K$_{\alpha 2}$	5.888	0.51	5.895
Mn-K$_{\alpha 1}$	5.899	1.0	
Mn-K$_\beta$	6.490	0.205	

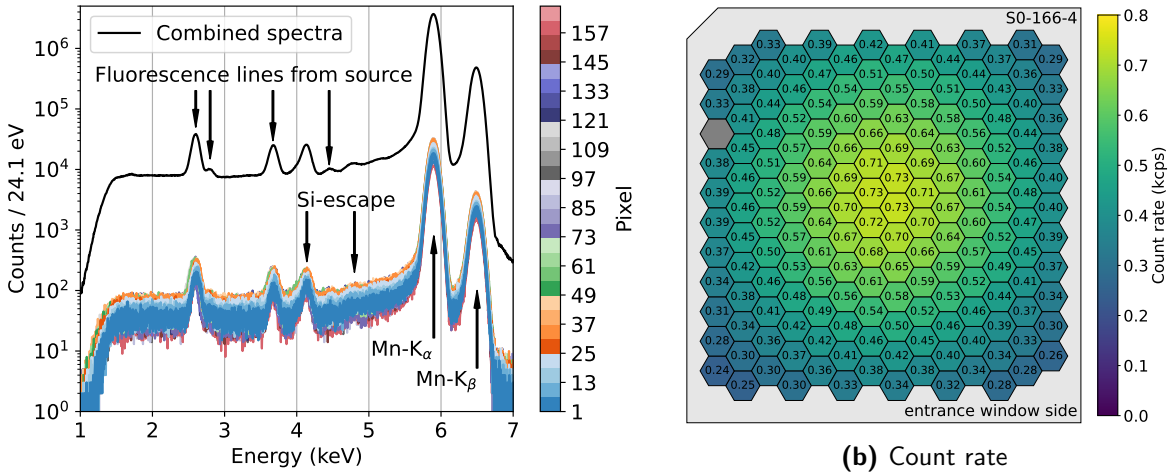

(a) ^{55}Fe energy spectrum **(b)** Count rate

Figure 6.5: Energy spectra of the ^{55}Fe source used in bench test setup
(a) Typical energy spectra for 165 pixels of a measurement with the (specific) ^{55}Fe source in the bench test setup. The source is placed inside the protection cap in front of the detector S0-166-4 at a distance of 12 mm. The additional fluorescence lines between 2 keV to 5 keV can be seen in the spectrum and their corresponding energies are listed in Table 6.2. The superposition of all spectra is shown in black. (b) Corresponding pixel map showing the count rate distribution for events with energies above 1.5 keV. The pixel 01-07 marked in grey has been disabled due to a loose contact. The pixels are shown as seen from the entrance window side.

additional fluorescence lines at energies between 2 keV to 4 keV. These lines have not been observed with other ^{55}Fe sources. Therefore, it is assumed that these fluorescence lines originate from impurities inside the source itself and not the detector or the experimental environment. The elements that likely lead to the observed lines are chlorine, calcium, and barium. Their corresponding energies of the elements are listed in Table 6.2. For the rest of this work, these additional fluorescence lines are neglected since the analysis focuses on the energy resolution and the spectrum in the ROI near the Mn-K$_\alpha$ and Mn-K$_\beta$ lines. The typical count rate during the measurements in this work with the ^{55}Fe source is in the order of several 100 cps per pixel as illustrated in Figure 6.5b.

Encapsulated ^{241}Am source The second X-ray source used in the bench test setup is an encapsulated ^{241}Am source. ^{241}Am is produced as a side product in fission reactors and decays via α-decay to ^{237}Np with a half-life of 432.2 yrs [123]. X-rays and Auger electrons are emitted during the de-excitation process of ^{237}Np. The α-particle and electrons are stopped in the packaging material of the used disk source (type M). A typical energy spectrum taken in this work is shown in Figure 6.6. The X-ray lines between energies of 11.9 keV to 26.3 keV and the more remote line at an energy of 59.5 keV can be used for calibration purposes. Since the packaging material of the ^{241}Am source is coated with a 254 µm thin platinum layer, additional fluorescence lines are visible. An extensive list of all X-ray lines for the used ^{241}Am source can be found in [124]. The most dominant X-ray lines used in this thesis are listed in Table 6.3. The weighted mean energy is used for further analysis for the lines that are separated by less than the detector energy resolution.

Table 6.2: Fluorescence lines of the ^{55}Fe source used in the bench test setup
The table contains the possible elements that could create the additionally measured fluorescence lines seen in the energy spectrum of the ^{55}Fe source, see Figure 6.5. The energies of the fluorescence lines are taken from [100].

Measured energy (keV)	Element	Line	Energy (keV)	Relative intensity
2.62	Cl	$L_{\alpha 1}$	2.620	1.0
	Cl	$L_{\alpha 2}$	2.621	0.5
2.80	Cl	$L_{\beta 1}$	2.816	0.06
3.68	Ca	$L_{\alpha 1}$	3.692	1.0
	Ca	$L_{\alpha 2}$	3.688	0.5
4.47	Ba	$L_{\alpha 1}$	4.466	1.0
	Ba	$L_{\alpha 1}$	4.451	0.11

Table 6.3: X-ray lines of a sealed ^{241}Am source used for calibration
The table contains a selection of X-ray lines emitted by an ^{241}Am source. These lines were chosen since there is one dominant line that is clearly separated from other dominant lines. To calculate the weighted energy, the weighted sum of nearby lines is taken using the relative intensities as weights. A full list of all X-rays emitted by the source can be found in [124].

Element	Line	Energy (keV)	Relative intensity	Weighted Energy (keV)
^{78}Pt	$L_{\alpha 2}$	9.362	1.26	9.435
^{78}Pt	$L_{\alpha 1}$	9.443	11.2	
^{237}Np	L_l	11.871	0.58	
^{237}Np	$L_{\alpha 2}$	13.761	0.0115	13.930
^{237}Np	$L_{\alpha 1}$	13.946	0.1188	
^{237}Np	$L_{\beta 1}$	17.751	0.1160	17.774
^{237}Np	$L_{\beta 3}$	17.992	0.01222	
^{237}Np	γ_1	26.345	2.40	
^{237}Np	γ_3	33.196	0.126	
^{237}Np	γ_5	59.541	35.9	

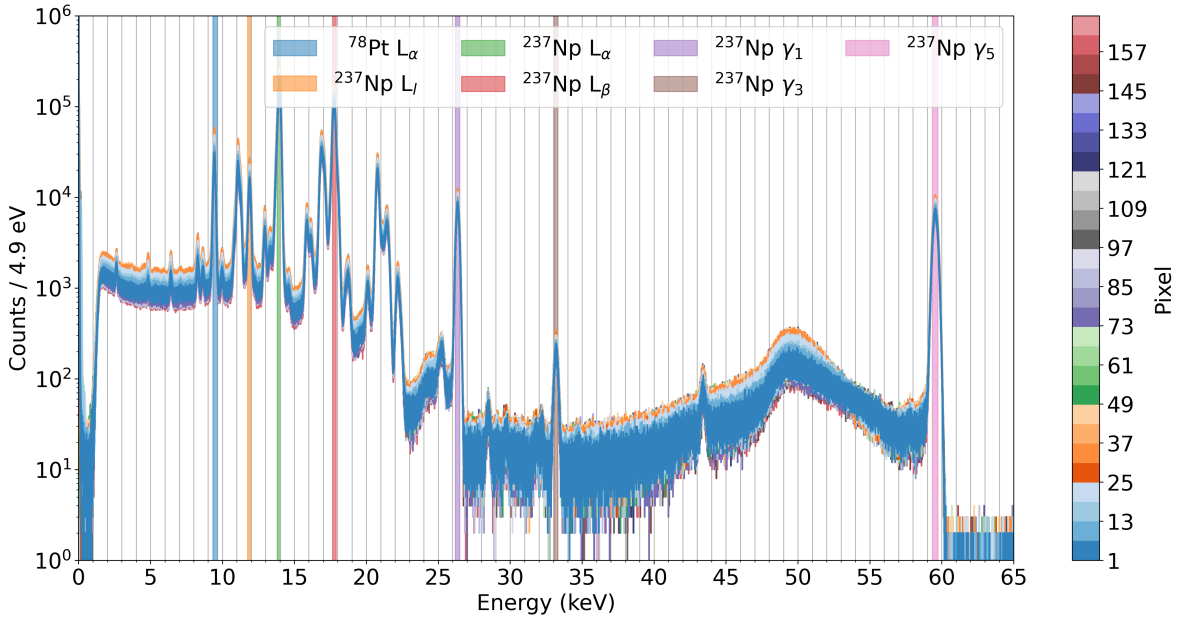

Figure 6.6: Energy spectra of the ^{241}Am source
The source has been placed inside the protection cap of detector S0-166-4 at a distance of 12 mm. The most dominant and separated lines listed in Table 6.3 are highlighted with the vertical bars. The spectra for 165 pixels are shown following the cooler code on the right-hand side. In this measurement, pixel 01-07 has been disabled due to a loose contact in the signal readout chain.

6.2 Optimization of Detector Voltages

For the commissioning of the detector module S0-166-4 the most critical detector voltages have been varied inside their suitable parameter space to find an optimal working point. Since it is not feasible to test all combinations of possible set points, an iterative approach is being used. Therefore, the different detector voltages are optimized after each other, starting with the parameters that influence the nJFET. Next, the drift and depletion voltages are investigated. Since the RX and BC voltage both depend on the set R1 voltage, these parameters are varied together. As a metric for the working point mainly the number of working pixels and the average energy resolution are being used. Additionally, the stability of the total count rate and calibration parameters is investigated. The measurements are performed using an ^{55}Fe source inside the protection cover and a temperature of −33 °C at the SDD chip. The energy spectrum is fitted with two Gaussian functions and two shelf terms to describe the region around the Mn-K$_\alpha$ and Mn-K$_\beta$ lines. More details on the detector response to X-rays are given in Chapter 4.6. This fit is used to calibrate the detector in situ and to extract the energy resolution for the Mn-K$_\alpha$ line in terms of FWHM. The total count rate of the detector is calculated for all events above an energy of 1.5 keV, which is slightly higher than the energy threshold. In this measurement campaign, pixel 01-07 has been excluded from the analysis due to a loose contact in the signal readout chain.

In the following chapter, mainly the energy resolution and the effect on the detector response are shown against the varied parameters, since they are affected the most. Additional effects on the total count rate and calibration are discussed in the appendix in Chapter C.3.

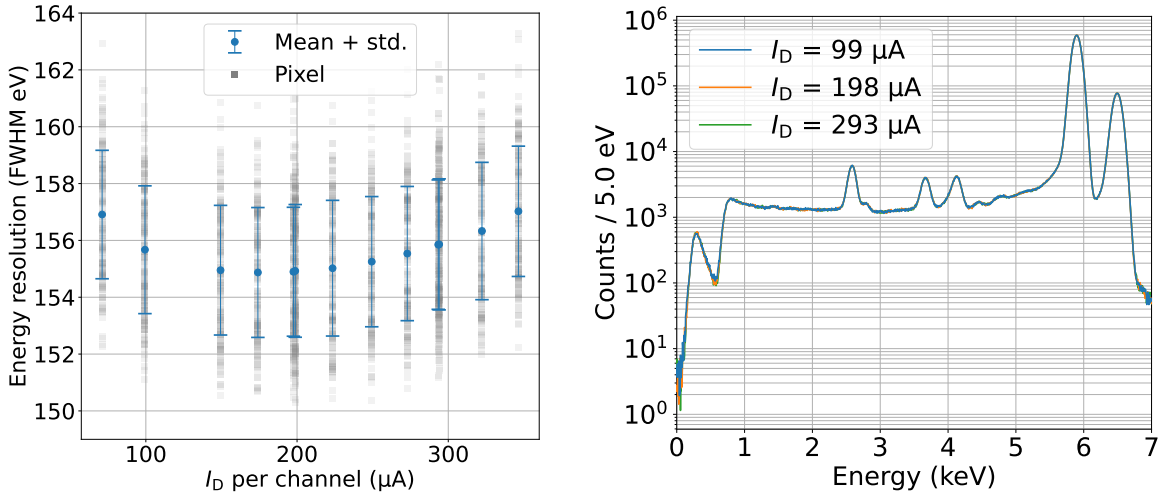

(a) Energy resolution against nJFET current I_D **(b)** Combined energy spectrum for nJFET currents I_D

Figure 6.7: Effect of the nJFET current I_D on detector performance
In the measurement all pixels except of 01-07 are functional. This pixel had an unrelated connection issue and has been excluded from the measurement. (a) The measured energy resolution of each individual pixel is illustrated by the transparent grey squares. The mean and standard deviation per measurement is shown in blue. (b) Combined energy spectrum of all functional pixels for a selection of I_D currents. Supplementary material is shown in Figure C.2.

6.2.1 *nJFET Parameters*

For the integrated nJFETs in the SDD chip, the main parameters that can be set externally are the drain current I_D and voltage U_D. By varying the drain current I_D, the transconductance g_m of the nJFET changes. As seen in Figure 6.7a, an optimum in terms of energy resolution is achieved for a drain current around $I_D = 200\,\mu A$. During the whole measurement campaign, all pixels were functional, and no effect on the total count rate or detector calibration could be observed. The combined energy spectra across all pixels for three representative measurements are shown in Figure 6.7b. Also here, no difference could be observed.

Next, the drain voltage U_D is being varied[10]. As shown in Figure 6.8a, this parameter has a larger impact on the energy resolution than the drain current I_D. Overall, for lower drain voltages U_D, the average energy resolution worsens, i.e., increases. For a drain voltage of 7.5 V and 8.5 V an average energy resolution of 154.1 eV FWHM and 153.7 eV FWHM is achieved, respectively. Additionally, at $U_D = 9.5\,V$ the energy resolution worsens strongly, and the spread between the pixels becomes larger (see Figure C.4). This behavior might be explained by impact ionization but has not been investigated in further detail. Since the difference between 7.5 V and 8.5 V is marginal and the spread in energy resolution across the pixels is slightly better for the 7.5 V setting, this voltage is used for the further measurements in this work.

[10] The voltage is measured at the test point of the XGLab biasing and control system.

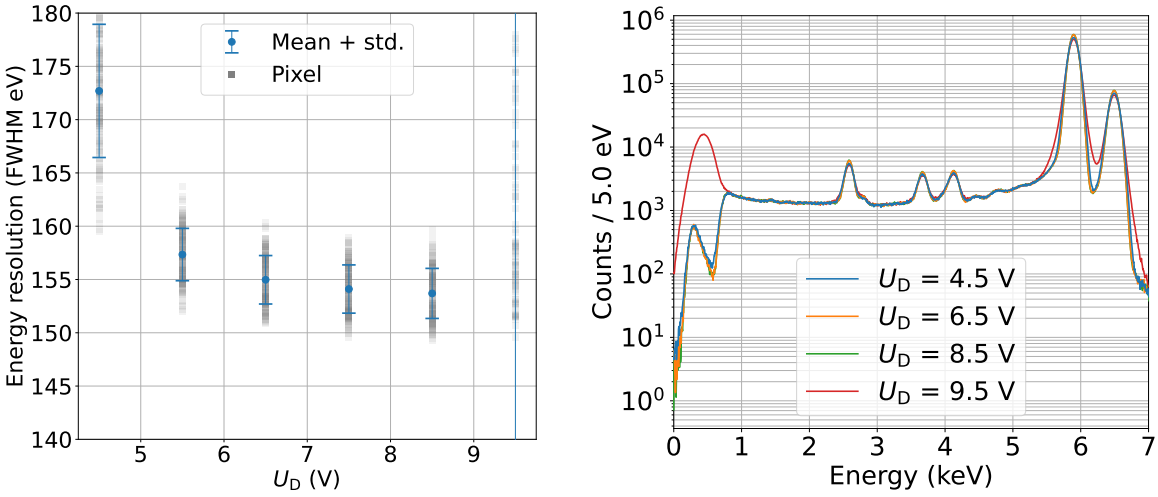

(a) Energy resolution against drain voltage U_{D} **(b)** Combined energy spectrum for drain voltages U_{D}

Figure 6.8: Effect of the drain voltage U_{D} on detector performance
In the measurement all pixels except of 01-07 are functional. This pixel had an unrelated connection issue and has been excluded from the measurement. (a) The measured energy resolution of each individual pixel is illustrated by the transparent grey squares. The mean and standard deviation per measurement is shown in blue. (b) Combined energy spectrum of all functional pixels for a selection of drain voltages U_{D}. Supplementary material is shown in Figure C.3 and Figure C.4.

6.2.2 *Reset Parameters*

Since the detector is operated in a pulsed reset mode, the detector anode needs to be emptied in periodic intervals before the first stage of the CSA circuit of the ETTORE ASIC saturates. During the operation of the detector module, the reset line is set to a negative voltage U_{ResL}, which closes the diode towards the anode. At the time of the reset pulse, the reset line is set to the positive voltage U_{ResH}, allowing electrons collected at the anode to drain away over the time window T_{Reset}. As long as these parameters are chosen within their specifications, they should not significantly influence the detector module's performance.

As seen in the measured energy resolution of the Mn-K$_\alpha$ line in Figure 6.9a, the opening voltage U_{ResH} for the reset diodes has almost no effect on the average energy resolution ($< 0.3\,\mathrm{eV}$). A shallow minimum is found for $U_{\mathrm{ResH}} = 4.0\,\mathrm{V}$. This value is consistent with the expectation and used for all the measurements in this work.

Also, for the closing voltage U_{ResL} of the reset diodes, no effect is visible in the average energy resolution, see Figure 6.9b. The expected operation region for U_{ResL} is $U_{\mathrm{IGR}} < U_{\mathrm{ResL}} < U_{\mathrm{R1}}$. Here, it is interesting to note that for voltages larger (more positive) than $U_{\mathrm{R1}} = -9.8\,\mathrm{V}$, the detector also showed the same performance. Since all other previous measurements used $U_{\mathrm{ResL}} = 10\,\mathrm{V}$, this value has been used for all measurements in this work to keep consistency.

The reset pulse length T_{Reset} describes the length of the time window in which the reset line potential is set to U_{ResH}. In this phase, the electrons are drained from the anode. As illustrated in energy resolution measurement in Figure 6.9c, no effect of the reset pulse length T_{Reset} can be seen. For every measurement, all pixels were functional. Only if the reset pulse length is set to a shorter length in the order of 0.5 µs, pixels start malfunctioning. In previous measurements a reset pulse length $T_{\mathrm{Reset}} = 1.5\,\mu\mathrm{s}$ has been used with success.

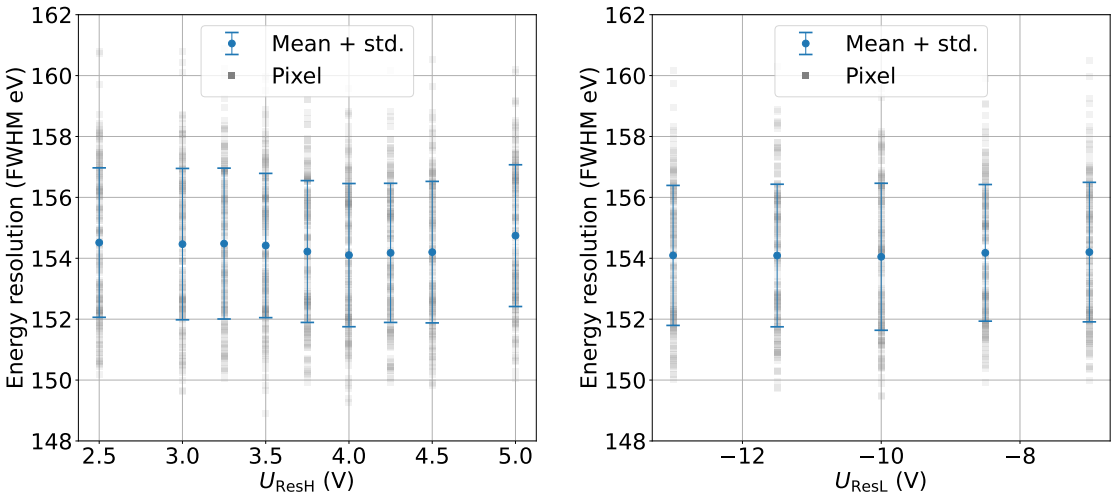

(a) Energy resolution against U_{ResH}

(b) Energy resolution against U_{ResL}

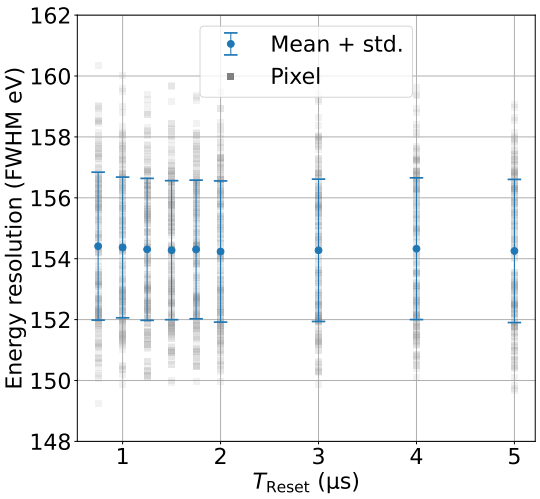

(c) Energy resolution against T_{Reset}

Figure 6.9: Effect of reset parameter on detector performance
In the measurement all pixels except of 01-07 are functional. This pixel had an unrelated connection issue and has been excluded from the measurement. The measured energy resolution of each pixel is illustrated by the transparent grey squares. The mean and standard deviation per measurement is shown in blue. (a) Variation of the opening voltage U_{ResH} for the diode on the reset lines. (b) Variation of the blocking voltage U_{ResL} for the diode on the reset lines. (c) Variation of the reset pulse length T_{Reset} in which the voltage U_{ResH} is applied to the reset lines to drain the anodes. Supplementary material is shown in Figure C.5, C.6 and C.7.

Therefore, this value is kept for all measurements in this work to keep consistency between them.

6.2.3 *Depletion Voltages U_{BC} and Inner Drift Ring Voltage U_{R1}*

To investigate the effect of the BC voltage U_{BC} on the detector performance, it is varied in combination with the R1 voltage U_{R1}. This combination is chosen since both together have a large impact on the electric field near the anode region. The back frame voltage U_{BF} is always set $-10\,\mathrm{V}$ lower than the back contact voltage U_{BC}. In Figure 6.10a the number of malfunctioning pixels is shown against the set voltages of U_{BC} and U_{R1}. Here, malfunctioning pixels describe pixels that show no or a heavily distorted energy spectrum. Only for a back contact voltage U_{BC} between $-115\,\mathrm{V}$ and $-125\,\mathrm{V}$ an operation point where all pixels are functional can be found. In terms of energy resolution, there is no large difference ($< 5\,\mathrm{eV}$) between the operation points where all pixels are functional as shown in Figure 6.10b[11]. In this graphic, the greyed-out regions correspond to the settings where at least one pixel is malfunctioning. Since the back contact voltage $U_{\mathrm{BC}} = -115\,\mathrm{V}$ has the largest operation point, it is selected for further characterizations.

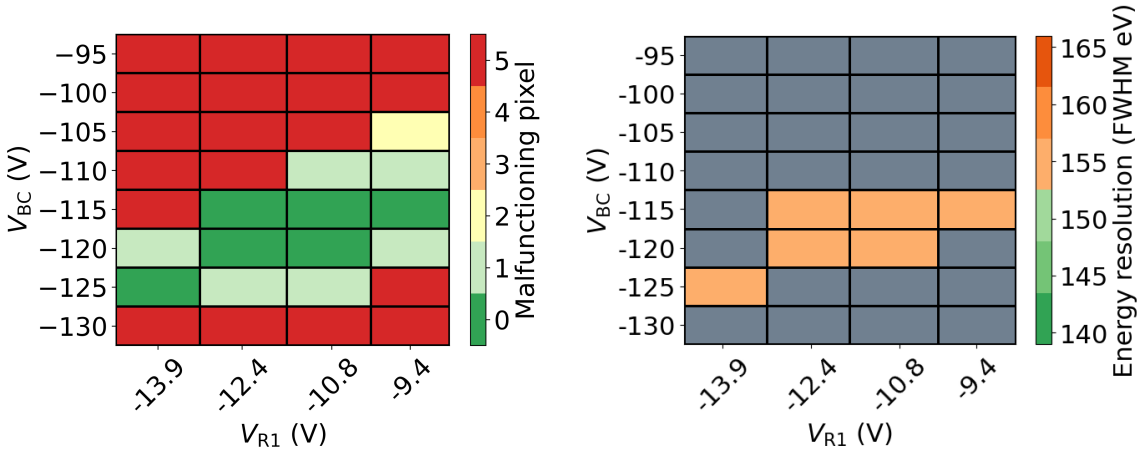

(a) Malfunctioning pixel against U_{R1} and U_{BC} **(b)** Energy resolution against U_{R1} and U_{BC}

Figure 6.10: Effect of depletion voltage on the detector performance
Impact of back contact voltage U_{BC} and inner drift ring voltage U_{R1} on functionality and average energy resolution of detector S0-166-4. In this measurement, the SDD chip temperature is slightly increased to $T_{\mathrm{SDD}} = -25\,^{\circ}\mathrm{C}$ due to a malfunctioning of the refrigerated circulator. (a) Number of malfunctioning pixels which show no or a heavily distorted energy spectrum. (b) Average energy resolution over all pixels. The regions with at least one malfunctioning pixel are greyed out. Courtesy of C. Bruch [125].

6.2.4 *Inner Guard Ring Voltage U_{IGR}*

Next, the effect of the IGR voltage U_{IGR} on the detector response is investigated. As described in [87] for $U_{\mathrm{IGR}} \geq 19\,\mathrm{V}$ a saddle point in the electric fields near the anode is created, in

[11] In this measurement, the energy resolution is slightly higher compared to the other measurements due to ice formation in the thermal bath of the refrigerated circulator. This limited the temperature of the cooling liquids to $-40\,^{\circ}\mathrm{C}$ compared to the normally reached $-50\,^{\circ}\mathrm{C}$. As a consequence the SDD chip temperature increased by approximately 10 K to $T_{\mathrm{SDD}} = -23\,^{\circ}\mathrm{C}$ in comparison to other measurements at around $T_{\mathrm{SDD}} = -33\,^{\circ}\mathrm{C}$.

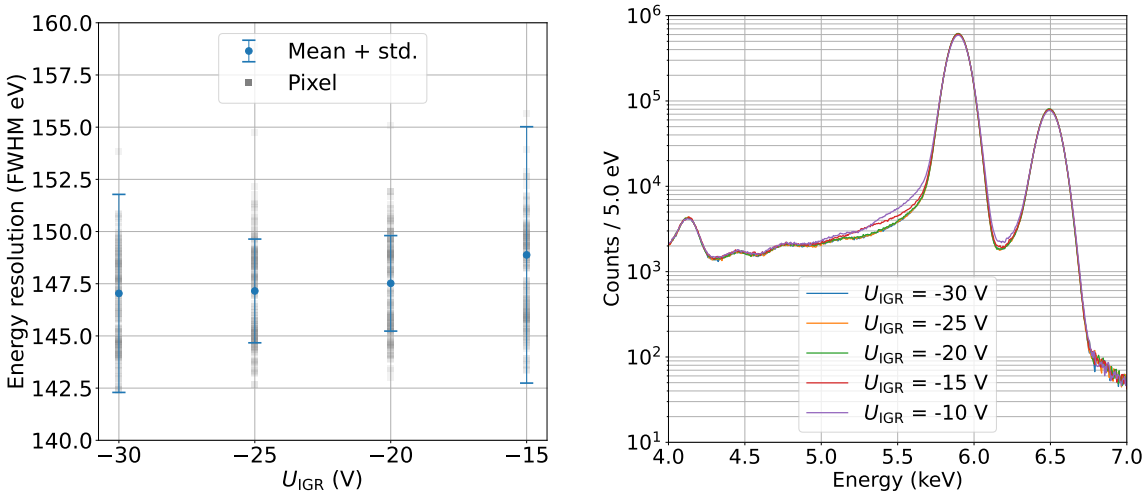

(a) Energy resolution for U_{IGR} variation

(b) Combined energy for U_{IGR} variation

Figure 6.11: Effect of the inner guard ring voltage U_{IGR} on detector performance
In the measurement all pixels except of 01-07 are functional. This pixel had an unrelated connection issue and has been excluded from the measurement. (a) The measured energy resolution of each individual pixel is illustrated by the transparent grey squares. The mean and standard deviation per measurement is shown in blue. (b) Zoom on the combined energy spectrum of all functional pixels, where an effect on the detector response is visible. Supplementary material is shown in Figure C.8.

which electric charges can be lost. This effect can be seen in the measurement at the energy region below the Mn-K$_\alpha$ peak for inner guard ring voltages $U_{\mathrm{IGR}} \geq -15\,\mathrm{V}$, as illustrated in Figure 6.11b. Here, more counts are visible in the energy region below the main peak compared to the measurements performed at $U_{\mathrm{IGR}} \geq 20\,\mathrm{V}$. As shown in Figure 6.11a, the inner guard ring voltage U_{IGR} has only a small effect on the average energy resolution. Nevertheless, for too low and too high U_{IGR}, the standard deviation of the detector resolution and, therefore, the spread between pixels increases.

6.2.5 *Drift Ring Voltages U_{RX} and U_{R1}*

Last, the impact of the RX and R1 voltages U_{RX} and U_{R1} in combination with the IGR voltage U_{IGR} is investigated. Therefore, the drift ring voltages are varied as shown in Figure 6.12 for three different inner guard ring voltages U_{IGR}. The areas in grey denote the set points in which at least one pixel malfunctioned. The colored regions describe the average energy resolution across all pixels. For an IGR voltage of $U_{\mathrm{IGR}} = -20\,\mathrm{V}$ the largest operation region between $-130\,\mathrm{V} \leq U_{\mathrm{RX}} \leq -110\,\mathrm{V}$ and $-12.5\,\mathrm{V} \leq U_{\mathrm{R1}} \leq -7.5\,\mathrm{V}$ is achieved, as shown in Figure 6.12a. For more negative IGR voltages U_{IGR}, the operation point seems to shift towards more negative RX and R1 voltages. Additionally, the average energy resolution across the detector slightly improves (decreases) by 1 eV to 2 eV for more negative IGR voltages U_{IGR}. Nevertheless, since the improvements on the energy resolution are small and a more stable detector has been preferred in this work, the set points $U_{\mathrm{IGR}} = -20\,\mathrm{V}$, $U_{\mathrm{R1}} = -10\,\mathrm{V}$ and $U_{\mathrm{RX}} = -120\,\mathrm{V}$ have been selected.

6.2.6 *Summary of Optimization of Detector Voltages*

With the presented investigations, an optimized operation point for detector S0-166-4 could be found. Here, the largest impact on pixel functionality could be seen for the variation of

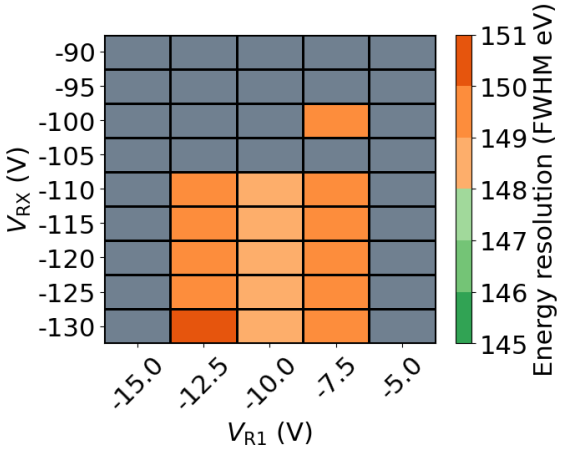

(a) Variation of U_{R1} and U_{RX} with $U_{\mathrm{IGR}} = -20\,\mathrm{V}$

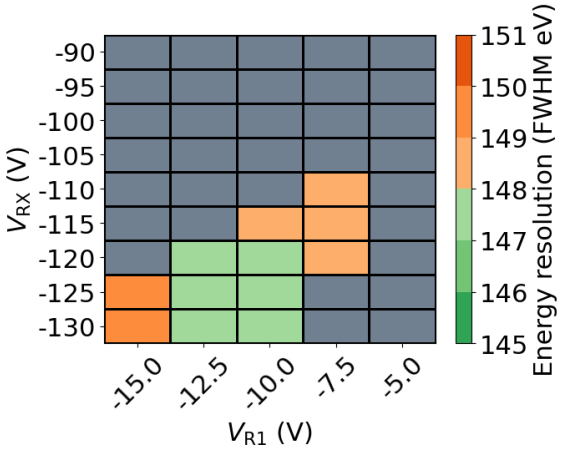

(b) Variation of U_{R1} and U_{RX} with $U_{\mathrm{IGR}} = -25\,\mathrm{V}$

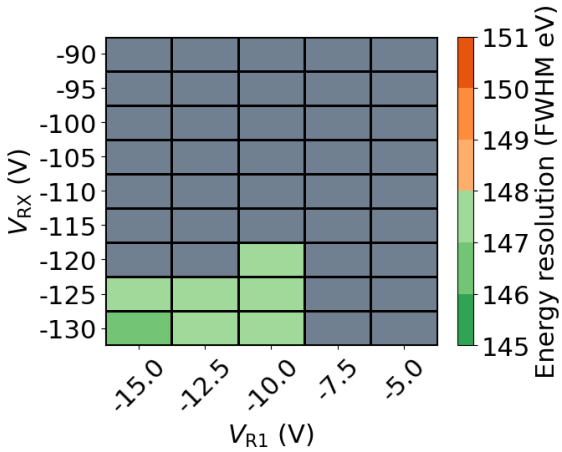

(c) Variation of U_{R1} and U_{RX} with $U_{\mathrm{IGR}} = -30\,\mathrm{V}$

Figure 6.12: Effect of drift voltage on the detector performance
The average energy resolution across the detector for the Mn-K_α line is shown in color for the variation of the drift ring voltages Optimized voltages for detector S0-166-4 and U_{R1} in combination with the inner guard ring voltage U_{IGR}. The regions with at least one malfunctioning pixel are greyed out. Courtesy of C. Bruch [125].

the depletion voltage U_{BC} and the drift ring voltages U_{RX} and U_{R1} in combination with the IGR voltage U_{IGR}. In terms of average energy resolution across the detector, mainly the set drain voltage U_{D} has an impact, while the other parameters marginally improve it by a few eV. As expected, the voltages regulating the reset of the anode have almost no effect on the detector performance. A list of the here selected optimal operation voltages can be found in Table 6.4. It is expected that these values vary between detectors, but this could not be crosschecked within the scope of this work.

Table 6.4: Optimized voltages for detector S0-166-4
Final selected operation voltage settings of detector S0-166-4 after the optimizations have been completed. These settings will be used for all measurements performed in this work.

U_{SSS}	I_{D}	U_{D}	U_{ResH}	U_{ResL}	U_{R1}	U_{RX}	U_{BC}	U_{BF}	U_{IGR}
−3.9 V	200 µA	7.3 V	4.0 V	−10 V	−9.8 V	−120 V	−115 V	−125 V	−20 V

6.3 Temperature Dependence and Electronic Noise

SDDs can already be operated at room temperature due to their low leakage current in the order of 100 pA with reasonable energy resolution. However, cooling down the detector further reduces the leakage current. For the TIRSTAN SDD chips a minimal leakage current of approximately 2 pA at temperatures around $T_{\mathrm{SDD}} = -33\,^{\circ}\mathrm{C}$ can be achieved. To investigate the detector performance in terms of electronic noise, energy resolution, and calibration, the detector module S0-166-4 has been operated at different temperatures between −35 °C and 25 °C (see Figure 6.13) in the bench test setup. Each measurement was performed over a time of 30 min, using an ^{55}Fe source installed in front of the detector (in the protection cap). Typical energy spectra observed in this set of measurements are shown in Figure 6.13b. The effects of the SDD chip temperature[12] are investigated in Chapter 6.3.1. As seen in Figure 6.13, the temperature between the northern and southern ASIC board differs by up to 40 K in this measurement campaign. This is because the southern ASIC board was not properly connected to the copper cooling block in this measurement campaign. As a result of the poor thermal contact, the southern ASIC board was much hotter than the northern ASIC board. The impact of this temperature difference between the ASIC boards is described in Chapter 6.3.2.

6.3.1 *Effects of SDD Temperature on Detector Performance*

First, the effect of the SDD temperature on the electronic noise and the energy resolution is being investigated. To this end, the measured energy resolution of the Mn-K$_\alpha$ line is shown in Figure 6.14a as a function of the SDD temperature. To convert the energy resolution to ENC and extract the noise properties, Equation (4.16) is used. A simple exponential noise model shown in Equation (4.22) is fitted to the mean energy resolution to illustrate the temperature dependence. For temperatures at the SDD chip below −10 °C an average energy resolution smaller than 150 eV FWHM can be achieved. This corresponds to an ENC with a value of $n_{\mathrm{ENC}} \leq 11\,e_{\mathrm{rms}}$. Further cooling down the detector to $T_{\mathrm{SDD}} = -34\,^{\circ}\mathrm{C}$ resulted in an average energy resolution of 144.5 eV FWHM ($n_{\mathrm{ENC}} \leq 9.9\,e_{\mathrm{rms}}$). The standard deviation between the pixels for this measurement is 2.3 eV with maximal spread of 8.9 eV[13]. As indicated by the model, the energy resolution only marginally improves for

[12] And strictly speaking also the temperature of the ASIC boards.
[13] The uncertainty on the individual pixel energy resolution $\sigma_{\Delta E}$ in FWHM is in the order of 0.2 eV to 0.6 eV.

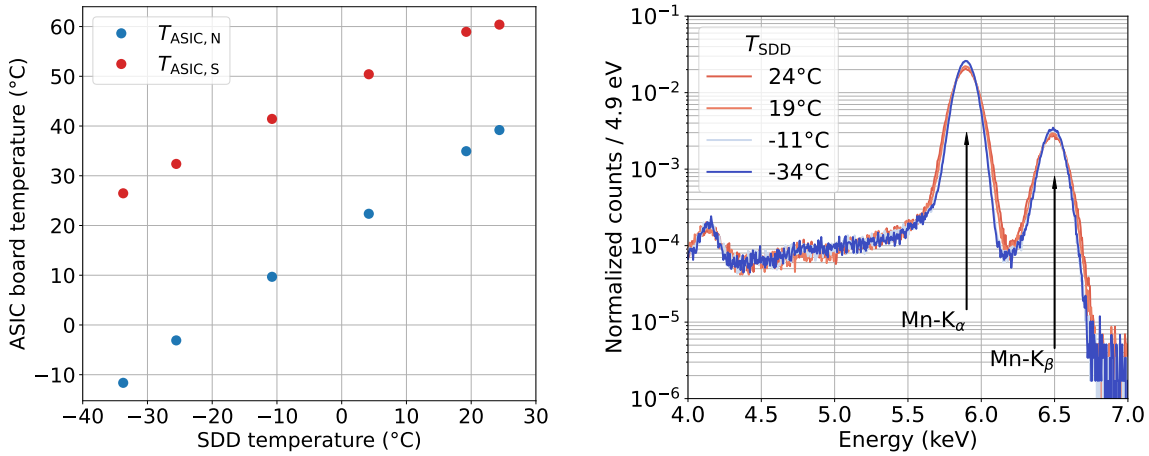

(a) Temperatures at the detector module

(b) Typical ^{55}Fe spectra for 165 pixels

Figure 6.13: ASIC board temperature vs SDD chip temperature and typical ^{55}Fe spectra (a) Temperatures measured at the detector module S0-166-4 in the bench test setup for different settings of the chiller temperature. The temperature dependence of the northern (blue) and southern (red) ASIC board is shown as a function of the SDD chip temperature. In this specific measurement, the southern ASIC board was not connected properly to the copper block, resulting in a poor thermal connection and much higher temperatures. (b) Typical ^{55}Fe spectra of pixel 01-02 representing the 30 min long measurements at different temperatures. The individual spectra are normalized to the total number of counts above an energy of 1.5 keV.

even lower temperatures, and therefore, in the scope of this thesis, a target temperature of $-33\,°\mathrm{C}$ at the SDD chip was used. For comparison, in the measurement at roughly room temperature ($T_{\mathrm{SDD}} = 19.2\,°\mathrm{C}$) an average energy resolution of 169.5 eV FWHM with a standard deviation of 2.6 eV and a maximal spread of 14.4 eV could be achieved.

In Figure 6.14b, the noise curve over the energy filter rise time τ_{rise} for different detector temperatures are given. For energy filter rise times $\tau_{\mathrm{rise}} > 1\,\mu\mathrm{s}$, the energy resolution decreases only for the warmer measurements due to the increased leakage current. The optimum for the measurement at room temperature is at approximately 1.5 µs. For the colder measurements, the optimum lies at around 4 µs. At filter rise times below 1 µs, the detector resolution is dominated by series noise ($n^2_{\mathrm{ENC,series}} \propto T$) of the system, and the difference between measurements stays almost constant.

To check in a first approximation if the SDD temperature has an impact on the calibration of the detector module, the change of the peak position $\delta\mu_{1,\mathrm{px}}$ and $\delta\mu_{2,\mathrm{px}}$, of the Mn-K$_\alpha$ and Mn-K$_\beta$ lines are shown in Figure 6.15a and Figure 6.15b, respectively. As a reference, the measurement at $T_{\mathrm{SDD}} = -34\,°\mathrm{C}$ is used to calculate the relative change in the peak position $\delta\mu_{\mathrm{l,px}}$ as shown in Equation (6.2).

$$\delta\mu_{l,px}(T) = \mu_{l,px}(T) - \mu_{l,px}(T = -34\,°\mathrm{C}) \tag{6.2}$$

Here, l denotes the X-ray line, and px is the pixel index. Overall the peak positions μ_l varies inside a range of $[40\,\mathrm{eV}, -25\,\mathrm{eV}]$ for the different temperatures. A similar behavior was seen for both peak positions. Compared to a separate stability measurement (over 63 h) at a fixed temperature of $T_{\mathrm{SDD}} = (34.1 \pm 0.1)\,°\mathrm{C}$ (see Chapter 6.6) the expected variation of the peak position is $[6\,\mathrm{eV}, -4\,\mathrm{eV}]$ as illustrated by the gray bands. First, the peak position μ_l of both peaks shifts to higher values with increasing temperatures. In the measurement at $-10\,°\mathrm{C}$,

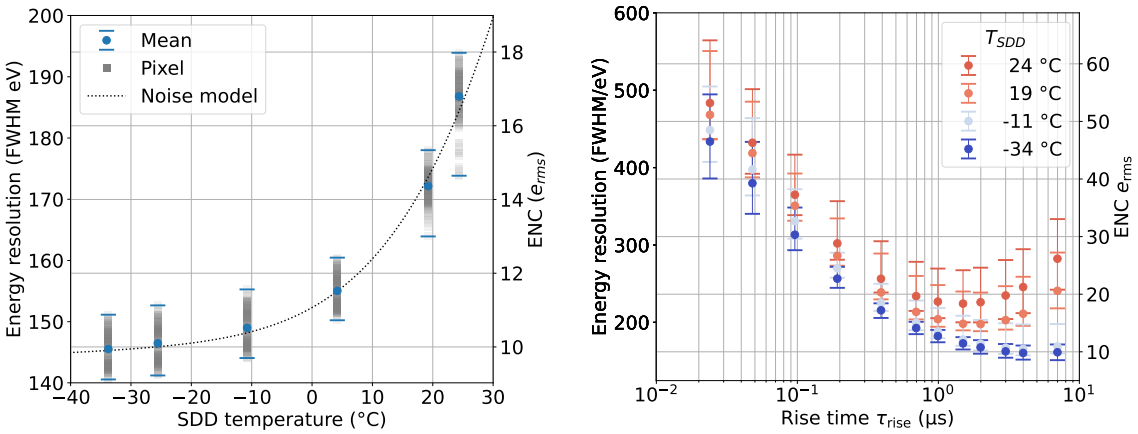

(a) Temperature dependence of energy resolution **(b)** Temperature dependence of noise curve

Figure 6.14: Temperature dependence of energy resolution and noise curve
Measurement with an ^{55}Fe source at different temperatures T_{SDD} at the SDD chip level of detector S0-166-4. (a) Energy resolution of the Mn-K$_\alpha$ line (filter rise time of $T_{\mathrm{rise}} = 2\,\mu\mathrm{s}$) as a function of the SDD temperature. The average value of all functional pixels is shown in blue. The horizontal bars denote the maximal and minimal value of all pixels. The values for the individual pixels at a given temperature are shown in grey. Results published in [8]. (b) Noise curve of the measured energy resolution of the Mn-K$_\alpha$ line as a function of energy filter rise time τ_{rise} for different SDD temperatures.

most pixels are outside the expected variation from the stability measurement. For higher temperatures, the spread between the pixels increases, while the mean across the pixels shifts again closer to the reference measurement at $-34\,^{\circ}\mathrm{C}$. Since the two lines in ^{55}Fe spectrum are close to each other, the slope s and offset o parameters are correlated, and it is difficult to estimate the origin of this small change in calibration. Here, a measurement with more X-ray lines across a larger energy range with, e.g., an ^{241}Am source could be useful to further investigate the temperature dependence of the calibration.

6.3.2 *Effects of ASIC Board Temperature on Detector Performance*

As seen in Figure 6.13a, the temperature of the southern ASIC board ($T_{\mathrm{ASIC,S}} = 26.5\,^{\circ}\mathrm{C}$) was almost 40 K hotter than the northern ASIC board ($T_{\mathrm{ASIC,N}} = -11.7\,^{\circ}\mathrm{C}$) during the measurements at different temperatures[14], since it has not been tightened firmly to the copper cooling block (by accident). To check if this significant temperature difference between the two hemispheres has any effect on the detector module performance, the measured energy resolution ΔE of the Mn-K$_\alpha$ line is illustrated in Figure 6.16. In the pixel map, the northern hemisphere corresponds to the upper half of the pixels, while the southern hemisphere corresponds to the lower half. As shown in the histogram of the energy resolution ΔE (right-hand side), the distribution per hemisphere follows the same shape. This is a good indication that in terms of energy resolution, the absolute ASIC board temperature does not play an important role.

To estimate if the different ASIC board temperatures have any effect on the calibration, the peak position μ_1 of the Mn-K$_\alpha$ line is shown in Figure 6.17. Here, no clear difference between the two hemispheres can be seen, hinting that the absolute ASIC board temperature does not affect the detector calibration. Nonetheless, in this measurement, two

[14] The position of the temperature sensor on the ASIC board is illustrated in Figure D.3.

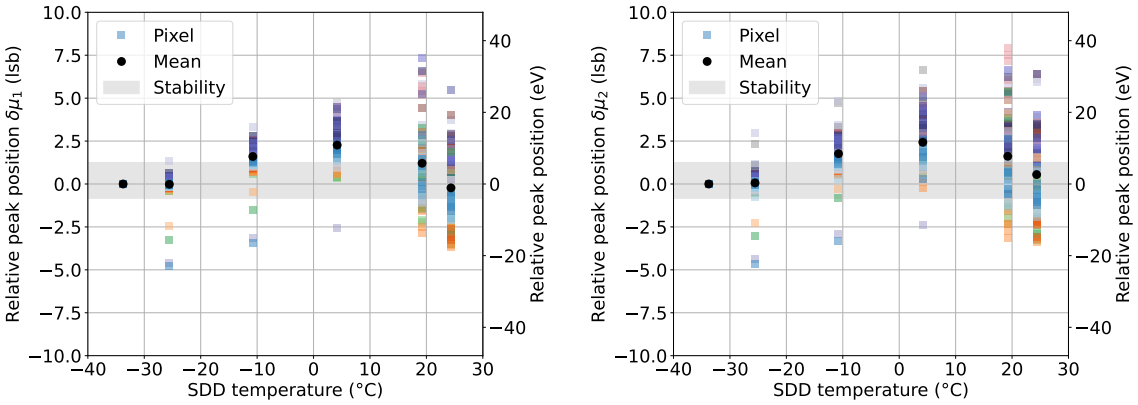

(a) Temperature dependence of μ_1 **(b)** Temperature dependence of μ_2

Figure 6.15: Temperature dependence of peak position
Measurement with an ^{55}Fe source at different temperatures T_{SDD} at the SDD chip level of detector S0-166-4. The relative peak position $\delta\mu_{\mathrm{l,px}}$ is calculated with respect to the measurement $T_{\mathrm{SDD}} = -34\,^{\circ}\mathrm{C}$ for the Mn-K$_\alpha$ (a) and Mn-K$_\beta$ (b) lines. The squares illustrate the different pixels px following the color code shown in Figure D.9a. The black dot illustrates the mean across the pixels. The grey band illustrates an estimation of the expected stability of the peak positions for a fixed temperature $T_{\mathrm{SDD}} = (34.1 \pm 0.1)\,^{\circ}\mathrm{C}$ (see Chapter 6.6).

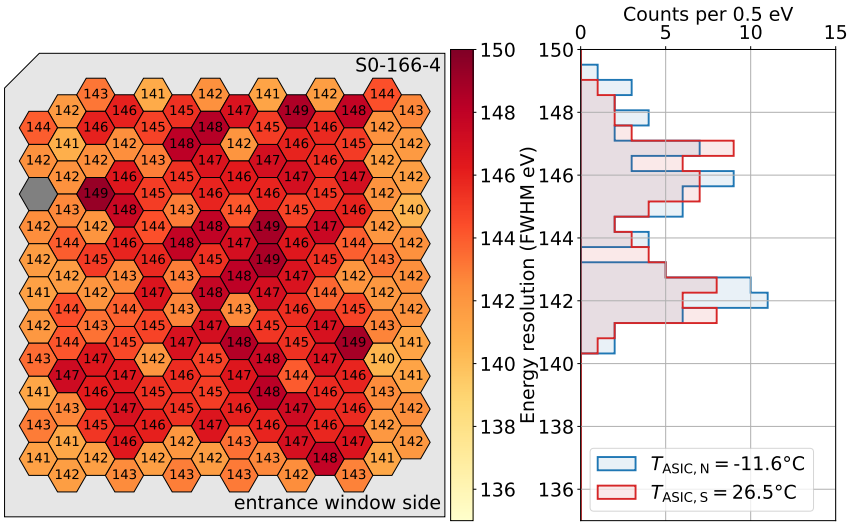

Figure 6.16: ASIC board temperature effect on energy resolution
On the left-hand side, the pixel map of the energy resolution for the Mn-K$_\alpha$ line is shown. The measurement is performed in the bench test setup with detector module S0-166-4. On the right, the histograms of the energy resolution divided into the two hemispheres, north and south, are shown. The detector is cooled down to $T_{\mathrm{SDD}} = -34\,^{\circ}\mathrm{C}$ but since the south side ASIC board has not been tightened properly to the copper cooling structure, its temperature is almost 40 K hotter than the north side. The error on the energy resolution from the fit is approximately 0.5 eV. Each spectrum per pixel contains approximately $1 \cdot 10^8$ counts above 1.5 keV. The measurement has been performed over 63 h.

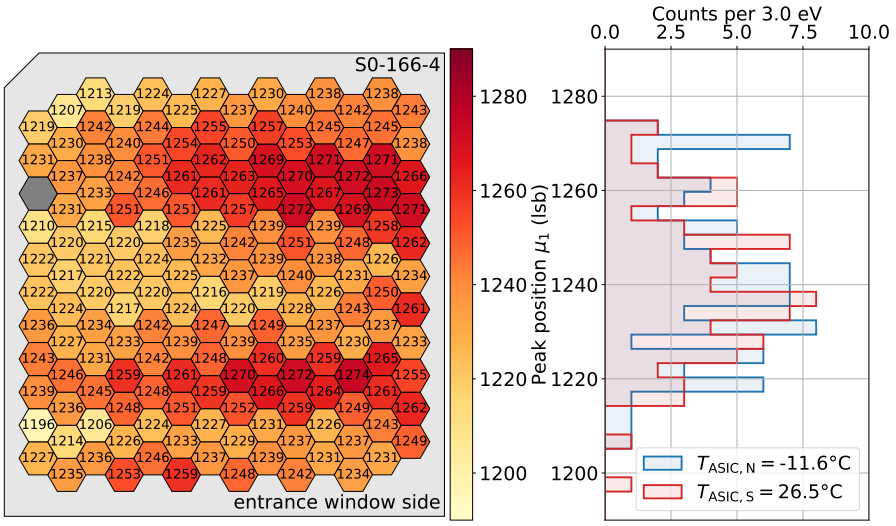

Figure 6.17: ASIC board temperature effect on peak position
On the left-hand side, the pixel map of the peak position μ_1 for the Mn-K$_\alpha$ line is shown. The measurement is performed in the bench test setup with detector module S0-166-4. The histograms of the peak position μ_1 divided into the two hemispheres, north and south, are shown on the right. The detector is cooled down to $T_{\mathrm{SDD}} = -34\,^{\circ}\mathrm{C}$ but since the south side ASIC board has not been tightened properly to the copper cooling structure, its temperature is approximately 40 K hotter than the north side. Each spectrum per pixel contains approximately $1 \cdot 10^8$ counts above 1.5 keV. The measurement has been performed over 63 h.

different ASIC boards are compared relative to each other and not directly with themselves. Therefore, to further investigate the effect of the absolute ASIC board temperature, the measurement could be repeated in such a way that the same ASIC board is operated at different temperatures, by, e.g., installing an external heating element beneath on ASIC board. Additionally, an, e.g., ^{241}Am source could be used instead of the ^{55}Fe source to investigate the detector performance on a larger energy scale.

6.4 Energy Calibration and Linearity

For the smaller 7 pixel TRISTAN prototype detectors, a linearity of the energy scale below 1 % has been observed in [124]. To crosscheck these results for the detector module design, a measurement with an ^{241}Am source has been performed using detector S0-166-4. The detector is operated at $T_{\mathrm{SDD}} = -33\,^{\circ}\mathrm{C}$ in the test bench setup with the source placed inside the protection cover. The measured energy spectra of the individual pixels are shown in Figure 6.6. Also, in this measurement, pixel 01-07 has been disabled due to a loose contact in the signal readout chain. Since many X-ray and fluorescence lines overlap in the ^{241}Am spectrum, only the most dominant and independent peaks have been selected for the analysis as given in Table 6.3. Each peak is fitted in a narrow ROI of approximately one and a half FWHM with a Gaussian function and a flat background. For the peaks with multiple lines close to each other (one dominant and another smaller one nearby), the weighted average by intensity is assumed as the total peak position energy. The fitted peak position (in lsb) as a function of X-ray energy is given in the upper part of Figure 6.18. Each pixel is calibrated individually with a linear function to the true energy in eV. The calibration curve is given in Equation (6.3).

$$E[eV] = s \cdot E[lsb] + o \tag{6.3}$$

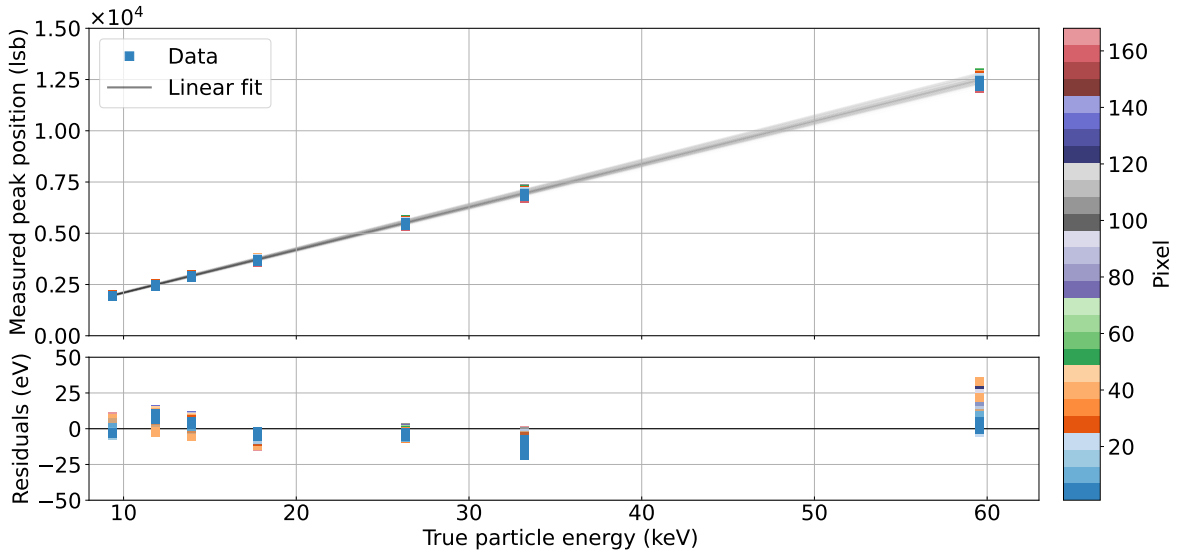

Figure 6.18: Energy calibration curve using an ^{241}Am source
For the calibration measurement the dominant peaks listed in Table 6.3 are being used. The color coding on the right-hand side illustrates the pixel number of the detector in both plots. The relation between the measured peak positions and the true particle energies is given in the upper part. The linear calibration curves, fitted to each pixel, are illustrated by transparent black lines. The residuals between the linear calibration curve and the corresponding data are shown in the lower plot. For a better comparison, the residuals are converted from lsb to units of eV. Plot published in [8].

Here, s denotes the slope parameter of the calibration curve and o the offset. In the lower part of Figure 6.18, the residuals between the measured peak position and the calibration curve are shown. To better compare the absolute size of the residuals, they are converted from units of lsb to eV by multiplying them with the calibration slope s. For all pixels, the residuals vary by less than 40 eV from the calibration curves. This corresponds to less than 0.5 % compared to the absolute energy scale and is comparable with the results observed in [124]. The absolute values for the calibration parameters s and o are shown in Figure 6.19a and Figure 6.19b, respectively. It is worth mentioning that the calibration slope s varies between the pixels by around 4 % compared to its absolute value, requiring a pixel-based calibration. A horizontal stripe pattern is visible in the calibration slope parameter s. It could not be related to any pattern on the electronic readout structure and is expected to originate from minor variations in the feedback capacitance C_{FB} of the SDD chip itself. As expected, most calibration curves have a slight offset in the same order of magnitude as the residuals and are close to zero. The measured residuals in the calibration curves are currently used in sensitivity studies to estimate the effect of the calibration uncertainty on the keV sterile neutrino search with KATRIN. These studies are out of the scope of this thesis.

6.5 Energy Resolution as Function of X-Ray Energy

The energy resolution observed for the X-ray measurements performed with the ^{55}Fe source (see Chapter 6.3) and the ^{241}Am source (see Chapter 6.4) in the test bench setup are shown in Figure 6.20. The horizontal bars illustrate the maximal and minimal value of the energy resolution across all pixels. An average energy resolution of 228 eV FWHM is obtained at an energy of 17.8 keV, with a maximal spread of 10 eV across all pixels. For the measurement at 60 keV an average energy resolution of 383 eV FWHM with a maximal spread of 12 eV is observed. For X-rays, the energy resolution mainly depends on the Fano

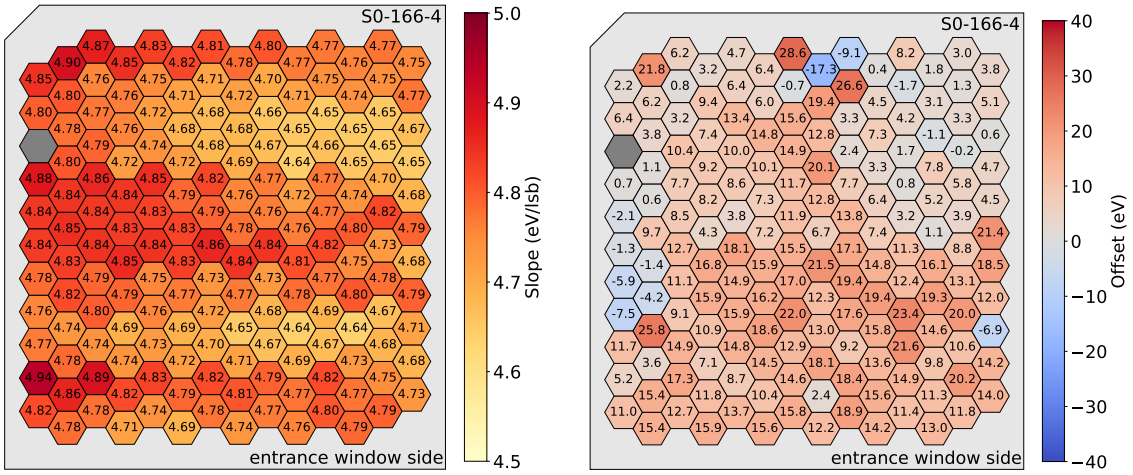

(a) Calibration slope s **(b)** Calibration offset o

Figure 6.19: Calibration parameter from ^{241}Am measurement
Pixel map of the linear calibration parameters slope s (a) and offset o (b) for detector S0-166-4 in the X-ray test bench setup. The parameters correspond to the measurement shown in Figure 6.18.

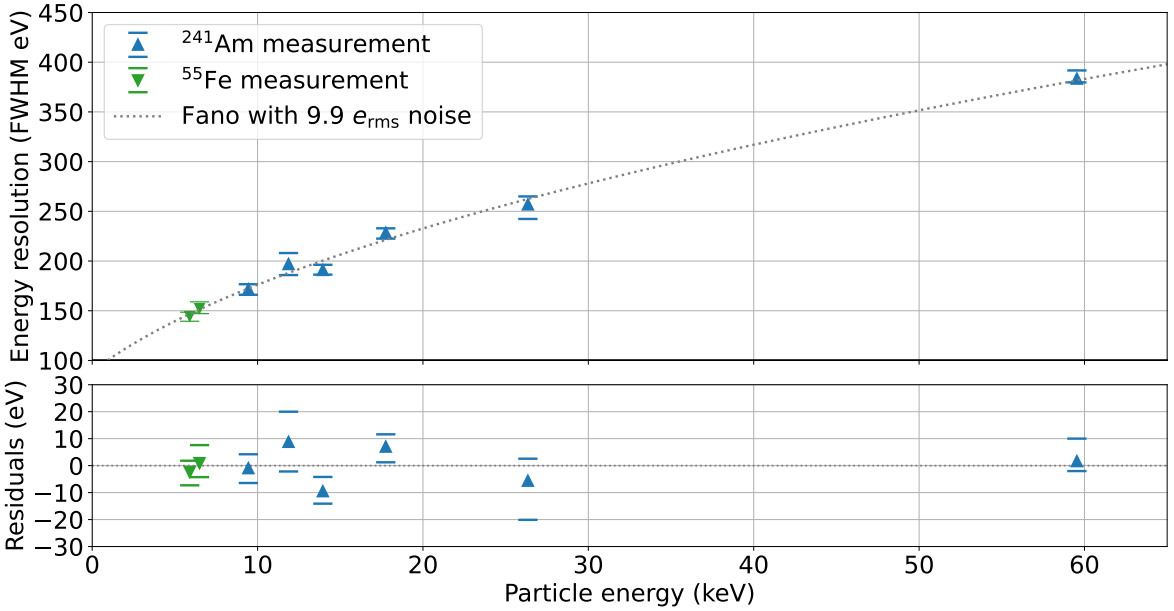

Figure 6.20: X-ray energy resolution as a function of energy
The energy resolution observed for a measurement with an ^{241}Am source (blue) and an ^{55}Fe source (green) are shown in the upper plot. Both measurements are performed in the test bench setup at $T_{\mathrm{SDD}} \approx -33\,^{\circ}\mathrm{C}$. The horizontal bars denote the maximal and minimal value of all pixels. The expected energy resolution given by the Fano statistics and the measured electronic noise of $n_{\mathrm{ENC}} = 9.9\,e_{\mathrm{rms}}$ is illustrated by the dotted gray line. The residuals between the measurements and the expectation are shown in the lower plot. Results partially published in [8].

statistics and the electronic noise in the detector system. Using the measured electronic noise of $n_{\mathrm{ENC}} = 9.9\,e_{\mathrm{rms}}$, the expectation of the energy resolution (dotted grey line) is in good agreement with the measurements. The residuals between the expectation and the measured energy resolution are in the order of 10 eV, comparable to the spread across pixels.

6.6 Detector Stability and Stacking

To investigate the stability of the energy calibration and the energy resolution, a measurement over 63 h has been conducted using an ^{55}Fe source. To investigate the time dependence, the measurement has been divided into smaller 30 min sub-runs. The detector module S0-166-4 has been cooled down to a temperature of $T_{\mathrm{SDD}} = -34.1\,^{\circ}\mathrm{C}$, which varied by at most 1 K in the course of the measurement.

The total measured count rate across all pixels (energy threshold of 2 keV) is shown in Figure 6.22a. The observed decline in the total count rate is attributed to the natural decay of ^{55}Fe isotope. It can be modeled with an exponential decay function shown in Equation (6.4).

$$N(t) = N_0 \exp\left(-\frac{\ln(2)}{T_{1/2}} \cdot t\right) \tag{6.4}$$

Here, N_0 describes the initial rate at the time $t = 0$. The least-squares method is used to fit the exponential decay function to the measured count rate. The best-fit with a half-life of $T^{\star}_{1/2} = 2.72^{+0.04}_{-0.05}$ yrs is in good agreement with the expected value of $T_{1/2} = 2.736$ yrs [122]. The uncertainties on the half-life $T_{1/2}$ are estimated using the profile chi-squared function $\chi^2(T_{1/2}) - \chi^2_{\mathrm{min}}$. Following Wilks's theorem [126] the critical chi-squared difference for one free parameter (here N_0) is $\Delta\chi^2_{\mathrm{crit.}} = 1$. This corresponds to an uncertainty at a 68.3 % confidence level. The resulting profile chi-squared function and the intersection with the critical chi-squared difference $\Delta\chi^2_{\mathrm{crit.}}$ is shown Figure 6.21.

To assess the stability of the detector module, the residuals between the best-fit and the data points are calculated and normalized to the total count rate. Throughout the measurement, the rate varied by at most 0.08 %.

To investigate the stability of the energy calibration, the ^{55}Fe spectra of each sub-run and pixel are fitted with the detector response described in Chapter 4.6. The relative shift of the peak position of the Mn-K$_\alpha$ line is used to estimate the change in the energy calibration. It is calculated using the formula shown in Equation (6.5).

$$\delta\mu_{\mathrm{px,run}} = \mu_{\mathrm{px,run}} - \overline{\mu_{\mathrm{px}}} \tag{6.5}$$

The peak position (in units of lsb) is extracted from the Gaussian part of the fit and is denoted as $\mu_{\mathrm{px,run}}$. Here, the index run indicates the given sub-run number and px the pixel number. Since the calibration varies by up to 4 % between the pixels (see Chapter 6.4), every pixel is compared to its average peak position $\overline{\mu_{\mathrm{px}}}$ across all sub-runs. For a better comparison, the relative shift of the peak position $\delta\mu_{\mathrm{px,run}}$ is converted from units of lsb to eV. The conversion is performed by multiplying the relative peak position shift $\delta\mu_{\mathrm{px,run}}$ with the average calibration slope s of each pixel (consequence of Equation (6.3)). The time dependence of the relative peak position shift $\delta\mu_{\mathrm{px,run}}$ is illustrated in Figure 6.22b. Notably, the peak position for nearly all pixels experiences a variation of less than 5 eV. Four pixels exhibit a slightly

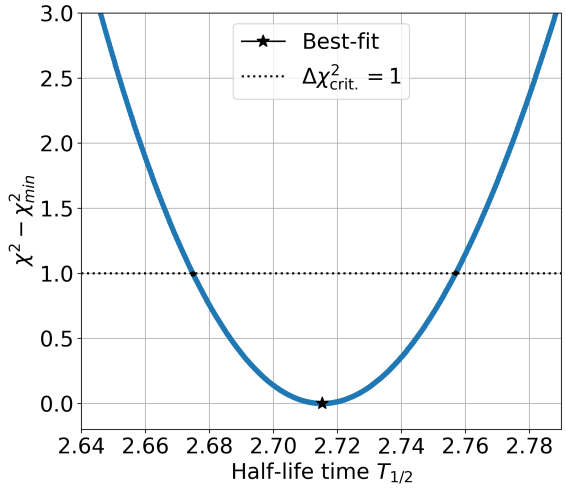

Figure 6.21: Likelihood profile for half-life $T_{1/2}$ fit
The shown profile chi-squared function $\chi^2(T_{1/2}) - \chi^2_{\text{min}}$ is calculated using the least-squares method. For each point of the curve, the decay function given in Equation (6.4) is fitted with a fixed half-life $T_{1/2}$ and a free initial normalization N_0 to the data shown in Figure 6.22a. For the error of the total rate per data point, $\sigma_N = \sqrt{N}$ is used. The best-fit is achieved for $T^{\star}_{1/2} = 2.715$ yrs with a 68.3 % confidence interval between 2.675 yrs and 2.757 yrs.

higher drift, which reaches up to 10 eV in magnitude. The cause of this drift is currently unknown and under further investigation. However, when compared to the energy of the Mn-K_α line at 5.9 keV, the maximum drift accounts for less than 0.2 % of the absolute energy.

To examine the stability of the detector response, the energy resolution ΔE of the Mn-K_α line is investigated as a first approximation. For all pixels and sub-runs, the energy resolution ΔE is extracted from the fitted detector response of the ^{55}Fe spectra. With the obtained fit results, every sub-run is also calibrated individually. Since the energy resolution ΔE varies by around 10 eV across the pixels (see Chapter 6.3) the relative change of the energy resolution $\delta(\Delta E)_{\text{px,run}}$ for every pixel is investigated, it is calculated using Equation (6.6).

$$\delta(\Delta E)_{\text{px,run}} = \Delta E_{\text{px,run}} - \overline{\Delta E_{\text{px,run}}} \tag{6.6}$$

The average energy resolution of one pixel across all sub-runs is denoted as $\overline{\Delta E_{\text{px}}}$. The stability of the relative energy resolution $\delta(\Delta E)_{\text{px,run}}$ is shown in Figure 6.22c. Throughout the measurement period, the energy resolution for all pixels fluctuates by at most 1 eV. This variation is considerably smaller than the energy resolution spread across individual pixels.

As a crosscheck, all sub-runs are stacked before the energy calibration, and the detector response is fitted to the summed spectra for each pixel. As expected, the energy resolution of the stacked spectra for the individual pixels increases by less than 1 eV compared to their best energy resolution in the individual runs. At least in terms of energy resolution, it is acceptable to perform measurements over multiple days without the need for an energy calibration. The resulting slight worsening of the energy resolution in the order of a few eV does not limit the sensitivity of the keV sterile neutrino search with KATRIN [6].

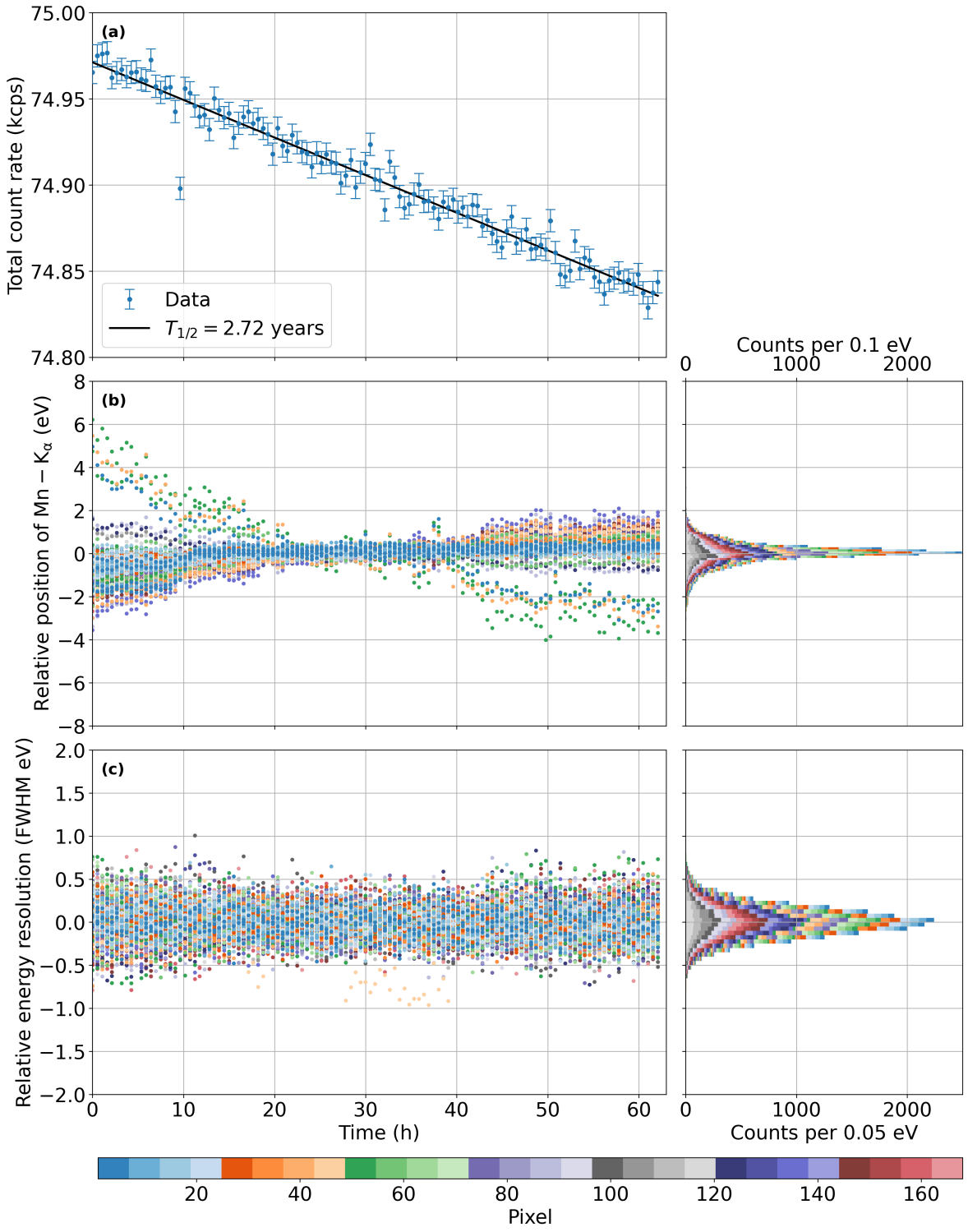

Figure 6.22: Detector stability measurement with an ^{55}Fe source
For the measurement detector S0-166-4 has been used. Each data point corresponds to a sub-run measurement of 30 min. (a) Total measured count rate (blue) summed over all pixels as a function of measurement time. An artificial energy threshold of 2 keV is used. The best fit with a half-life of $T_{1/2} = 2.72^{+0.04}_{-0.05}$ yrs is shown in black. (b) On the left-hand side, the relative shift of the peak position of the Mn-K$_\alpha$ line for every pixel and sub-run is shown. A stacked histogram of all data points is shown on the right-hand side. (c) On the left-hand side, the relative change of the energy resolution of the Mn-K$_\alpha$ line is shown as a function of measurement time. The stacked histogram of all data points is given on the right-hand side. The values for individual pixels in (b) and (c) follow the color coding shown in the color bar at the bottom. Results published in [8].

6.7 Summary

In this work, the detector module S0-166-4 has been commissioned and characterized with X-rays to measure its general performance and prepare the detector module for the integration in the more realistic MAC-E filter environment of the MoS. To this end, a dedicated test bench setup has been developed in which the detector module has been characterized. The detector voltages have been optimized (see Table 6.4) to improve the average energy resolution at the Mn-K_α line of ^{55}Fe from approximately 155 eV FWHM to 144.5 eV FWHM. Furthermore, the temperature dependence of the electronic noise, energy resolution, and calibration have been investigated. It has be shown that at temperatures below −10 °C already a good energy resolution of less than 150 eV FWHM ($n_{\mathrm{ENC}} \leq 11\,e_{\mathrm{rms}}$) can be achieved at the Mn-K_α line. At the temperature of around −34 °C, the energy resolution improves to 144.5 eV FWHM ($n_{\mathrm{ENC}} = 9.9\,e_{\mathrm{rms}}$). Since the energy resolution scales exponentially with the temperature, further cooling the detector system will only marginally improve the energy resolution and this temperature has been used for the measurements in this work, if not noted differently. In addition, it could be shown that the temperature of the ASIC boards ($\Delta T_{\mathrm{ASIC}} \approx 40\,\mathrm{K}$) likely does not affect the performance of the detector module. The measurements performed with an ^{241}Am source, which has many X-ray lines between 7 keV and 60 keV, have demonstrated that the calibration curve varies by less than 40 eV or 0.5 % from linearity and the energy resolution for X-rays follows the Fano statistics. Moreover, the stability of the detector module over multiple days has been investigated. It could be shown that the calibration parameters, measured in the metric of the Mn-K_α line peak position, vary by less than 10 eV and the energy resolution varies by less than 1 eV FWHM over the course of the measurement.

7

CHARACTERIZATIONS IN THE MONITOR SPECTROMETER

To investigate the performance of the detector modules in a more realistic environment similar to the KATRIN beam line (magnetic field, vacuum, high voltage, etc.), the detector module S0-166-4 has been installed into the Monitor Spectrometer (MoS). The general experimental setup of the MoS and the commissioning of the detector module S0-166-4 inside are described in Chapter 7.1 and Chapter 7.2, respectively. An important characteristic of a detector system is its electronic noise curve. It quantitatively connects the different noise contributions in the time domain of the energy filter with the measured energy resolution. This is an important characteristic for the keV sterile neutrino search with KATRIN since it also connects the pileup probability with the measured energy resolution. The measurement of the electronic noise curve is described in Chapter 7.3. In the keV sterile neutrino search with KATRIN, the detector module will measure electrons in the energy range of the tritium decay in the order of a few ten keV. To this end, the detector module has been investigated with the electrons from an implanted ^{83m}Kr source with energies of up to 32 keV as described in Chapter 7.4. Here, the energy resolution is being investigated as a first measure of the performance and homogeneity between pixels of the detector module as described in Chapter 7.4.5. In addition, the detector module has been investigated with quasi-monoenergetic wall electrons with selected energies between 5 keV and 32 keV. The characterizations with the wall electrons are described in Chapter 7.5. At the end, a short summary of the characterizations in the MoS is given in Chapter 7.6.

7.1 Experimental Setup

To characterize the performance of a detector module in a MAC-E filter environment, the detector S0-166-4 has been installed into the KATRIN MoS. The MoS consists of the hardware of the former Mainz neutrino mass experiment [127], a predecessor of the KATRIN experiment. The MoS was initially used as a high voltage monitor for the KATRIN neutrino mass measurements. Information on the assembly and commissioning of the MoS can be found in [66, 128]. More recently, it has been repurposed as a test environment for various hardware upgrades for the KATRIN beam line due to its similarities in terms of ultra-high vacuum requirements, magnetic and electric fields. A picture of the MoS is displayed in Figure 7.1. The setup can be divided into the spectrometer section, the source section, and the detector section.

Spectrometer Section The spectrometer vessel consists of a vacuum-tight stainless steel vessel with a length of 3 m and a diameter of 1 m. It is operated under ultra-high vacuum in the order of 10^{-10} mbar. A set of cylindrical stainless steel electrodes is placed inside the spectrometer vessel to apply the retarding potential U of up to -35 kV. These electrodes form

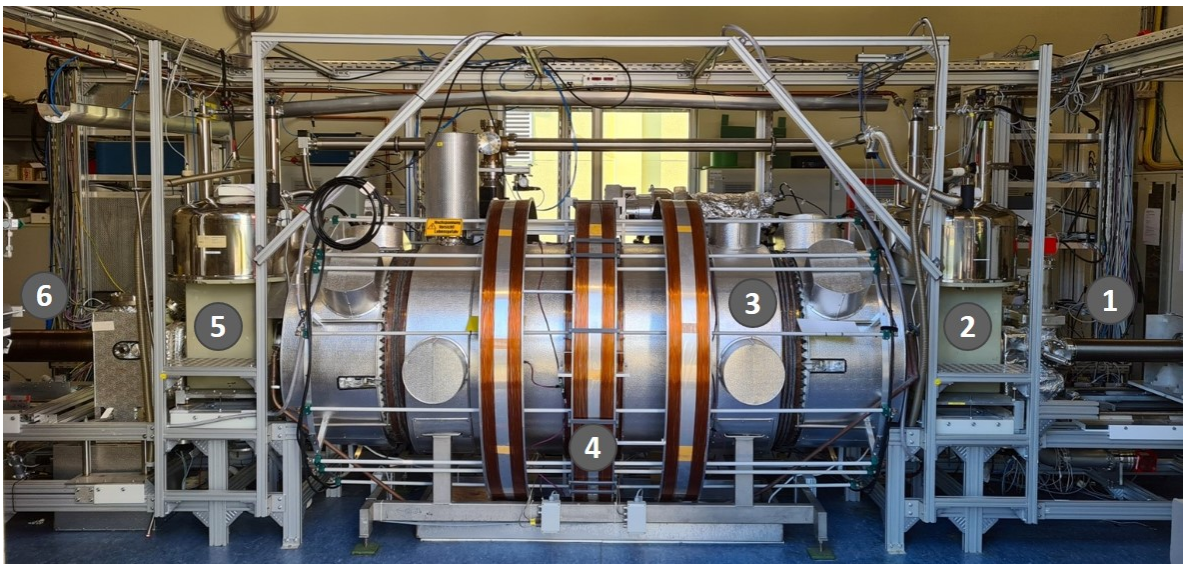

Figure 7.1: Photograph of the monitor spectrometer (MoS)
The detector module is placed inside the detector section (1). Two superconducting magnets (2) and (5) generate the magnetic fields for the MAC-E filter across the spectrometer vessel (3). The magnetic field is additionally shaped by the LFCS and EMCS coils (4) which are installed around the spectrometer vessel. The ^{83m}Kr source is installed inside the source section (6). Adapted from [8].

an electric potential barrier for the electrons inside the spectrometer. The main magnetic field in the spectrometer is created by the two solenoid superconducting magnets with each 36 500 turns. In normal operation, a current of 50 A is applied to the solenoids to create an axially symmetric magnetic field. In the bore of the magnets a maximal field strength of $B_{\mathrm{max}} = 6\,\mathrm{T}$ is present. The minimal magnetic field strength at the analyzing plane has a value of $B_{\mathrm{min}} = 0.35\,\mathrm{mT}$. To further shape the magnetic field near the analyzing plane, the spectrometer is surrounded by two sets of normal conducting coils (air coils). The low field compensation system (LFCS) consists of four cylindrical copper coils that surround the spectrometer vessel and are used to further refine the magnetic field inside the spectrometer. To compensate for the Earth's magnetic field in the order of 50 µT, an additional set of horizontal and vertical air copper coils (silver-white tubes) is placed around the spectrometer. These coils form the earth magnetic field compensation system (EMCS) and create a magnetic field to preserve the axial symmetry of the magnetic fields in the spectrometer. The electric and magnetic field in the normal measurement mode can be seen in Figure 7.2. Using Equation (3.8) an energy resolution of the MoS MAC-E filter of $\Delta E_{18.6\,\mathrm{keV}} \approx 1.08\,\mathrm{eV}$ at the tritium endpoint and $\Delta E_{30.4\,\mathrm{keV}} \approx 1.78\,\mathrm{eV}$ at the ^{83m}Kr L-32 line can be estimated.

Source Section Inside the source section of the MoS up to four electron sources can be installed. They are mounted on a movable 3-axis cross table, which allows for the axial and radial positioning of the different sources. The axial position z can be varied between $-2.40\,\mathrm{m}$ to $-2.12\,\mathrm{m}$ measured from the analyzing plane, which corresponds to a magnetic field strength B_{S} of approximately 0.1 T to 5.5 T. An additional potential U_{S} with respect to ground can be applied to the sources of down to $-1\,\mathrm{keV}$. This has two effects on the energy spectrum of the emitted electrons from the source. On the one hand, the

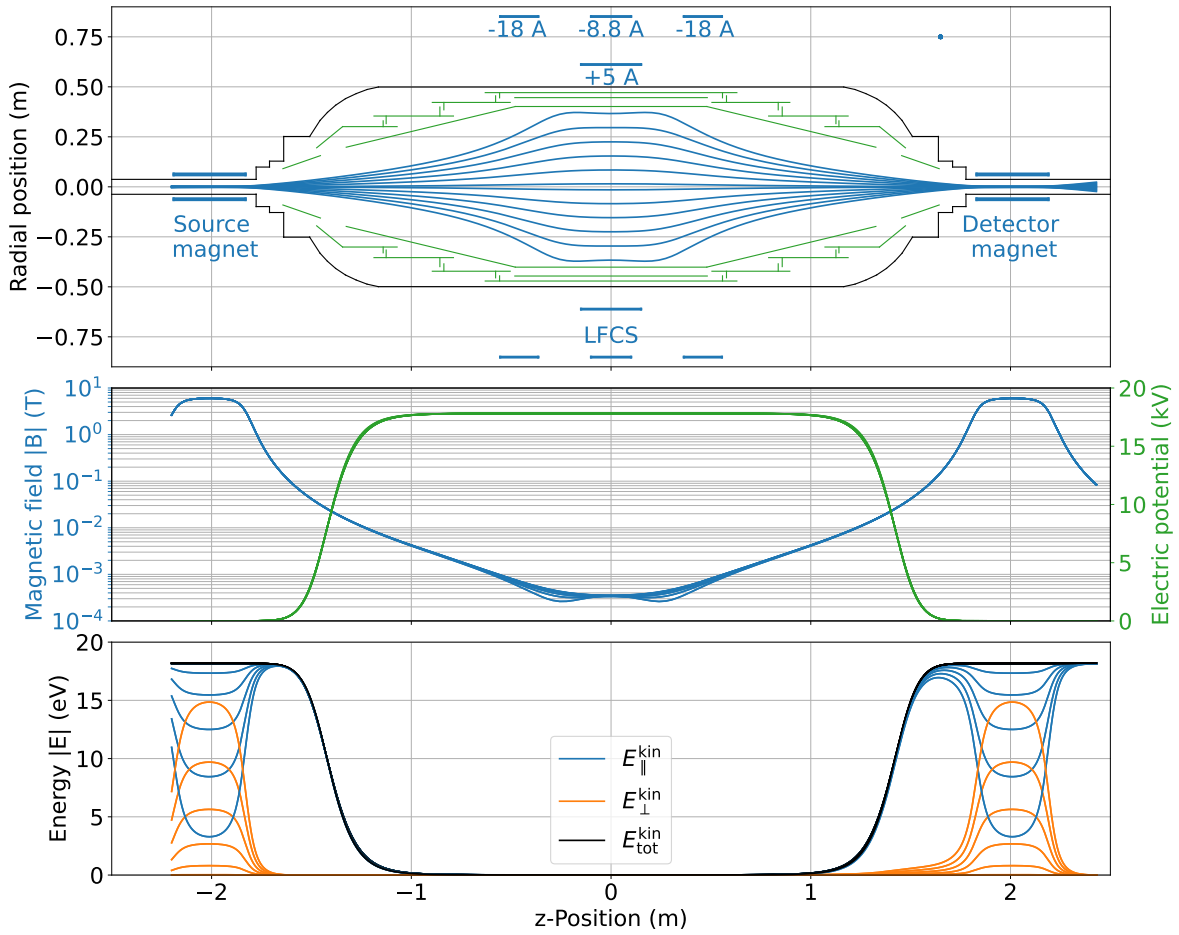

Figure 7.2: EM-fields of the MoS in normal measurement mode
In the plot at the top a cross-section of the MoS along its radial symmetry axis is shown. The black lines illustrate the spectrometer vessel, and the electrodes are shown in green. The two superconducting magnets and air coil system are illustrated by the blue squares around the spectrometer hull. The blue lines inside the spectrometer illustrate the path of electrons generated in the source section along the magnetic field. For illustration purposes, the effect of the Earth's magnetic field is neglected. In the center plot, the magnetic field strength along the different electron paths is shown in blue, and the electric potential is shown in green. For this simulation, the two superconducting magnets are supplied with a current of 50 A corresponding to a magnetic field strength of 6 T. The electric potential on the electrodes is set to 17.82 kV. In the lower plot, the different components of the kinetic energy for electrons with a surplus energy of 8 eV are shown. Each line corresponds to an electron path in the top plot. Figure adapted from [66] and modified with Kassiopeia [129] simulations by D. Hinz.

electron energy E_{Kr} measured in the detector shifts by the applied negative source voltage U_{S} as shown in Equation (7.1).

$$E_{\mathrm{Kr}} = E_{\mathrm{line}} + |e \cdot U_{\mathrm{S}}| - |e \cdot U_{\mathrm{bias}}| \tag{7.1}$$

Here, e denotes the elementary charge, U_{bias} the BC detector depletion voltage, and E_{line} the electron energy of a given $^{83\mathrm{m}}$Kr line. For the measurements in this thesis, the source potential is set to $U_{\mathrm{S}} = -500\,\mathrm{V}$, if not noted differently. On the other hand, the applied negative source potential U_{S} changes the isotropic emission of electrons from the source more towards the analyzing plane, increasing the measured rate at the detector.

Detector Section The detector module S0-166-4 has been installed into the MoS in September 2022. It is placed on a 65 cm long cooling structure as illustrated in Figure 7.3a and moved into the detector section. The connecting flange is mounted on a 3-way cross table, which allows for the radial (x,y) and longitudinal (z) positioning of the detector module. If not noted differently, the SDD chip of the detector module is positioned at $z = 2.425\,\mathrm{m}$ (measured from the analyzing plane[1]) at a magnetic field strength of 100 mT. A refrigerated circulator is connected to the cooling pipes and allows for a sufficient cooling down to $-35\,^{\circ}\mathrm{C}$ at the SDD chip. The stainless steel cap surrounding the front of the detector module (but not the entrance window) protects the SDD chip from mechanical damage. Originally, this cap was designed to reduce the conductance between the detector section and the spectrometer vessel in combination with a matching alignment ring. This ring was installed during the integration of a 47 pixels prototype detector module [113] in front of the detector magnet and sealed the detector side with the outgassing ASIC board from the spectrometer. However, since this alignment ring largely limited the positioning of the prototype detector module and the outgassing of the ASIC boards on the vacuum in the spectrometer was small, it has been decided to only use the cap in the installation of detector module S0-166-4. In this configuration a vacuum level of 10^{-10} mbar in the spectrometer vessel and 10^{-8} mbar in the detector section could be achieved. These values are in the same order of magnitude as design goals for the keV sterile neutrino search with KATRIN [7]. The same electronic readout system described in Chapter 6.1 is being used with the small exception that the in-vacuum FPC cables are 67 cm long instead of 30 cm. The air side electronics consisting of the XGLab biasing and control system and three CAEN VX2740B units, are placed next to the 3-way cross table as illustrated in Figure 7.3b. The location has been selected since these systems are not designed for use in high magnetic fields close to the detector. At the position of the biasing and control system, a low magnetic field in the order of 3 mT was measured. An overview of the magnetic field strength at different positions in the detector section is shown in Figure 7.4.

An ^{55}Fe calibration source is installed inside the detector section at the 6-way vacuum cross directly before the detector magnet. It can be moved on a linear actuator in front of the detector to perform characterization measurements. The distance between the source and the detector module itself can be varied as well. In the course of this work, the distance to the source was around 30 cm. During measurement with electrons, it can be retracted into one side of the 6-way vacuum cross such that it does not influence the measurement.

[1] Conversion from MoS z-position sensor 449-RGI-0-4015 l_{4015} to the actual distance of the detector module to analyzing plane $z = l_{4015} + 1.907\,\mathrm{m}$.

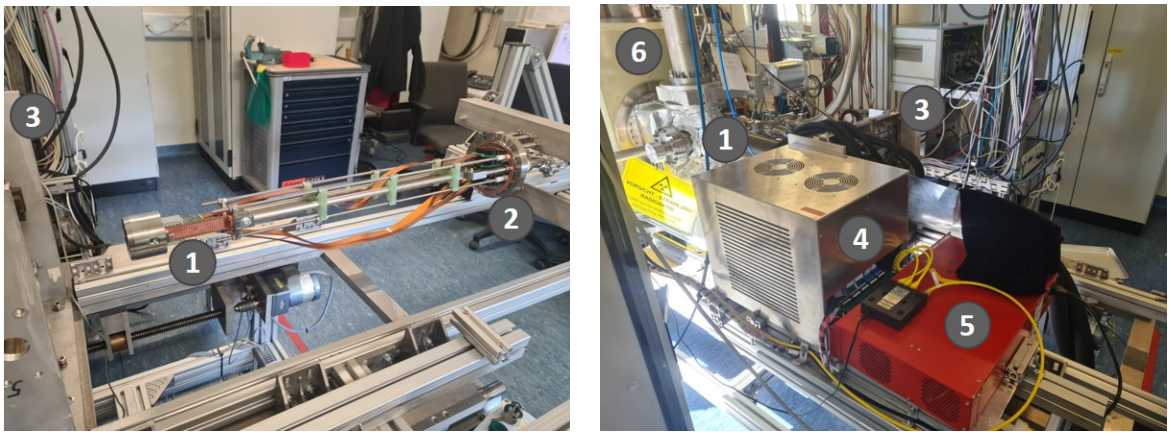

(a) Detector module on cooling structure **(b)** Detector section of the MoS

Figure 7.3: Photograph of monitor spectrometer detector section
Pictures of the installation of the detector module S0-166-4 into the MoS detector section. (a) Detector module (1) installed on the two pipes of the cooling structure in front of the MoS detector section. It is connected to the vacuum feedthrough (2) with four FPC cables with a length of 67 cm. The vacuum feedthrough is pushed onto the detector manipulator cross (3). Around the detector front, a stainless steel vacuum shield is installed. (b) Photograph of the detector section with the detector module roughly installed at the position of (1). On the air side, the detector module is electrically connected to the biasing and control system (4) with 1 m long twisted pair cables. The signals are digitized with three synchronized CAEN VX2740B units (5).

7.2 Detector Module Commissioning with an ^{55}Fe Source

For the commissioning of the detector module, the first measurements in the MoS were performed with an ^{55}Fe source. The isotope ^{55}Fe has been selected since it was also used for many characterizations of the detector module in the X-ray bench test setup described in Chapter 6. Additionally, the energy spectrum of ^{55}Fe is simple with distinct features, which makes debugging of the detector system easier compared to a more complex energy spectrum from, e.g., an ^{241}Am source. The available ^{55}Fe source at the MoS had an activity of around 85 MBq at the time of the installation. As shown in Figure 7.5, this would lead to a total count rate of 1600 kcps, which is around ten times larger than the one measured in the test bench setup. To keep the two setups comparable in terms of count rate, a thin aluminum foil with a thickness of around 80 µm is installed in front of the source to reduce the rate to around 1 kcps.

The measured energy spectra for 165 pixels is shown in Figure 7.6a. The Mn-K$_\alpha$ and Mn-K$_\beta$ lines are clearly visible, as well as the two silicon escape peaks. Since a thin aluminum foil has been placed in front of the ^{55}Fe source, an additional fluorescence line of aluminum can be seen at 1.49 keV [100]. An energy threshold with a value around 500 eV has been achieved. The total count rate on the detector module is around 137 kcps, which is compatible with the expectation given in Figure 7.5. Its dependence on the pixel position is shown in Figure 7.6b. Pixel 04-10 had to be disabled due to distortions on the waveform level. Since the signal readout lines to the pixel were fully functioning in the setup, and waveforms with clear reset pulses could be seen, it is likely that the problem originates from the SDD or ETTORE ASIC supply and biasing voltages or damages inside the SDD chip. All attempts to recover this pixel were not successful and this pixel is disabled for all following measurements.

An average energy resolution of the Mn-K$_\alpha$ line with a value of 147.8 eV FWHM is

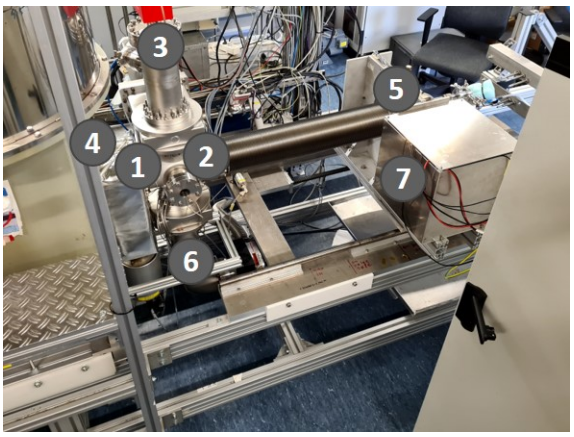

Position	Magnetic field
1	63.34 mT
2	24.22 mT
3	5.82 mT
4	71.34 mT
5	3.05 mT
6	12.76 mT
7	3.27 mT

Figure 7.4 and Table 7.1: Measurement of magnetic field in the MoS detector section
Photograph of the different measurement positions using a magnetometer. The magnetic field strength is measured parallel to the radial symmetry axis of the MoS for a detector magnet current of 50.9 A, which is used for the measurements in this work.

observed with a standard deviation of 2.2 eV and a maximal spread of 11.2 eV across the pixels. Its distribution is shown in the pixel map and histogram of Figure 7.7. These results are very compatible with the best values[2] observed in the bench test setup under optimal lab conditions ($\overline{\Delta E} = (145.5 \pm 2.3)$ eV FWHM with a maximal spread of 8.9 eV, see Chapter 6.3), and show that the detector module is functional in the MoS environment. The slightly higher energy resolution likely originates from a higher parallel noise component observed in the detector module for the measurements in the MoS, see Chapter 7.3.

7.3 Comparison of Electronic Noise Level

The electronic noise curve is measured for the detector module to investigate its robustness against external noise sources, which can originate from a more complex experimental environment like the MoS. In Figure 7.8, the noise curve of the Mn-K$_\alpha$ line of ^{55}Fe is shown for a measurement in the MoS and a reference measurement in the test bench setup. As described in Chapter 6.1.2 the total energy filter time of a trapezoidal filter is $\tau = 2 \cdot \tau_{\mathrm{rise}} + \tau_{\mathrm{gap}}$. In the measurement of the noise curves, only the energy filter rise time τ_{rise} has been varied. The energy filter gap time[3] is kept constant with a value of $\tau_{\mathrm{gap}} = 0.3\,\mu\mathrm{s}$.

For energy filter rise times $\tau_{\mathrm{rise}} \leq 1\,\mu\mathrm{s}$, which are planned to be used in the keV sterile neutrino search with KATRIN, the average energy resolution measured in the two setups are in good agreement with each other. This confirms the detector module's resilience against external electronic noise sources, especially those stemming from the experimental conditions of the MAC-E filter environment in the MoS. As a reference, at an energy filter time of $\tau_{\mathrm{rise}} = 1\,\mu\mathrm{s}$, the average energy resolution in the MoS has a value of 156.0 eV FWHM ($n_{\mathrm{ENC}} = 12.1\,e_{\mathrm{rms}}$) with a maximal spread across all pixels of 13 eV. The best average energy resolution was obtained at energy filter rise time of $\tau_{\mathrm{rise}} = 3\,\mu\mathrm{s}$ with a value of 145.7 eV FWHM and a maximal spread of 10 eV in the MoS. In comparison, in the bench test setup, the best energy resolution was obtained at energy filter rise time $\tau_{\mathrm{rise}} = 5\,\mu\mathrm{s}$

[2] For an energy filter rise time of $\tau_{\mathrm{rise}} = 2\,\mu\mathrm{s}$.
[3] This value has to be chosen for all measurements in this work. The motivation for the value is that the energy filter gap time should definitely be larger than the rise time of the signal pulses (in the order of a few 100 ns [87]) to ensure a correct energy reconstruction.

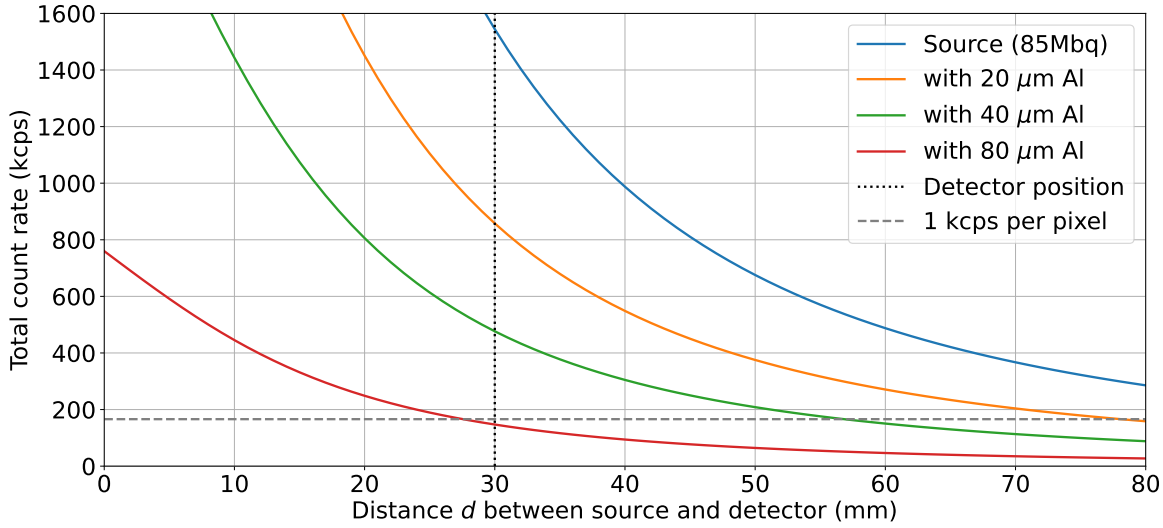

Figure 7.5: Estimation of count rate for the ^{55}Fe source in the MoS
The installed source has an activity of 85 MBq with an emission rate of $e \approx 1.27 \cdot 10^6$ sr/s. The total rate r at the detector is approximated by a cone with a diameter of 40 mm (roughly the SDD chip size). It is given by $r = 2\pi(1 - \cos(\beta)) \cdot e$ using the opening angle of $\beta = \arctan(40\,\text{mm}/d)$ for the cone. The reduced rate r^* due to the absorption of X-rays in the thin aluminum foil with a thickness l, is estimated via $r^* = r \cdot \exp(-l \cdot \alpha_{\text{Al}})$. Here, the attenuation coefficient of aluminum with a value of $\alpha_{\text{Al}} = 2.94 \cdot 10^2/\text{cm}$ for X-ray with an energy of 6 keV is being used [97].

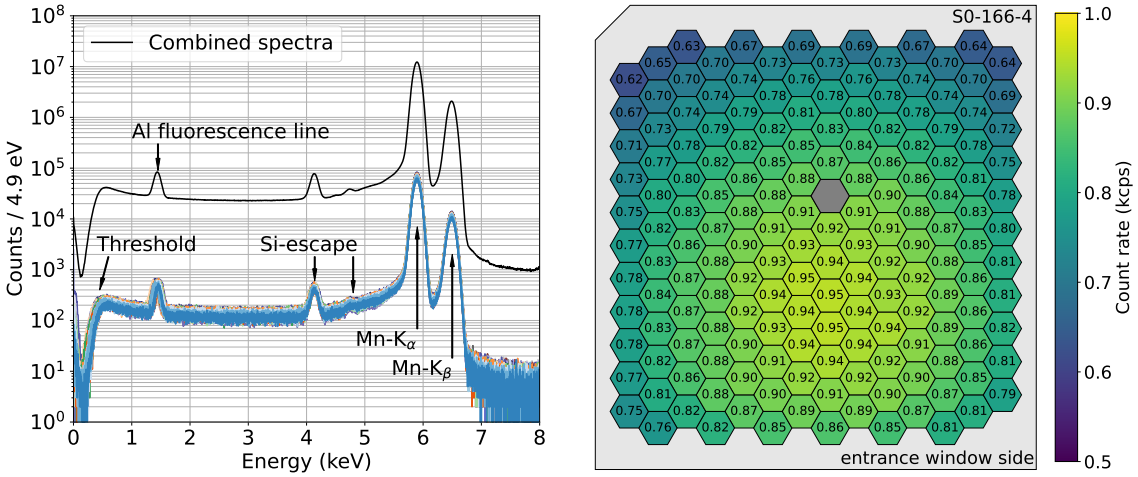

(a) ^{55}Fe energy spectra **(b)** Count rate above 2 keV

Figure 7.6: Commissioning measurement with an ^{55}Fe source in the MoS
(a) Energy spectra of the working 165 pixels. An additional fluorescence line at 1.49 keVis visible due to the thin aluminum foil in front of the source [100]. The color of the individual pixels follow the color map given in Figure D.9a. The combined energy spectrum of all pixels is shown in black. (b) Pixel map of the count rate observed above an artificial threshold of 2 keV with a total count rate with a value of $r* = 137$ kcps. The source is placed approximately 30 mm in front of the detector module. Pixel 04-10 had to be disabled due to distortions on the waveform level.

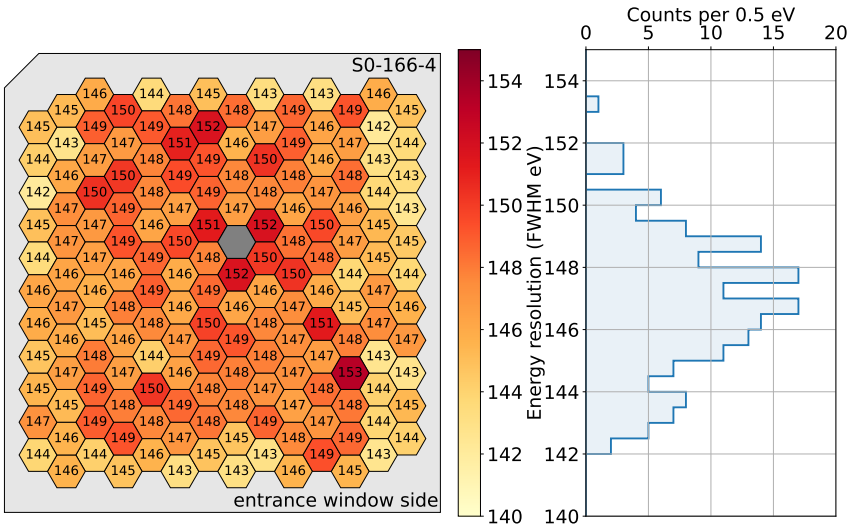

Figure 7.7: Energy resolution at the Mn-K$_\alpha$ line of an ^{55}Fe source
The energy resolution is shown as a pixel map on the left-hand side and as a histogram on the right-hand side. The measurement is performed in the MoS with the detector module S0-166-4. The error on the energy resolution from the fit is below 0.3 eV for all pixels. Each spectrum per pixel contains approximately $3 \cdot 10^6$ counts above the energy threshold at 2 keV. Pixel 04-10 has been disabled due to problems on the waveform level.

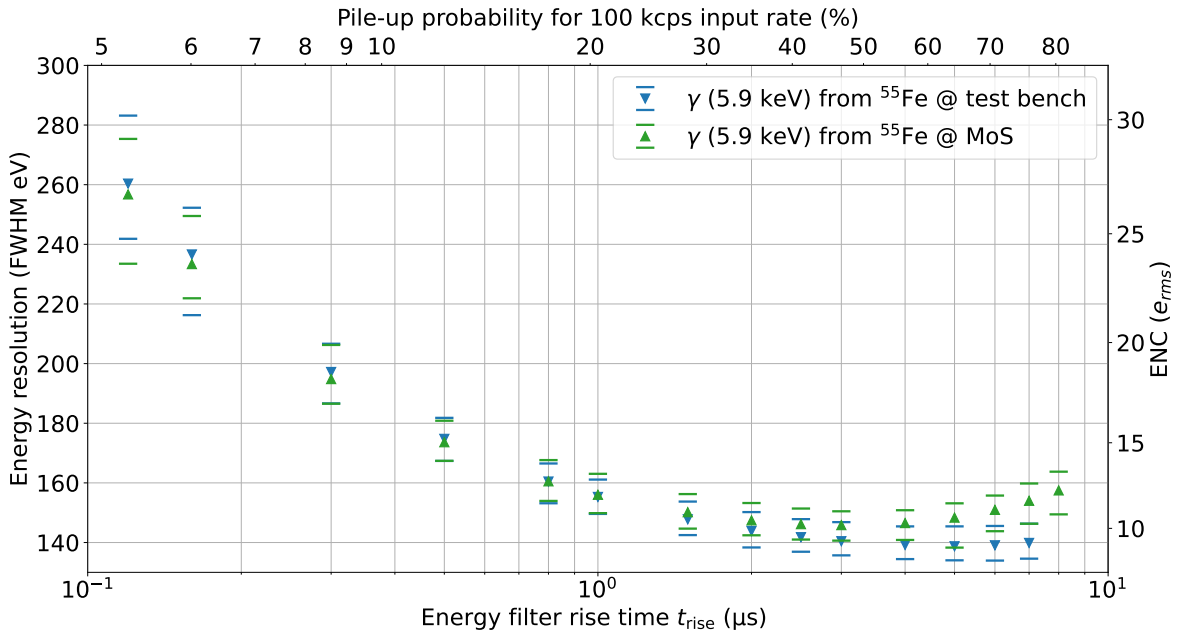

Figure 7.8: Comparison of X-ray noise curve between bench test setup and MoS
Measured energy resolution of the Mn-K$_\alpha$ line from ^{55}Fe sources as a function of shaping time t_{rise}. The average value for all functional pixels is shown by the data points, and the horizontal bars illustrate the minimal and maximal values of all pixels, respectively. For comparison, the measurement in the test bench setup (see Chapter 6.3.1) is illustrated in blue. For all data points, a filter flat top time of $t_{\mathrm{gap}} = 0.3\,\mu\mathrm{s}$ has been used. The total energy filter time is $\tau = 2 \cdot \tau_{\mathrm{rise}} + \tau_{\mathrm{gap}}$. The pile-up probability is calculated for a detector input rate of 100 kcps using Equation (7.2). Results published in [8].

with a value of 138.7 eV FWHM and a maximal spread of 11 eV. The slight difference in energy resolution observed for energy filter rise times $\tau_{\mathrm{rise}} \geq 1\,\mu\mathrm{s}$ is likely caused by an additional parallel noise source only apparent in the MoS. Such a behavior has been observed in another setup independent of this work as well. In this case, the ionization gauge of a vacuum pressure sensor emitted some small amount of light, which was visible in the detector as an increased leakage current. Many different sensors (e.g., vacuum pressure sensors and a residual gas analyzer) and some not perfectly light-tight view-ports are in the near vicinity of the detector module. It is likely that some amount of light is created or enters the experimental setup and causes the observed higher parallel noise component for longer energy filter shaping times τ_{rise}. More investigations on the electronic noise apparent in the detector module can be found in [125].

Furthermore, in the keV sterile neutrino search with KATRIN, the detector system will measure at count rates of up to 100 kcps per pixel. If two events arrive in short succession to each other, which is smaller than half the energy filter time τ, the energy filter can not resolve them individually anymore and reconstructs the (partial) sum of the two energies. For the case of an energy filter rise time with a value of $\tau_{\mathrm{rise}} = 3\,\mu\mathrm{s}$ the pile-up probability is almost 50 %, which drastically reduces the detector efficiency. This pile-up probability for a Poisson process is given in Equation (7.2). A nice explanation of the formula is described in [130] and [131].

$$P(\lambda|r) = 1 - \exp(-r \cdot \lambda) = 1 - \exp(-r \cdot \lambda) \tag{7.2}$$

The decay rate of the process is described as r, and the time window length λ in which the two events arrive is given by the energy filter time[4] τ. Using this formula, the measured noise curve can be used to estimate the trade-off between the energy resolution and the pile-up probability. For an energy filter rise time of $\tau_{\mathrm{rise}} = 1\,\mu\mathrm{s}$ (total energy filter time $\tau = 2.3\,\mu\mathrm{s}$) the probability for pile up is around 20 %. By reducing the energy filter rise time to a value of $\tau_{\mathrm{rise}} = 0.3\,\mu\mathrm{s}$ (total energy filter time $\tau = 0.9\,\mu\mathrm{s}$) the pile-up probability can be more than halved to about 8 %. The trade-off in energy resolution is around 30 eV across the ROI of the keV sterile neutrino search (with post acceleration) as shown in Figure 7.9. Since an energy resolution of up to 500 eV ($n_{\mathrm{ENC}} \approx 50\,e_{\mathrm{rms}}$) does not limit the sensitivity of the keV sterile neutrino search [6] this trade-off is worth considering and is currently under investigation.

[4] For the derivation of the formula, it is assumed that one event happens at a time t_0. The other event has to happen either $\tau/2$ before or after the time t_0 to create a pile-up event. As a consequence, the time window in Equation (7.2) is given by the entire length of the energy filter $\lambda = \tau$.

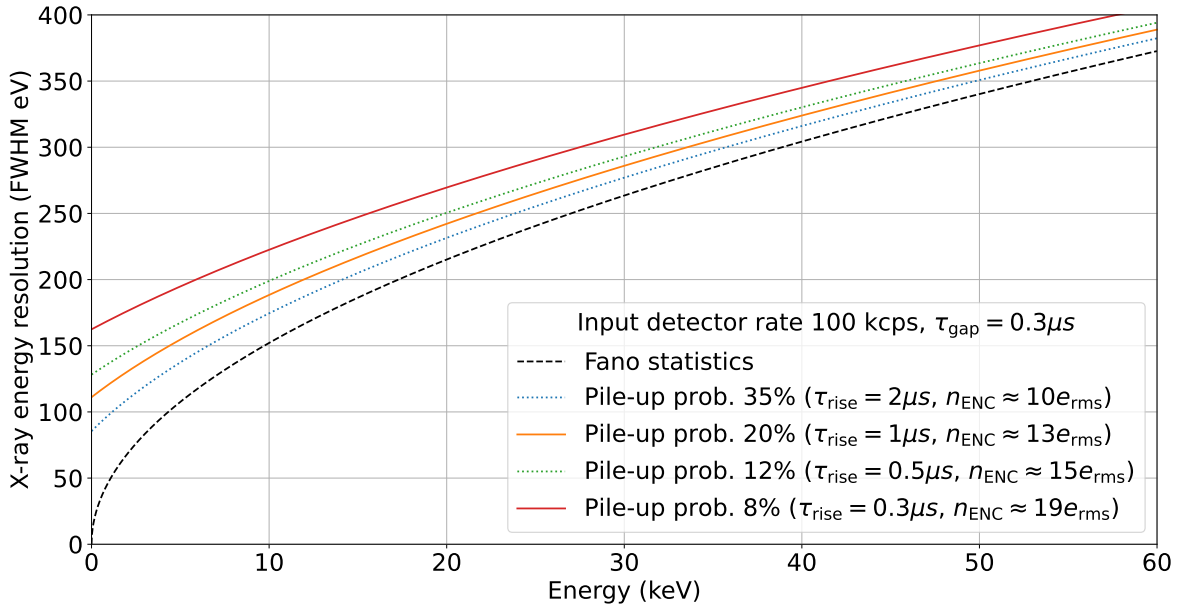

Figure 7.9: Expected X-ray energy resolution for different pile-up probabilities
The different curves are calculated for different ENC value using the formula for the energy resolution given in Equation (4.16). The correlation between the ENC to the energy filter rise time τ_{rise} and, in turn, the pile-up probability is given in Figure 7.8.

7.4 Measurement with the ^{83m}Kr Sources

The first characterizations of a detector module with electrons have been performed with implanted ^{83m}Kr sources in the MoS. The properties of the used implanted ^{83m}Kr sources and their alignment with the detector module are described in Chapter 7.4.1. A typical energy spectrum and a rough estimation of the transmission probability for the measurements with the ^{83m}Kr source are given in Chapter 7.4.2. In Chapter 7.4.3 three different possibilities to calibrate the detector module across the ROI between 0 keV and 35 keV are being discussed. Furthermore, the spectral distortions observed due to damage to the surface of source HOPG-8-13 are discussed in Chapter 7.4.4. The observation of two distinct regions with different values in terms of energy resolution for the detector module S0-166-4 is described in Chapter 7.4.5. These distinct regions can be related to an additional substance on the entrance window as further described in Chapter 8.

7.4.1 *Alignment of the Detector Module with the ^{83m}Kr Source*

To characterize the detector module with electrons and investigate its detector response in an MAC-E filter environment, two implanted ^{83m}Kr sources have been used. These sources emit multiple quasi-monoenergetic internal conversion electrons in the de-excitation of the meta-stable isotope ^{83m}Kr ($T_{1/2} = 1.83\,\mathrm{h}$ [132]). To produce these solid sources the parent isotope ^{83}Rb ($T_{1/2} = 86.2\,\mathrm{d}$ [132]) is ion-implanted into a highly-oriented pyrolitic graphite (HOPG) carrier substrate. ^{83}Rb decays via EC and results in most of the cases in the meta-stable isomer ^{83m}Kr as illustrated in Figure 7.10. This meta-stable state further decays by a cascade of nuclear γ-transitions with energies of 32.2 keV, and 9.4 keV. These transitions can also produce mono-energetic electrons via internal conversion. Here, the decay energy is transferred to a shell electron, which leaves the nucleus. Its energy is reduced by the binding energy of the corresponding shell from which it is emitted. The energies of the emitted electrons that are used in this work are listed in Table 7.2. Since

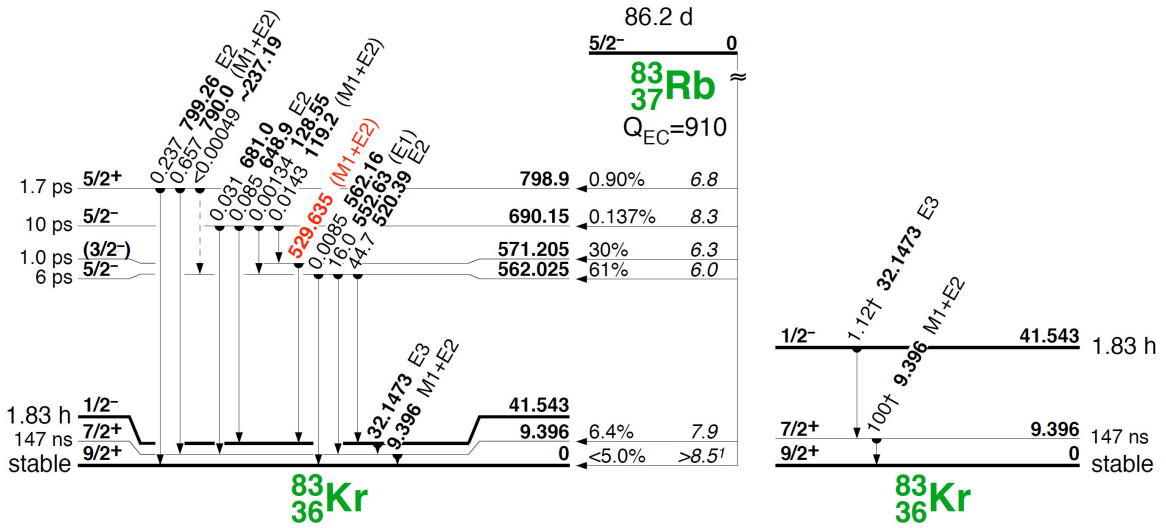

Figure 7.10: Decay scheme of ^{83}Rb to ^{83m}Kr
On the left hand side, the decay scheme of ^{83}Rb to the different excited and stable state of ^{83}Kr is illustrated. The decay is a pure electron capture process with the branching ratio of 77.9 % into the meta-stable isomeric state ^{83m}Kr ($T_{1/2} = 1.83$ h). The right-hand side emphasizes the 32.2 keV, and 9.4 keV γ transitions of the meta-stable state, that generate the internal conversion electrons with energies between 7 keV to 33 keV. Figure taken from [133], which is an adaptation from [132].

many of these electron lines overlap inside the detector resolution (in the order of 300 eV FWHM at 30 keV), the weighted average by intensity is calculated. Therefore, if a line is denoted as, e.g., the L-32 line of ^{83m}Kr , it describes the average across the sub-lines L_1, L_2 and L_3 corresponding to the 32.2 keV gamma transition. For the measurement in this work, the sources HOPG-8-13 ($\approx$ 5 MBq in September 2022) and HOPG-8-14 ($\approx$ 3 MBq in September 2022) have been used[5]. Their corresponding intensity profile has been measured with a Timepix charge-coupled device (CCD) detector just before the installation into the MoS source section and is depicted in Figure 7.11. If not noted differently, the HOPG-8-14 source has been used for the measurements in this thesis since the surface of the HOPG-8-13 source showed mechanical damages which lead to distortions of the energy spectrum, see Chapter 7.4.4. More details on the sources and their production can be found in [66, 133, 134].

The two ^{83m}Kr sources are installed near the source magnet inside the source section on a movable 3-axis cross table. The spatial separation between the two sources is large enough that only one source illuminates the detector module at a time. As a first step, the electron flux emitted from the HOPG-8-14 source has been aligned with the position of the detector module. For this investigation, the retarding potential has been set to a value of $U = 30.2$ keV, which is close to the energy of the L-32 line. A typical count rate observed during this alignment process for the HOPG-8-14 source is shown in the pixel map seen in Figure 7.12a. The image of the bean-shaped active area of the source is clearly visible. Since the magnetic flux $\Phi = A \cdot B$ is conserved in an MAC-E filter environment like the MoS, the size of the electron flux tube seen on the detector module can be calculated as a function of magnetic field strength at the source B_S. Using Equation (3.10) and assuming a diameter

[5] Elog entry: https://iap-neu-katrin.iap.kit.edu/elog/monitor-spectrometer/1369

Table 7.2: Conversion electrons from the ^{83m}Kr source
The listed values correspond to the 32.2 keV γ-decay of the isotope. The weighted average of the L and M lines is calculated using the intensity per decay. An extended list of the electron lines is given in the appendix in Table C.7. Values taken from [134].

Line	Energy (eV)	Intensity per decay (%)	Weighted average (eV)
	γ transition with 32 151.6 eV		
K	17824.2(5)	24.8(5)	
L_1	30226.8(9)	1.56(2)	
L_2	30419.5(5)	24.3(3)	30446.1
L_3	30472.2(5)	37.8(5)	
M_1	31858.7(6)	0.249(4)	
M_2	31929.3(5)	4.02(6)	
M_3	31936.9(5)	6.24(9)	31933.9
M_4	32056.4(5)	0.0628(9)	
M_5	32057.6(5)	0.0884(12)	
N_1	32123.9(5)	0.0255(4)	
N_2	32136.7(5)	0.300(4)	32136.7
N_3	32137.4(5)	0.457(6)	

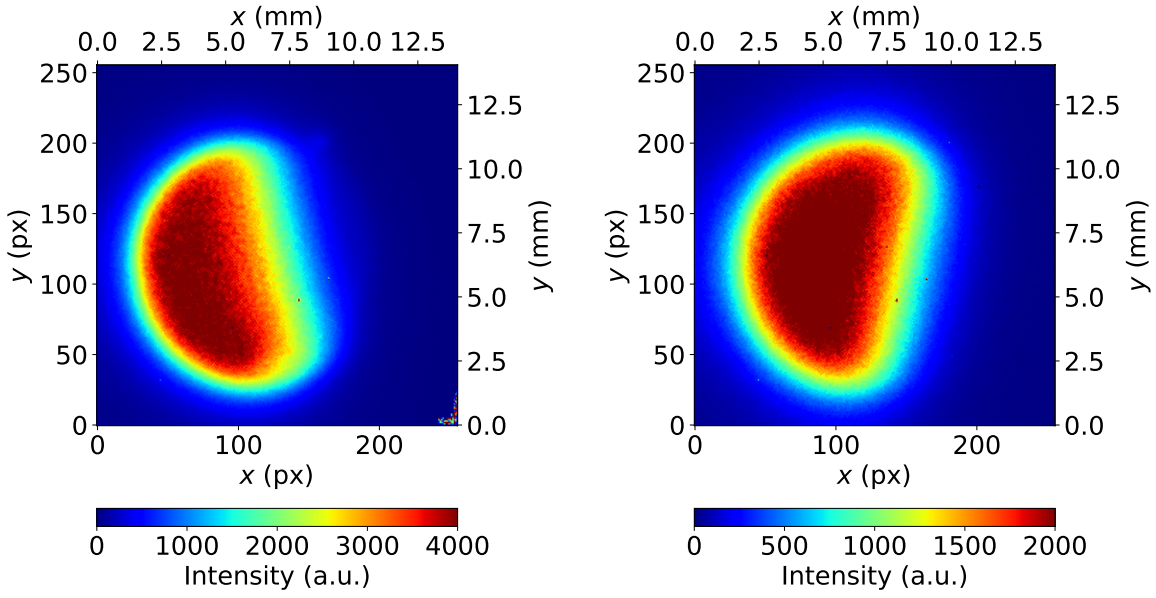

(a) HOPG-8-13 structure **(b)** HOPG-8-14 structure

Figure 7.11: Intensity profile of the solid ^{83m}Kr sources
The solid ^{83m}Kr sources are implanted into a HOPG substrate with a diameter of 12 mm. Before the installation into the MoS the two sources have been measured with a 256 pixels × 256 pixels Timepix CCD detector with a pixel size of 55 µm × 55 µm. The intensity profile measured in September 2022 is shown as a color gradient with the corresponding scale on the bottom. (a) The activity of the HOPG-8-13 source is in the order of 5 MBq. (b) The activity of the HOPG-8-14 source is lower with approximately 3 MBq. For most of the measurements in this thesis, the HOPG-8-14 source has been used since the HOPG-8-13 source showed artifacts in the electron spectrum as described in Chapter 7.4.4.

of $d_S \approx 10\,\text{mm}$ for the active area of the ^{83m}Kr sources the formula can be converted to Equation (7.5).

$$\Phi = A_D \cdot B_D = A_S \cdot B_S \tag{7.3}$$
$$\Leftrightarrow \pi(d_D/2)^2 \cdot B_D = \pi(d_D/2)^2 \cdot B_D \tag{7.4}$$
$$\Leftrightarrow d_D = \sqrt{\frac{B_S}{B_D}} \cdot d_S \tag{7.5}$$

Taking the magnetic field strength with a value of $B_D = 100\,\text{mT}$ at the detector module and $B_S = 900\,\text{mT}$ at the source into account, the image seen on the detector should roughly have a diameter of 30 mm or 10 pixels. This estimation agrees very well with the image seen in the count rate pixel map in Figure 7.12a.

To illuminate the entire detector module with electrons, the ^{83m}Kr source is moved further into the source magnet. An intermediate measurement at 1.8 T and the final (near) position at the maximal source magnetic field of 3.6 T are shown in Figure 7.12b and Figure 7.12c, respectively. The final source position has also been optimized in its radial position to maximize the absolute count rate on the detector and has been used for all measurements in this thesis if not noted differently.

7.4.2 *Typical Energy Spectra Measured with the ^{83m}Kr Sources*

Typical energy spectra measured with the HOPG-8-14 source are illustrated in Figure 7.13. For the measurement with a retarding potential of $U = 30.2\,\text{kV}$, shown in Figure 7.13b, the two peaks correspond to the L-32 and M-32 lines and are clearly visible. The silicon escape peak corresponding to the L-32 is visible at around 29.1 keV while the silicon escape peak corresponding to the M-32 line (energy around 30.6 keV) is superimposed to the main peak of the L-32 line. For the analysis in this work, the first electron line above the retarding potential is fitted with the full electron response described in Chapter 4.7. Any other line at higher energies is fitted with a reduced detector response to extract the energy resolution and the maximum peak position. It is composed of a Gaussian function $G(E|\mu_1, \sigma, N_G)$ and one exponential step function $D(E|\mu, \sigma, \beta_1, N_{D1})$ which is fitted to the peak in a narrow region of 400 eV below and 350 eV above the maximum of the peak.

For all measurements, the retarding potential U is set to a value of approximately 500 V below the electron energy of the investigated line, to ensure adiabatic transport and minimize effects originating from the MAC-E filter, like back-reflection at the retarding potential U. As a quick cross-check, if the adiabatic transport is preserved, the transmission probability of the M-32 line in comparison to the L-32 line is investigated. To this end, the measurement at a retarding potential with a value of $U = 30.2\,\text{kV}$ is used. Here, the electrons of the M-32 line have a surplus energy of around 2 keV. As a rough estimate of the measured intensity of lines, the maximum of each peak in the spectrum is taken. The ratio between the two peaks, corrected for the intensities of the decay (see Table 7.2) is shown in Figure 7.14a. In the lower center of the SDD chip, the ratio between the two lines is one-to-one, while it reduces to about 80 % to the outer edges. It is important to note that the maximum peak height is only a very rough estimation of the total count rate observed for the electron lines. Therefore, these results only show the order of magnitude of the transmission. For the measurements in this thesis, with a surplus energy of 500 eV, it is expected that the transmission is higher than the results shown in Figure 7.14a and is very close to 100 % across the entire detector. For comparison, the same transmission probability

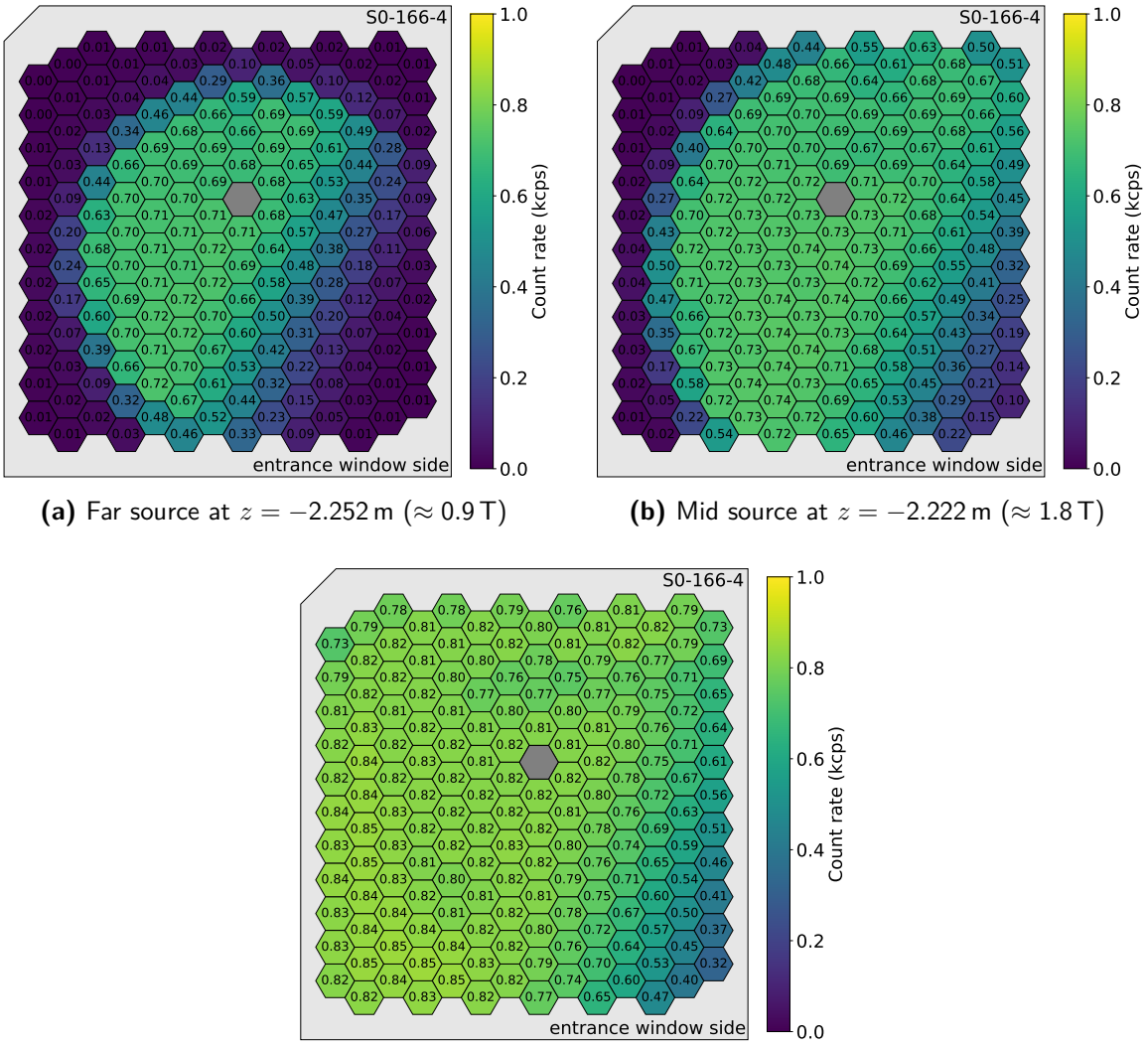

(a) Far source at $z = -2.252\,\mathrm{m}$ ($\approx 0.9\,\mathrm{T}$)

(b) Mid source at $z = -2.222\,\mathrm{m}$ ($\approx 1.8\,\mathrm{T}$)

(c) Near source at $z = -2.182\,\mathrm{m}$ ($\approx 3.6\,\mathrm{T}$)

Figure 7.12: Measured count rate for alignment of source position
For the measurement the $^{83\mathrm{m}}$Kr source HOPG-8-14 has been used with a retarding potential of $U = 30.2\,\mathrm{kV}$. The source position is adjusted in its z-direction toward the source magnet to increase the magnetic field at its position. In the different pixel maps (a), (b), and (c), three typical measurements at different source positions are shown. An artificial energy threshold of approximately 2 keV has been used to calculate the count rate for the individual pixels.

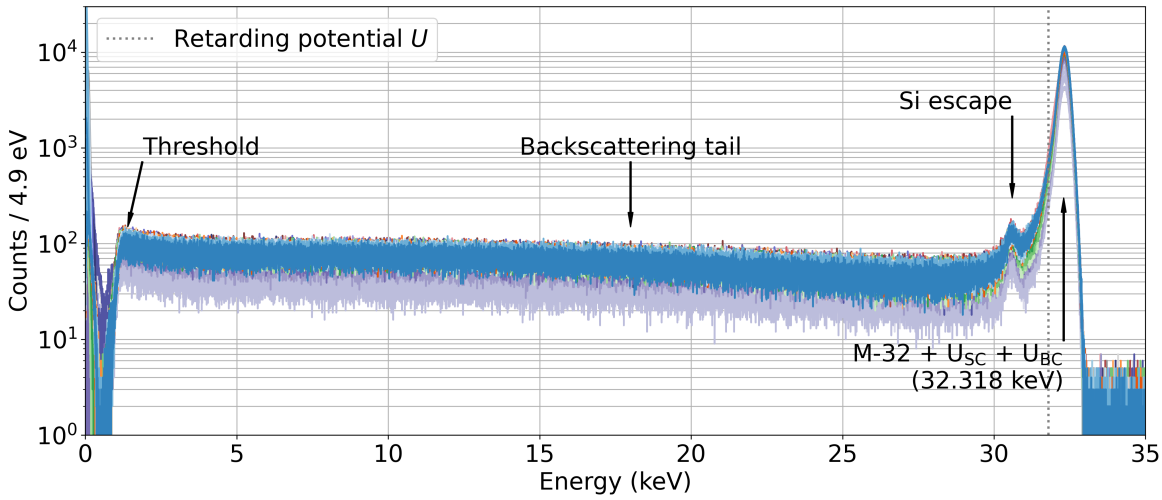

(a) Retarding potential at $U = 31.8\,\mathrm{kV}$

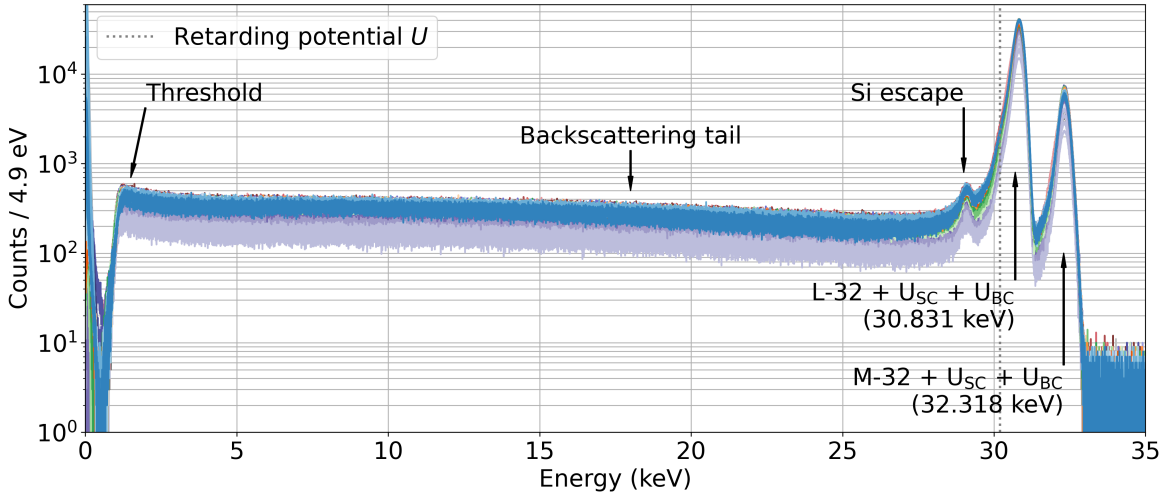

(b) Retarding potential at $U = 30.2\,\mathrm{kV}$

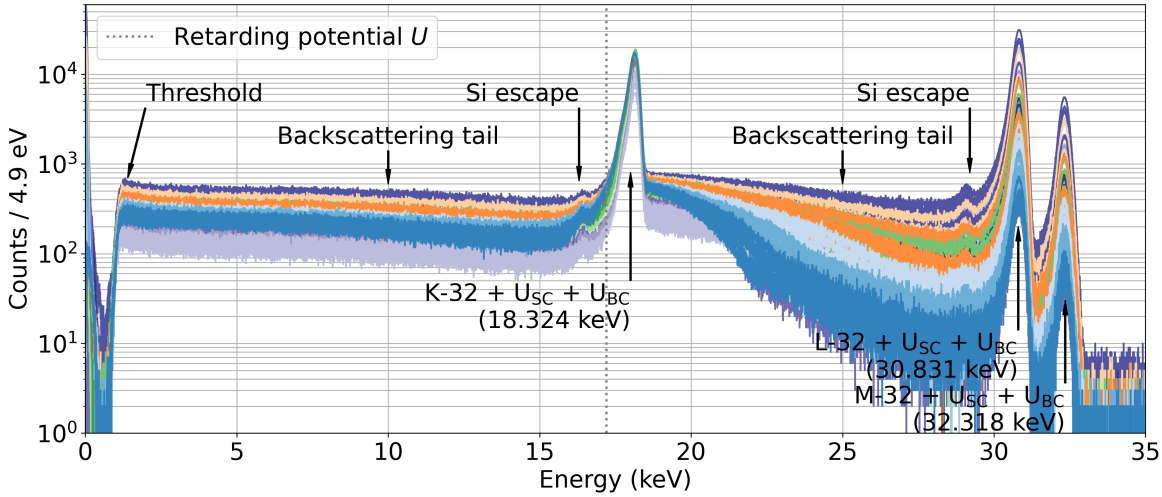

(c) Retarding potential at $U = 17.8\,\mathrm{kV}$

Figure 7.13: Typical ^{83m}Kr energy spectrum at different retarding potentials
In the energy spectra the working 165 pixels are shown. In the measurements, the retarding potential U is set around 500 V below the ^{83m}Kr line, which is investigated to ensure adiabatic transport along the magnetic field lines. The source potential was set to a value of $U_\mathrm{S} = -500\,\mathrm{V}$ and the depletion voltage BC to a value of $U_\mathrm{BC} = -115\,\mathrm{V}$. The pixels follow the color coding shown in Figure D.9a.

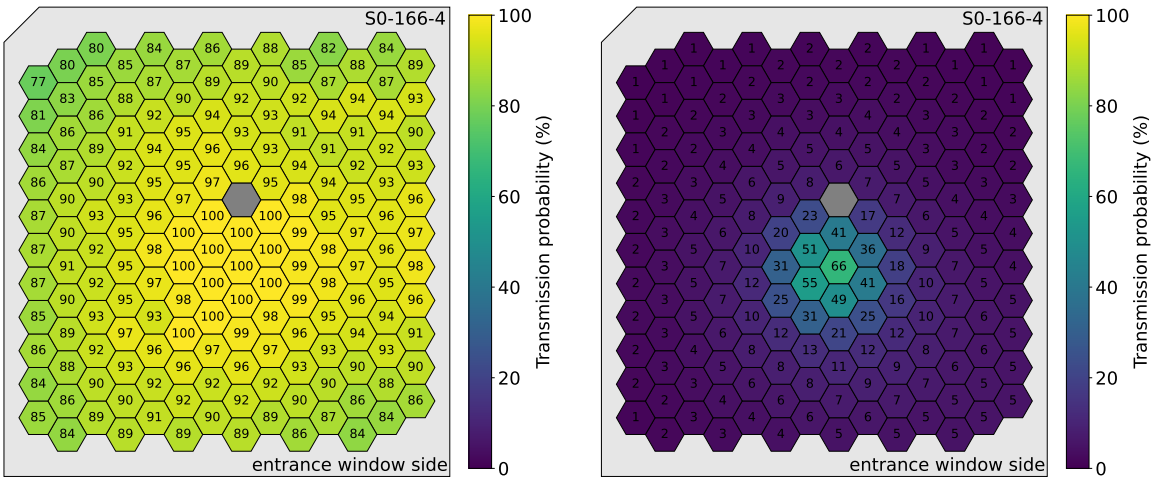

(a) Transmission L-32 to M-32 line ($U = 30.2\,\mathrm{kV}$) **(b)** Transmission K-32 to L-32 line ($U = 17.8\,\mathrm{kV}$)

Figure 7.14: Estimation of transmission probability for electrons in the MoS
To estimate the transmission probability the ratio between the maximum of the peaks to the corresponding lines is taken. For the calculation of the transmission probability, the decay intensities of the different lines are taken into account, as listed in Table 7.2. (a) Transmission probability between the L-32 and M-32 for a retarding potential of $U = 30.2\,\mathrm{kV}$, with a surplus energy of 0.5 keV and 2 keV, respectively. (b) Transmission probability between the K-32 and L-32 for a retarding potential of $U = 17.8\,\mathrm{kV}$, with a surplus energy of 0.5 keV and 13 keV, respectively.

can be calculated for the ratio between the K-32 and L-32 lines with a surplus energy of 13 keV. As seen in the transmission ratio in Figure 7.14b and also in the energy spectrum in Figure 7.13c, the transmission probability for the L-32 is drastically reduced, especially towards the outer edges of the detector. More detailed investigations on the transmission probability are out of the scope of the thesis. To check the transmission probability as a function of the surplus energy, a dedicated measurement could be performed, where the count rate of one of the $^{83\mathrm{m}}$Kr lines is monitored as a function of surplus energy.

7.4.3 *Energy Calibration in the MoS*

For the measurements performed in the MoS, the detector module has to be calibrated across a ROI between 0 keV and 35 keV, to cover all mono-energetic electrons measured in this thesis. As described in Chapter 4.7 an energy calibration with X-rays would be beneficial compared to a calibration with mono-energetic electrons since it is almost independent of any detector effects, like the reduced CCE at the entrance window. However, for the measurements in this work, the sole X-ray source available in the MoS is the ^{55}Fe source in the detector section[6]. As an alternative, the calibration parameters observed in the linearity measurement with ^{241}Am in the test bench setup, see Chapter 6.4, could be applied. The last method investigated in this work uses the M-32 line of the quasi mono-energetic electrons emitted from the $^{83\mathrm{m}}$Kr source as a calibration point. To check the feasibility of the different energy calibration methods, the deposited energy of mono-energetic electrons emitted from the $^{83\mathrm{m}}$Kr source and the spectrometer surface (wall electrons) are investigated. Here, the maximum of the main peak μ_{max} in the detector response is taken as a measure for the deposited energy. This value is an alternative measure for the deposited energy in the detector,

[6] In theory, also the installed $^{83\mathrm{m}}$Kr sources emit X-ray but due to the distance to the detector in the order of 4 m the rate is negligible.

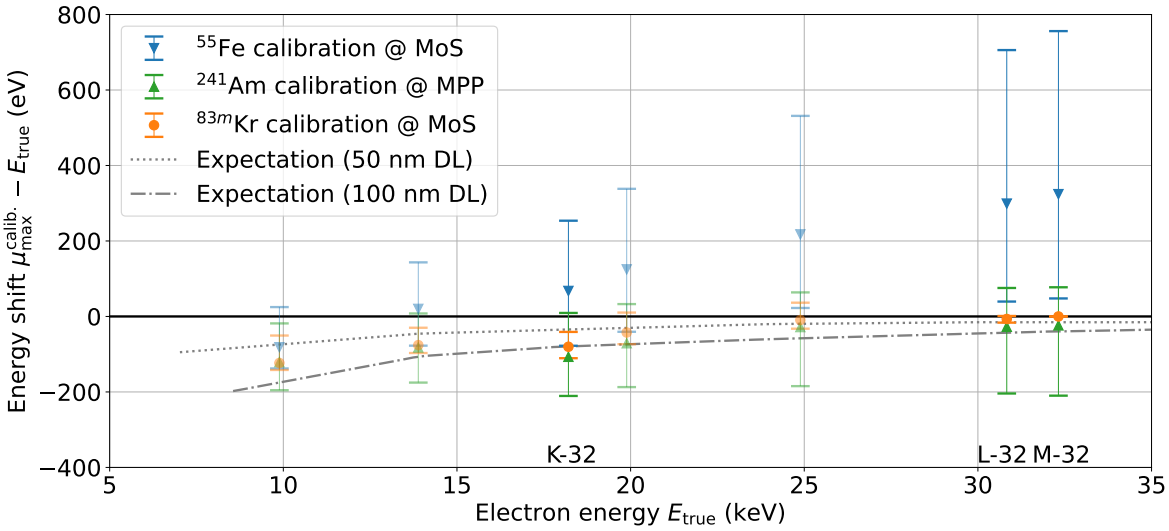

Figure 7.15: Comparison of deposited electron energy for different calibration method
In the figure the energy shift between the deposited energy $\mu_{\mathrm{max}}^{\mathrm{calib.}}$ for different calibration methods and the initial electron energy E_{true} is illustrated. As a measure for the deposited energy, the position of the peak maximum μ_{max} in the electron response is being used. The different calibration methods are applied to convert the measured peak position μ_{max} from units of lsb to eV, here denoted as $\mu_{\mathrm{max}}^{\mathrm{calib.}}$. The solid data points correspond to the different ^{83m}Kr electron lines, while the semi-transparent data points correspond to the measurements of wall electrons at different energies, see Chapter 7.5. The deposited energy of the electrons $\mu_{\mathrm{max}}^{\mathrm{calib.}}$ is expected to be smaller than their initial energy E_{true}. Based on simulations, this behavior is illustrated by the grey lines for different entrance window thicknesses [82]. These curves are only a rough estimation since a simplified step-like dead layer model is being used in the simulations. A more realistic model can be found in [96].

compared to the position of the Gaussian function μ in the detector response. However, since the main peak for electrons is not dominated by the Gaussinan function, and its position fluctuates especially for lower incident energies, the position of the peak maximum μ_{max} has been used as a measure of the deposited energy in this analysis. The energy shift between the incident energy E_{true} and the measured energy μ_{max} is shown for the different calibration methods in Figure 7.15. Since the electrons lose, on average, some energy due to entrance window effects (see Chapter 4.7), the peak position of the maximum μ_{max} is shifted to lower energies. This expected energy shift is estimated based on simulation for the simplified dead-layer model with a thickness of 50 nm and 100 nm [82] and is illustrated by the grey lines.

Calibration with ^{55}Fe source in MoS The first possible calibration method investigated in this thesis uses the ^{55}Fe source installed in the detector section of the MoS. In principle, the two Mn-K$_\alpha$ and Mn-K$_\beta$ lines can be used to calibrate the detector module. However, these lines are in near proximity to each other at energies of 5.9 keV and 6.5 keV and do not cover the ROI of up to 35 keV. As expected, the calibration for higher energies becomes unreliable. This can be seen in Figure 7.15 by the fact that the measured deposited energy μ_{max} is much larger than the initial energy $E_{\mathrm{true}}^{\mathrm{calib.}}$ at higher energies. The opposite behavior would be expected for electrons, as illustrated by the simulations (grey lines). For electrons at energies of 32.3 keV (^{83m}Kr M-32 line), the difference is up to 750 eV, which is insufficient for the investigations performed in this work.

Application of ^{241}Am Calibration Parameters measured in the Test Bench Setup As shown in Chapter 6.4, the isotope ^{241}Am has many mono-energetic X-ray lines across an energy range between 10 keV and 60 keV and would provide an excellent energy calibration for the detector module in the MoS. However, in the scope of this thesis, no ^{241}Am source could be installed inside the detector section. The sole calibration measurement for the detector module S0-166-4 with ^{241}Am was performed in the test bench setup at the MPP laboratories. They have been applied to the electron measurements to check if these calibration parameters could be, in principle, transferred to the MoS setup. As shown in Figure 7.15, for most of the pixels, the deposited energy μ_{max} is smaller than the initial energy E_{true}, which makes it more feasible than the ^{55}Fe calibration method. However, the maximal spread between pixels is more than 300 eV at higher energies, which is much larger than could be explained by entrance window effects or the uncertainty of the calibration parameter, see Chapter 8 and Chapter 6.4, respectively. It is likely that the calibration parameters between the two measurements have slightly changed due to the modifications performed on the electronic readout chain, which could explain this larger spread between pixels. This calibration agrees better than the one using the ^{55}Fe source. However, to be on the safe side, a calibration method that can be repeated in the MoS is preferred. As a note, putting this observation into perspective for the keV sterile neutrino search with KATRIN, it might be feasible to roughly calibrate the detector modules in an external test stand before the installation. However, to be on the safe side, a precise calibration in the final experimental environment is required for the final measurement.

Calibration using the M-32 line of $^{83\mathrm{m}}$Kr In the end, to have a calibration performed inside the MoS, which is also accurate at higher energies, the electrons from the M-32 line of the $^{83\mathrm{m}}$Kr source have been used. From the linearity measurement described in Chapter 6.4, it can be assumed that the calibration curve is linear and intersects with the origin at 0 lsb and 0 eV. The uncertainty of this assumption is estimated to be in the same order of magnitude as the maximal variation of the offset parameter of around 30 eV. As a second calibration point, the maximum of the electron peak μ_{max} of the M-32 line of the $^{83\mathrm{m}}$Kr source are being used since they have the highest energy measured in this work. Using the highest possible electron energy minimizes the effects related to the entrance window, which shifts the maximum of the electron peak μ_{max} to smaller energies. This shift can be roughly estimated via simulations to be in the order of 50 eV for an electron energy of 30 keV, assuming a simplified entrance window with a conservative dead-layer thickness of 100 nm[7]. In the scope of this work, this correction to the energy has not been applied to the calibration since it varies across the detector and is only used as an order of magnitude for the uncertainty of the energy calibration at higher energies. Taking more electron lines at lower energies into account[8] would worsen the energy calibration since their peak positions are shifted more to lower energy values and, therefore, do not lie on the expected linear calibration curve anymore.

Out of the three calibration methods discussed in this work, the usage of the M-32 line showed the best results with the smallest expected uncertainty in the order of 50 eV and is used for all measurements if not noted differently. In theory, also the electrons emitted from the spectrometer wall (wall electrons) can be used to calibrate the detector module similar to the method of the M-32 line of $^{83\mathrm{m}}$Kr. However, as shown in Chapter 7.5, not all pixels of the detector module could be illuminated at a sufficient rate, and therefore

[7] This value of the entrance window thickness has been chosen as an upper limit to estimate the electron shift since the entrance window thickness of the detector module S0-166-4 installed in the MoS is not homogeneous with values between 50 nm to 100 nm, see Chapter 7.4.5.

[8] Without correcting the energy shift via simulation.

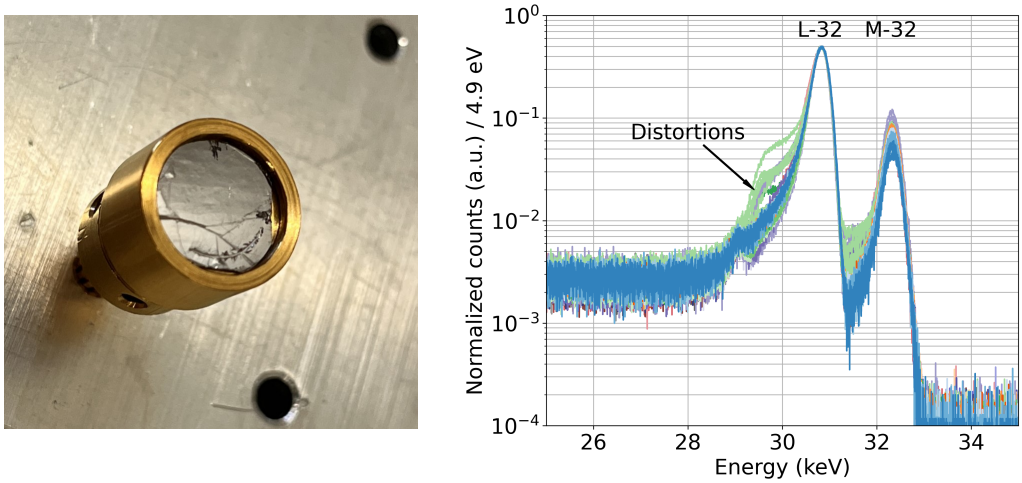

(a) HOPG-8-13 source **(b)** Distortions in energy spectra

Figure 7.16: Distortions in energy spectrum of HOPG-13-8 source
(a) Photograph of the HOPG-8-13 source. The active area of the source is on the silver reflecting carrier substrate, which shows unintentional damages and cracks. (b) Energy spectrum measured for the illuminated 146 pixels pixels at a retarding potential of $U = 29.5\,\mathrm{kV}$ and a source position of $z = -2.23\,\mathrm{m}$ ($B_\mathrm{S} \approx 2\,\mathrm{T}$). The individual spectra are scaled by the maximum of the peak of the L-32 line. The illuminated pixels are illustrated in Figure 7.17a. The pixel follows the color coding shown in Figure D.9a.

this method has not been used. Since the calibration with electrons has its drawbacks, for the next measurement campaign at the MoS and in the future for the installation into the KATRIN beamline, it would be beneficial to install an additional X-ray source, like an ^{241}Am source, with many mono-energetic lines across the ROI.

7.4.4 *Spectra Distortions due to Damaged Surface of HOPG-8-13 Source*

The second ^{83m}Kr source, which has been installed in the MoS, is the source HOPG-8-13. As seen in the photograph in Figure 7.16a, the surface of the source is severely damaged. Since the electrons of the source are emitted on or near the surface of the source, the effect of the damage on the energy spectrum is briefly investigated. In Figure 7.16b, a measurement of the energy spectrum at a retarding potential of $U = 29.5\,\mathrm{kV}$ is shown for all illuminated pixels. For a better comparison between the pixels, the energy spectra are scaled to the maximum peak height of the L-32 line. In this measurement the source was positioned at $z = -2.23\,\mathrm{m}$ ($B_\mathrm{S} \approx 2\,\mathrm{T}$). On the low energy shoulder of the L-32 peak, the energy spectrum varies drastically between the pixels. The positions of these distortions are illustrated by the red and yellow colored pixels shown in Figure 7.17a. To check if these distortions are created by the source, its position has been moved to $z = -2.23\,\mathrm{m}$ with a lower magnetic field of $B_\mathrm{S} \approx 0.9\,\mathrm{T}$. This has the effect that the source seen on the detector is scaled by approximately 70 % (see Equation (7.5)), and the position between a specific point on the source shifts relative to the detector pixels. As seen in the pixel map in Figure 7.17c, different pixels are affected by the shape distortions compared to the measurement shown in Figure 7.17a. The changes between distorted and undistorted energy spectra measured for three typical pixels are shown for the two source positions in Figure 7.17a and Figure 7.17c. It is likely that the semi-circular pattern of the distorted energy spectra seen in the pixel maps, corresponds to the semi-circular scratch in the surface of the source. However, since the precise orientation of the source inside the MoS is not known, it can not be further

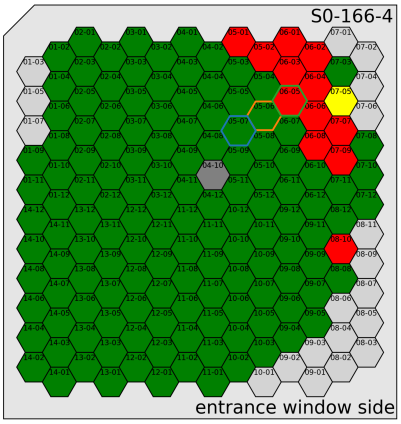

(a) Source position $z = -2.23\,\mathrm{m}$

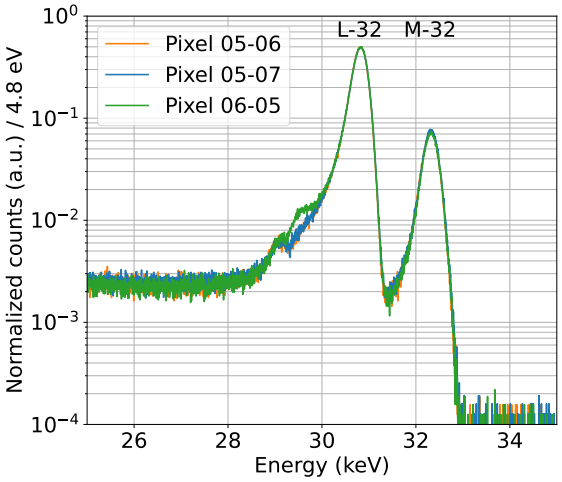

(b) Energy spectrum at $z = -2.23\,\mathrm{m}$

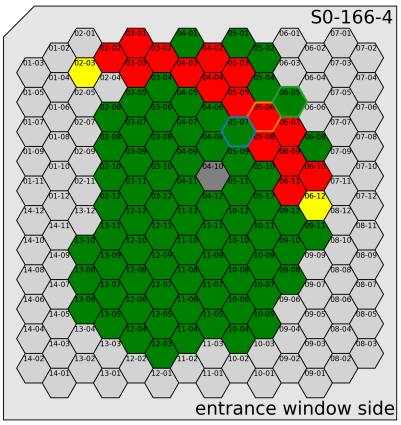

(c) Source position $z = -2.25\,\mathrm{m}$

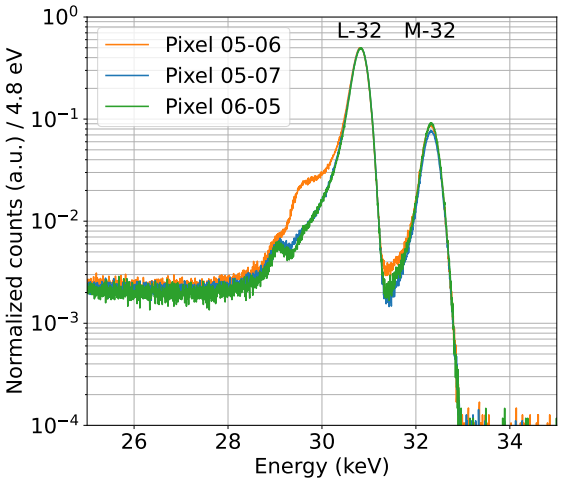

(d) Energy spectrum at $z = -2.25\,\mathrm{m}$

Figure 7.17: Position of distortions created HOPG-8-13 source
The color scheme for the pixel maps shown in (a) and (c) is: green - pixel shown no distortion, yellow - slight distortion visible, red - strong distortions visible, light grey - low or no rate, dark grey: pixel disabled. The energy spectra shown on the right-hand side correspond to three representative pixels to illustrate the change in the position of the energy distortions. The measurements are performed at a retarding potential of $U = 29.5\,\mathrm{kV}$. The selected pixels are framed in the pixel maps by the corresponding colors shown in the energy spectra.

validated in the course of this thesis. Since these spectral distortions are unwanted for the characterization of the detector module, all other measurements in this thesis are performed with the HOPG-8-14 source.

7.4.5 *Energy Resolution and Pixel Homogeneity for Electons*

As an approximation for the detector module performance in the MoS the energy resolution is being investigated in this work. To this end, the detector response described in Chapter 4.7 is fitted to the different ^{83m}Kr lines, which are closest to the retarding potential of the different measurements. Since the finest energy binning defined by the DAQ is around 5 eV, the fitted detector response is used to extrapolate the shape of the peak and more precisely estimate the FWHM. Representative for the measurements performed in this work the energy resolution observed for the ^{83m}Kr K-32 and L-32 lines are shown in Figure 7.18a and Figure 7.18a, respectively. Two distinct areas are visible in the energy resolution pixel maps. One region resembles the shape of a semi-circle with a better energy resolution, while a worse energy resolution is observed in the outer area of the detector module. This behavior can be related to an effectively thicker entrance window of the outer area. It is likely caused by the deposition of an additional water-solvable substance on the SDD chip surface during the assembly procedure of the detector module[9]. The investigations performed to support this hypothesis are described in Chapter 8. There, it could be shown that the deposited substance on the outer area can be removed using a dedicated cleaning procedure, resulting in a homogeneous detector response across all pixels comparable to ones in the area of the semi-circle. Since this cleaning procedure has only been applied to the detector module S0-166-4 after the measurements in the MoS were completed, only the 29 representative pixels in the semi-circle (marked by the black labels) are used in the further analysis as the representation of the expected detector performance. To specify this selection, the energy resolution signs are marked by a * symbol. For completeness the excluded pixels are labeled in grey in the pixel maps of the electron energy resolution of this detector module.

For the detector module S0-166-4 in the MoS an average energy resolution of $\overline{\Delta E}^* = 336.7$ eV FWHM has been observed for the L-32 line ($E = 30.8$ keV) of ^{83m}Kr in the representative region inside the semi-circle. The standard deviation across the pixels is 2.3 eV and a maximal spread has a value of 8.5 eV, which corresponds to a variation of around 3 % compared to the energy resolution. For completeness, the energy resolution across the entire detector is 350.5 eV FWHM. For the K-32 line ($E = 18.3$ keV) an average energy resolution of $\overline{\Delta E}^* = 291.9$ eV FWHM with a standard deviation of 2.7 eV and a maximal spread of 11.7 eV is observed. Here, the average energy resolution across the entire detector is 316.5 eV FWHM.

Looking at the distribution of the energy resolution in the histograms on the right-hand side of Figure 7.18, it is visible that the difference in energy resolution between the two regions increases for lower electron energies. This observation is consistent with the thicker entrance window hypothesis.

[9] Since the effect of the entrance window thickness on the energy resolution is much smaller for X-rays compared to electrons, this pattern is not visible in the energy resolution pixel maps taken with X-rays (see, e.g., Figure 7.7). However, also for X-rays, the detector response is slightly changed due to the additional entrance window thickness, and the same pattern can be seen, see Chapter 8.2.2.

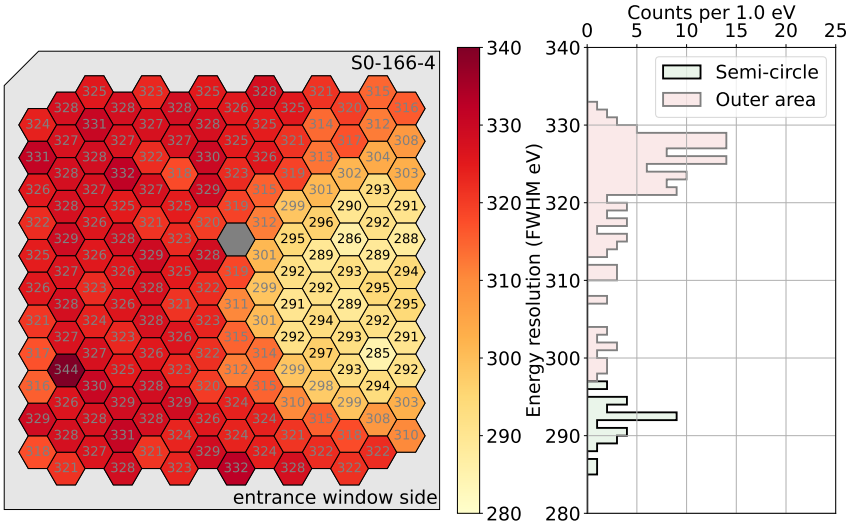

(a) Energy resolution of K-32 line of ^{83m}Kr ($U = 17.8\,\mathrm{kV}$)

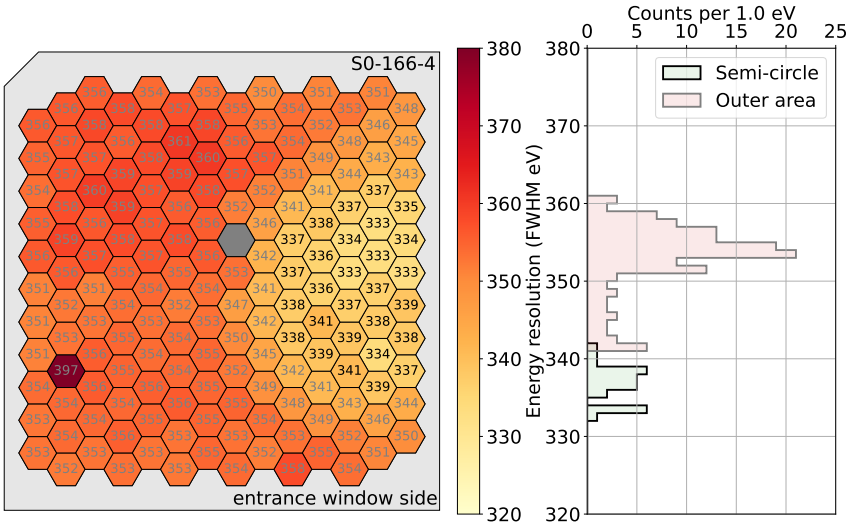

(b) Energy resolution of L-32 line of ^{83m}Kr ($U = 30.2\,\mathrm{kV}$)

Figure 7.18: Measured energy resolution for the ^{83m}Kr K-32 and L-32 lines
For the two measurements the retarding potential U was set approximately 500 V below the electron energy of the different lines. On the left-hand side, the pixel map of the energy resolution in FWHM is shown, and on the right-hand side, the corresponding histogram of the measured values. The separation into the semi-circular area and the outer area with an additional entrance window thickness is illustrated by the black and grey labels, respectively. The pixel 04-10 colored fully in grey has been disabled. Results partially published in [8].

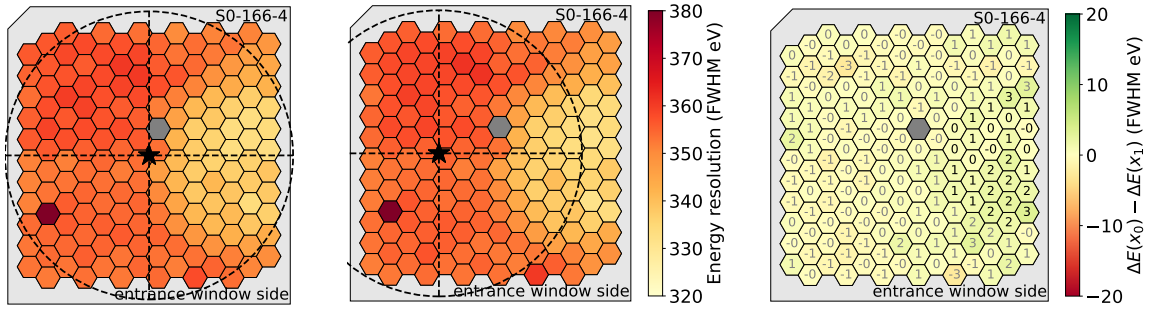

(a) Detector at $x_0 = 19\,\text{mm}$ **(b)** Detector at $x_1 = 26\,\text{mm}$ **(c)** Difference of energy resolution

Figure 7.19: Influence of the radial detector position on energy resolution
In the pixel maps (a) and (b) the energy resolution measured for the L-32 line of the ^{83m}Kr source are shown. The color scale is the same for both figures. The star and circle in the two figures illustrate (an arbitrary) position of the detector relative to the symmetry axis of the magnetic field lines in the MoS and the position of the source. (c) Difference of energy resolution between the two measurements.

7.4.6 *MoS Environment Effects on the Energy Resolution*

In order to exclude the MoS environment and the experimental conditions as the cause of the observed inhomogeneity of the energy resolution in the order of 20 eV, multiple tests have been performed. The most important ones are summarized briefly in this chapter.

Potential Effects related to the Magnetic Field and ^{83m}Kr Source As a first test, to exclude any effects related to the magnetic field lines or the (mechanical) geometry of the MoS, as well as the ^{83m}Kr source itself, the position of the detector module has been changed radial to the symmetry axis of the MoS. The measurements of the energy resolution at the L-32 line for the two detector positions $x_0 = 19\,\text{mm}$ and $X_1 = 26\,\text{mm}$ are shown in Figure 7.19a and Figure 7.19b, respectively. The star and circle in the pixel maps illustrate roughly the symmetry axis of the MoS and the position of the source relative to the detector module. Between the two measurements, the detector is shifted by 7 mm to the right-hand side. Any effect that would originate from the source or is connected to the magnetic field lines (e.g., the electron incident angle, additional electron background sources, etc.) would shift to the left-hand side by approximately 2 pixels. However, no change in the energy resolution between the two detector positions is being observed as illustrated by Figure 7.19c. Additional tests of the z-position of the detector and source can be found in the appendix in Chapter C.4.1 and Chapter C.4.2 to further exclude the geometry of the MoS as the cause of the inhomogeneity. Summarizing, these measurements likely exclude any effects that are connected to the magnetic field lines and the ^{83m}Kr source as the origin of the observed inhomogeneity in the energy resolution.

Comparison of Electronic Noise In order to exclude an additional electronic noise component as the cause of the increased energy resolution in the ^{83m}Kr electron measurements, detailed studies have been performed in [125]. Here, the primary outcome of these investigations will be summarized shortly. In the conducted analyses, the noise density spectrum has been measured under the exact same experimental conditions as the measurements presented in Chapter 7.4.5. No difference between pixels in the semi-circular area (good region) and the outer region (bad region) of the detector can be seen in the noise density spectra, see Figure 7.20. This is a strong indication that the observed inhomogeneity is independent of

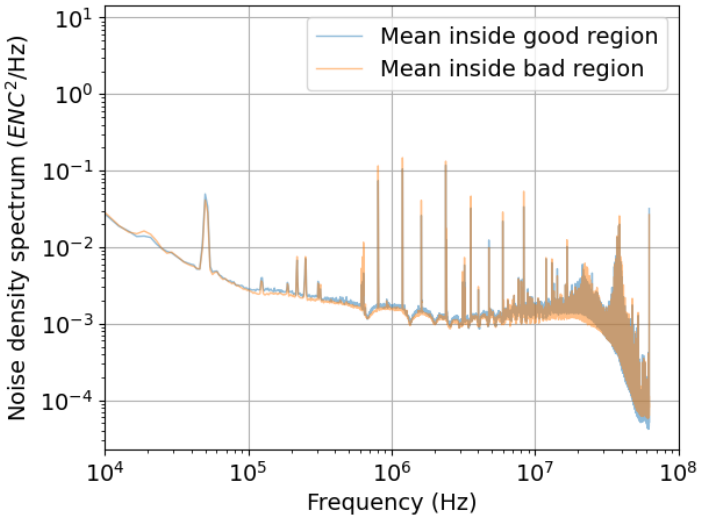

Figure 7.20: Comparison of noise density spectrum measured in MoS
Comparison of the noise power spectrum of the pixels inside the semi-circle area (good region) and the outer region (bad region). The spectrum is extracted from wave form data taken in the MoS, during the investigations with the ^{83m}Kr source. Figure taken from [125].

the electronic readout chain and must be created before the charge carriers are collected a the anodes.

7.5 Characterization with Wall Electrons

Another source of quasi-monoenergetic electrons that have been used to characterize the detector module in the MoS are the so-called wall electrons. These (secondary) electrons, are emitted from the spectrometer electrodes due to cosmic radiation and are then accelerated due to the retarding potential U towards the detector. A detailed analysis of the measurements performed with the wall electrons at energies between 5 keV and 31 keV can be found in [125]. In this chapter, the most important results will be presented. A typical measurement taken with wall electrons and obtained energy resolution across of the detector module S0-166-4 are described in Chapter 7.5.1 and Chapter 7.5.2, respectively.

7.5.1 *Typical Energy Spectra Measured with Wall Electrons*

The here-called wall electrons are created by low-energetic secondary electrons that are accelerated by the retarding potential U on the detector. These secondary electrons are generated by cosmic muons (which have an energy of a few GeV at sea level) that interact primarily via ionization with the matter of, e.g., the spectrometer electrodes. In the first step, ionization electrons with energies in the MeV scale are generated inside the material. These ionization electrons scatter in cascade-like processes inside the material and create further secondary electrons. If this process happens near the surface of the material, some of these secondary electrons can escape. The energy of the emitted secondary electrons E_{sec} is below 30 eV, with the main peak being at around 1 eV to 2 eV and a FWHM of usually below 10 eV [135–137]. If they are generated between the detector and the analyzing plane, they are accelerated by the retarding potential U, and their energy at the detector is given by Equation (7.6).

$$E_{\mathrm{wall}} = E_{\mathrm{sec}} + |e \cdot U| - |e \cdot U_{\mathrm{bias}}| \tag{7.6}$$

For simplicity reasons, the energy of the secondary electrons E_{sec} and the fluctuation of the retarding potential in the order of 1 eV are neglected in this work, since they are small compared to the detector energy resolution in the order of 300 eV FWHM. Additionally, it is assumed that all secondary electrons start on the spectrometer electrodes and, therefore at the retarding potential U. For the Mainz neutrino mass experiment or the KATRIN experiment, these electrons potentially contributed to the background on top of the tritium β electrons. Since they are generated with an energy slightly larger than the retarding potential U they end up in the ROI of an integral measurement. To suppress them, additional countermeasures like the inner wire electrode system [60, 135] have been implemented. In the case of the Mainz experiment, this background was below 50 mHz [138]. Nevertheless, since these electrons are quasi-monoenergetic, they are also a suitable electron source to characterize the installed detector module in the MoS. Therefore, to increase the measured rate on the detector, the magnetic fields are modified in such a way, that the flux tube going through the detector points onto the electrode system as shown in Figure 7.21. The wall electron count rate observed with the detector module is shown in Figure 7.22. Here, the minimal count rate is observed in a circle-like structure in the lower center of the detector model, which likely corresponds to the symmetry axis of the magnetic field lines in the MoS. The position is consistent with the observations of the symmetry axis seen in the transmission probability shown in Figure 7.14. In this region, only a small fraction of the magnetic field lines are mapped onto the spectrometer wall, which can explain the reduced rate. The pixels 11-10, 11-11 and 11-12 colored in light grey show almost no wall electron rate and are superimposed with a $^{83\mathrm{m}}$Kr spectrum originating form the source section (in this measurement the valve to the source has not been closed). Therefore, they have been excluded from the further analysis. The exact origin of the higher count rate in the upper left corner is still under investigation. It might be related to the fact that a larger (solid metal) surface inside the spectrometer vessel is mapped on this region of the detector due to a small misalignment of the LFCS and EMCS coils. However, this hypothesis could not be clarified within this work.

Representable for the measurements performed in this work, a typical energy spectrum for 20 keV wall electrons is shown in Figure 7.23. As expected, the main peak is slightly shifted towards lower energies due to entrance window effects and the applied detector depletion voltage with a value of $U_{\mathrm{bias}} = -115\,\mathrm{V}$.

7.5.2 *Energy Resolution and Pixel Homogeneity*

Also, for the measurements with the wall electrons, the energy resolution is being used as a first measure for the detector performance. To this end, the energy spectrum of each pixel and energy is being fitted with the detector response described in Chapter 4.7. The energy resolution in terms of FWHM is extracted for all energies except for the 5 keV measurement from the fitted detector response. In the case of the 5 keV measurement, the model of detector response is not sufficient enough to fully describe the shape of the main peak, and the energy resolution is extracted directly from the measured spectrum. Due to the bin size of around 5 eV, this method is less precise than the extraction from the fitted detector response, which can interpolate between the bins. Typical energy resolution pixel maps for wall electrons with an energy of 14 keV and 20 keV are shown in Figure 7.24a and Figure 7.24b, respectively. Especially for lower energies, the same pattern already seen in the measurements with the $^{83\mathrm{m}}$Kr source (see Chapter 7.4.5) is observed in the energy resolution pixel map for the wall electrons. The pixels with the black labels correspond to the semi-circle region with a good energy resolution. In contrast, the pixels with a grey label correspond to the outer

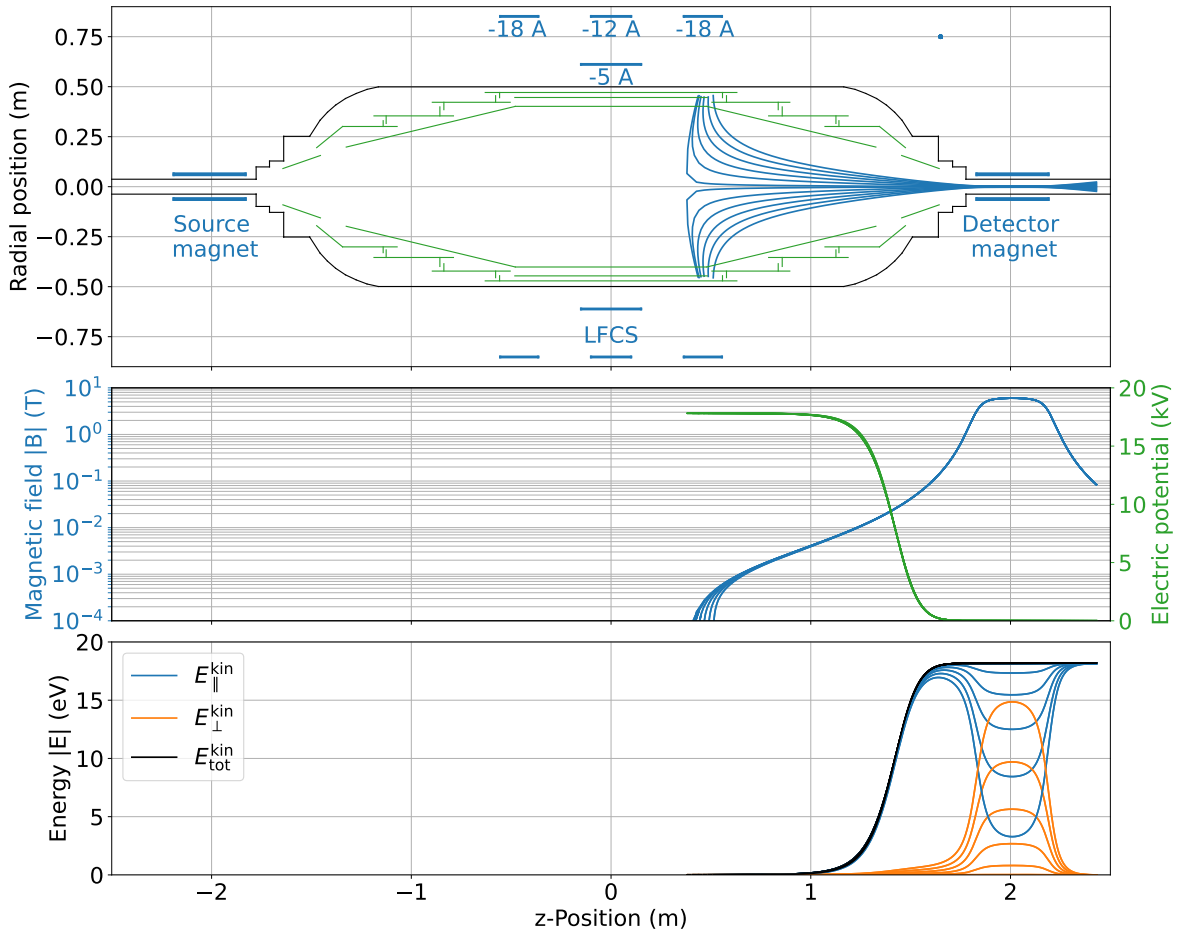

Figure 7.21: EM-fields of the MoS in wall electron mode
In the plot at the top a cross-section of the MoS along its radial symmetry axis is shwon. The black lines illustrate the vacuum spectrometer vessel hull, and the inner electrodes are shown in green. The two superconducting magnets and air coil system are illustrated by the blue squares around the spectrometer hull. For this simulation, only the superconducting detector magnet (right-hand side) is set to a magnetic field strength of 6 T. The blue lines inside the spectrometer illustrate the path of secondary electrons emitted from the electrodes due to cosmic radiation. They leave the surface with energy in the order of $E_{\mathrm{sec}} = 1\,\mathrm{eV}$ to $2\,\mathrm{eV}$ and get accelerated by the applied electrical retarding potential U towards the detector on the ground potential. For illustration purposes, the effect of the Earth's magnetic field is neglected. In the center plot, the distribution of the magnetic field strength along the electron path is shown in blue, and the electric potential is shown in green. The electric potential on the electrodes is set to 17.82 kV. In the lower plot, the different components of the kinetic energy for the emitted electrons are shown. Each line corresponds to an electron path in the top plot. Figure adapted from [66] and modified with Kassiopeia [129] simulations by D. Hinz.

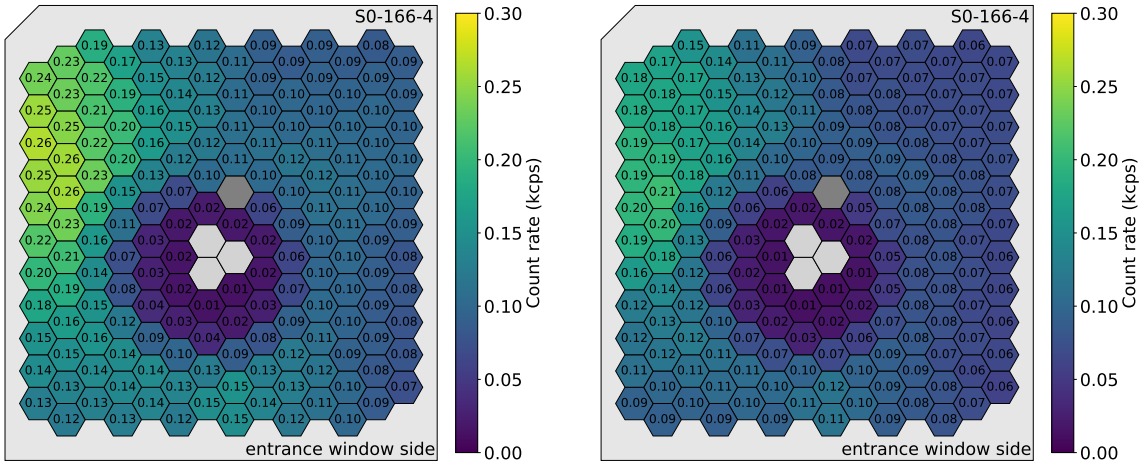

(a) Count rate at 14 keV **(b)** Count rate at 20 keV

Figure 7.22: Wall electron count rate in optimized magnetic fields
Measured count rate above 1.5 keV for two typical wall electron energies using a retarding potential U to accelerate the electrons to 14 keV (a) and 20 keV (b). The light grey pixels are excluded since they show almost no rate. The pixel 04-10 colored fully in grey has been disabled.

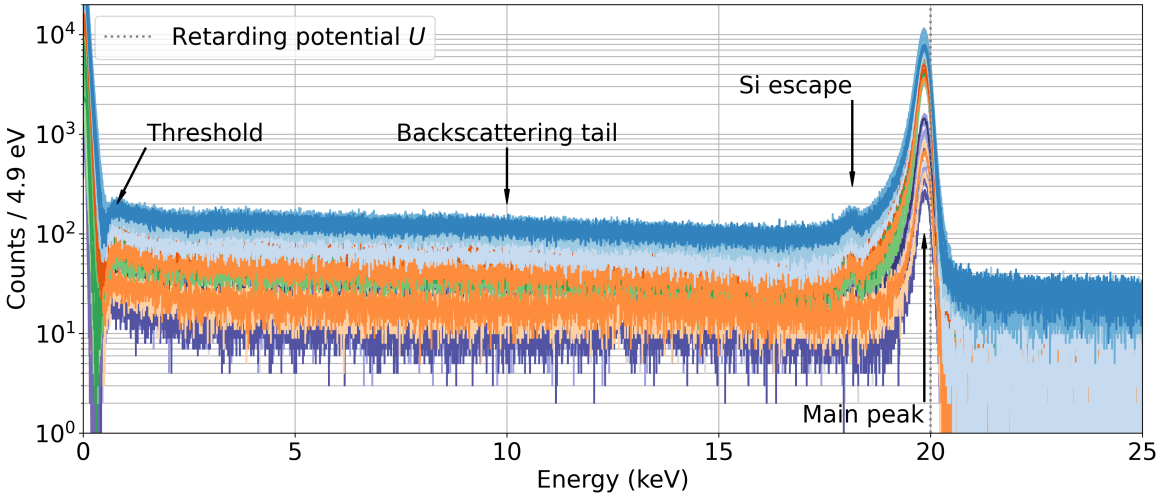

Figure 7.23: Typical energy spectra for wall electrons with an energy of 20 keV
In the measurement of the wall electrons 162 pixels are shown. The pixels 11-10, 11-11 and 11-12 have been disabled since the wall electron rate is negligible, and only electrons originating from the ^{83m}Kr source could be observed. In the measurements, the retarding potential U is set to 20 kV, and the valve towards the ^{83m}Kr source was open. Pixel 04-10 has been disabled. The remaining pixels follow the color coding shown in Figure D.9a.

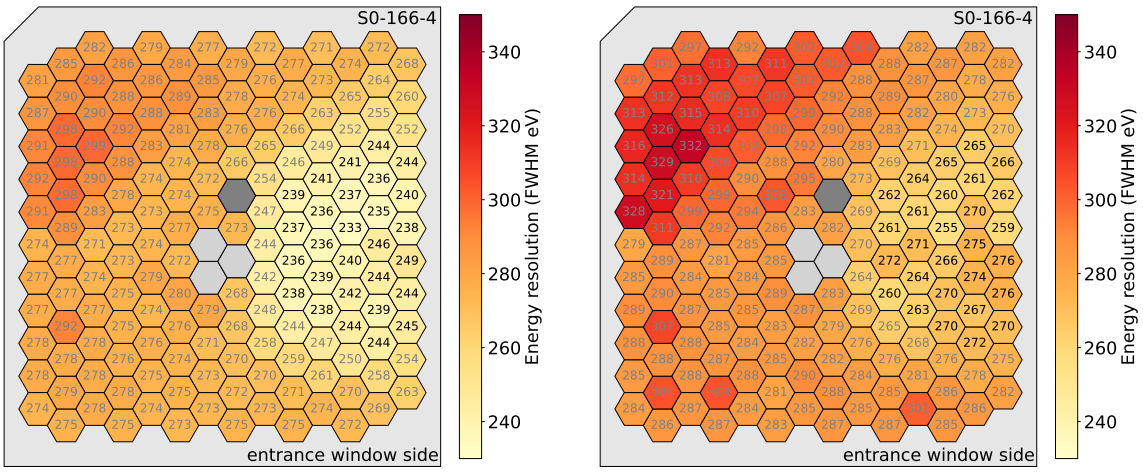

(a) Energy resolution at 14 keV

(b) Energy resolution at 20 keV

Figure 7.24: Typical energy resolution pixel map for wall electrons
For the two measurements the retarding potential U has been set to a value of 14 keV (a) and 20 keV (b). The values of the energy resolution are extracted from the fitted detector response to the energy spectrum. The light grey pixels are excluded since they show almost no rate. The pixel 04-10 colored fully in grey has been disabled. The separation into the semi-circular area and the outer area with an additional entrance window thickness is illustrated by the black and grey labels, respectively.

region with a worse energy resolution due to an additional substance on the entrance window. In addition to the pattern, due to the additional substance on the entrance window, the energy resolution in the upper left corner is worse, especially at higher energies. The origin is likely unrelated to the detector module since this feature is not seen in the measurements with the ^{83m}Kr source, that have been performed directly before and after the measurements with the wall electrons. The area in which the feature is visible in the energy resolution also corresponds to the area in which the wall electron rate is higher, see Figure 7.22. It is likely that the two observations are correlated, but the cause of it is still under investigation.

The mean energy resolution across the measured energy range of 5 keV to 31 keV is shown in Figure 7.25 for the semi-circle and the outer area of detector module S0-166-4. Especially at lower energies, the difference between the two regions drastically increases to more than double the value. This observation supports the additional entrance window hypothesis. Overall, an energy resolution of $\overline{\Delta E}^{*} = 266.3$ eV FWHM at 20 keV with a maximal spread of 20 eV is achieved for the pixels in the semi-circle region. For completeness, the energy resolution observed across the entire detector module is $\overline{\Delta E} = 287.5$ eV FWHM at an energy of 20 keV. Both values are compatible with the targeted energy resolution of 300 eV FWHM for the keV sterile neutrino search with KATRIN.

7.6 Summary

In order to test the TRISTAN detector module design in experimental conditions closer to the KATRIN beam line, the detector module S0-166-4 has been successfully installed into the MoS. The detector module was operated over multiple weeks in the detector section at a magnetic field strength of around 100 mT and a vacuum pressure better than 10^{-8} mbar at the detector, and 10^{-10} mbar in the spectrometer vessel. The electronic noise curve has been

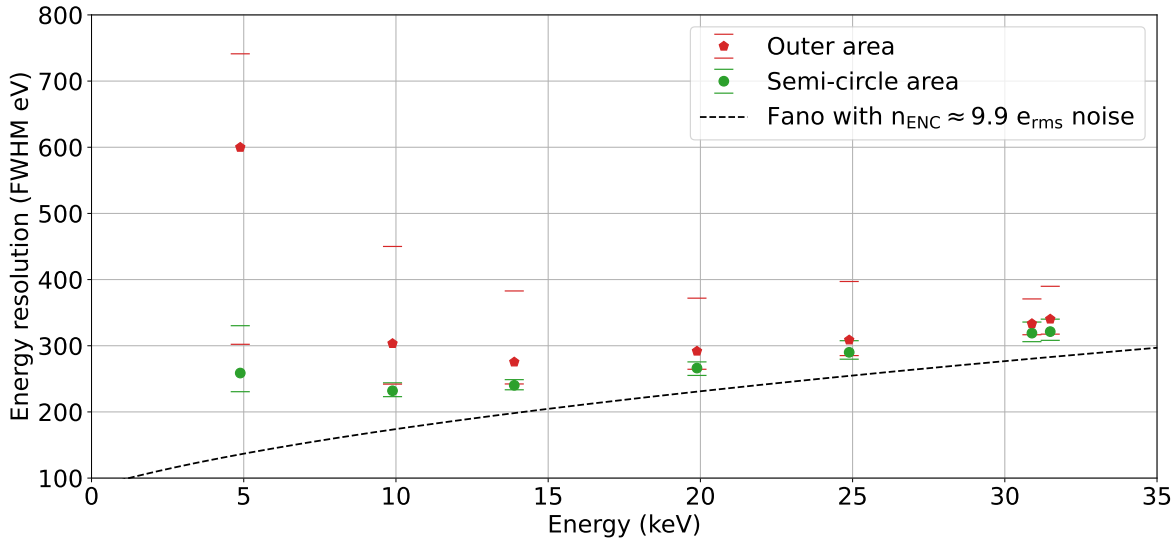

Figure 7.25: Energy resolution of wall electron measurements
The energy resolution in terms of FWHM is shown for the semi-circle area and the outer area with an additional substance on the entrance window. The separation in the two areas follows the color code in the labels of Figure 7.24. The horizontal bars denote the maximal and minimal value of all pixels per region. The expected energy resolution given by the Fano statistics and the measured electronic noise of $n_{\mathrm{ENC}} = 9.9\,e_{\mathrm{rms}}$ is illustrated by the dotted gray line. Results partially published in [8].

measured using an ^{55}Fe source in the MoS to estimate the trade-off between the energy resolution and the pile-up probability. At an energy filter rise time of $\tau_{\mathrm{rise}} = 2\,\mu\mathrm{s}$, which was used for most of the measurements in this work, an electronic noise of $n_{\mathrm{ENC}} = 9.9\,e_{\mathrm{rms}}$ has been observed. Additionally, the noise curve taken in the MoS has been compared to one taken under optimal lab conditions. Both measurements are in good agreement with each other for energy filter rise times $\tau_{\mathrm{rise}} \leq 1\,\mu\mathrm{s}$, which will be used for the keV sterile neutrino search with KATRIN. To calibrate the detector in the MoS, three different calibration methods have been investigated. In the end, the electrons of the M-32 line of the $^{83\mathrm{m}}$Kr source have been used to calibrate the detector module. However, this method is sensitive to entrance window effects, which influence the deposited energy in the detector module non-linearly depending on the electron energy and angle. Therefore, in future measurements, at the MoS and also for the keV sterile neutrino search with KATRIN, an X-ray source like ^{241}Am , which covers the entire ROI of the investigations, would be beneficial to more precisely calibrate the detector module. Furthermore, the detector module has been investigated with electrons emitted from an implanted solid $^{83\mathrm{m}}$Kr source and wall electrons. This has been the first time in which the detector S0-166-4 has been illuminated with electrons. In the pixel maps of the energy resolution for electrons, two distinct regions could be observed. One semi-circle region with the expected energy resolution and an outer region in which the energy resolution is worse. The investigations in the MoS and follow-up investigations described in Chapter 8 have shown that this pattern can be related to an additional substance on the entrance window of the detector module. This additional substance could be cleaned away after the measurements in the MoS have been completed (see Figure 8.5). The energy resolution as a function of particle energy is shown in Figure 7.26 for the representative region in the semi-circle of the detector module. Overall, an energy resolution of $\overline{\Delta E}^{*} = 336.7\,\mathrm{eV}$ FWHM at the L-32 line ($E = 30.8\,\mathrm{keV}$) of $^{83\mathrm{m}}$Kr could be observed with a maximal spread in the representative region of the detector module of 8.5 eV. At an energy of $E = 20\,\mathrm{keV}$ an average energy resolution of $\Delta E^{*} = 266.3\,\mathrm{eV}$ FWHM has been measured in the representative region

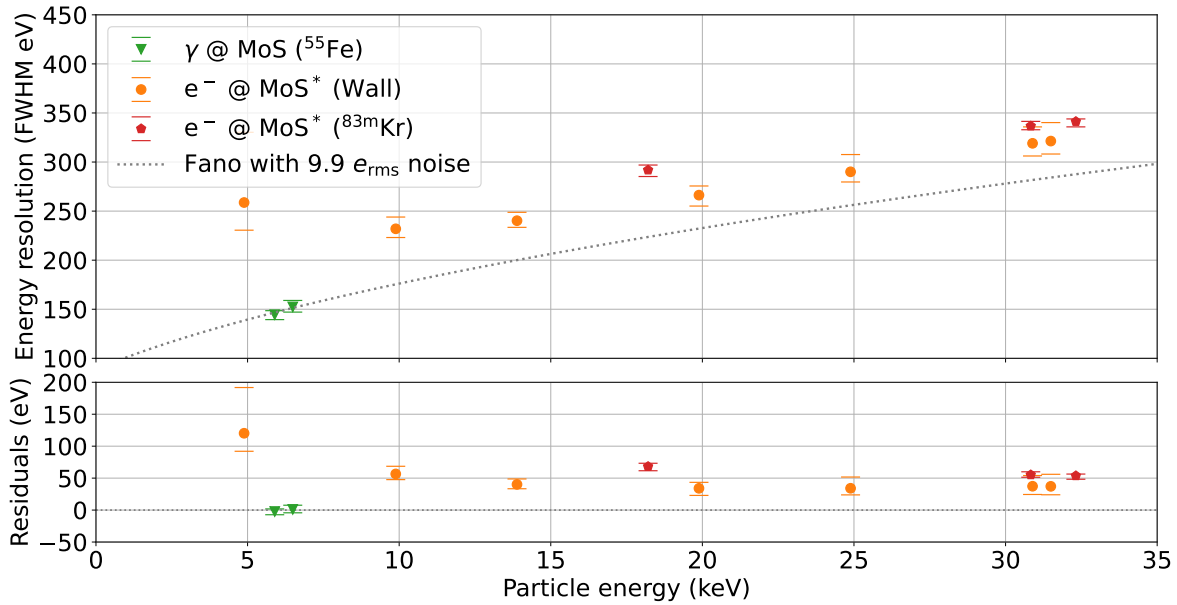

Figure 7.26: Measured energy resolution as a function of particle energy in the MoS
The data points illustrate the average energy resolution measured in the MoS, while the horizontal bars illustrate the maximal and minimal value across all considered pixels. For the X-ray measurements, all functional 165 pixels have been considered, while for the electron measurements, only the representative 29 pixels in the semi-circle region have been considered. The expected energy resolution given by the Fano statistics and the measured electronic noise of $n_{\mathrm{ENC}} = 9.9\,e_{\mathrm{rms}}$ is illustrated by the dotted gray line. The residuals between the measurements and the expectation are shown in the lower plot. Results partially published in [8].

of the detector. This result is compatible with the targeted energy resolution of 300 eV for the keV sterile neutrino search with KATRIN.

8

ENTRANCE WINDOW INVESTIGATIONS

As shown in Chapter 7.4.5, the energy resolution measured with electrons for the detector module S0-166-4 can be separated into two distinct regions. One area with the shape of a semi-circle with a better energy resolution and an outer area with a worse energy resolution. The cause for this worse energy resolution originates most likely from an additional substance deposited onto the SDD chip surface during the assembly procedure. This additional substance acts like an effectively thicker entrance window, which can explain the behavior seen in the energy resolution. To investigate the effects of this additional substance, the e-gun vacuum setup described in Chapter 8.1 has been used. Here, the detector module S0-166-4 and the identically manufactured detector modules S0-166-5 and S0-166-6 have been investigated after the measurements in the MoS were completed. In Chapter 8.2, the investigations performed to support the hypothesis of an additional substance on the entrance window are being discussed. The cleaning procedure to remove the substance on the entrance window and its effect on the energy resolution are described in Chapter 8.3. Furthermore, the effect of the light emitted by the electron gun and its effect on the energy resolution is briefly investigated in Chapter 8.4. At last, a summary of this chapter is given in Chapter 8.5.

8.1 E-Gun Vacuum Chamber Setup

For the investigation of the entrance window effect, the e-gun vacuum setup shown in Figure 8.1a is being used. It consists of a cylindrical vacuum chamber with a large cooling plate on the bottom and fits one detector module and an electron gun. Inside the chamber, a vacuum pressure of around 10^{-7} mbar and a detector temperature of around $-30\,°C$ can be achieved. The electron gun itself is based on the thermionic emission of low energetic electrons (in the order of a few eV), and its inner structure is illustrated in Figure 8.1b. By applying a voltage difference between the two ends of a thin tantalum wire (25 µm) and thus heating it, electrons are emitted as soon as their thermal energy exceeds the work function of the material (4.3 eV for tantalum) [139]. To accelerate these electrons on the detector module (on ground potential), the entire tantalum wire is additionally set to a high potential of up to 20 kV. Depending on the heating voltage, electron rates between 1 kcps and 30 kcps can be achieved on the detector module with a circular beam spot, illuminating approximately 10 pixels at a time. The magnetic steering coils mounted in front of the electron gun are used to (periodically) deflect the electron beam in such a way that the entire detector module can be illuminated over time. In the design of the electron gun, the tantalum wire has been placed off-axis with respect to the hole in the stainless steel cup around the tantalum wire to minimize the emitted light seen on the detector module. Further details on the design and commissioning of the electron gun can be found in [131, 140].

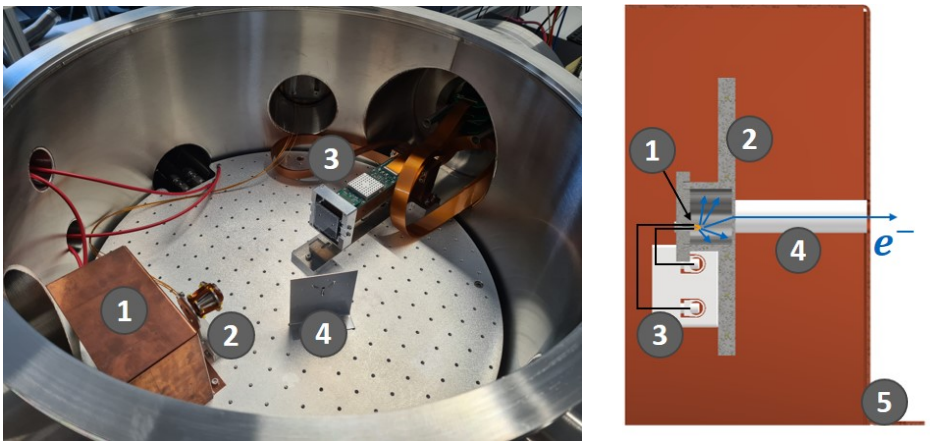

(a) Big vacuum chamber **(b)** Electron gun

Figure 8.1: Electron gun vacuum setup
(a) Photograph of the vacuum chamber with cooling plate and installed electron gun (1). Electrons emitted from a hot tantalum wire are accelerated with an electric field up to 20 keV. Using a set of electromagnetic steering coils (2), the electron beam can be guided onto the detector module (3). The detector module is installed at a distance of approximately 25 cm from the electron gun. In this picture, parts of the aluminum protection cover are installed on the detector module, and an additional calibration source is placed on the metal sheet at position (4). (b) Schematic cross section of electron gun. Tantalum wire (1) placed off-axis with respect to the hole in the stainless steel cup (2) on which the high-voltage is applied via a connector (3). The electrons illustrated in blue are accelerated inside the ceramic insulator (3) towards the exit in the copper box (5), which is on ground potential.

For the calibration of the detector module with X-rays, an ^{55}Fe source is placed next to the detector module, out of the line of sight of the electron beam. In the investigations in this work, the detector modules S0-166-4, S0-166-5 and S0-166-6 have been installed after each other in the e-gun vacuum setup. Here, the same electronic readout chain as described in Chapter 6.1 is being used.

8.2 Investigations to Support Substance on Entrance Window Hypothesis

After the measurements at the MoS have been completed, multiple investigations have been performed to find the origin of the inhomogeneous energy resolution observed in the electron data of detector module S0-166-4. In this chapter, the most critical characterizations that lead to the conclusion that it originates from an additional substance on the entrance window are summarized. First, the measurements with 5 keV electrons are repeated for the detector module S0-166-4 in the e-gun vacuum setup. Then, the impact of an effectively thicker entrance window on the X-ray spectrum is discussed. At the end, the 5 keV electron measurements are repeated for the identically manufactured (and not cleaned) detector modules S0-166-5 and S0-166-6. The final confirmation that the effect originates from an additional substance on the entrance window is shown in Chapter 8.3. Here, it could be shown that the substance can be removed from the entrance window with a dedicated cleaning procedure.

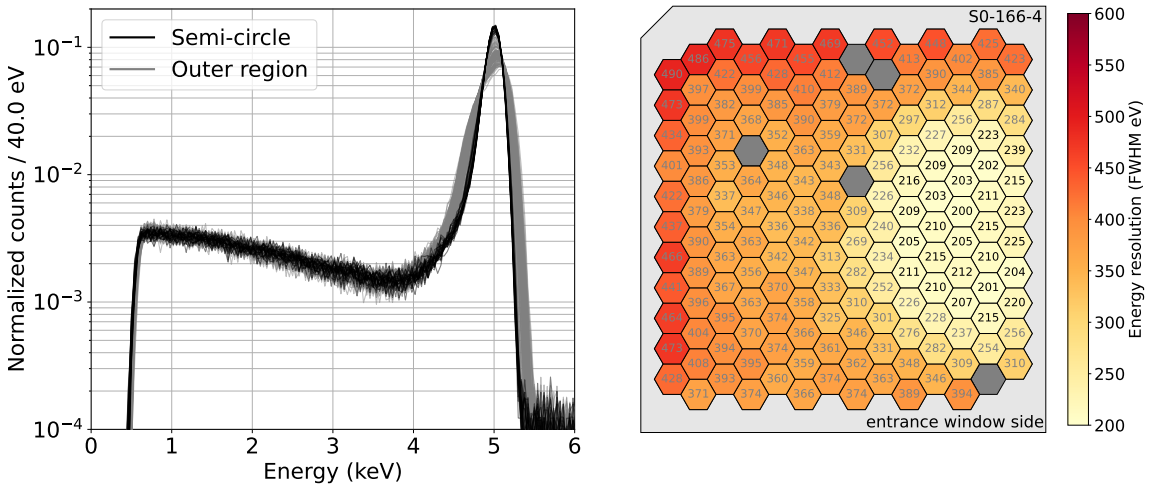

(a) Energy spectra **(b)** Energy resolution

Figure 8.2: 5 keV measurement with detector module S0-166-4
(a) Energy spectra of 161 pixels for monoenergetic electrons with an energy of 5 keV measured in the e-gun vacuum setup (after the MoS measurements). All energy spectra of the pixels in the semi-circle are colored black, while the energy spectra of the pixels in the outer region are colored grey. For better visibility of the shape of the detector response, 8 bins are always combined and normalized on the total counts in the spectrum. The spectrum was calibrated using the maximum peak position. (b) Pixel map of the energy resolution in terms of FWHM. The values are extracted from the energy spectra with a bin size with of 5 eV (before the combination seen in (a)). In this measurement, 5 pixels have been disabled due to connection issues in the electronic readout chain. The black and grey labels illustrate the separation into the semi-circular area and the outer area with a ticker entrance window.

8.2.1 *Cross-check of Ticker Entrance Window in the e-Gun Vacuum Setup*

First, the detector module S0-166-4 has been illuminated with 5 keV electrons. This energy has been chosen since lower energetic electrons deposit their energy closer to the detector surface, see Figure 4.9b, and therefore are much more sensitive to the thickness of the entrance window. The observed energy spectra and the measured energy resolution are shown in Figure 8.2a and Figure 8.2b, respectively. The shape of the detector response and the energy resolution clearly differ between the pixels in the good semi-circular region (black) and the worse outer region (grey). These measurements are consistent with measurements observed in the MoS, see Chapter 7.4.5 and Chapter 7.5.2. They confirm that the effect is related to the detector module itself and is independent of the MoS environment. The overall change in the shape of the detector response between the two regions is consistent with observations of 7 pixel prototype detectors with different entrance window thicknesses [82].

8.2.2 *Impact of a Thicker Entrance Window an the X-Ray Spectrum*

The influence of an effectively thicker entrance window is also visible in X-ray measurements. However, since the interaction of X-rays takes mostly place in the fully sensitive detector volume, see Figure 4.9a, it is much less pronounced compared to the spectral distortion seen for low energetic electrons. With a larger entrance window thickness, the probability that an X-ray interacts in this region of reduced CCE increases. Here, a fraction of the generated charge carriers are lost, which leads to a reduction in the measured energy. The ratio between the events that deposited their entire energy (main peak) and the lower energy shoulder

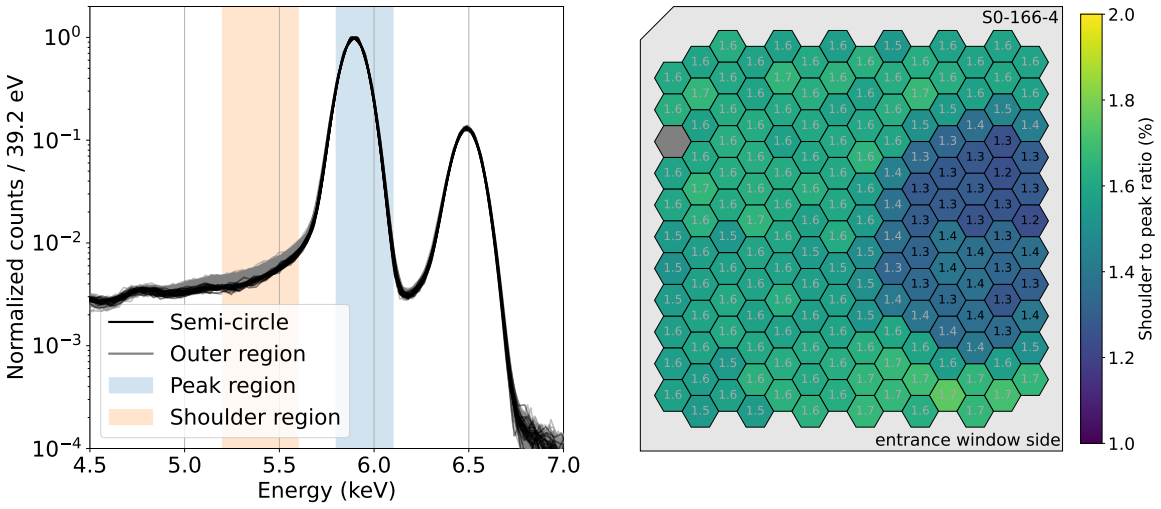

(a) Normalized ^{55}Fe spectrum **(b)** Ratio between counts shoulder and peak

Figure 8.3: Entrance window effects observed in X-ray measurement
Measurement of the ^{55}Fe source installed at the test bench setup at a temperature of $T_{\mathrm{SDD}} = -34\,^{\circ}\mathrm{C}$, described in Chapter 6.3.1. (a) To illustrate the entrance window effect seen in detector module S0-166-4, the energy spectra are normalized to the maximum peak height of the Mn-K$_\alpha$ line and 8 bins are combined. The energy spectra of the pixels in the region in the shape of a semi-circle are colored black, and the ones in the outer region are colored grey. (b) Pixel map of the ratio between the sum of the counts in the peak region (5.8 keV to 6.1 keV) and the shoulder region (5.2 keV to 5.6 keV). The ROI for the main peak has been selected asymmetrically at higher energies to reduce the impact of the reduced CCE at lower energies. The black and grey labels illustrate the separation into the semi-circular area and the outer area with a ticker entrance window.

where a small percentage of the energy is lost (diffusion region $D(E|\mu, \sigma, \beta, N_D)$) contains to some extend the information about the thickness of the entrance window. To illustrate this effect, the measurement of an ^{55}Fe source in the bench test setup at a temperature of $T_{\mathrm{SDD}} = -34\,^{\circ}\mathrm{C}$ is being used, see Chapter 6.3.1. The normalized energy spectra for all functional 165 pixels is shown in Figure 8.3a. In the spectra region between 5.2 keV and 5.6 keV, which corresponds to the lower energy shoulder of the Mn-K$_\alpha$ line, the shape of the detector response varies between the two detector regions. To be precise, the counts in the lower energy shoulder are higher for the pixels in the outer region of the detector module compared to the ones in the semi-circular region. The fraction between the counts in the main peak (full absorption) and the lower energy shoulder (partial absorption due to entrance window effects) is illustrated in Figure 8.3b. Here, the same pattern of the semi-circular region with a thinner entrance window and an outer region with a thicker entrance window can be seen. Since this measurement has been performed shortly after the assembly of the detector module S0-166-4 (without entrance window cleaning) and before installation in the MoS, the transport, installation, and measurements performed at the MoS can be excluded as the potential cause. Since the effect is visible already in the first test of the detector module, it is likely that the additional substance is deposited during the assembly procedure or manufacturing of the SDD chip.

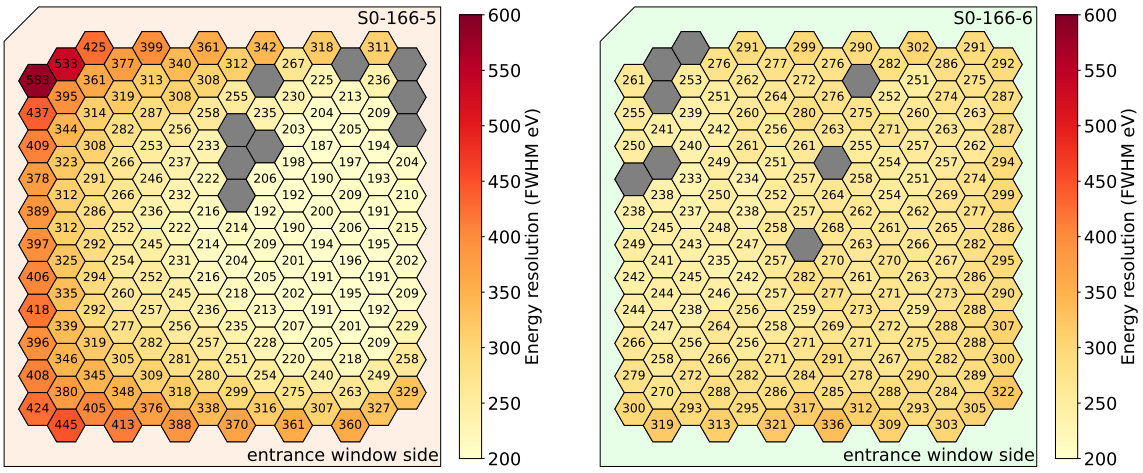

(a) Detector module S0-166-5 **(b)** Detector module S0-166-6

Figure 8.4: Energy resolution for 5 keV electrons before cleaning
The measurements have been performed in the e-gun vacuum setup with monoenergetic electrons with an energy of 5 keV. The energy resolution in terms of FWHM is extracted directly from the energy spectra with a bin size of approximately 5 eV. At the time of the measurement, the entrance window of these detectors has not been cleaned, yet. The pixels fully colored in gray have been disabled.

8.2.3 *Thicker Entrance Window Observed in other Detector Modules*

In order to investigate if the ticker entrance window is also observed in other detector modules, the identically manufactured detector modules S0-166-5 and S0-166-6 (without entrance window cleaning) have been investigated in the e-gun vacuum setup. The measured energy resolution for 5 keV electrons is shown for the two detectors in Figure 8.4a and Figure 8.4b. An increased energy resolution is seen towards the outer edges, especially for the detector module S0-166-5. In comparison, the energy resolution for X-rays is homogeneous for both detector modules (in the order of a few eV) as shown in the appendix in Figure B.5a and Figure B.6a. This excludes the electronic readout chain and noise as a potential cause for the seen inhomogeneity and strongly indicates that these detector modules are also affected by the additional substance on top of the entrance window surface.

8.3 Test of the Entrance Window Cleaning Procedure

During the manufacturing of the SDD chips on the wafer level, mainly acetone, isopropyl, and de-ionized water are used for cleaning. Since these cleaning agents have been proven to be reliable and do not damage the SDD chip, they have been used to clean the entrance window of the assembled detector modules in this work. In the first test, the SDD chip of the assembled detector module S0-166-4 has been rinsed with acetone and isopropyl to clean the entrance window surfaces as described in Chapter 5.6.2. The measured energy resolution for 5 keV electrons before and after the cleaning is shown in Figure 8.5a and Figure 8.5b, respectively. The difference between the two measurements is shown in Figure 8.5c. It is clearly visible that after the cleaning, the energy resolution in the outer region improves by around 100 eV for most pixels. This is a solid indication that the effect seen in the energy resolution is created by an additional substance on the entrance window, which can be cleaned away. The same procedure has been repeated for the detector module S0-166-5 as illustrated by Figure 8.6a and Figure 8.6b. Here, the energy resolution also improves for

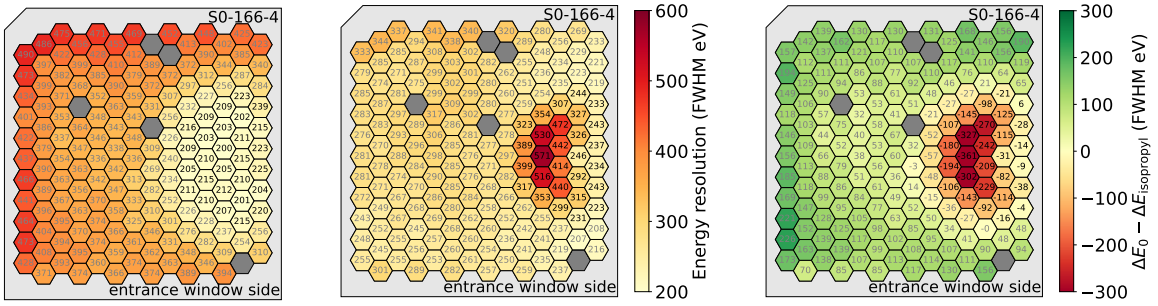

(a) Not cleaned **(b)** Acetone and isopropyl cleaning **(c)** Difference of energy resolution

Figure 8.5: Energy resolution during cleaning of detector module S0-166-4
Measurement of the energy resolution of 5 keV electrons in the e-gun vacuum setup at a detector temperature of $T_{\text{SDD}} \approx -30\,^{\circ}\text{C}$. The pixels fully colored in grey have been disabled during the measurement. (a) Energy resolution of the uncleaned detector module. The average energy resolution across all pixels is $\overline{\Delta E_0} = 336\,\text{eV}$ FWHM. (b) Energy resolution after the entrance window has been cleaned with acetone and isopropyl. The cleaning has been performed in the clean room of the HLL laboratories. An average energy resolution across all pixels of $\overline{\Delta E_{\text{isopropyl}}} = 284\,\text{eV}$ FWHM is achieved. (c) Difference of the measured energy resolution between the measurement before and after the cleaning.

most of the pixels after the detector module has been cleaned with acetone and isopropyl. However, for both detector modules, the energy resolution of a distinct group of pixels worsens due to the cleaning with acetone and isopropyl. This region can be related to the wafer center, as illustrated in Figure 8.7. Since many processes during the manufacturing of the SDD chips start in the center of the wafer, this is a special spot that might have slightly different surface properties compared to the rest wafer. The decrease in energy resolution in this region might be related to the fact that residuals of the additional substance on the entrance window get stuck on this specific spot during the cleaning procedure. There, it would again lead to an effectively thicker entrance window due to the additional material in the way of the electrons. In an attempt to also clean the region of the wafer center, the entrance window of the detector module S0-166-5 has been carefully rinsed with approximately 500 mL de-ionized water. The measured energy resolution after the cleaning is shown in Figure 8.6c. It is clearly visible that the energy resolution in the wafer center drastically improves from up to 520 eV to below 300 eV FWHM. Additionally, the energy resolution measured in the other pixels improves by a few eV, hinting that still some residual material was left on the entrance window after the cleaning with acetone and isopropyl, which could be removed with the de-ionized water.

A more thorough cleaning with de-ionized water, with much more water and pressure similar to the cleaning on the wafer level, might also remove the remaining substrate on the pixels in the wafer center. However, in the assembled configuration, the de-ionized water can lead to deformations of the bond wires due to the adhesion forces of water droplets ending up between them. In an attempt to more thoroughly clean the entrance window of the assembled detector module S0-166-4 in a de-ionized water bath, it has been damaged to the point that it was not functional anymore. To not also damage the detector module S0-166-5, this procedure has not been repeated, and the detector surface was only gently rinsed with de-ionized water as described above. Also, detector S0-166-6 has been carefully cleaned with acetone, isopropyl, and de-ionized water after the assembly was completed. As shown in the pixel maps of Figure 8.8, the energy resolution from the uncleaned detector module with an average energy resolution of $\overline{\Delta E_0} = 270\,\text{eV}$ FWHM improves drastically

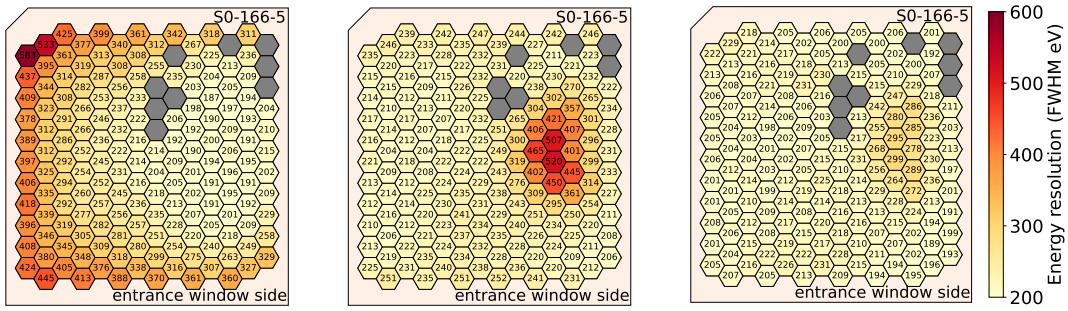

(a) Not cleaned **(b)** Acetone and isopropyl **(c)** De-ionized water cleaning

Figure 8.6: Energy resolution during cleaning of detector module S0-166-5
Measurement of the energy resolution of 5 keV electrons in the e-gun vacuum setup at a detector temperature of $T_{\mathrm{SDD}} \approx -30\,^{\circ}\mathrm{C}$ after different steps of the cleaning procedure. The pixels fully colored in grey have been disabled during the measurement. (a) Energy resolution of the uncleaned detector module. The average energy resolution across all pixels is $\overline{\Delta E_0} = 278\,\mathrm{eV}$ FWHM. (b) Measurement after the entrance window has been cleaned with acetone and isopropyl. The cleaning was performed in the clean room of the HLL laboratories. An average energy resolution across all pixels of $\overline{\Delta E_{\mathrm{isopropyl}}} = 247\,\mathrm{eV}$ FWHM is obtained. (c) Measurement after the entrance window has been additionally cleaned with de-ionized water. An average energy resolution of $\overline{\Delta E_{\mathrm{water}}} = 216\,\mathrm{eV}$ FWHM has been achieved.

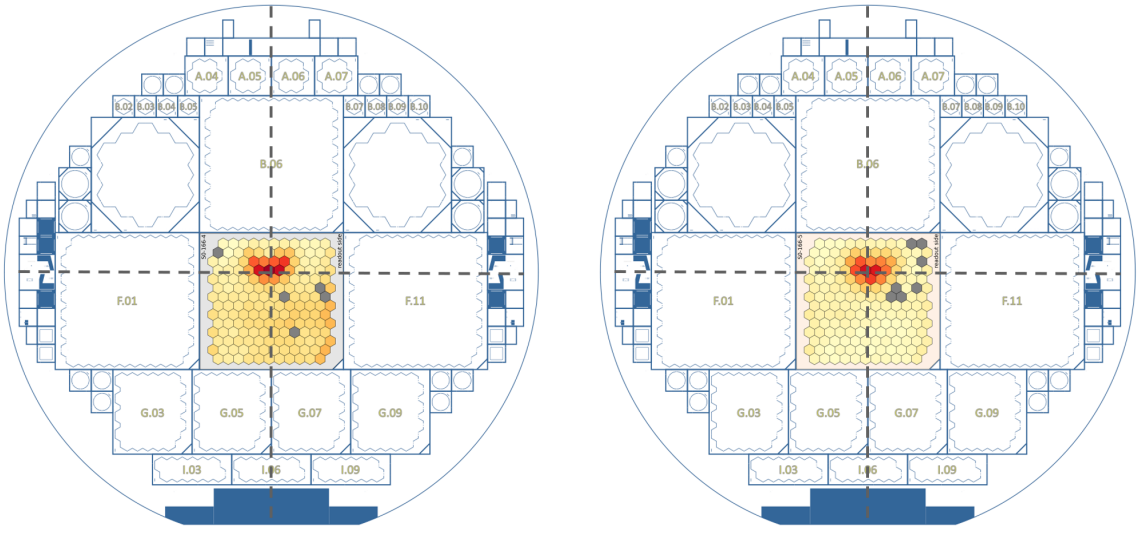

(a) S0-166-4 after cleaning **(b)** S0-166-5 after cleaning

Figure 8.7: Entrance window effect related to wafer center
Position of the SDD chips from detector module S0-166-4 and S0-166-5 on the wafer level. For both detector modules, the energy resolution for 5 keV electrons is shown after the cleaning with acetone and isopropyl. The dashed grey lines illustrate the position of the wafer center. The SDD chips and the wafer are depicted from the readout side.

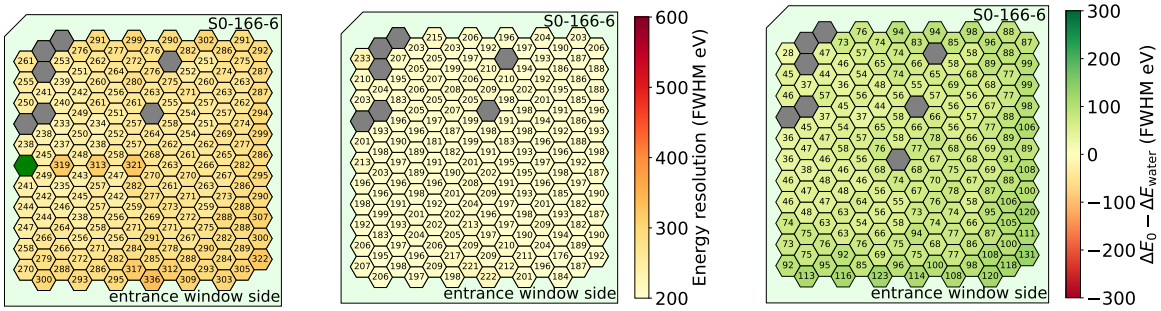

(a) No cleaning **(b)** Full cleaning **(c)** Difference of energy resolution

Figure 8.8: Energy resolution during cleaning of detector module S0-166-6
Measurement of the energy resolution of 5 keV electrons in the e-gun vacuum setup at a detector temperature of $T_{\text{SDD}} \approx -30\,^{\circ}\text{C}$. The pixels fully colored in grey have been disabled during the measurement. (a) Measurement of the uncleaned detector module. The average energy resolution across all pixels is $\overline{\Delta E_0} = 270\,\text{eV}$. (b) Measurement after the entrance window has been cleaned with acetone, isopropyl, and de-ionized water. The cleaning has been performed in the clean room of the HLL laboratories. An average energy resolution across all pixels of $\overline{\Delta E_{\text{water}}} = 198\,\text{eV}$ is achieved. (c) Difference of the measured energy resolution between the measurement before and after the cleaning.

to $\overline{\Delta E_{\text{water}}} = 198\,\text{eV}$ FWHM after the cleaning. Since the used SDD chip of this detector module is from the upper center of the wafer (position B.06, see Figure 8.8), the effect of the wafer center is not visible, and the energy resolution measured across all pixels is much more homogeneous. The maximal spread in the energy resolution across the pixels reduces to 57 eV and a standard deviation of 9 eV. This is much smaller compared to the maximal spread of 103 eV and a standard deviation of 21 eV of the uncleaned detector module.

These investigations verify that the observed distortions in the detector response, e.g., the increased and inhomogeneous energy resolution, are related to a substance on the surface of the SDD chip, which can be cleaned away. The origin of this substance is currently under investigation. To exclude the manufacturing on the wafer level as a potential cause, multiple SDD chips have been investigated under an ellipsometer. This method optically measures the dielectric properties of thin materials and surfaces and can be compared to a refraction model. The ellipsometry measurements of three SDD chips from the same wafer production as the detector modules in this work show no additional substance on the entrance window surface. Since the entrance window effect is seen already in the first measurements directly after the assembly, it is likely that the substance is introduced during the assembly procedure of the detector front described in Chapter 5.6.2. Potential sources of the substance could be the outgassing during the bake-out of the glue or residuals of the cutting oils used in the manufacturing of the Cesic interposer. These different hypotheses are currently under investigation but are out of the scope of this thesis.

8.4 Effect of Light Created by Electron Gun on Energy Resolution

During the operation of the electron gun, the tantalum wire is heated to emit low-energetic electrons, which are accelerated onto the detector module. However, as a side effect, the tantalum wire also starts to glow, which causes photon emission. Even though the tantalum wire is installed off-axis with respect to the small hole in the stainless steel cup, a small amount of light can be seen on the detector module, which worsens the measured energy

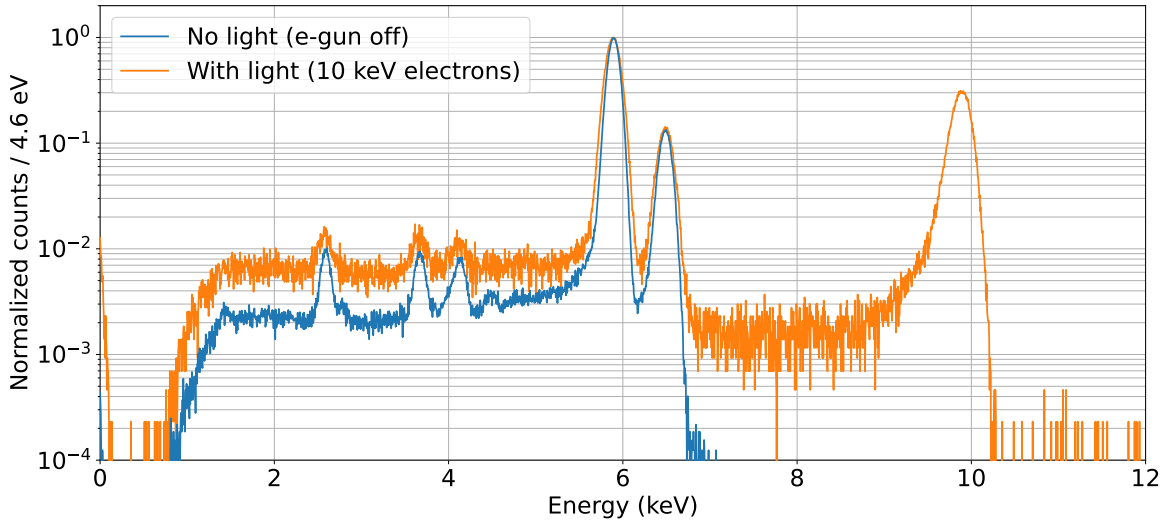

Figure 8.9: Effect of light emission of electron gun on the energy spectrum
Measured energy spectrum of an ^{55}Fe source inside the e-gun vacuum setup at a detector temperature of $T_{\mathrm{SDD}} \approx -30\,^{\circ}\mathrm{C}$. For the reference measurement (blue), the electron gun is turned off, i.e. no light is emitted. In the second energy spectrum (orange), a subsequent measurement is shown in which the electron gun is turned on and set to an acceleration potential of 10 kV. Both energy spectra are shown for pixel 04-05, which is primarily affected by the light emission of the electron gun.

resolution in the illuminated pixels. For the investigations of the entrance window thickness, this effect is not as important since mainly the difference in energy resolution between measurements (or cleaning steps) has been considered. Since all measurements are affected similarly by the light, it is nullified when comparing two measurements. However, to estimate the magnitude of the effect on the energy resolution and the pixel position, the Mn-K$_\alpha$ line is measured first with the electron gun turned off (no light), and then turned on (with light). The energy spectra measured in the two settings are shown for a typical pixel that is affected by the light in Figure 8.9. The energy resolution maps for the two measurements are illustrated in Figure 8.10a and Figure 8.10b, respectively. Here, the emission of the light is seen as a circular pattern which likely corresponds to the small hole in the stainless steel cup of the electron gun.

Similar to the leakage current, the light from the electron gun acts as an additional parallel noise component $\sigma^2_{\mathrm{light}}$, which introduces an additional Gaussian broadening and worsens the measured energy resolution σ_E. To take this contribution into account, Equation (4.16) is extended to Equation (8.1).

$$\sigma^2_{\mathrm{E\,with\,light}} = \sigma^2_{\mathrm{E,Fano}} + \sigma^2_{\mathrm{el}} + \sigma^2_{\mathrm{light}} \tag{8.1}$$

Assuming that the electronic noise σ^2_{el} and the Fano Statistic $\sigma^2_{\mathrm{E,Fano}}$ are constant between the two measurements, Equation (8.1) can be transformed to Equation (8.2).

$$\sigma^2_{\mathrm{light}} = \sigma^2_{\mathrm{E\,with\,light}} - \sigma^2_{\mathrm{E}} \tag{8.2}$$

Here, σ^2_{E} and $\sigma^2_{\mathrm{E\,with\,light}}$ denote the measured energy resolution of the Mn-K$_\alpha$ line at an energy of $E = 5.9\,\mathrm{keV}$ with the electron gun turned off and on, respectively. The Gaussian contribution of the light σ_{light} to the energy resolution of the Mn-K$_\alpha$ line is shown in Figure 8.10c. This value can be used to roughly estimate the effect of the light on the measured energy resolution for electrons and correct for it. Analog to Equation (8.2), the

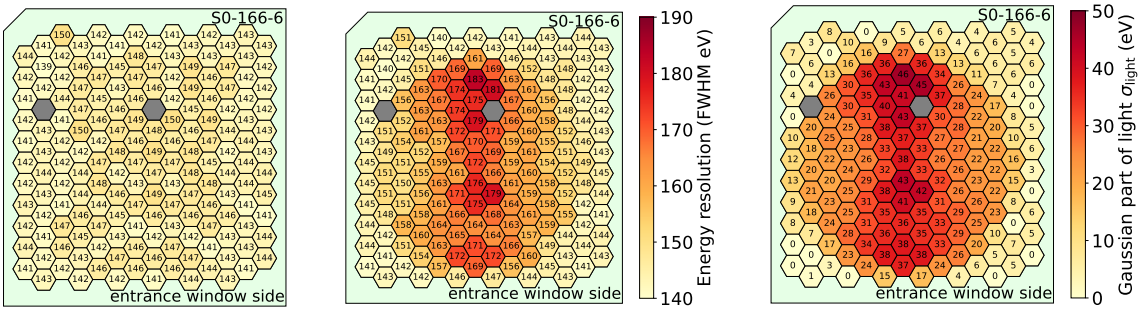

(a) Electron gun off **(b)** Electron gun on **(c)** Effect of light

Figure 8.10: Effect of the light emission of electron gun on the Mn-K$_\alpha$ energy resolution Measurement of the energy resolution at the Mn-K$_\alpha$ line of an ^{55}Fe source in the e-gun vacuum setup at a detector temperature of $T_{\text{SDD}} \approx -30\,^{\circ}\text{C}$. The pixels fully colored in grey have been disabled during the measurement. (a) Reference measurement with the electron gun turned off. (b) Measurement of with the electron gun turned on and set to an acceleration potential of 10 kV. (c) The additional Gaussian contribution of the light σ_{el} to the measured energy resolution is estimated using Equation (8.2) and the measurements shown in (a) and (b). For the energy resolutions that were slightly better (less than 1 eV) in the measurement with the electron gun turned on (due to, e.g., statistical fluctuations), the value is set to 0.

energy resolution for electrons $\Delta E_{\text{E, corr.}}$ in FWHM is corrected by the effect of the light as given in Equation (8.3).

$$\Delta E_{\text{E, corr.}} \approx 2\sqrt{2\ln 2} \cdot \sigma_{\text{E, corr.}} \approx 2\sqrt{2\ln 2} \cdot \sqrt{\left(\frac{\Delta E_{\text{E}}}{2\sqrt{2\ln 2}}\right)^2 - \sigma_{\text{light}}^2} \tag{8.3}$$

Here, ΔE_{E} denotes the measured energy resolution in FWHM of the electron peak. Since the emission of the light only depends on the heating current and not the applied acceleration potential, the light contribution to the energy resolution is independent of the measured electron energy. In Figure 8.11, the measured energy resolution with and without the light correction is shown for electrons with an energy of 5 keV and 10 keV. Representative for the measurements, the average energy resolution at 10 keV improves from $\overline{\Delta E_{10\,\text{keV}}} = 207$ eV FWHM with a maximal spread of 41 eV to $\overline{\Delta E_{10\,\text{keV, corr.}}} = 200$ eV FWHM with a much smaller maximal spread of 28 eV. The largest improvement of up to 30 eV is achieved for the pixels in the center, which see the most light. Important to note for the characterizations of the detector modules in the context of the keV sterile neutrino search with KATRIN, this effect likely has to be mitigated or at least taken into account since it is in the order of up to 10 % of the absolute energy resolution. In the shown experimental setup, the light beam has roughly a diameter of 35 mm. Placing the detector module off-axis to the electron gun and steering coils by around 40 mm to the side would shift the light cone out of the field of view of the detector module. However, as mentioned before, for comparing energy resolutions between measurements (or cleaning steps) the effect of the light is nullified. It only affects the absolute energy resolution and absolute pixel homogeneity but on a smaller level.

8.5 Summary

The investigations in this chapter have shown that the inhomogeneity measured in the electron energy resolution originates from an additional substance likely deposited on the entrance window surface during the assembly procedure. Fortunately, rinsing the entrance

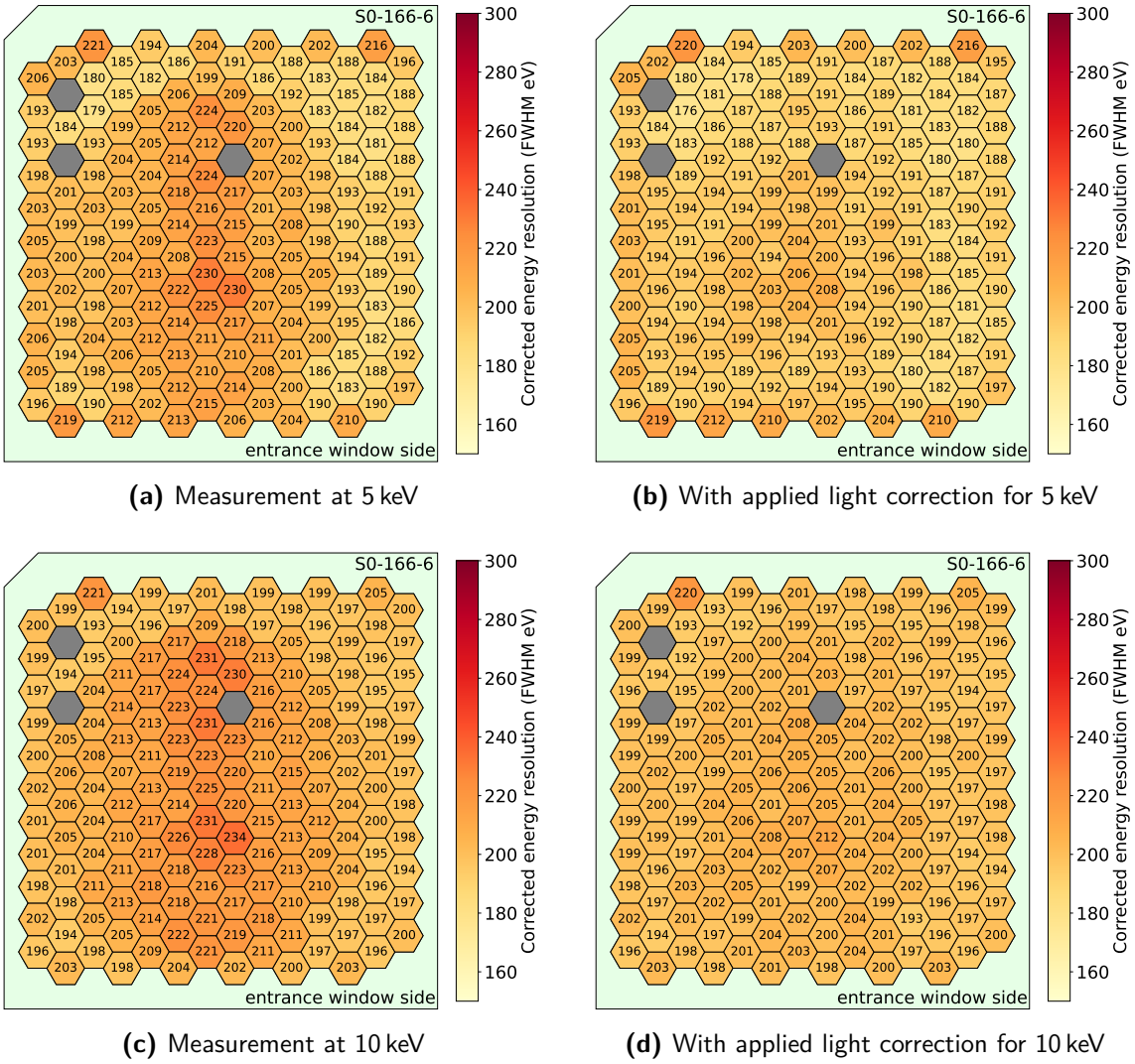

(a) Measurement at 5 keV

(b) With applied light correction for 5 keV

(c) Measurement at 10 keV

(d) With applied light correction for 10 keV

Figure 8.11: Effect of light on the electron energy resolution
The measurements are performed for the cleaned detector module S0-166-6 at a detector temperature of $T_{\mathrm{SDD}} \approx -30\,^{\circ}\mathrm{C}$. (a) shows the measured energy resolution for 5 keV electrons with a mean of $\overline{\Delta E_{5\,\mathrm{keV}}} = 201\,\mathrm{eV}$ FWHM. The pixels fully colored in grey have been disabled during the measurement. (b) Illustrates the expected energy resolution after the effect of the light σ_{light} is subtracted using Equation (8.3). An average energy resolution of $\overline{\Delta E_{5\,\mathrm{keV,\,corr.}}} = 193\,\mathrm{eV}$ FWHM is achieved. In (c) and (d) the same plots are shown for a measurement at 10 keV. The average measured energy resolution is $\overline{\Delta E_{10\,\mathrm{keV}}} = 207\,\mathrm{eV}$ FWHM and after the light correction it is $\overline{\Delta E_{10\,\mathrm{keV,\,corr.}}} = 200\,\mathrm{eV}$ FWHM.

window surface subsequently with acetone, isopropyl, and de-ionized water can remove the additional substance and restore a much more homogeneous energy resolution for electrons. For the detector module S0-166-4, the energy resolution of the most affected pixels improves by almost a factor of two, which is up to 200 eV for the measurement of 5 keV electrons. It could be shown that the cleaning with acetone and isopropyl removes most of the residual substance. However, especially at the location of the wafer center, an additional cleaning with de-ionized water is necessary to remove (most) of the additional substance on the entrance window. As a result of these observations, the cleaning of the entrance window with acetone, isopropyl, and de-ionized water has been implemented as a default in the detector module's assembly procedure. The step is introduced before the wire bonding of the readout side to prevent any deformations of the wire bonds. In addition to the investigations of the entrance window substance, the effect of the electron gun has been briefly explored. Due to the necessary heating current of the tantalum wire, a small amount of light is seen on the detector module in a circular pattern. This worsens the energy resolution similar to an additional parallel noise component. By comparing a reference X-ray measurement when the electron gun is turned off to a measurement when the electron gun is turned on, the effect can be estimated and corrected. For the measurements in the experimental configuration of this work, the effect is in the order of up to 30 eV FWHM or 10 % of the absolute energy resolution. For the precise characterizations of the detector modules in the context of the keV sterile neutrino search, this effect needs to be accounted for or, in the best case, mitigated by small modifications to the experimental setup.

9

CONCLUSIONS AND SUMMARY

As a minimal extension to the Standard Model of particle physics (SM), sterile neutrinos in the keV mass range are a suitable dark matter candidate. Besides their impact on cosmology, the existence of an additional sterile mass eigenstate m_s would lead to a spectral distortion in the β-decay spectrum at energies below the kinetic endpoint energy at $E_0 - m_s$. After the currently ongoing neutrino mass measurements have been completed by the end of 2025, the Karlsruhe Tritium Neutrino (KATRIN) experiment will be upgraded with a novel detector system, the TRISTAN detector, to search for keV sterile neutrinos.

In this work, the mechanical design and assembly procedure for the TRISTAN detector modules have been developed. The assembly process includes a save and reliable gluing technique for the SDD chip, and a cleaning method for the SDD surface to ensure optimal spectroscopic properties. Along with the design of the module parts, and the jigs for the assembly procedure, also a robust transportation system for a safe transfer of the detector modules between institutes has been created. This procedure has been successfully employed to assemble five fully functional detector modules.

One of those detector modules has been characterized in detail with X-rays and electrons. As a first step, the detector operation voltages and temperature dependence have been studied in a dedicated vacuum test setup to determine the optimal working point. Furthermore, the spectroscopic properties of the detector module have been studied with X-rays. An excellent energy resolution of 144.5 eV FWHM ($n_{\mathrm{ENC}} = 9.9\, e_{\mathrm{rms}}$) was measured for the Mn-K$_\alpha$ line of an ^{55}Fe source. In the energy range between 7 keV to 60 keV, the X-ray energy resolution is consistent with the expectation from Fano statistics, and the calibration curve varies by less than 0.5 % from linearity.

To test the detector module in a more realistic environment, comparable to the KATRIN beamline (ultra-high vacuum and MAC-E filter environment), it has been installed in the KATRIN Monitor Spectrometer (MoS). Here, the detector module was successfully operated over multiple weeks in vacuum (10^{-8} mbar at the detector, 10^{-10} mbar in the spectrometer vessel), and in a magnetic field with a value of 100 mT. The measured detector performance (electronic noise and energy resolution) is in good agreement with the results obtained under optimal laboratory conditions. Most importantly, the electronic noise is low enough that it does not limit the sensitivity of the keV sterile neutrino search. Furthermore, the trade-off between energy resolution and pile-up probability has been characterized, and it is now used as an input for ongoing sensitivity studies to optimize the detector rate and the source activity. A solid $^{83\mathrm{m}}$Kr source, as well as mono-energetic electrons emitted from the spectrometer wall, have been used to investigate the detector performance with electrons. Here, an average energy resolution of 266.3 eV FWHM at 20 keV has been measured, which

meets the target for the keV sterile neutrino search. In these measurements, however, an inhomogeneity in the electron energy resolution for different pixels was observed compared to the X-ray measurements. It could be shown that this inhomogeneity can be related to an additional substance deposited on the detector surface, which could be removed successfully with a dedicated cleaning procedure. This cleaning procedure was implemented in the assembly procedure for the consecutive detector modules.

In summary, the assembly procedure developed in the scope of this thesis will be used to construct the nine detector modules required for the final TRISTAN detector system. It was shown that the detector module can be operated together with a MAC-E filter and meets the targeted energy resolution of 300 eV FWHM for the keV sterile neutrino search. In addition, the measured detector properties, such as energy resolution, pixel homogeneity, and linearity, serve as the basis for ongoing sensitivity studies and are used to optimize the beamline configuration for the keV sterile neutrino search. At the time of writing, a replica of the KATRIN detector section with the required modifications to host the TRISTAN detector system is under construction. The first tests with some of the detector modules assembled in this work are foreseen to take place at the end of 2024. The final detector modules will be built in the next months with an expected installation into the KATRIN beamline in 2026 after the neutrino mass measurement campaign has been completed.

APPENDIX

A

SUPPLEMENTARY MATERIAL FOR THE MODULE ASSEMBLY PROCEDURE

In this chapter, additional material that is related to the assembly procedure of the detector module is given. In Chapter A.1 the electrical tests of the SDD chip on the probe station are described in detail. The adaptation of the assembly jigs for the smaller 47 pixel SDD chip are given Chapter A.2. Furthermore, additional tests and observations related to the functionality of detector module assembly are given in Chapter A.3. Last, the detection cover for the safe transportation of the detector modules is described in Chapter A.4.

A.1 Electrical Functionality Tests of the SDD Chip with a Probe Station

Before the assembly of the detector front, the SDD chips are investigated on a probe station in the clean room of the HLL, to check their electrical functionality. The general experimental setup is depicted in Chapter 5.6.1. In the following, the different tests performed on each SDD chip are described.

A.1.1 *Functionality Test of the Integrated Voltage Divider Network*

In the first test, the functionality of the integrated voltage divider between the R1 and RX contacts is checked. As described in Chapter 5.3, there are two separate R1 contacts for each hemisphere and one global RX contact. For each hemisphere, the I-U curve between the R1 and RX contact is measured. A linear behavior following Ohm's law is expected with a resistance of $R_{83} \approx 56.6\,\mathrm{k\Omega}$. To prevent any parasitic currents from flowing between the drift rings through the silicon substrate, its potential is defined by setting the OS contact to ground potential. The equivalent electrical circuit and the parameters used for the measurements are shown in Figure A.1 and listed in Table A.1, respectively.

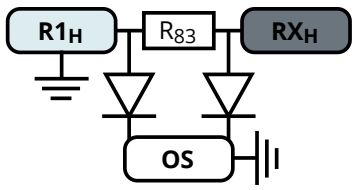

Contact	RX	R1	OS
Applied voltage	0 V to −100 V $\Delta U = -5$ V	0 V	0 V
Compliance	< 10 mA	< 10 mA	< 1 µA

Figure A.1 and Table A.1: Schematic and settings for test of R1-RX network
The figure on the left-hand side shows the equivalent electrical circuit of the measurement of the voltage divider of one hemisphere H between the contacts R1 and RX. The table on the right-hand side lists the applied voltages for each contact and the corresponding maximal currents to not damage any structures on the SDD chip. For a more secure test procedure, the applied voltage starts at 0 V, and then the voltage difference increases in absolute values.

A.1.2 *Functionality Test of the R1-OS Diode*

The drift rings of the voltage divider network are p-doped and, therefore, create diodes in the transition region towards the slightly n-doped silicon substrate. To test the integrity of these diodes and to ensure that their breakthrough voltage is high enough, a negative voltage is applied to the R1 contacts as opposed to the OS contact. An equivalent electrical circuit of the measurement is illustrated in Figure A.2. For a functional TRISTAN SDD chip, the reverse current is expected to be in the order of a few nA for the applied voltages listed in Table A.2.

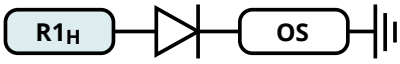

Contact	R1	OS
Applied voltage	0 V to −20 V $\Delta U = -0.5$ V	0 V
Compliance	< 1 µA	< 1 µA

Figure A.2 and Table A.2: Schematic and settings for test of R1-OS diode
The figure on the left-hand side shows the equivalent electrical circuit of the diode measurement between the voltage divider network for each hemisphere H between the R1 and OS contacts. The table on the right-hand side lists the applied voltages for each contact and the corresponding maximal currents to not damage any structures on the SDD chip. For a more secure test procedure, the applied voltage starts at 0 V, and then the voltage difference increases in absolute values.

A.1.3 *Functionality Test of the IGR-DR Diode*

To investigate the integrity of the diode created by the IGR implantation, its reverse bias I-U curve is measured with respect to the global DR contact. The DR contact is used since it is connected to the n-doped implantation in proximity (inside) the IGR. The equivalent electrical circuit for the measurement is illustrated in Figure A.3. For each hemisphere, the IGR implantations are connected to one common bond pad in parallel. The same holds for the DR implantations. Therefore, all 83 IGR-DR diodes are measured in parallel. The measurement is performed once per hemisphere, and for a functional SDD chip, the measured reverse current is below 1 nA.

Contact	IGR	DR
Applied voltage	0 V to −20 V $\Delta U = -0.5$ V	0 V
Compliance	< 1 µA	< 1 µA

Figure A.3 and Table A.3: Schematic and settings for test of IGR-DR diode
The figure on the left-hand side shows the equivalent electrical circuit of the diode measurement between the IGR and DR implantation for each hemisphere H. The table on the right-hand side lists the applied voltages for each contact and the corresponding maximal currents to not damage any structures on the SDD chip.

A.1.4 *Functionality Test of the Diode between Reset Lines and DR*

As described in Chapter 5.4, the collected charges at the anode are drained via the pulsed reset mechanism. The integrity of the corresponding reset diodes on each anode can be tested by applying a negative voltage between the DR contact and the reset (Res) contacts of the individual reset groups. The currents flow from the n-doped DR implantation through the silicon substrate to the nearby anode, which is connected to the reset diode. The measurement is performed for all 14 reset groups, in which twelve reset diodes (in two cases eleven diodes) are connected in parallel. The simplified equivalent electrical circuit is illustrated in Figure A.4. The applied voltages for the measurement are listed in Table A.4. For a functional SDD chip, the reverse bias current is expected to be below 1 nA.

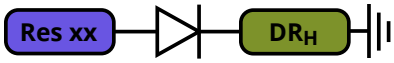

Contact	Res xx	DR
Applied voltage	0 V to −20 V $\Delta U = -0.5$ V	0 V
Compliance	< 1 µA	< 1 µA

Figure A.4 and Table A.4: Schematic and settings for test of Reset-DR diodes
The figure on the left-hand side shows the equivalent electrical circuit of the diode measurement between the anodes of one reset group Res xx and the DR contact. The anodes themselves can only be accessed indirectly via the DR contact. The table on the right-hand side lists the applied voltages for each contact and the corresponding maximal currents to not damage any structures on the SDD chip.

A.1.5 *Integrity Test of the Insulator for the Feedback Capacitors*

To test the FB capacitor insulation of each anode, a positive and negative voltage is applied to the anode of each pixel. Since the anodes are not accessible directly, they are connected through the silicon substrate to the n-doped DR implantation in the center of the anodes. The simplified equivalent electrical circuit and the applied voltages for the measurement are shown in Figure A.5 and listed in Table A.5, respectively. This measurement is performed individually for each FB xx-yy contact with an automatic probe needle. A constant current below 1 pA is expected for all applied voltages for a functional pixel.

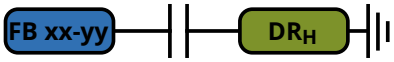

Contact	FB xx-yy	DR
Applied voltage	$-5\,\mathrm{V}$ to $5\,\mathrm{V}$ $\Delta U = 0.5\,\mathrm{V}$	$0\,\mathrm{V}$
Compliance	$< 1\,\mu\mathrm{A}$	$< 1\,\mu\mathrm{A}$

Figure A.5 and Table A.5: Schematic and settings for feedback capacitor insulation tests The figure on the left-hand side shows the equivalent electrical circuit to test the FB capacitors of each anode for the individual pixels. The anodes can only be accessed indirectly via the global DR contacts of each hemisphere H. The table on the right-hand side lists the applied voltages for each contact and the corresponding maximal currents to not damage any structures on the SDD chip.

A.1.6 *Drain Characteristics of the Integrated nJFETs*

To test the functionality and homogeneity of the nJFET integrated into the anode of each pixel, its drain and input characteristics are measured. The gate contact of the nJFET cannot be accessed directly. However, due to its connection to the n-implantation of the anode, it can be accessed indirectly through the OS contact. To protect the nJFET from any parasitic current, a negative voltage is applied to the IGR.

The drain characteristic is measured as illustrated in the equivalent electrical circuit in Figure A.6. The measurement is performed using a shorted gate-source configuration ($U_{\mathrm{GS}} = 0\,\mathrm{V}$), where the drain-source voltage U_{DS} is varied in the range form $0\,\mathrm{V}$ to $-5\,\mathrm{V}$. The applied voltages for the individual contacts are listed in Table A.6. A typical measurement of the drain characteristic is shown in Figure A.8a.

In the next step, the input characteristics of the nJFETs are measured using the same connection scheme but with different voltage settings as shown in Figure A.7 and listed in Table A.7, respectively. The gate-source voltage U_{GS} is varied in a range from $0\,\mathrm{V}$ to $-5\,\mathrm{V}$ via the indirect connection through the OS contact. A typical measurement is shown in Figure A.8b.

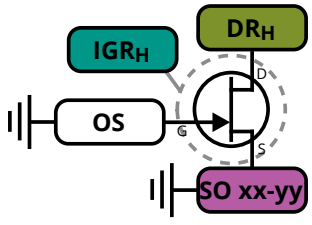

Contact	DR	SO xx-yy	OS	IGR
Applied voltage	$0\,\mathrm{V}$ to $-5\,\mathrm{V}$ $\Delta U = 0.2\,\mathrm{V}$	$0\,\mathrm{V}$	$0\,\mathrm{V}$	$-8\,\mathrm{V}$
Compliance	$< 10\,\mathrm{mA}$	$< 10\,\mathrm{mA}$	$< 1\,\mu\mathrm{A}$	$< 1\,\mu\mathrm{A}$

Figure A.6 and Table A.6: Schematic and settings for the nJFET drain investigations The figure on the left-hand side shows a simplified equivalent electrical circuit to measure the drain characteristics of the nJFETs integrated into the anode of each pixel. The gate can only be accessed indirectly through the silicon substrate and its OS connection. On the right-hand side, the applied voltages for each contact and the corresponding maximal currents to not damage any structures on the SDD chip are listed in the table.

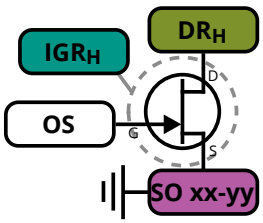

Contact	OS	SO xx-yy	DR	IGR
Applied voltage	0 V to −5 V $\Delta U = -0.2$ V	0 V	5 V	−8 V
Compliance	< 10 mA	< 10 mA	< 1 µA	< 1 µA

Figure A.7 and Table A.7: Schematic and settings for the nJFET input investigations
The figure on the left-hand side shows a simplified equivalent electrical circuit to measure the input characteristics of the nJFETs integrated into the anode of each pixel. The gate can only be accessed indirectly over the silicon substrate and its OS connection. On the right-hand side, the applied voltages for each contact and the corresponding maximal currents to not damage any structures on the SDD chip are listed in the table.

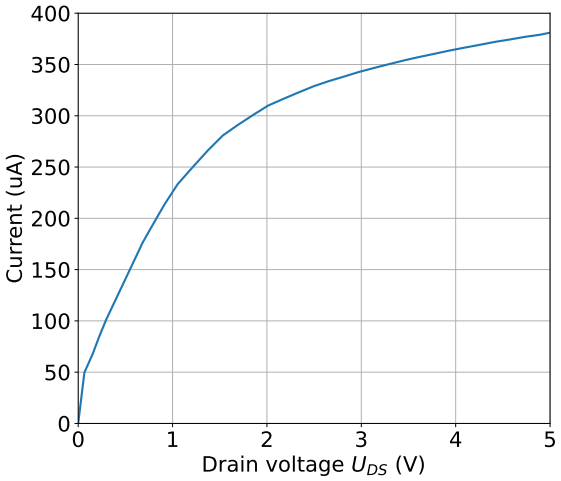

(a) nJFET drain characteristic

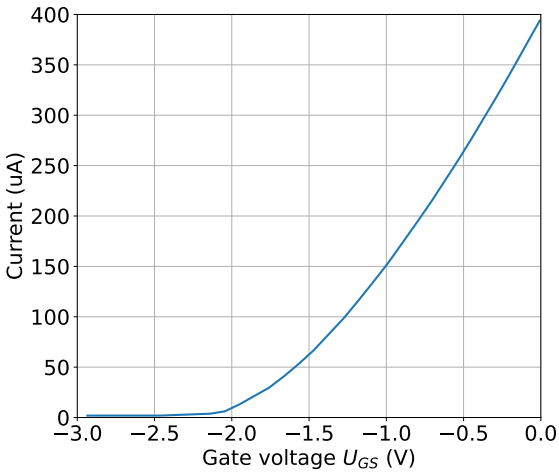

(b) nJFET input characteristic

Figure A.8: Typical measurement of the nJFET characteristics
(a) nJFET drain characteristics in a shorted gate-source configuration using the settings listed in Table A.6. This measurement has been performed on detector S0-166-4. (b) nJFET input characteristics varying the source-gate voltage as described in Figure A.7 and Table A.7. Data provided by P. Lechner.

A.1.7 *Functionality Test of the Entrance Window Diode*

The prober tests described above have been performed using the contacts on the readout side of the SDD chip. To test the functionality of the BC entrance window implantation, the chip is turned to the opposite side. Just as before, the reverse bias I-U curve for the diode between the p-doped implantation for the BC and BF towards the OS is measured. The equivalent electric circuit and the applied voltages are shown in Figure A.9 and listed in Table A.8, respectively. For the TRISTAN SDD chips, a leakage current between 20 pA/cm^2 and 70 pA/cm^2 is expected.

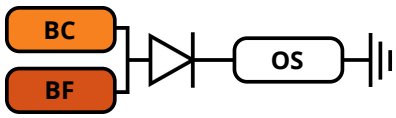

Contact	OS	BC	BF
Applied voltage	0 V to 150 V $\Delta U = 5$ V	0 V	0 V
Compliance	< 1 µA	< 10 µA	< 10 µA

Figure A.9 and Table A.8: Schematic and settings for the BC-OS diode tests
The figure on the left-hand side shows the equivalent electrical circuit to test the BC/BF p-doped implantation on the entrance window side. The table on the right-hand side lists the applied voltages for each contact and the corresponding maximal currents to not damage any structures on the SDD chip.

A.2 Adaptation of the Assembly Procedure for a 47 Pixel SDD Chip

Due to the complexity of the on-module electronics, the ASIC boards were designed in two iterations with an increasing number of channels. In the first iteration, a prototype ASIC board was designed to operate an SDD chip with up to 47 pixels, see [89]. To also test the assembly procedure in this stage of the project, small adaptions were made to the final design in order to account for the geometry of the 47 pixel SDD chip.

A.2.1 *Mechanical Adaptations to Detector Front and Jig*

Similar to the 166 pixel SDD chip, a wire bond has to be connected from a bond pad on the electronic readout side to the RX network, see Figure 5.15b. To account for these wire bond connections in the 166 pixel case, two cavities are machined into the sides of the Cecic interposer. To align the bond connection of the 47 pixel SDD chip with one of the cavities, the 47 pixel SDD chip has to be installed in the corner of the Cesic interposer as illustrated in Figure A.10a. In this configuration, the cut-out of the SDD chip (for the BC and BF contacts) is not aligned with the nose of the rigid-flex PCB. To electrically bypass this gap and to roughly match the dimensions of a 166 pixel SDD chip, a fill-in dummy (L-shaped) from silicon has been designed. It features two aluminum traces and a cut-out edge close to the nose of the rigid-flex PCB.

To support the smaller 47 pixel SDD chip during the assembly, a modified PEEK jig with a smaller inner frame has been designed as shown in Figure A.10b. First, the fill-in dummy is placed inside the jig, since it constrains the position of the 47 pixel SDD chip. Then the glue is applied onto the Cesic interposer[1].

A.2.2 *Bond Connections and Rigid-Flex PCB for 47 Pixel SDD Chip*

The rigid-flex PCB has been designed for the 166 pixel SDD chip. Consequently, it is a priori not compatible with the 47 pixel SDD chip and the ASIC board design. To compensate for this difference, the wire bonding scheme had to be slightly adjusted as shown in Figure A.11a. Due to the positioning of the 47 pixel SDD chip on the Cesic interposer with respect to the rigid-flex PCB, the reset group numbers on the rigid-flex PCB are shifted by 3 compared to

[1] As opposed to the gluing procedure for the 166 pixel SDD chip, the glue was just applied and has not been scraped. This optimization has only been introduced in later iterations of the assembly procedure.

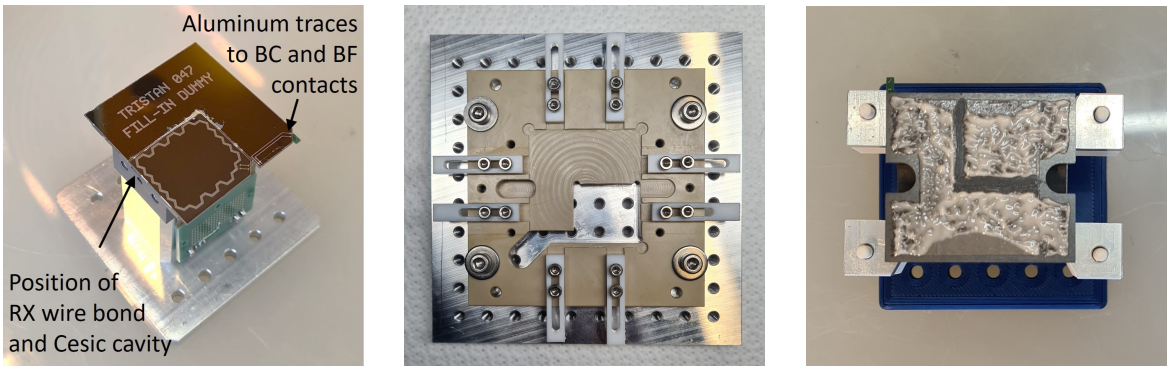

(a) 47 pixel detector front **(b)** Modified PEEK jig **(c)** Glue pattern for 47 pixels

Figure A.10: Assembly modifications for mounting a 47 pixel SDD chip
(a) Photograph of a finished 47 pixel SDD chip with an additional silicon fill-in dummy glued onto a Cesic interposer. (b) Modified PEEK jig to accommodate a 47 pixel SDD chip wit a surrounding silicon fill-in dummy. (c) Adaptation of the glue pattern to reduce the leaking through the gap between the SDD chip and the fill-in dummy.

the SDD chip reset group numbers[2]. For pixel 01-03, the direct connection (illustrated by the red arrows) would be connected to channel 04-01 on the prototype ASIC board. This channel does neither exist on the 47 pixel SDD chip[3] nor on the prototype ASIC board. To connect pixel 01-03 to a working channel of the prototype ASIC board, another set of wire bonds is placed towards channel 04-11 on the rigid-flex PCB as illustrated by the second set of the red arrows[4]. Due to the additional line on the rigid-flex PCB, the two next pixels (in the figure indicated by the grey arrows) do not end up on their corresponding channel numbers on the prototype ASIC board. In this configuration with the red and grey connections, all channels terminate on the prototype ASIC board, but the permutation of the channel numbers has to be taken into account.
The second modification of the bonding scheme is illustrated by the blue arrow in Figure A.11a. The drain bus connection (DR) of the SDD chip is bonded to the source line source (SO)-03-10 of the rigid-flex PCB. Also, this connection does not terminate on the prototype ASIC board. To connect this line to the drain contact on the prototype ASIC board, an additional wire is added to the rigid-flex PCB between the via of line SO-03-10 and the filter capacitor of the drain line as illustrated in Figure A.11b.

[2] As an example, pixel 01-05 is connected to line 04-05 on the rigid-flex PCB, pixel 02-xx to line 05-xx etc.
[3] This pixel has to be removed in the chip layout due to the cut-out required for the BC and BF contacts.
[4] In theory, a direct connection between the bond pads of the SDD chip for pixel 01-03 to the lines of channel 04-11 would be beneficial, but this intermediate step over the not connected bond pads 04-01 is much easier to be bonded and did not show any drawbacks in the pixel performance.

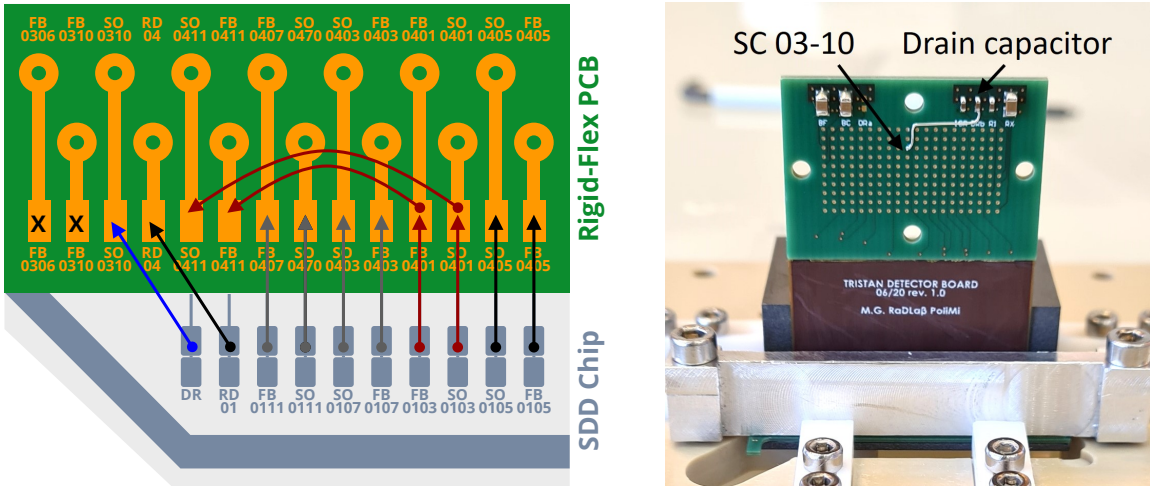

(a) Wire bond modifications for 47 pixels **(b)** Rigid-flex PCB patch for 47 pixels

Figure A.11: Modifications of the electrical connections for the 47 pixel SDD chip
The patch is designed for the 47 channel prototype ASIC board. (a) Schematic of the wire bonding scheme between the 47 pixel SDD chip and the rigid-flex PCB. The red arrows indicate the modifications with two additional wire bonds for pixel 01-03. In gray, the direct bond connections that end up on different channel numbers are illustrated. The modifications for the drain connection are depicted in blue. (b) Photograph of the modified rigid-flex PCB with an additional wire soldered between the SC-03-10 via and the drain capacitor to account for the modifications in the wire bonds.

A.3 Observations connected to the Assembly Procedure

In Chapter A.3.1, the functionality test of the rigid-flex PCB is given. Furthermore, the likely damage of a SDD chip due to an uneven PEEK assembly jig is described in Chapter A.3.2.

A.3.1 *Functionality Check of Rigid-Flex PCB for Detector S0-47-4*

During the assembly of the first detector fronts (using the glue with spacer pills mixed into it) approximately 10 % of the pixels are malfunctioning. To exclude the rigid-flex PCB as the cause of this issue, the bond scheme of the already assembled detector S0-47-4 has been modified. Here, the idea is that for pixels which show an undistorted waveform, both the pixel on the SDD chip and the corresponding FB and SC lines of the rigid-flex PCB are intact and functional, while for the malfunctions the rigid-flex PCB lines could be damaged. As illustrated by the red arrows in Figure A.12a the bonds from a working pixel 01-09 are connected to the presumably malfunctioning lines 01-05 of the rigid-flex PCB. The same modification has been performed on pixel 02-07. In this modified configuration no distortions on the waveforms could be observed, excluding the rigid-flex PCB as the cause of the damaged pixels 01-05 and 02-07.

For completes, also the opposite test has been performed, where the functional lines 02-04 and 02-02 from the rigid-flex PCB are connected to the malfunctioning pixels 02-08 and 02-06 as shown in Figure A.12b. For these pixels the distortions on the waveform level stayed the same.

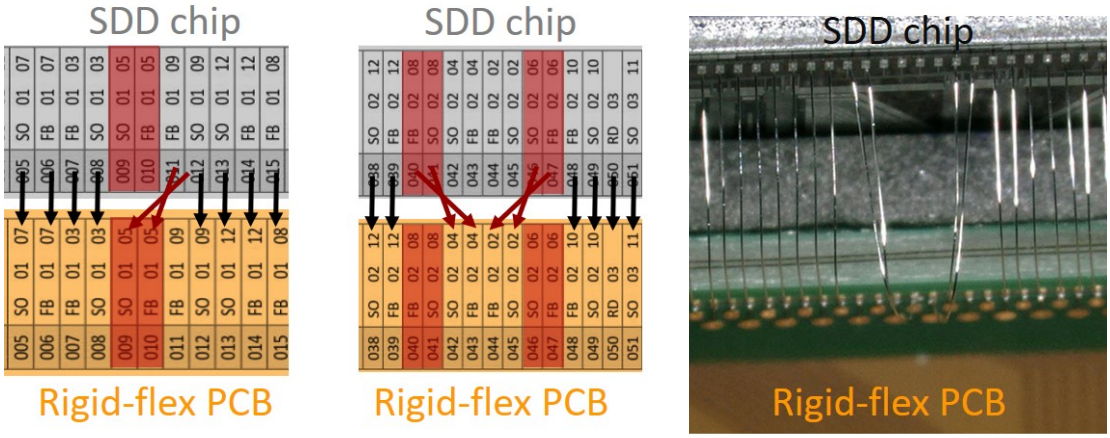

(a) Broken flex test **(b)** Broken pixel test **(c)** Picture of bond modification

Figure A.12: Assembled test of rigid-flex PCB with detector S0-47-4
Illustration of the bond contacts between the SDD chip and rigid-flex PCB. For the standard bonding scheme (illustrated by the black arrows) distorted waveform are observed for pixels 01-05, 02-06, 02-07 and 02-08. The adaptation of the bonding scheme of detector S0-47-4 to test the functionality of the rigid-flex PCB lines are illustrated by the red arrows. (a) Modification of the bond wires from a working pixel to a presumably defective lines on the rigid-flex PCB. (b) Modification to the bond wires from a malfunctioning pixel to working lines on the rigid-flex PCB. (c) Microscope picture of the bond modification seen in (b).

A.3.2 *Uneven Surface of PEEK Base Plate Contact Area to SDD Chip*

During the assembly of the prototype detector S0-47-2 with 47 pixels and Cesic interposer, a crack of the SDD chip has been observed. An approximately rectangular piece of the SDD chip snapped at one corner. It can be seen in Figure A.13a as the slightly darker region in the corner of the SDD chip. This corner aligns with an imperfection of the used spare assembly jig seen in Figure A.13b. Due to a manufacturing mistake, one corner of the jig was not perfectly flat and had a small offset by less than 0.05 mm. The offset in the jig was created, since the milling cutter ended its program at this position in the corner and continued rotating. Due to the rotation without any lateral feed (movement), the milling cutter took a little bit more material away than for the rest of the part (where the cutter was also moving lateral).

The current explanation of the crack is that during the bonding of the outer most bond wires the SDD chip was pushed into free space. This created a leaver arm in the chip along the edge of the two different heights of the jig. The applied force and vibrations from the bonding bend the chip and created the crack. Due to this crack the detector was not functional.

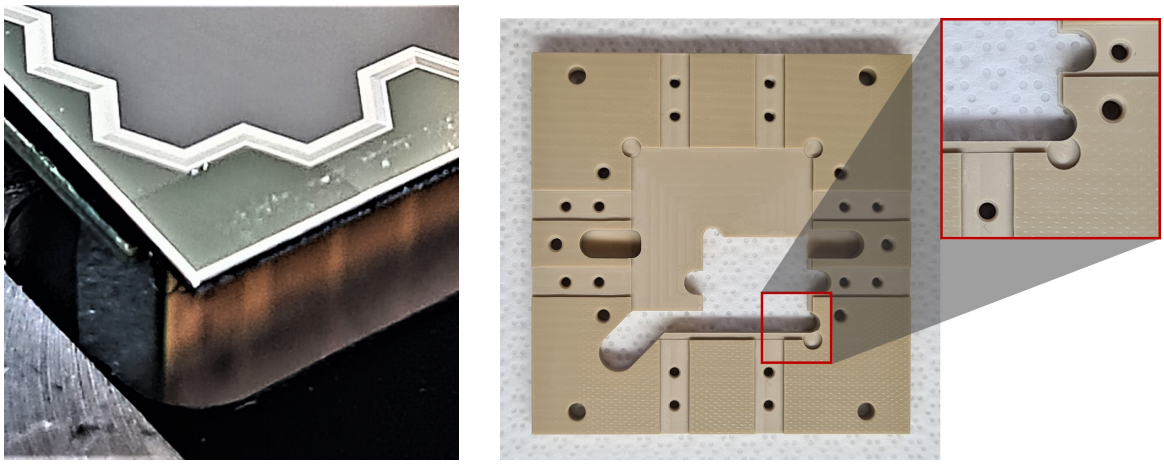

(a) Crack on 47 pixels SDD chip **(b)** Uneven PEEK jig for 47 pixels 3D detector

Figure A.13: Effect of uneven contact area between SDD chip and spare PEEK jig
(a) shows a crack in one corner of the SDD chip of the 47 pixels prototype detector S0-47-2. (b) shows the used spare PEEK jig during the gluing to the Cesic interposer and bonding. In the lower right corner of the jig a small imperfection can be seen. Here the surface is slightly lower ($< 0.05\,\text{mm}$) than the rest of the jig where the SDD chip contacts.

A.4 Protection Cover for the Detector Front

To safely transport the detector front of the SDD chip and Cesic interposer a protection cover has been developed. Two protection jaws are fixed to the Cesic interposer with the M2.5 threads on its side and are connected together with two long M3 bolts. They are designed in such a way, that they can not damage any bond wires of the electronics side, as soon as all screws are installed (but not necessarily tightened). Additionally, these protection jaws can be mounted to the Cesic interposer, while the detector front is installed inside the PEEK jig. Nevertheless, with the experience gained during the first assemblies this feature is not really used anymore. The protection hat can be installed from the top, to cover the SDD chip and encapsulate the detector front with only small gaps where the rigid flex PCBs leave. As a safety feature the two 'ears' on the sides of the protection hat prevent the access to the M2.5 bots. If they are loosened before the protection hat is removed, it could fall into the SDD chip.

The parts are manufactured from aluminium to minimize the out gassing. Therefore, it is possible to leave, e.g., the protection jaws installed on the detector module for measurements under vacuum. Additionally, it should minimize the risk of any material being deposited on the entrance window of the SDD chip coming from the protection cap.

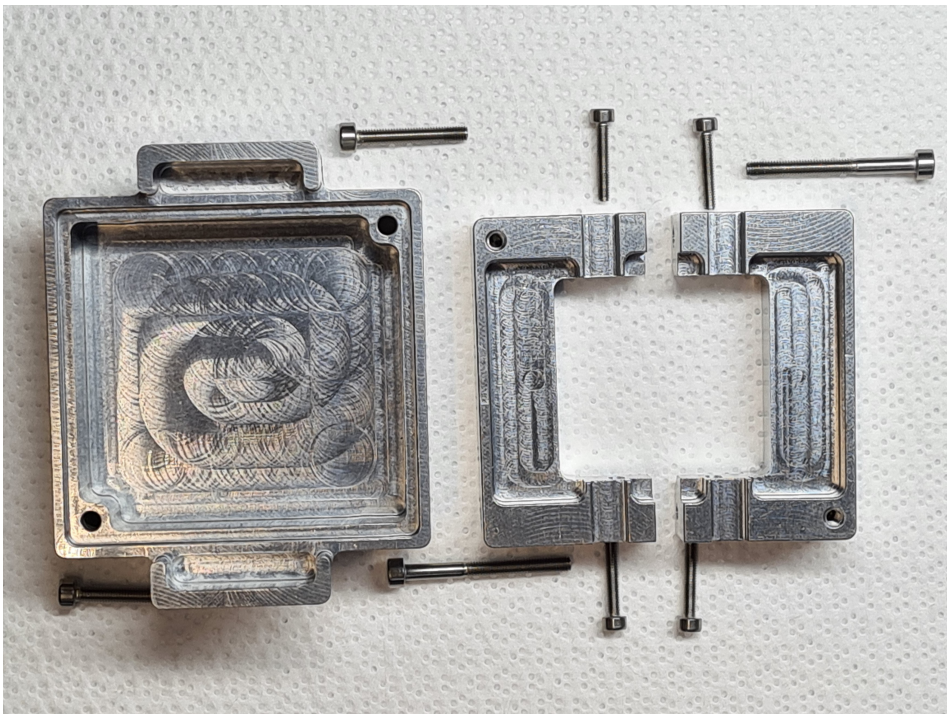

Figure A.14: Photograph of protection cap
The protection hat is shown on the left hand slide, seen from the direction of the SDD chip. It can be installed on top of the two identical protection jaws shown on the right hand side. The various stainless steel bolts required for the assembly of the protection cover are shown roughly at the position where they get installed. Two identical protection jaws

B

OVERVIEW OF THE ASSEMBLED MODULES

In this chapter, an overview of the technical details and most important characteristics of the detector fronts S0-166-1 to S0-166-6 assembled in this work are given. For the characterization of all detector fronts, the same (first) ASIC board design has been used. In the following, they are listed in the order in which they have been assembled.

Table B.1: Overview of assembled detector modules

Detector	Glue method	Working pixel	$\overline{\Delta E}$ X-Ray	$\overline{\Delta E}$ 5 keV e^-
S0-166-1	Glue with spacer pills (70 µm)	146	-	-
S0-166-2	Kapton stripes (125 µm)	165	198 eV*	377 eV
S0-166-3	PET stripes (190 µm)	165	194 eV*	357 eV
S0-166-4	PET stripes (190 µm)	166	144 eV	336 eV
S0-166-5	PET stripes (190 µm)	162	158 eV	216 eV
S0-166-6	PET stripes (190 µm)	165	143 eV	198 eV

B.1 Detector S0-166-1 (D.Va)

This detector front made from wafer chip SDD33.2 W01-F.06 (code name D.Va) (S0-166-1) has been build with the glue (EPO-TEC 920-F [110]) containing spacer pills with a diameter of approximately 70 µm. After the commissioning of the detector, 20 pixels show distortions on the waveform level, which makes them unusable for any spectroscopic measurement. Representative waveforms from the ETTORE first stage output are shown in Figure B.1a. In green, the exemplary waveform of the functional pixel 01-02 is shown. Each other color shows an exemplary pixel representative for a pixel group with similar behavior.

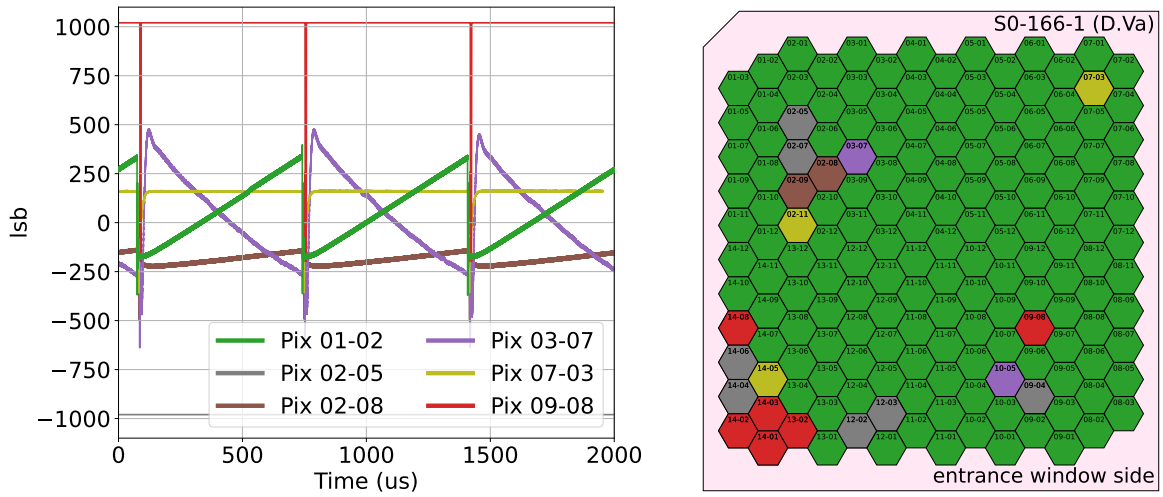

(a) Typical waveform per shape

(b) S0-166-1 Working pixels

Figure B.1: Typical waveform shapes for malfunctioning pixels of detector S0-166-1
(a) Measured waveforms for the first stage ETTORE output of detector S0-166-1. The reset period in this measurement is approximately 650 µs. Each color and pixel represents a group of pixels with similar behaviours on the waveform level. Green represents the functional pixels. (b) Pixel map using the same color scheme as (a) to indicate the positions of pixels with similar behaviors.

Table B.2: Technical data of detector S0-166-1
For the assembly of this detector, the glue containing spacer pills with a diameter of 70 µm has been used. These spacer pills are likely the cause of the malfunctioning pixels, see Chapter 5.6.5.

Detector ID	S0-166-1
Code name	D.Va
Chip number	SDD33.2 W01-F.06
Assembly date	21.07.2021
Glue method	Glue with spacer pills (70 µm)
Entrance window cleaning	No
Working pixels	146

B.2 Detector S0-166-2 (Mercy)

This detector front made from wafer chip SDD33.2 W08-F.11 (code name Mercy) (S0-166-2) is the first detector that has been assembled using four 125 mm-thick Kapton stipes and the glue without spacer pills. All pixels are functional, but pixel 14-04 shows signs of random telegraph noise (RTN) noise which distorts the spectrum. In this wafer production SDD33.2, a higher resistivity on the DR bus lines has been observed, which worsens (increases) the energy resolution towards the center of the SDD chip.

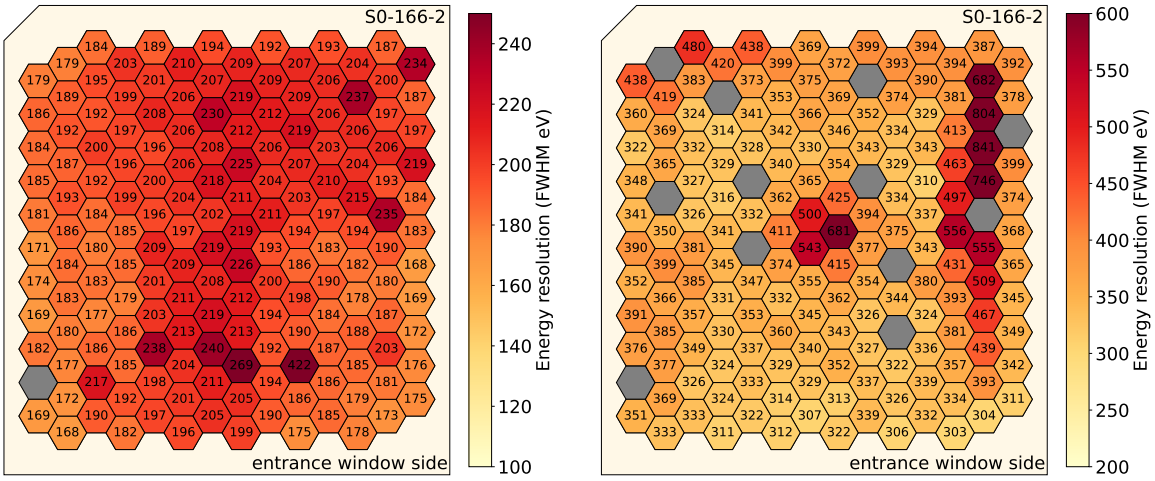

(a) X-ray energy resolution for Mn-K$_\alpha$ line

(b) Electron energy resolution at 5 keV

Figure B.2: Typical energy resolution pixel map of detector S0-166-2
An X-ray and electron measurement has been performed at $T_{\mathrm{SDD}} \approx 15\,^{\circ}\mathrm{C}$ and $T_{\mathrm{SDD}} \approx -30\,^{\circ}\mathrm{C}$, respectively. The pixels filled in grey had connection problems or RTN during the measurement. (a) Typical pixel map obtained for the Mn-K$_\alpha$ line from an ^{55}Fe calibration source. (b) Typical pixel map obtained for electrons with an energy of 5 keV. As a note, the entrance window of this detector has not been cleaned.

Table B.3: Technical data of detector S0-166-2
For the assembly of this detector, the procedure described in Chapter 5.6 has been used without the cleaning of the entrance window (see Chapter 5.6.2). *In the X-ray measurement, the detector was only slightly cooled down, and therefore, its temperature was $T_{\mathrm{SDD}} \approx 15\,^{\circ}\mathrm{C}$.

Detector ID	S0-166-2
Code name	Mercy
Chip number	SDD33.2 W08-F.11
Assembly date	25.02.2022
Glue method	Kapton stripes (125 µm)
Entrance window cleaning	No
Working pixels	165
Mean X-ray energy resolution Mn-K$_\alpha$ line (FWHM)	198 eV*
Mean electron energy resolution at 5 keV (FWHM)	377 eV

B.3 Detector S0-166-3 (Echo)

This detector front made from wafer chip SDD33.2 W07-B.06 (code name Echo) (S0-166-3) is the first detector that has been assembled with the 190 mm-thick PET stripes attached to the Cesic interposer. No entrance window cleaning has been applied to this detector. In this wafer production SDD33.2, a higher resistivity on the drain bus lines has been observed, which increases the energy resolution towards the center of the SDD chip.

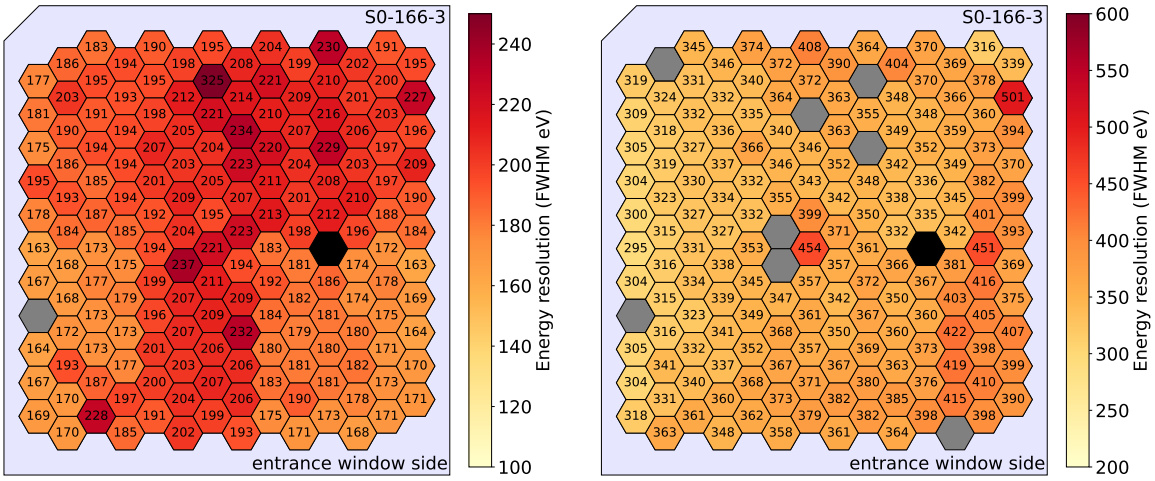

(a) X-ray energy resolution for Mn-K_α line **(b)** Electron energy resolution at 5 keV

Figure B.3: Typical energy resolution pixel map of detector S0-166-3
An X-ray and electron measurement has been performed at $T_{\mathrm{SDD}} \approx 15\,^{\circ}\mathrm{C}$ and $T_{\mathrm{SDD}} \approx -30\,^{\circ}\mathrm{C}$, respectively. The pixels filled in grey had connection problems during the measurement. The pixel in black is not functional, the origin is still under investigation. (a) Typical pixel map obtained for the Mn-K_α line from an ^{55}Fe calibration source. (b) Typical pixel map obtained for electrons with an energy of 5 keV. As a note, the entrance window of this detector has not been cleaned.

Table B.4: Technical data of detector S0-166-3
For the assembly of this detector, the procedure described in Chapter 5.6 has been used without the cleaning of the entrance window (see Chapter 5.6.2). *In the X-ray measurement, the detector was only slightly cooled down and therefore its temperature was $T_{\mathrm{SDD}} \approx 15\,^{\circ}\mathrm{C}$.

Detector ID	S0-166-3
Code name	Echo
Chip number	SDD33.2 W07-B.06
Assembly date	24.03.2022
Glue method	PET stripes (190 µm)
Entrance window cleaning	No
Working pixels	165
Mean X-ray energy resolution Mn-K_α line (FWHM)	194 eV*
Mean electron energy resolution at 5 keV (FWHM)	357 eV

B.4 Detector S0-166-4 (Winston)

This detector front made from wafer chip SDD33.3 W04-F.06 (code name Winston) (S0-166-4) is the main detector used in this work. It has been utilized for most of the characterizations with X-rays, which are described in Chapter 6. Additionally, this detector module has been installed into the MoS, see Chapter 7. No entrance window cleaning has been applied to this detector for the shown measurements.

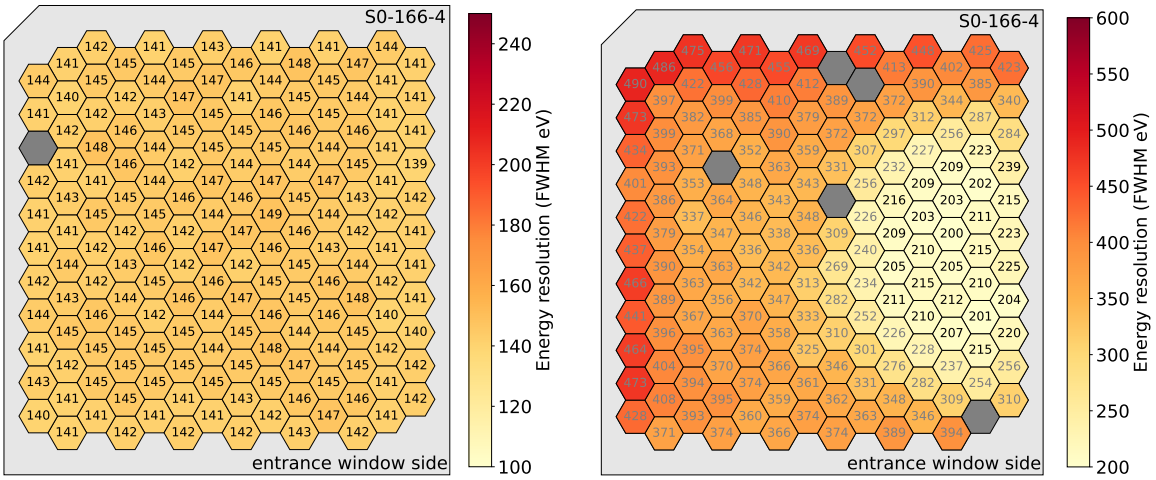

(a) X-ray energy resolution for Mn-K_α line **(b)** Electron energy resolution at 5 keV

Figure B.4: Typical energy resolution pixel map of detector S0-166-4
The measurements have been performed at $T_{\mathrm{SDD}} \approx -30\,^{\circ}\mathrm{C}$. The numbers and colors inside each pixel give the energy resolution in terms of FWHM. The pixels filled in grey had connection problems during the measurement. (a) Typical pixel map obtained for the Mn-K_α line from an ^{55}Fe calibration source. (b) Typical pixel map obtained for electrons with an energy of 5 keV. As a note, the entrance window of this detector has not been cleaned.

Table B.5: Technical data of detector S0-166-4
For the assembly of this detector, the procedure described in Chapter 5.6 has been used without the cleaning of the entrance window (see Chapter 5.6.2).

Detector ID	S0-166-4
Code name	Winston
Chip number	SDD33.3 W04-F.06
Assembly date	07.06.2022
Glue method	PET stripes (190 µm)
Entrance window cleaning	No
Working pixels	166
Mean X-ray energy resolution Mn-K_α line (FWHM)	144 eV
Mean electron energy resolution at 5 keV (FWHM)	336 eV

B.5 Detector S0-166-5 (Brigitte)

This detector front made from wafer chip SDD33.3 W05-F.06 (code name Brigitte) (S0-166-5) has been used to investigate the additional substance observed on the entrance window. The cleaning procedure has been applied after the full assembly of the detector module as described in Chapter 8.3.

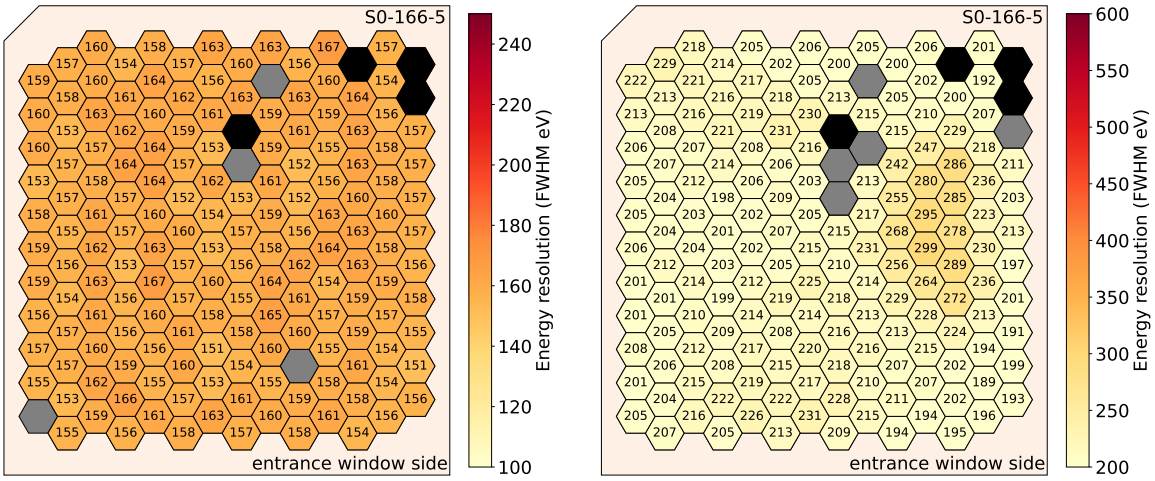

(a) X-ray energy resolution for Mn-K_α line **(b)** Electron energy resolution at 5 keV

Figure B.5: Typical energy resolution pixel map of detector S0-166-5
The measurements have been performed at $T_{\mathrm{SDD}} \approx -30\,^{\circ}\mathrm{C}$. The numbers and colors inside each pixel give the energy resolution in terms of FWHM. The pixels filled in grey had connection problems during the measurement. The pixels in black are not functioning, the origin is still under investigation. (a) Typical pixel map obtained for the Mn-K_α line from an ^{55}Fe calibration source. (b) Typical pixel map obtained for electrons with an energy of 5 keV after the entrance window cleaning with acetone, isopropyl and de-ionized water.

Table B.6: Technical data of detector S0-166-5
For the assembly of this detector, the procedure described in Chapter 5.6 has been. The cleaning procedure of the entrance window surface (see Chapter 5.6.2) has been tested for the first time on this detector.

Detector ID	S0-166-5
Code name	Brigitte
Chip number	SDD33.3 W05-F.06
Assembly date	27.10.2022
Glue method	PET stripes (190 µm)
Entrance window cleaning	After assembly
Working pixels	162
Mean X-ray energy resolution Mn-K_α line (FWHM)	158 eV
Mean electron energy resolution at 5 keV (FWHM)	216 eV

B.6 Detector S0-166-6 (Kiriko)

This detector front made from wafer chip SDD33.3 W05-B.06 (code name Kiriko) (S0-166-6) has been used to investigate the additional substance observed on the entrance window. The cleaning procedure has been applied after the full assembly of the detector module as described in Chapter 8.3.

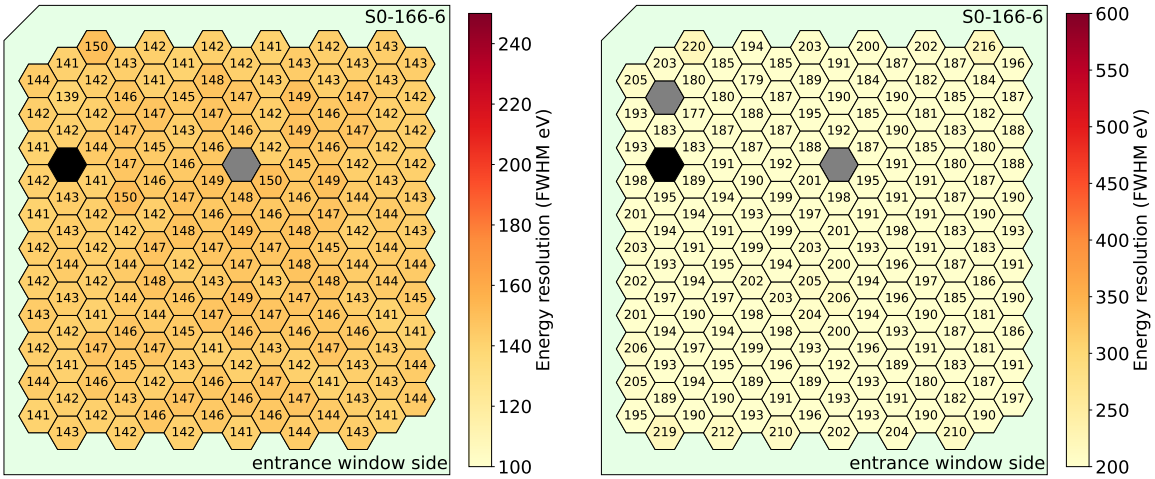

(a) X-ray energy resolution for Mn-K_α line **(b)** Electron energy resolution at 5 keV

Figure B.6: Typical energy resolution pixel map of detector S0-166-6
The measurements have been performed at $T_{\mathrm{SDD}} \approx -30\,^{\circ}\mathrm{C}$. The numbers and colors inside each pixel give the energy resolution in terms of FWHM. The pixels filled in grey had connection problems during the measurement. The pixels in black are not functioning, the origin is still under investigation. (a) Typical pixel map obtained for the Mn-K_α line from an ^{55}Fe calibration source. (b) Typical pixel map obtained for electrons with an energy of 5 keV after the cleaning with acetone, isopropyl and de-ionized water.

Table B.7: Technical data of detector S0-166-6
For the assembly of this detector, the procedure described in Chapter 5.6 has been. The cleaning procedure of the entrance window surface (see Chapter 5.6.2) has also been tested on this detector.

Detector ID	S0-166-6
Code name	Kiriko
Chip number	SDD33.3 W05-B.06
Assembly date	26.04.2023
Glue method	PET stripes (190 µm)
Entrance window cleaning	After assembly
Working pixels	165
Mean X-ray energy resolution Mn-K_α line (FWHM)	143 eV
Mean electron energy resolution at 5 keV (FWHM)	198 eV

C

CHARACTERIZATION MEASUREMENTS

In this chapter, supplementary estimations and characterization measurements are given. An estimation of the number of the electron-hole pairs generated due to leakage current is given in Chapter C.1. The measurement of the current supplied to the R1-RX network is described in Chapter C.2. Supplementary material for the optimization of the detector operation voltage in Chapter 6.2 are given in Chapter C.3. The additional tests performed to exclude the MoS environment as the cause of the inhomogeneity measured in the electron spectrum are shown in Chapter C.4.

C.1 Estimation of Electron-Hole Pairs due to Leakage Current

Semiconductor detectors use the fact that inside their depletion layer, basically, no free charge carriers are apparent, such that they can measure the generated electron-hole pairs induced by external radiation. Nevertheless, in a real device like the TRISTAN SDD at any temperature above absolute zero, electron-hole pairs are generated continuously due to thermal excitation. Due to (unwanted) impurities, this leakage current is increased. The following derivation very roughly estimates the ratio between leakage current-induced electron-hole pairs and ones induced by radiation. Using Equation (4.12) one can estimate that for the Mn-K_α line of ^{55}Fe at 5.9 keV approximately $n_{5.9\text{keV}} = 1625$ electron-hole pairs are generated over a time span of roughly $\Delta t_{\text{radiation}} \leq 1\,\text{ps}$ [75]. The leakage current typical for the TRISTAN SDD is $\dot{Q}_{\text{leak}} \leq 10\,\text{pA}$ already at room temperature (cooling down the detector the leakage current can decrease below 1 pA). The electron-hole pairs generated per second $\dot{Q}_{\text{leak}}$ can be estimated by Equation (C.1). Multiplying this value by the time $\Delta t_{\text{radiation}}$, one can estimate the number of electron-hole pairs n_{leak} generated in the same time span as the electrons generated by the radiation. As shown in Equation (C.5), the electron-hole pairs generated due to leakage current during the radiation process are many orders of magnitude smaller.

$$\dot{Q}_{\text{leak}} = e \cdot \dot{n}_{\text{leak}} \lesssim 10\,\text{pA} \tag{C.1}$$

$$\Leftrightarrow \dot{n}_{\text{leak}} = \frac{\dot{Q}_{\text{leak}}}{e} = \frac{10\,\text{pA}}{1.602 \cdot 10^{-19}\,\text{C}} \approx 6.2 \cdot 10^7/\text{s} \tag{C.2}$$

$$n_{\text{leak}} = \dot{n}_{\text{leak}} \cdot \Delta t_{\text{radiation}} \tag{C.3}$$

$$\Rightarrow n_{\text{leak}} \approx 6.2 \cdot 10^7/\text{s} \cdot 1\,\text{ps} \approx 6.2 \cdot 10^{-5} \tag{C.4}$$

$$1625 = n_{5.9\text{keV}} \gg n_{\text{leak}} \approx 6.2 \cdot 10^{-5} \tag{C.5}$$

Over the entire energy filter time of, e.g., $2 \cdot t_{\text{peaking}} + t_{\text{gap}} = 2 \cdot 2\,\mu\text{s} + 0.3\,\mu\text{s} = 4.3\,\mu\text{s}$ this attributes to approximately 270 electron-hole pairs at room temperature.

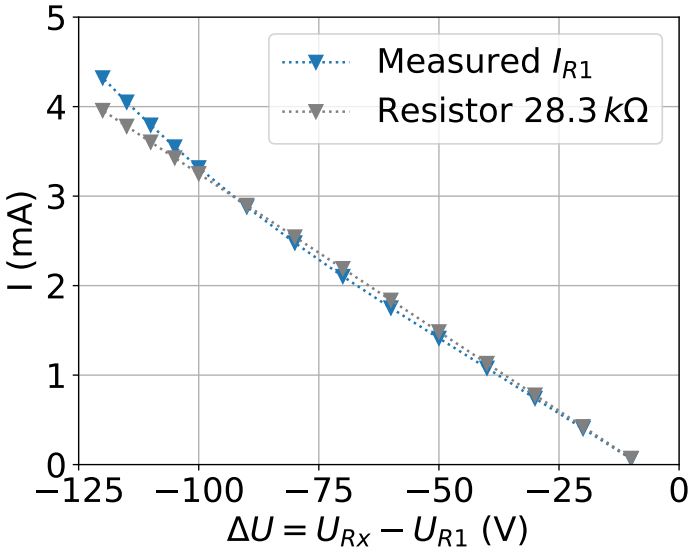

Figure C.1: Measurement of drift ring current
Measurement of the total provided R1 current I_{R1} as a function of applied voltage difference ΔU to the drift ring network. The measurement is performed for the assembled detector S0-166-3 with an externally connected source meter. The measured current is shown in blue, while the expectation with a resistance of 28.3 kΩ is shown in grey.

C.2 Measurement of Drift Ring Currents

To investigate if the SDD chip of detector S0-166-3 has been damaged during the assembly procedure the current through the R1/RX drift ring networks is measured. In Figure C.1 the total current provided to the R1 contacts against the voltage difference $\Delta U = U_{\mathrm{RX}} - U_{\mathrm{R1}}$ in the drift ring resistor network is shown. It is compatible with the expected behavior due to the total resistance of 28.3 kΩ of the drift ring resistor network described in Chapter 5.3.

C.3 Detector Working Point Investigations

Additional graphics for the investigation to find an optimized operation point of detector S0-166-4 which are described in Chapter 6.2.

C.3.1 *nJFet Parameters*

The drain current I_{D} is indirectly set via the voltage U_{SSS} on a constant current generator in the ETTORE ASIC. In Figure C.2 the total count rate and the peak position of the Mn-K$_\alpha$ line are shown for the variation of the drain current I_{D}. In Table C.1, all other detector voltages are listed for this measurement.

In Figure C.3 the total count rate and the peak position of the Mn-K$_\alpha$ line are shown for the variation of the drain voltage U_{D}. The energy resolution as pixel map for the used set point of $U_{\mathrm{D}} = 7.5\,\mathrm{V}$ and the setting of $U_{\mathrm{D}} = 9.5\,\mathrm{V}$ are shown in Figure C.4. For the later measurement, the energy resolution worsens (increases) in many pixels, likely due to impact ionization due to the positive voltage. In Table C.2 all other detector voltages are listed for this measurement.

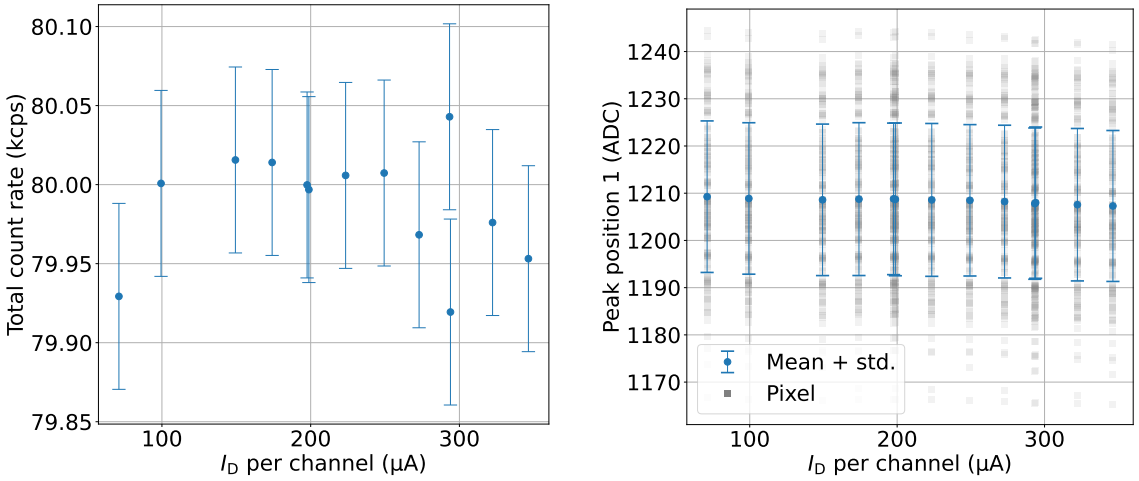

(a) Total count rate against nJFET current I_D **(b)** Peak position for nJFET currents I_D

Figure C.2: Effect of the nJFET current I_D on detector stability
In the measurement all pixels except of 01-07 are functional, which had unrelated connection issue. (a) Total count rate in the detector and the corresponding statistical uncertainty for all functional pixels is shown in blue. (b) The measured peak position of the Mn-K$_\alpha$ line in lsb of each individual pixel is illustrated by the transparent grey squares. The mean and standard deviation per measurement is shown in blue. Additional material to this measurement is shown in Figure 6.7 and Table C.1.

Table C.1: Settings of the nJFET current I_D measurement
Settings for the characterisation of detector S0-166-4. Chiller was set to −50 °C resulting in SDD chip temperature $T_{SDD} \approx -33\,°C$. The reset time is set to $T_{Reset} = 1.5\,\mu s$. These settings correspond to the measurement illustrated in Figure 6.7 and Figure C.2.

U_{SSS}	I_D	U_D	U_{ResH}	U_{ResL}	U_{R1}	U_{RX}	U_{BC}	U_{BF}	U_{IGR}
varied	varied	6.5 V	4.0 V	−10 V	−9.8 V	−121 V	−115 V	−125 V	−20 V

Table C.2: Settings of the drain voltage I_D measurement
Settings for the characterisation of detector S0-166-4. Chiller was set to −50 °C resulting in SDD chip temperature $T_{SDD} \approx -33\,°C$, The reset time is set to $T_{Reset} = 1.5\,\mu s$. These settings correspond to the measurement illustrated in Figure 6.8 and Figure C.3.

U_{SSS}	I_D	U_D	U_{ResH}	U_{ResL}	U_{R1}	U_{RX}	U_{BC}	U_{BF}	U_{IGR}
−3.9 V	200 µA	varied	4.0 V	−10 V	−9.8 V	−121 V	−115 V	−125 V	−20 V

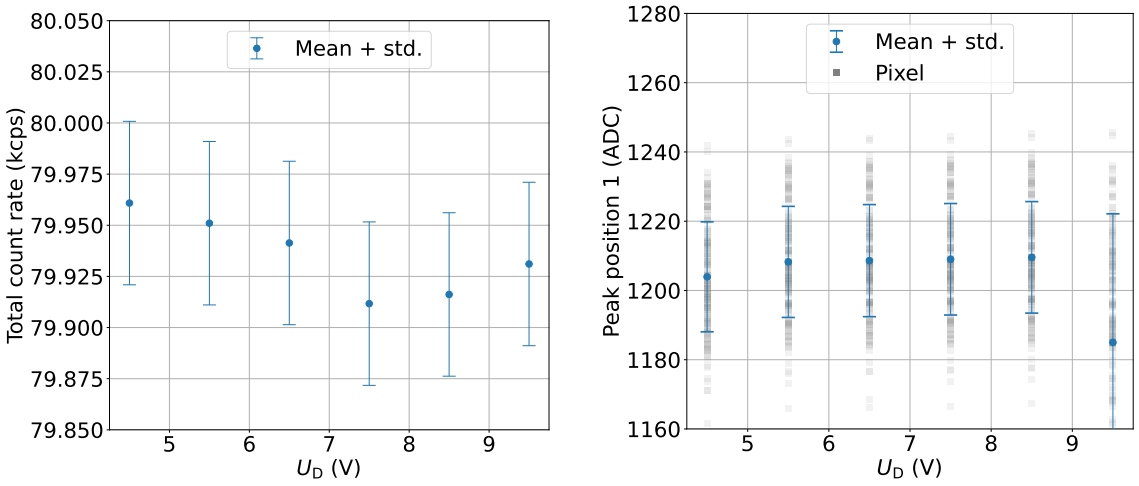

(a) Total count rate against drain voltage U_D **(b)** Peak position against drain voltage U_D

Figure C.3: Effect of the nJFET voltage U_D on detector stability
In the measurement all pixels except of 01-07 are functional, which had unrelated connection issue. (a) Total count rate in the detector and the corresponding statistical uncertainty for all functional pixels is shown in blue. (b) The measured peak position of the Mn-K$_\alpha$ line in lsb of each individual pixel is illustrated by the transparent grey squares. The mean and standard deviation per measurement is shown in blue. Additional material to this measurement is shown in Figure 6.8, Figure C.4 and Table C.2.

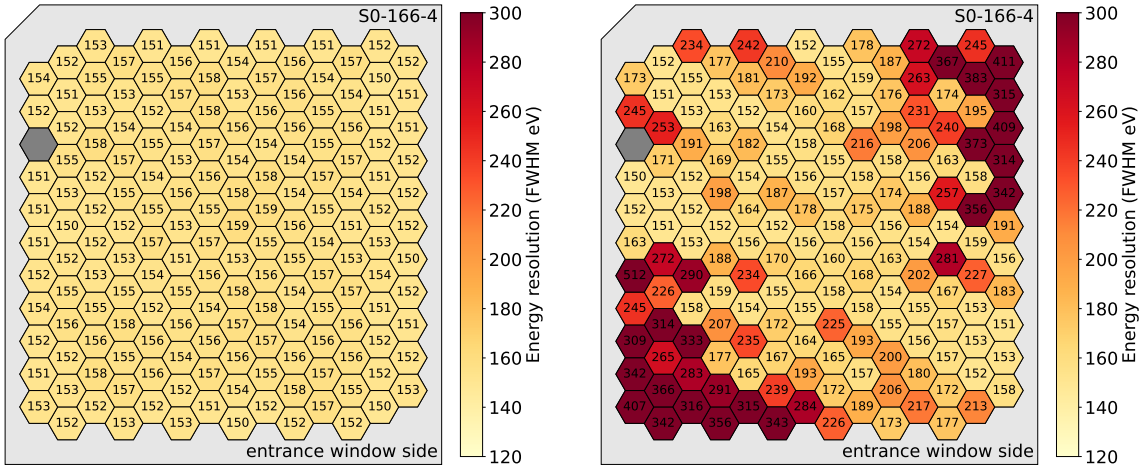

(a) Energy resolution for $U_\mathrm{D} = 7.5\,\mathrm{V}$ **(b)** Energy resolution for $U_\mathrm{D} = 9.5\,\mathrm{V}$

Figure C.4: Pixel map on effect of the nJFET voltage U_D on detector stability
Pixel maps of the measured energy resolution for the Mn-K$_\alpha$ line for different nJFET voltage U_D. The grey pixel 01-07 has an unrelated connection issue already before the measurement. Additional material to this measurement is shown in Figure 6.8, Figure C.3 and Table C.2.

C.3.2 *Reset Parameters*

This chapter contains the additional material for optimizing the reset parameters U_{ResH}, U_{ResL} and T_{Reset} described in Chapter 6.2.2.

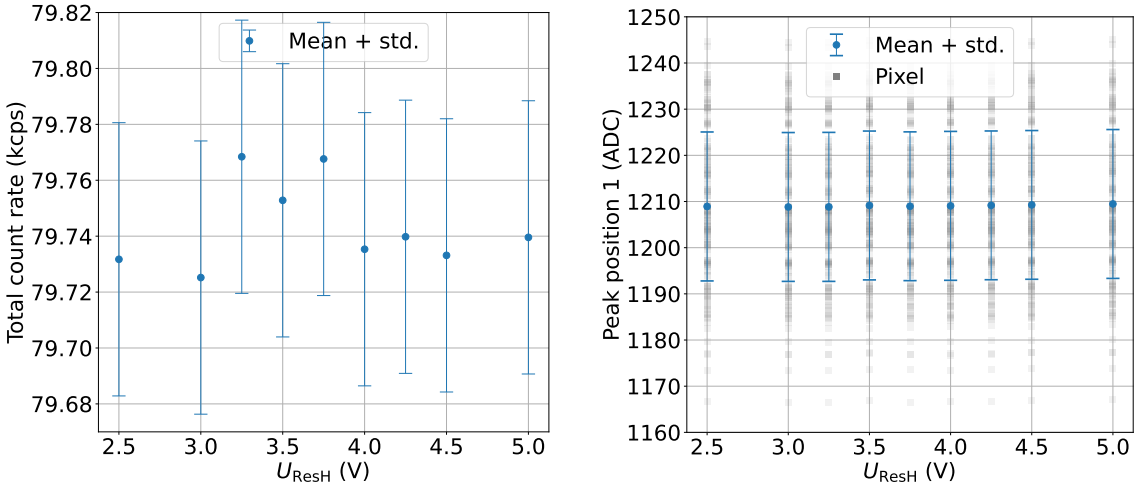

(a) Total count rate against U_{ResH}

(b) Peak position against U_{ResH}

Figure C.5: Effect of U_{ResH} on detector stability
In the measurement all pixels except of 01-07 are functional, which had unrelated connection issue. (a) Total count rate in the detector and the corresponding statistical uncertainty for all functional pixels is shown in blue. (b) The measured peak position of the Mn-K$_\alpha$ line in lsb of each individual pixel is illustrated by the transparent grey squares. The mean and standard deviation per measurement is shown in blue. Additional material to this measurement is shown in Figure 6.9 and Table C.3.

Table C.3: Settings of the U_{ResH} measurement
Settings for the characterisation of detector S0-166-4. Chiller was set to −50 °C resulting in SDD chip temperature $T_{\mathrm{SDD}} \approx -33\,^{\circ}\mathrm{C}$. The reset time is set to $T_{\mathrm{Reset}} = 1.5\,\mu\mathrm{s}$. These settings correspond to the measurement illustrated in Figure 6.9 and Figure C.5.

U_{SSS}	I_{D}	U_{D}	U_{ResH}	U_{ResL}	U_{R1}	U_{RX}	U_{BC}	U_{BF}	U_{IGR}
−3.9 V	200 µA	7.3 V	varied	−10 V	−9.8 V	−121 V	−115 V	−125 V	−20 V

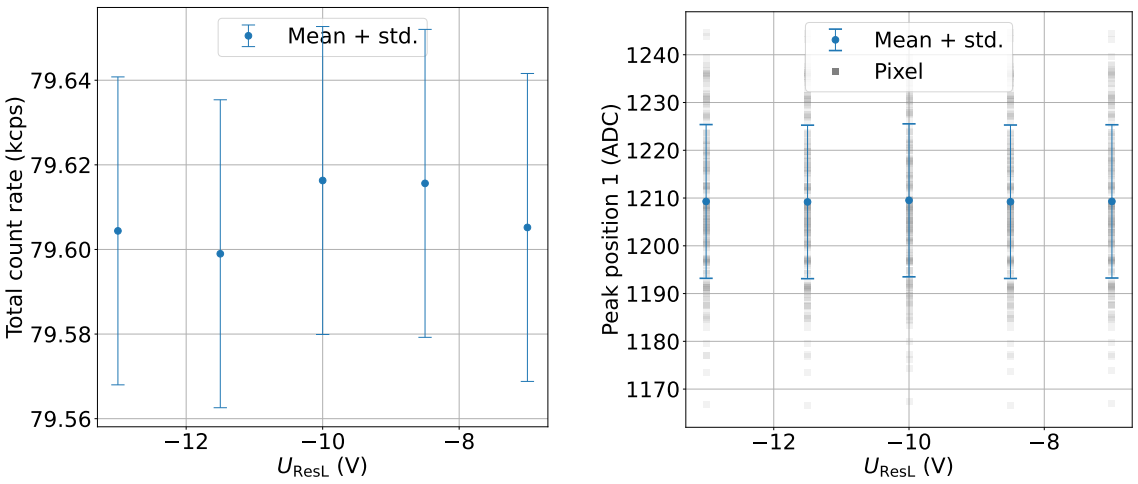

(a) Total count rate against U_{ResL} **(b)** Peak position against U_{ResL}

Figure C.6: Effect of U_{ResL} on detector stability
In the measurement all pixels except of 01-07 are functional, which had unrelated connection issue. (a) Total count rate in the detector and the corresponding statistical uncertainty for all functional pixels is shown in blue. (b) The measured peak position of the Mn-K$_\alpha$ line in lsb of each individual pixel is illustrated by the transparent grey squares. The mean and standard deviation per measurement is shown in blue. Additional material to this measurement is shown in Figure 6.9 and Table C.4.

Table C.4: Settings of the U_{ResL} measurement
Settings for the characterisation of detector S0-166-4. Chiller was set to −50 °C resulting in SDD chip temperature $T_{\mathrm{SDD}} \approx -33\,°\mathrm{C}$ .The reset time is set to $T_{\mathrm{Reset}} = 1.5\,\mu\mathrm{s}$. These settings correspond to the measurement illustrated in Figure 6.9 and Figure C.6.

U_{SSS}	I_{D}	U_{D}	U_{ResH}	U_{ResL}	U_{R1}	U_{RX}	U_{BC}	U_{BF}	U_{IGR}
−3.9 V	200 µA	7.3 V	4.0 V	varied	−9.8 V	−121 V	−115 V	−125 V	−20 V

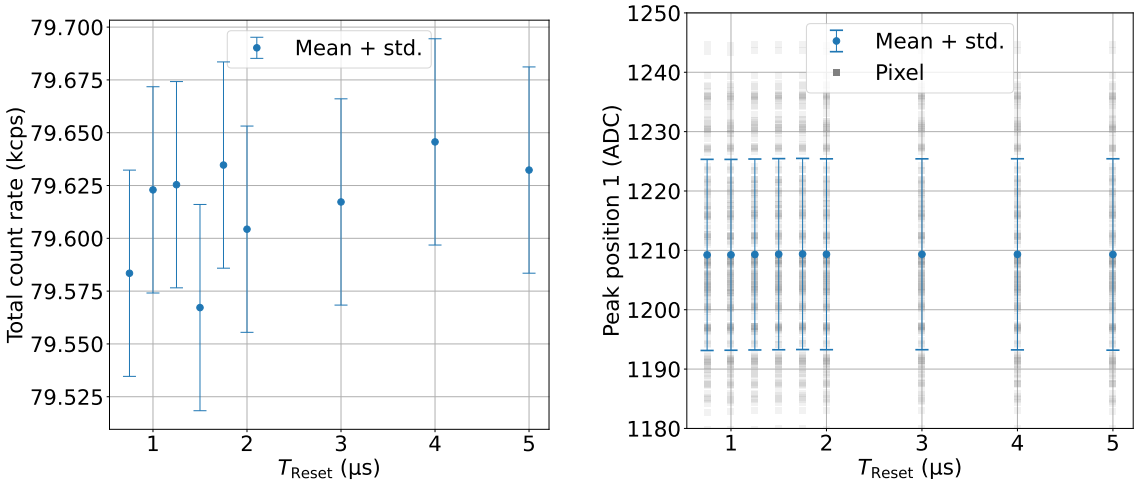

(a) Total count rate against T_{Reset}

(b) Peak position against T_{Reset}

Figure C.7: Effect of T_{Reset} on detector stability
In the measurement all pixels except of 01-07 are functional, which had unrelated connection issue. (a) Total count rate in the detector and the corresponding statistical uncertainty for all functional pixels is shown in blue. (b) The measured peak position of the Mn-K$_\alpha$ line in lsb of each individual pixel is illustrated by the transparent grey squares. The mean and standard deviation per measurement is shown in blue. Additional material to this measurement is shown in Figure 6.9 and Table C.4.

Table C.5: Settings of the T_{Reset} measurement
Settings for the characterisation of detector S0-166-4. Chiller was set to −50 °C resulting in SDD chip temperature $T_{\mathrm{SDD}} \approx -33\,^{\circ}\mathrm{C}$. These settings correspond to the measurement illustrated in Figure 6.9 and Figure C.7.

U_{SSS}	I_{D}	U_{D}	U_{ResH}	U_{ResL}	U_{R1}	U_{RX}	U_{BC}	U_{BF}	U_{IGR}
−3.9 V	200 µA	7.3 V	4.0 V	−10 V	−9.8 V	−121 V	−115 V	−125 V	−20 V

C.3.3 *Inner Guard Ring Voltage U_{IGR}*

This chapter contains the additional material for optimizing the IGR voltage U_{IGR} described in Chapter 6.2.4.

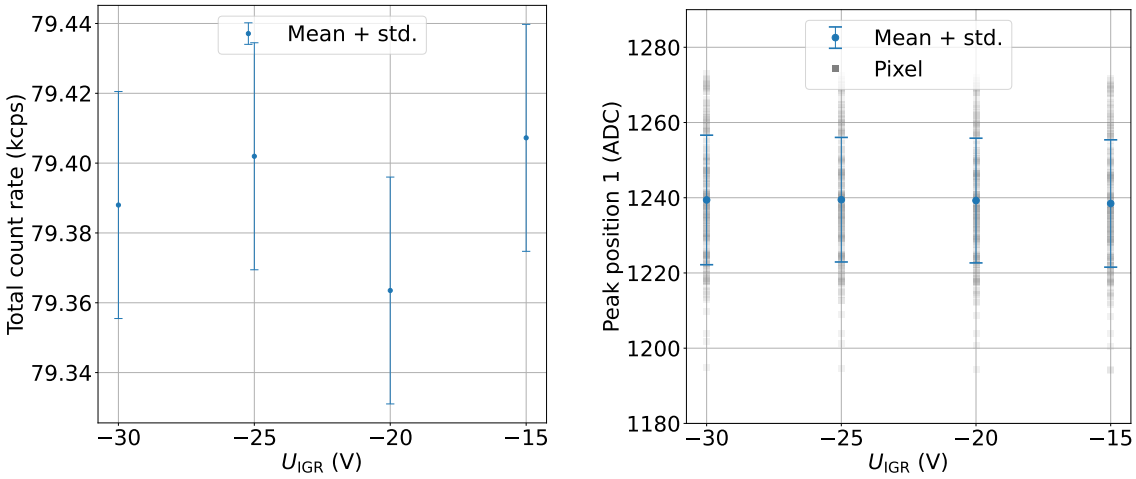

(a) Total count rate against IGR voltage U_{IGR} **(b)** Peak position for IGR voltage U_{IGR}

Figure C.8: Effect of the inner guard ring voltage U_{IGR} on the detector stability
In the measurement all pixels except of 01-07 are functional, which had unrelated connection issue. (a) Total count rate in the detector and the corresponding statistical uncertainty for all functional pixels is shown in blue. (b) The measured peak position of the Mn-K$_\alpha$ line in lsb of each individual pixel is illustrated by the transparent grey squares. The mean and standard deviation per measurement is shown in blue. Additional material to this measurement is shown in Figure 6.11 and Table C.6.

Table C.6: Settings of the inner guard ring voltage U_{IGR} measurement
Settings for the characterisation of detector S0-166-4. Chiller was set to −50 °C resulting in SDD chip temperature $T_{\mathrm{SDD}} \approx -33\,^{\circ}\mathrm{C}$. The reset time is set to $T_{\mathrm{Reset}} = 1.5\,\mu\mathrm{s}$. These settings correspond to the measurement illustrated in Figure 6.11 and Figure C.8.

U_{SSS}	I_{D}	U_{D}	U_{ResH}	U_{ResL}	U_{R1}	U_{RX}	U_{BC}	U_{BF}	U_{IGR}
−3.9 V	200 µA	7.3 V	4.0 V	−10 V	−9.8 V	−121 V	−115 V	−125 V	varied

C.4 Investigations of Pixel Inhomogenaitiy in the MoS

In this chapter, the additional investigations to exclude the MoS environment as the cause of the inhomogeneity observed in the electron energy resolution from Chapter 7.4.6 are given.

C.4.1 *Effect of Detector z-Position on Pixel Inhomogeneity*

Complementary to the measurements of the radial detector module position described in Chapter 7.4.6, the longitudinal z-position of the detector module has been investigated. The energy resolution of the L-32 line observed at the nominal detector position at $z_0 = 2.425\,\mathrm{mm}$ and the shifted detector position at $z_1 = 2.575\,\mathrm{mm}$ are shown in Figure C.9a and Figure C.9b, respectively. The difference in the energy resolution between the two measurements is shown

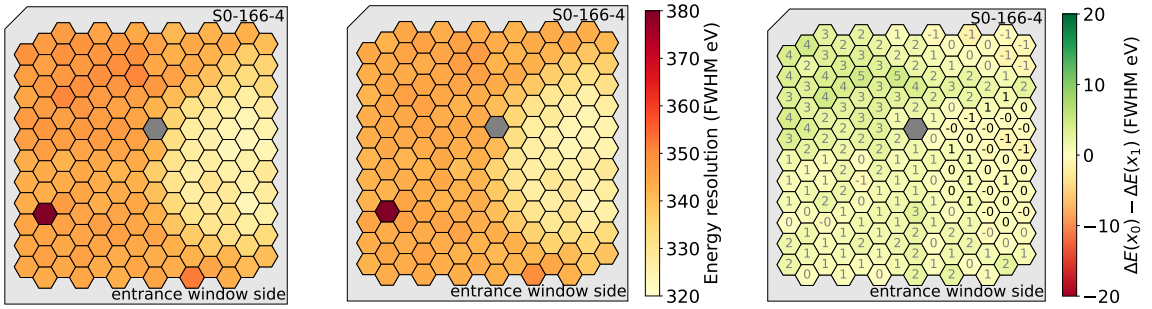

(a) Detector at $z_0 = 2.425\,\mathrm{m}$ **(b)** Detector at $z_1 = 2.575\,\mathrm{m}$ **(c)** Difference of energy resolution

Figure C.9: Influence of the detector z-position on energy resolution
In the pixel maps (a) and (b) the energy resolution measured for the L-32 line of the ^{83m}Kr source are shown. The color scale is the same for both figures. The detecor has been moved from the nominal position $z_0 = 2.425\,\mathrm{m}$ ($\approx 0.1\,\mathrm{T}$) to $z_1 = 2.575\,\mathrm{m}$ ($\approx 0.03\,\mathrm{T}$). (c) Difference of energy resolution between the two measurements.

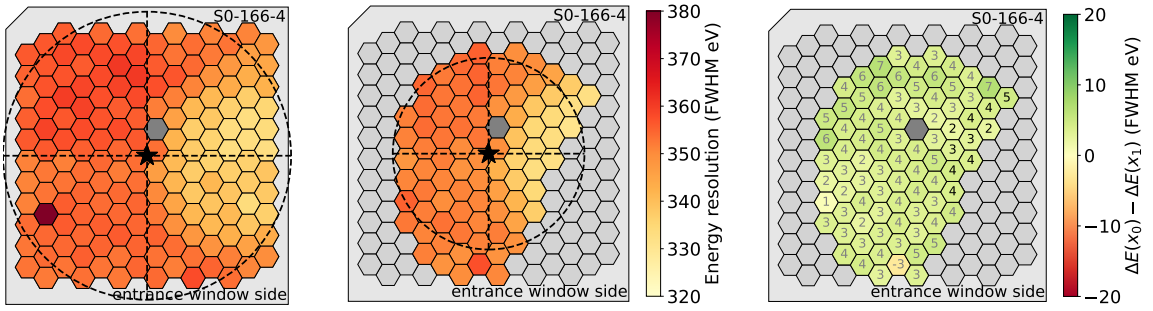

(a) Source at $z_0 = 2.18\,\mathrm{m}$ **(b)** Source at $z_1 = 2.25\,\mathrm{m}$ **(c)** Difference of energy resolution

Figure C.10: Influence of the source position on energy resolution
In the pixel maps (a) and (b) the energy resolution measured for the L-32 line of the ^{83m}Kr source are shown. The color scale is the same for both figures. The star and circle in the two figures illustrate (an arbitrary) position of the detector relative to the symmetry axis of the magnetic field lines in the MoS and the position of the source. (c) Difference of energy resolution between the two measurements. The light grey pixels are excluded from the analysis since the measured electron rate from the ^{83m}Kr source was negligible in these pixels.

in Figure C.9c. Also here, no significant change in the energy resolution could be observed, that could explain the inhomogenaity across the pixels.

C.4.2 *Effect of Source z-Position on Pixel Inhomogeneity*

To further exclude the source as a potential cause of the pixel-dependent inhomogeneity observed in the MoS (see Chapter 7.4.5), its z-position has been changed. The measurement at the nominal source position of $z_0 = 2.182\,\mathrm{m}$ ($\approx 3.6\,\mathrm{T}$) and the far position at $z_1 = 2.252\,\mathrm{m}$ ($\approx 3.6\,\mathrm{T}$) is shown in Figure C.10a and Figure C.10b, respectively. Due to the change in z-position and, therefore, magnetic field strength, different parts of the source are mapped onto different parts of the detector. However, no significant change in the pattern observed of the energy resolution could be seen, as shown in Figure C.10c. This further excludes the ^{83m}Kr source as the cause for the pattern seen in the energy resolution.

C.5 Table of ^{83m}Kr Electron Lines

Line	Energy (eV)	Intensity per decay (%)	Weighted average (eV)
	γ transition with 9405.7 eV		
L_1	7481.1(10)	66.8(13)	7516.6
L_2	7673.7(6)	7.47(15)	
L_3	7726.4(6)	5.70(11)	
M_1	9112.9(7)	10.8(3)	9125.3
M_2	9183.5(6)	1.19(3)	
M_3	9191.1(6)	0.897(21)	
M_4	9310.6(6)	0.0175(4)	
M_5	9311.9(6)	0.0156(4)	
N_1	9378.1(6)	1.11(3)	9379.7
N_2	9391.0(6)	0.0881(21)	
N_3	9391.6(6)	0.0655(16)	
	γ transition with 32 151.6 eV		
K	17824.2(5)	24.8(5)	
L_1	30226.8(9)	1.56(2)	30446.1
L_2	30419.5(5)	24.3(3)	
L_3	30472.2(5)	37.8(5)	
M_1	31858.7(6)	0.249(4)	31933.9
M_2	31929.3(5)	4.02(6)	
M_3	31936.9(5)	6.24(9)	
M_4	32056.4(5)	0.0628(9)	
M_5	32057.6(5)	0.0884(12)	
N_1	32123.9(5)	0.0255(4)	32136.7
N_2	32136.7(5)	0.300(4)	
N_3	32137.4(5)	0.457(6)	

Table C.7: Conversion electrons from the ^{83m}Kr source
The listed values correspond to the 32.15 keV γ-decay of the isotope. The weighted average of the L and M lines is calculated using the intensity per decay. Values taken from [134].

D

TECHNICAL INFORMATION OF THE DETECTOR MODULE ELECTRONICS

An overview of the various test points of the ASIC boards is given in Chapter D.1. The pin-out of the four μ-D connectors at the level of the vacuum feedthrough and the connection to the three CAEN VX2740B cards are shown in Chapter D.2 and Chapter D.3, respectively. In addition, practical pixel maps used for the operation of the detector modules are given in Chapter D.4. The modifications to the XGLab biasing system are described in Chapter D.5.

D.1 Detector Module Electronic Pin-outs and Test Points

D.1.1 *Test Points for Voltages and Setting Signals on ASIC Board*

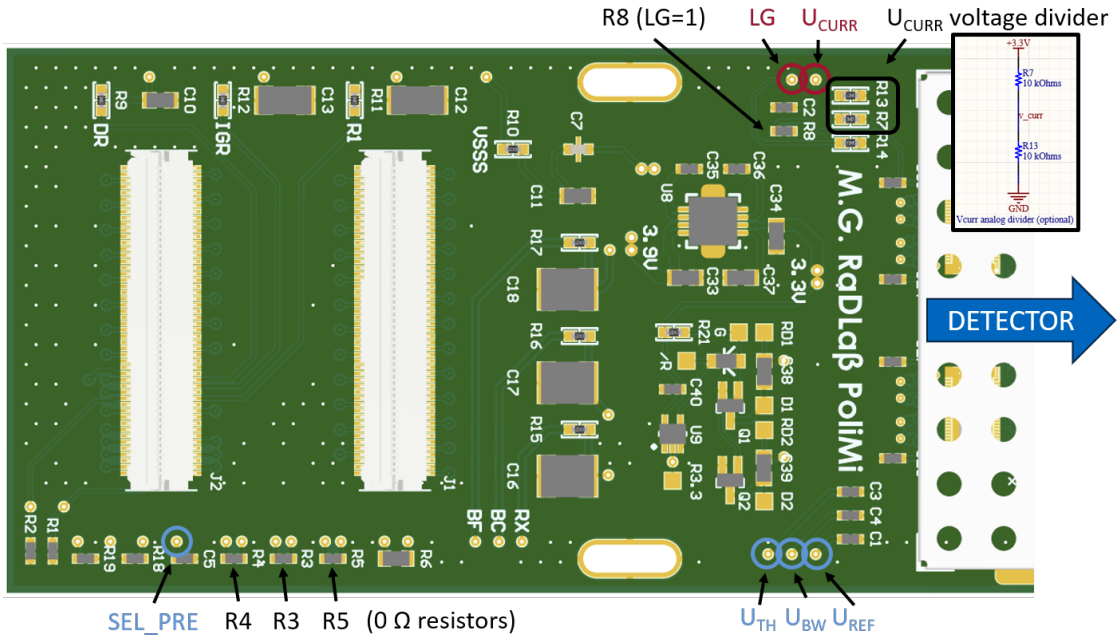

Figure D.1: Schematic of important power and signal line test points on the ASIC board Test points/resistor sides to check **continuity and voltage** of the signal towards the bias board are marked in blue. In red are **voltage only** test points since there is a filter resistor in series before. The voltages U_{TH}, U_{BW}, U_{Ref} can be set internally by the ASICs or overridden by the bias system (they can be overridden only if R4, R3, R5 are soldered with 0 Ω resistors, respectively). The low gain bit LG and U_{Curr} can only be set on the ASIC board and are **not connected** to the bias system. The default configuration is $LG = 0$. It can be set to 1 by soldering a 0 Ω resistor on place R8. The default configuration for $U_{\text{Curr}} = 2.7\,\text{V}$ set internally by the ASICs itself. It can be modified by soldering a voltage divider no the places R7 and R13. Courtesy M. Gugiatti [89].

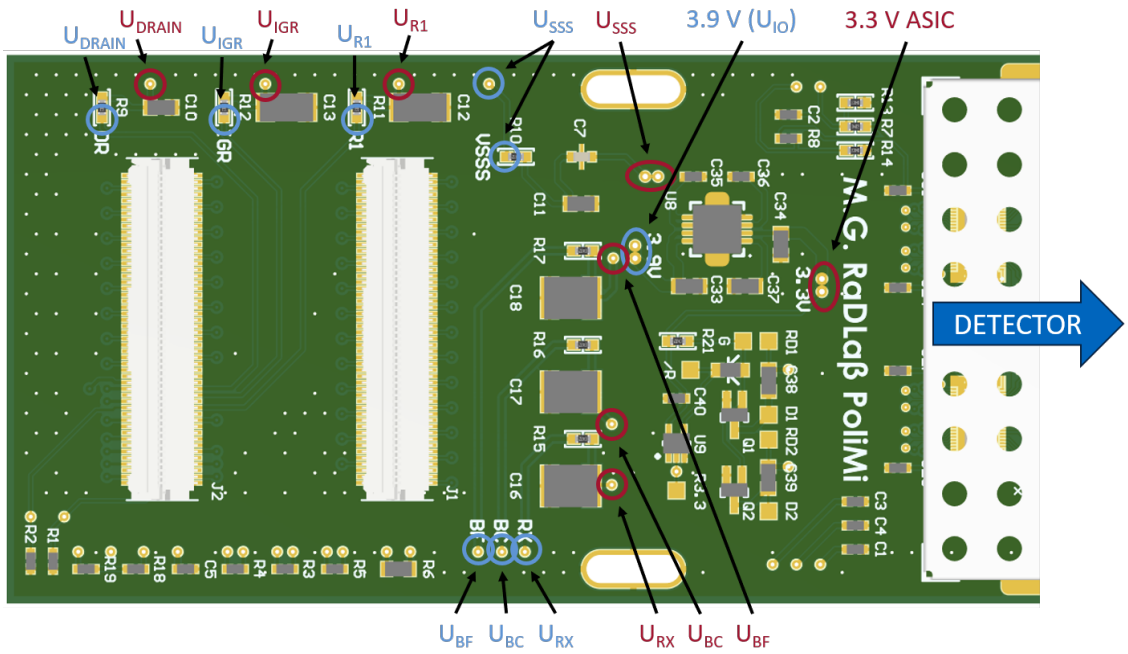

Figure D.2: Schematic of test points for detector voltages on the 83 channels ASIC board Test points/resistor sides to check **continuity and voltage** of the signal towards the bias board are marked in blue. Marked in red are **voltage only** test points since there is a filter resistor in series before. Courtesy M. Gugiatti [89].

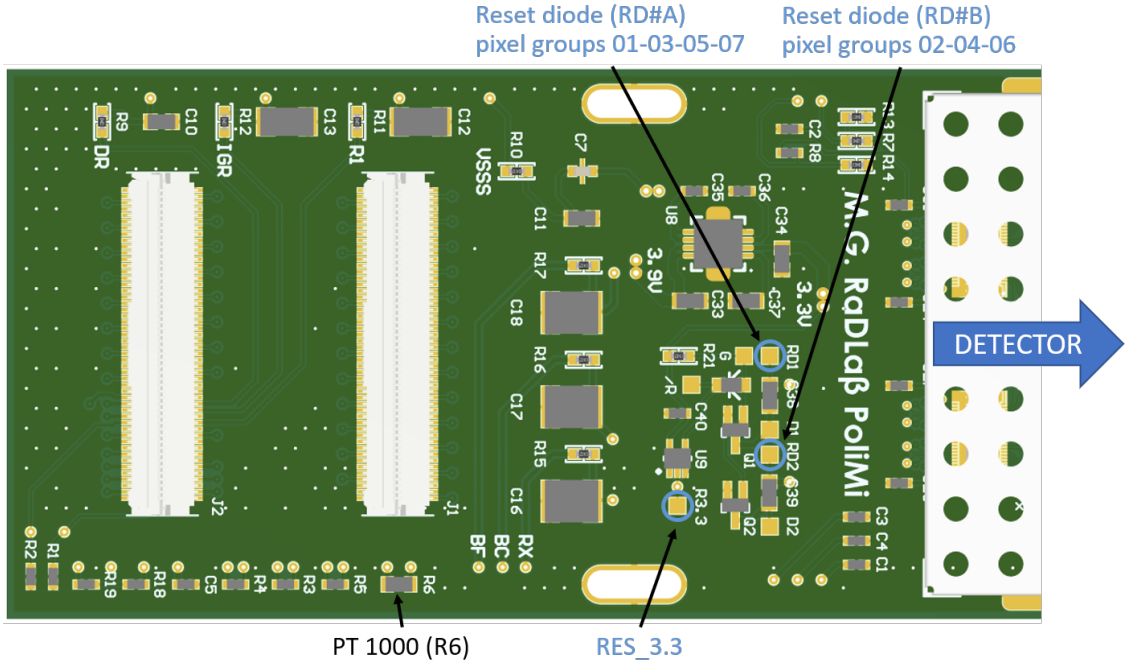

Figure D.3: Schematic of test points for the reset signals on the 83 channels ASIC board Test points/resistor sides to check **continuity and voltage** of the signal towards the bias board are marked in blue. Courtesy M. Gugiatti [89].

D.1.2 *Signal Layout of 200 Pin Connector on ASIC Board*

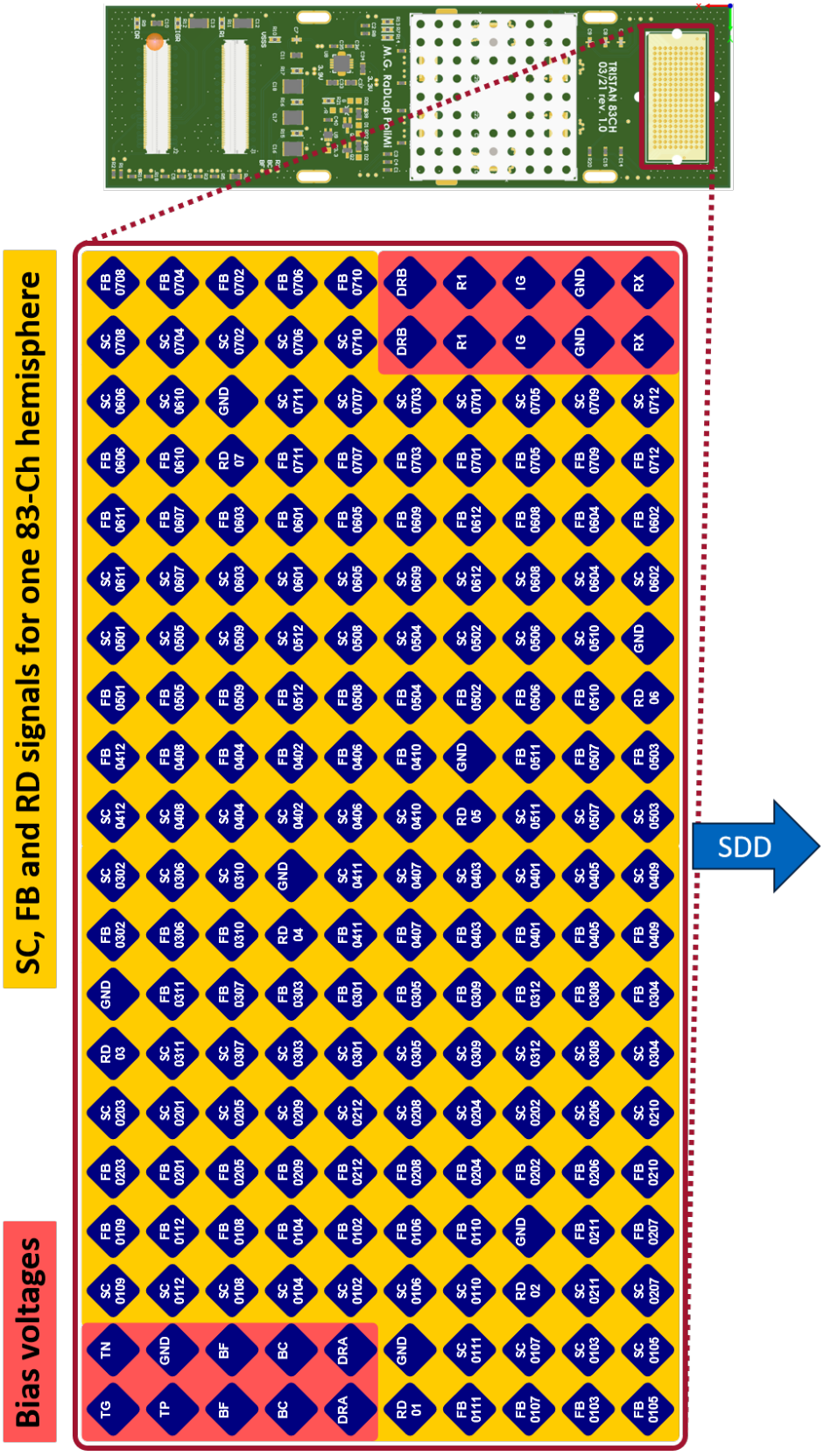

Figure D.4: Signal Layout of 200 Pin Connector on ASIC Board
Pin layout of 83 channel ASCI board connection towards the the rigid-flex PCB and SDD chip. View on pin layout as illustrated on the side. Courtesy M. Gugiatti [89].

D.2 Detector Module Pin-out at μ-D Connector

In this chapter, the pin-out at the four μ-D connectors is given in Table D.6 and Table D.7. The μ-D connector connected at the air side of the vacuum chamber is shown in Figure D.5.

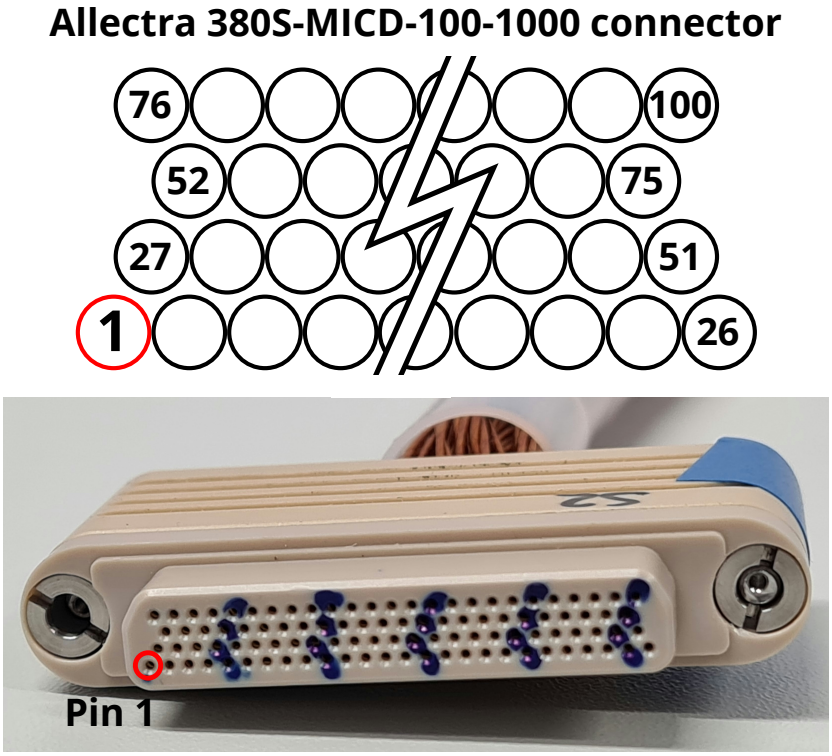

Figure D.5: Allectra 100 pins μ-D connector pin layout
Illustration of pin layout of mating face of Allectra 100 pins μ-D connector with 1.0m Kapton wire and PEEK casing. This connector interfaces with the vacuum feedthrough on the air side. Inside the vacuum the Airborn MK-452-100-335-620S[a] connector is used.

[a] https://mou.sr/3LFddez

100 Pin Cable S1	
Micro-D	Contact
1	GND
2	Pixel 2
3	GND
4	Pixel 3
5	GND
6	Pixel 4
7	GND
8	Pixel 5
9	GND
10	Pixel 6
11	GND
12	Pixel 7
13	GND
14	Pixel 8
15	GND
16	Pixel 9
17	GND
18	Pixel 10
19	GND
20	Pixel 11
21	GND
22	Pixel 12
23	GND
24	Pixel 13
25	GND
26	Pixel 14
27	GND
28	Pixel 15
29	GND
30	Pixel 16
31	GND
32	Pixel 17
33	GND
34	Pixel 18
35	GND
36	Pixel 19
37	GND
38	Pixel 20
39	GND
40	Pixel 21
41	GND
42	Pixel 22
43	GND
44	Pixel 23
45	GND
46	Pixel 24
47	GND
48	Pixel 25
49	GND
50	Pixel 26

100 Pin Cable S1	
Micro-D	Contact
51	GND
52	Pixel 27
53	GND
54	Pixel 28
55	GND
56	Pixel 29
57	GND
58	Pixel 30
59	GND
60	Pixel 31
61	GND
62	Pixel 32
63	GND
64	Pixel 33
65	GND
66	Pixel 34
67	GND
68	Pixel 35
69	GND
70	Pixel 36
71	GND
72	Pixel 37
73	GND
74	Pixel 38
75	GND
76	Pixel 39
77	GND
78	Pixel 40
79	GND
80	Pixel 41
81	GND
82	Pixel 42
83	GND
84	Pixel 43
85	GND
86	Pixel 44
87	GND
88	Pixel 45
89	GND
90	Pixel 46
91	GND
92	Pixel 47
93	GND
94	Pixel 48
95	GND
96	Pixel 49
97	GND
98	Pixel 50
99	GND
100	Pixel 51

100 Pin Cable P1	
Micro-D	Contact
1	PGND
2	PGND
3	3.9V
4	3.9V
5	PGND
6	PGND
7	3.9V
8	3.9V
9	PGND
10	PGND
11	Vref
12	TN_N
13	Vth
14	PGND
15	PGND
16	Bw
17	RD#B_N
18	Select_pre
19	PGND
20	PGND
21	Sat_out_N
22	Inhibit
23	Res3V3
24	PT1000
25	PT1000
26	R1
27	BC_N
28	RX
29	BF_N
30	IGR
31	Vd
32	Vsss
33	TP_N
34	RD#A_N
35	GND
36	Pixel 52
37	GND
38	Pixel 53
39	GND
40	Pixel 54
41	GND
42	Pixel 55
43	GND
44	Pixel 56
45	GND
46	Pixel 57
47	GND
48	Pixel 58
49	GND
50	Pixel 59

100 Pin Cable P1	
Micro-D	Contact
51	GND
52	Pixel 60
53	GND
54	Pixel 61
55	GND
56	Pixel 62
57	GND
58	Pixel 63
59	GND
60	Pixel 64
61	GND
62	Pixel 65
63	GND
64	Pixel 66
65	GND
66	Pixel 67
67	GND
68	Pixel 68
69	GND
70	Pixel 69
71	GND
72	Pixel 70
73	GND
74	Pixel 71
75	GND
76	Pixel 72
77	GND
78	Pixel 73
79	GND
80	Pixel 74
81	GND
82	Pixel 75
83	GND
84	Pixel 76
85	GND
86	Pixel 77
87	GND
88	Pixel 78
89	GND
90	Pixel 79
91	GND
92	Pixel 80
93	GND
94	Pixel 81
95	GND
96	Pixel 82
97	GND
98	Pixel 83
99	GND
100	Pixel 84

Figure D.6: Detector module pin-out at the μ-D connector level - Northern hemisphere
Pin-out at vacuum feedthrough level for the Allectra 100 pins μ-D connector with 1.0m Kapton wire. Pin 1 is on the lower left hand side, when the connector is seen from the mating face as illustrated in Figure D.5.

100 Pin Cable P2	
Micro-D	Contact
1	PGND
2	PGND
3	3.9V
4	3.9V
5	PGND
6	PGND
7	3.9V
8	3.9V
9	PGND
10	PGND
11	Vref
12	TN_S
13	Vth
14	PGND
15	PGND
16	Bw
17	RD#B_S
18	Select_pre
19	PGND
20	PGND
21	Sat_out_S
22	Inhibit
23	Res3V3
24	PT1000
25	PT1000
26	R1
27	(BC_S)
28	RX
29	(BF_S)
30	IGR
31	Vd
32	Vsss
33	TP_S
34	RD#A_S
35	GND
36	Pixel 136
37	GND
38	Pixel 137
39	GND
40	Pixel 138
41	GND
42	Pixel 139
43	GND
44	Pixel 140
45	GND
46	Pixel 141
47	GND
48	Pixel 142
49	GND
50	Pixel 143

100 Pin Cable P2	
Micro-D	Contact
51	GND
52	Pixel 144
53	GND
54	Pixel 145
55	GND
56	Pixel 146
57	GND
58	Pixel 147
59	GND
60	Pixel 148
61	GND
62	Pixel 149
63	GND
64	Pixel 150
65	GND
66	Pixel 151
67	GND
68	Pixel 152
69	GND
70	Pixel 153
71	GND
72	Pixel 154
73	GND
74	Pixel 155
75	GND
76	Pixel 156
77	GND
78	Pixel 157
79	GND
80	Pixel 158
81	GND
82	Pixel 159
83	GND
84	Pixel 160
85	GND
86	Pixel 161
87	GND
88	Pixel 162
89	GND
90	Pixel 163
91	GND
92	Pixel 164
93	GND
94	Pixel 165
95	GND
96	Pixel 166
97	GND
98	Pixel 167
99	GND
100	Pixel 168

100 Pin Cable S2	
Micro-D	Contact
1	GND
2	Pixel 86
3	GND
4	Pixel 87
5	GND
6	Pixel 88
7	GND
8	Pixel 89
9	GND
10	Pixel 90
11	GND
12	Pixel 91
13	GND
14	Pixel 92
15	GND
16	Pixel 93
17	GND
18	Pixel 94
19	GND
20	Pixel 95
21	GND
22	Pixel 96
23	GND
24	Pixel 97
25	GND
26	Pixel 98
27	GND
28	Pixel 99
29	GND
30	Pixel 100
31	GND
32	Pixel 101
33	GND
34	Pixel 102
35	GND
36	Pixel 103
37	GND
38	Pixel 104
39	GND
40	Pixel 105
41	GND
42	Pixel 106
43	GND
44	Pixel 107
45	GND
46	Pixel 108
47	GND
48	Pixel 109
49	GND
50	Pixel 110

100 Pin Cable S2	
Micro-D	Contact
51	GND
52	Pixel 111
53	GND
54	Pixel 112
55	GND
56	Pixel 113
57	GND
58	Pixel 114
59	GND
60	Pixel 115
61	GND
62	Pixel 116
63	GND
64	Pixel 117
65	GND
66	Pixel 118
67	GND
68	Pixel 119
69	GND
70	Pixel 120
71	GND
72	Pixel 121
73	GND
74	Pixel 122
75	GND
76	Pixel 123
77	GND
78	Pixel 124
79	GND
80	Pixel 125
81	GND
82	Pixel 126
83	GND
84	Pixel 127
85	GND
86	Pixel 128
87	GND
88	Pixel 129
89	GND
90	Pixel 130
91	GND
92	Pixel 131
93	GND
94	Pixel 132
95	GND
96	Pixel 133
97	GND
98	Pixel 134
99	GND
100	Pixel 135

Figure D.7: Detector module pin-out at the μ-D connector level - Southern hemisphere
Pin-out at vacuum feedthrough level for the Allectra 100 pins μ-D connector with 1.0m Kapton wire. Pin 1 is on the lower left hand side, when the connector is seen from the mating face as illustrated in Figure D.5.

D.3 Connection Overview for V2740B CAEN DPP Cards

CH0@ Card 1	**CH0**@ Card 2 -> Pixel **07 – 04**	**CH0**@ Card 3 -> Pixel **13 – 04**
CH1@ Card 1 -> Pixel **01 – 02**	**CH1**@ Card 2 -> Pixel **07 – 05**	**CH1**@ Card 3 -> Pixel **13 – 05**
CH2@ Card 1 -> Pixel **01 – 03**	**CH2**@ Card 2 -> Pixel **07 – 06**	**CH2**@ Card 3 -> Pixel **13 – 06**
CH3@ Card 1 -> Pixel **01 – 04**	**CH3**@ Card 2 -> Pixel **07 – 07**	**CH3**@ Card 3 -> Pixel **13 – 07**
CH4@ Card 1 -> Pixel **01 – 05**	**CH4**@ Card 2 -> Pixel **07 – 08**	**CH4**@ Card 3 -> Pixel **13 – 08**
CH5@ Card 1 -> Pixel **01 – 06**	**CH5**@ Card 2 -> Pixel **07 – 09**	**CH5**@ Card 3 -> Pixel **13 – 09**
CH6@ Card 1 -> Pixel **01 – 07**	**CH6**@ Card 2 -> Pixel **07 – 10**	**CH6**@ Card 3 -> Pixel **13 – 10**
CH7@ Card 1 -> Pixel **01 – 08**	**CH7**@ Card 2 -> Pixel **07 – 11**	**CH7**@ Card 3 -> Pixel **13 – 11**
CH8@ Card 1 -> Pixel **01 – 09**	**CH8**@ Card 2 -> Pixel **07 – 12**	**CH8**@ Card 3 -> Pixel **13 – 12**
CH9@ Card 1 -> Pixel **01 – 10**	**CH9**@ Card 2	**CH9**@ Card 3 -> Pixel **14 – 01**
CH10@ Card 1 -> Pixel **01 – 11**	**CH10**@ Card 2	**CH10**@ Card 3 -> Pixel **14 – 02**
CH11@ Card 1 -> Pixel **01 – 12**	**CH11**@ Card 2	**CH11**@ Card 3 -> Pixel **14 – 03**
CH12@ Card 1 -> Pixel **02 – 01**	**CH12**@ Card 2 -> Pixel **04 – 01**	**CH12**@ Card 3 -> Pixel **14 – 04**
CH13@ Card 1 -> Pixel **02 – 02**	**CH13**@ Card 2 -> Pixel **04 – 02**	**CH13**@ Card 3 -> Pixel **14 – 05**
CH14@ Card 1 -> Pixel **02 – 03**	**CH14**@ Card 2 -> Pixel **04 – 03**	**CH14**@ Card 3 -> Pixel **14 – 06**
CH15@ Card 1 -> Pixel **02 – 04**	**CH15**@ Card 2 -> Pixel **04 – 04**	**CH15**@ Card 3 -> Pixel **14 – 07**
CH16@ Card 1 -> Pixel **02 – 05**	**CH16**@ Card 2 -> Pixel **04 – 05**	**CH16**@ Card 3 -> Pixel **14 – 08**
CH17@ Card 1 -> Pixel **02 – 06**	**CH17**@ Card 2 -> Pixel **04 – 06**	**CH17**@ Card 3 -> Pixel **14 – 09**
CH18@ Card 1 -> Pixel **02 – 07**	**CH18**@ Card 2 -> Pixel **04 – 07**	**CH18**@ Card 3 -> Pixel **14 – 10**
CH19@ Card 1 -> Pixel **02 – 08**	**CH19**@ Card 2 -> Pixel **04 – 08**	**CH19**@ Card 3 -> Pixel **14 – 11**
CH20@ Card 1 -> Pixel **02 – 09**	**CH20**@ Card 2 -> Pixel **04 – 09**	**CH20**@ Card 3 -> Pixel **14 – 12**
CH21@ Card 1 -> Pixel **02 – 10**	**CH21**@ Card 2 -> Pixel **04 – 10**	**CH21**@ Card 3
CH22@ Card 1 -> Pixel **02 – 11**	**CH22**@ Card 2 -> Pixel **04 – 11**	**CH22**@ Card 3
CH23@ Card 1 -> Pixel **02 – 12**	**CH23**@ Card 2 -> Pixel **04 – 12**	**CH23**@ Card 3
CH24@ Card 1 -> Pixel **03 – 01**	**CH24**@ Card 2 -> Pixel **05 – 01**	**CH24**@ Card 3
CH25@ Card 1 -> Pixel **03 – 02**	**CH25**@ Card 2 -> Pixel **05 – 02**	**CH25**@ Card 3 -> Pixel **08 – 02**
CH26@ Card 1 -> Pixel **03 – 03**	**CH26**@ Card 2 -> Pixel **05 – 03**	**CH26**@ Card 3 -> Pixel **08 – 03**
CH27@ Card 1 -> Pixel **03 – 04**	**CH27**@ Card 2	**CH27**@ Card 3 -> Pixel **08 – 04**
CH28@ Card 1 -> Pixel **03 – 05**	**CH28**@ Card 2	**CH28**@ Card 3 -> Pixel **08 – 05**
CH29@ Card 1 -> Pixel **03 – 06**	**CH29**@ Card 2	**CH29**@ Card 3 -> Pixel **08 – 06**
CH30@ Card 1 -> Pixel **03 – 07**	**CH30**@ Card 2	**CH30**@ Card 3 -> Pixel **08 – 07**
CH31@ Card 1 -> Pixel **03 – 08**	**CH31**@ Card 2	**CH31**@ Card 3 -> Pixel **08 – 08**
CH32@ Card 1 -> Pixel **03 – 09**	**CH32**@ Card 2	**CH32**@ Card 3 -> Pixel **08 – 09**
CH33@ Card 1 -> Pixel **03 – 10**	**CH33**@ Card 2 -> Pixel **12 – 03**	**CH33**@ Card 3 -> Pixel **08 – 10**
CH34@ Card 1 -> Pixel **03 – 11**	**CH34**@ Card 2 -> Pixel **12 – 02**	**CH34**@ Card 3 -> Pixel **08 – 11**
CH35@ Card 1 -> Pixel **03 – 12**	**CH35**@ Card 2 -> Pixel **12 – 01**	**CH35**@ Card 3 -> Pixel **08 – 12**
CH36@ Card 1 -> Pixel **05 – 04**	**CH36**@ Card 2 -> Pixel **11 – 01**	**CH36**@ Card 3 -> Pixel **09 – 01**
CH37@ Card 1 -> Pixel **05 – 05**	**CH37**@ Card 2 -> Pixel **11 – 02**	**CH37**@ Card 3 -> Pixel **09 – 02**
CH38@ Card 1 -> Pixel **05 – 06**	**CH38**@ Card 2 -> Pixel **11 – 03**	**CH38**@ Card 3 -> Pixel **09 – 03**
CH39@ Card 1 -> Pixel **05 – 07**	**CH39**@ Card 2 -> Pixel **11 – 04**	**CH39**@ Card 3 -> Pixel **09 – 04**
CH40@ Card 1 -> Pixel **05 – 08**	**CH40**@ Card 2 -> Pixel **11 – 05**	**CH40**@ Card 3 -> Pixel **09 – 05**
CH41@ Card 1 -> Pixel **05 – 09**	**CH41**@ Card 2 -> Pixel **11 – 06**	**CH41**@ Card 3 -> Pixel **09 – 06**
CH42@ Card 1 -> Pixel **05 – 10**	**CH42**@ Card 2 -> Pixel **11 – 07**	**CH42**@ Card 3 -> Pixel **09 – 07**
CH43@ Card 1 -> Pixel **05 – 11**	**CH43**@ Card 2 -> Pixel **11 – 08**	**CH43**@ Card 3 -> Pixel **09 – 08**
CH44@ Card 1 -> Pixel **05 – 12**	**CH44**@ Card 2 -> Pixel **11 – 09**	**CH44**@ Card 3 -> Pixel **09 – 09**
CH45@ Card 1 -> Pixel **06 – 01**	**CH45**@ Card 2 -> Pixel **11 – 10**	**CH45**@ Card 3 -> Pixel **09 – 10**
CH46@ Card 1 -> Pixel **06 – 02**	**CH46**@ Card 2 -> Pixel **11 – 11**	**CH46**@ Card 3 -> Pixel **09 – 11**
CH47@ Card 1 -> Pixel **06 – 03**	**CH47**@ Card 2 -> Pixel **11 – 12**	**CH47**@ Card 3 -> Pixel **09 – 12**
CH48@ Card 1 -> Pixel **06 – 04**	**CH48**@ Card 2 -> Pixel **12 – 04**	**CH48**@ Card 3 -> Pixel **10 – 01**
CH49@ Card 1 -> Pixel **06 – 05**	**CH49**@ Card 2 -> Pixel **12 – 05**	**CH49**@ Card 3 -> Pixel **10 – 02**
CH50@ Card 1 -> Pixel **06 – 06**	**CH50**@ Card 2 -> Pixel **12 – 06**	**CH50**@ Card 3 -> Pixel **10 – 03**
CH51@ Card 1 -> Pixel **06 – 07**	**CH51**@ Card 2 -> Pixel **12 – 07**	**CH51**@ Card 3 -> Pixel **10 – 04**
CH52@ Card 1 -> Pixel **06 – 08**	**CH52**@ Card 2 -> Pixel **12 – 08**	**CH52**@ Card 3 -> Pixel **10 – 05**
CH53@ Card 1 -> Pixel **06 – 09**	**CH53**@ Card 2 -> Pixel **12 – 09**	**CH53**@ Card 3 -> Pixel **10 – 06**
CH54@ Card 1 -> Pixel **06 – 10**	**CH54**@ Card 2 -> Pixel **12 – 10**	**CH54**@ Card 3 -> Pixel **10 – 07**
CH55@ Card 1 -> Pixel **06 – 11**	**CH55**@ Card 2 -> Pixel **12 – 11**	**CH55**@ Card 3 -> Pixel **10 – 08**
CH56@ Card 1 -> Pixel **06 – 12**	**CH56**@ Card 2 -> Pixel **12 – 12**	**CH56**@ Card 3 -> Pixel **10 – 09**
CH57@ Card 1 -> Pixel **07 – 01**	**CH57**@ Card 2 -> Pixel **13 – 01**	**CH57**@ Card 3 -> Pixel **10 – 10**
CH58@ Card 1 -> Pixel **07 – 02**	**CH58**@ Card 2 -> Pixel **13 – 02**	**CH58**@ Card 3 -> Pixel **10 – 11**
CH59@ Card 1 -> Pixel **07 – 03**	**CH59**@ Card 2 -> Pixel **13 – 03**	**CH59**@ Card 3 -> Pixel **10 – 12**
CH60@ Card 1	**CH60**@ Card 2	**CH60**@ Card 3
CH61@ Card 1	**CH61**@ Card 2	**CH61**@ Card 3
CH62@ Card 1	**CH62**@ Card 2	**CH62**@ Card 3
CH63@ Card 1	**CH63**@ Card 2	**CH63**@ Card 3

Figure D.8: Connection overview for CAEN VX2740B DPP cards
Illustrates the distribution and connections of the individual CAEN VX2740B card channels to the individual pixels of the detector.

D.4 Useful Pixel Maps of Detector Module Connections

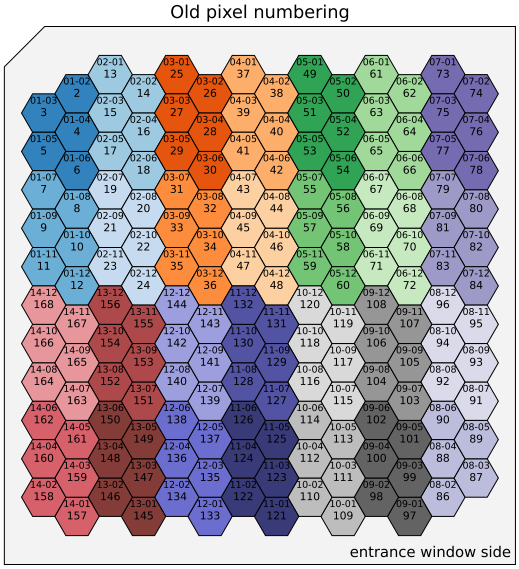

(a) Pixel color coding

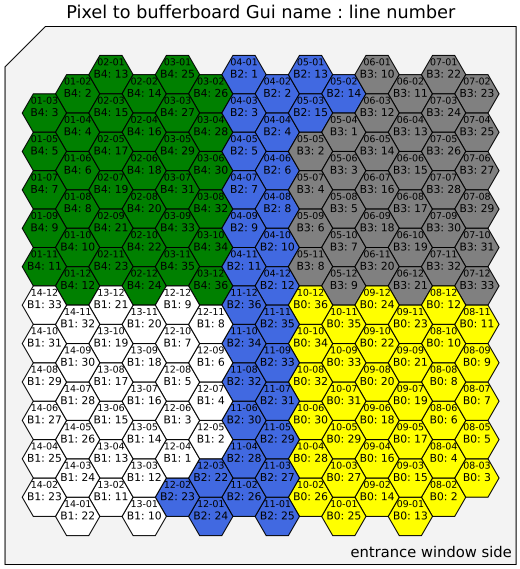

(b) Bias system connections

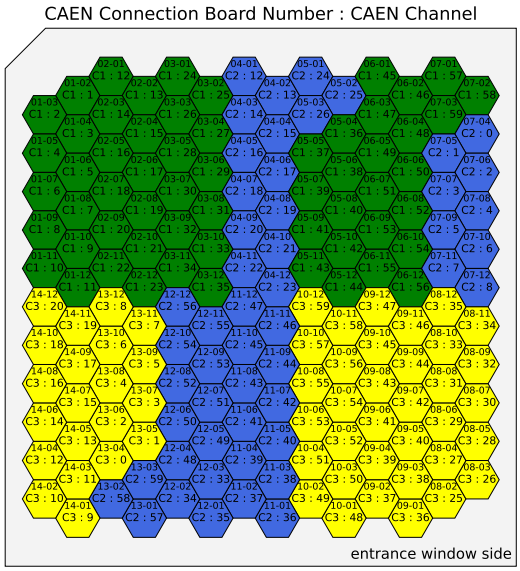

(c) CAEN VX2740B connections

Figure D.9: Useful pixel maps for the handling of detector module
Upper set of numbers describe the reset group - pixel number. (a) Color coding, which is used in the spectrum plots within this thesis. The number in the center describes the pixel numbering with the old nomenclature before 2023. (b) The number in the center describes on which bias board buffer board : channel the pixel is connected. (c) The number in the center describes on which CAEN card : channel the pixel is connected.

D.5 Modifications to XGLab Biasing and Control System

The XGLab biasing and control system has been specifically build to supply and control the detector modules during the first characterizations measurements. Due to some changes e.g the DAQ usage, some smaller modifications of the factory design have been preformed with the support of P. Trigilio.

D.5.1 *Buffer Board Patches*

The XGLab buffer boards on the biasing and control system have been build to drive a high impedance ($> 1\,\mathrm{k\Omega}$) DPP like DANTE by XGLab[141]. To make them functional with the input impedance of $50\,\Omega$ in the CAEN VX2740B units a modification had to be performed. Without modifications the lowest selectable baseline voltage of the ETTORE ASIC amplifier 2^{nd} stage output is at approximately 2 V. Due to this offset in combination with the lower impedance, a larger current has to be provided by the buffer board outputs. This higher current can not be provided by the LDOs installed on the buffer boards and cause malfunctioning. To reduce the load on the LDOs the offset of the baseline voltage is reduced to 1.5 V, by replacing the resistor $R14$ with $270\,\Omega$ on the underside of the buffer board PCB with a smaller $82\,\Omega$ resistor. Further reducing the offset is not possible without a major redesign of the buffer boards. The idea for this patch was suggested by P. Trigilio.

D.5.2 *R1-Rx Patch*

To extend the range of selectable R1 voltages a small patch has been performed on the XGLab biasing and control board. The resistor R71 near the R1 potentiometer with $4.7\,\mathrm{k\Omega}$ in the original design has been replaced with an $2.2\,\mathrm{k\Omega}$ resistor. This improved the achievable R1 voltages to values of -9 V to -15 V. The idea for this patch was suggested by P. Trigilio.

E

MECHANICAL DRAWINGS

In this chapter, all mechanical drawings required for the assembly jigs and the detector module are given.

E.1 Monitor Spectrometer - CAD Drawing

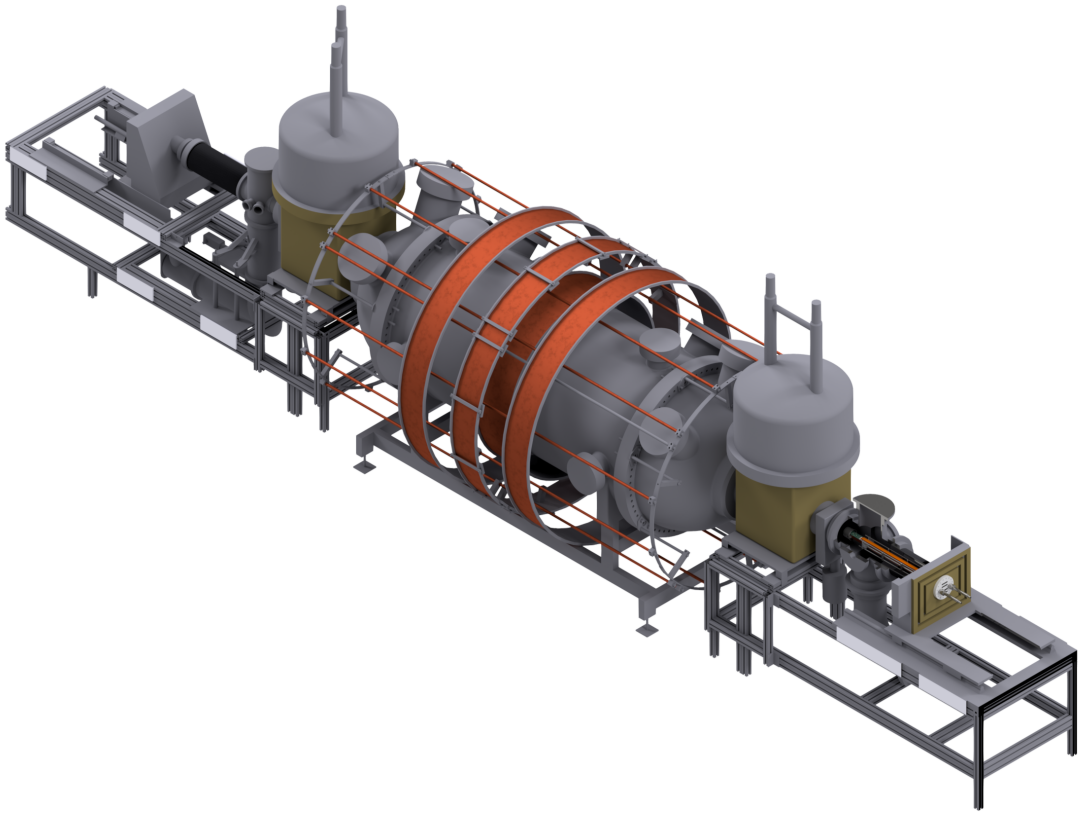

Figure E.1: CAD illustration of the MoS with a detector module
On the right hand side is the detector section. Parts of it are hidden to display the installed detector module. The LFCS and EMCS coils are illustrated by the copper colored parts.

E.2 Cesic Interposer

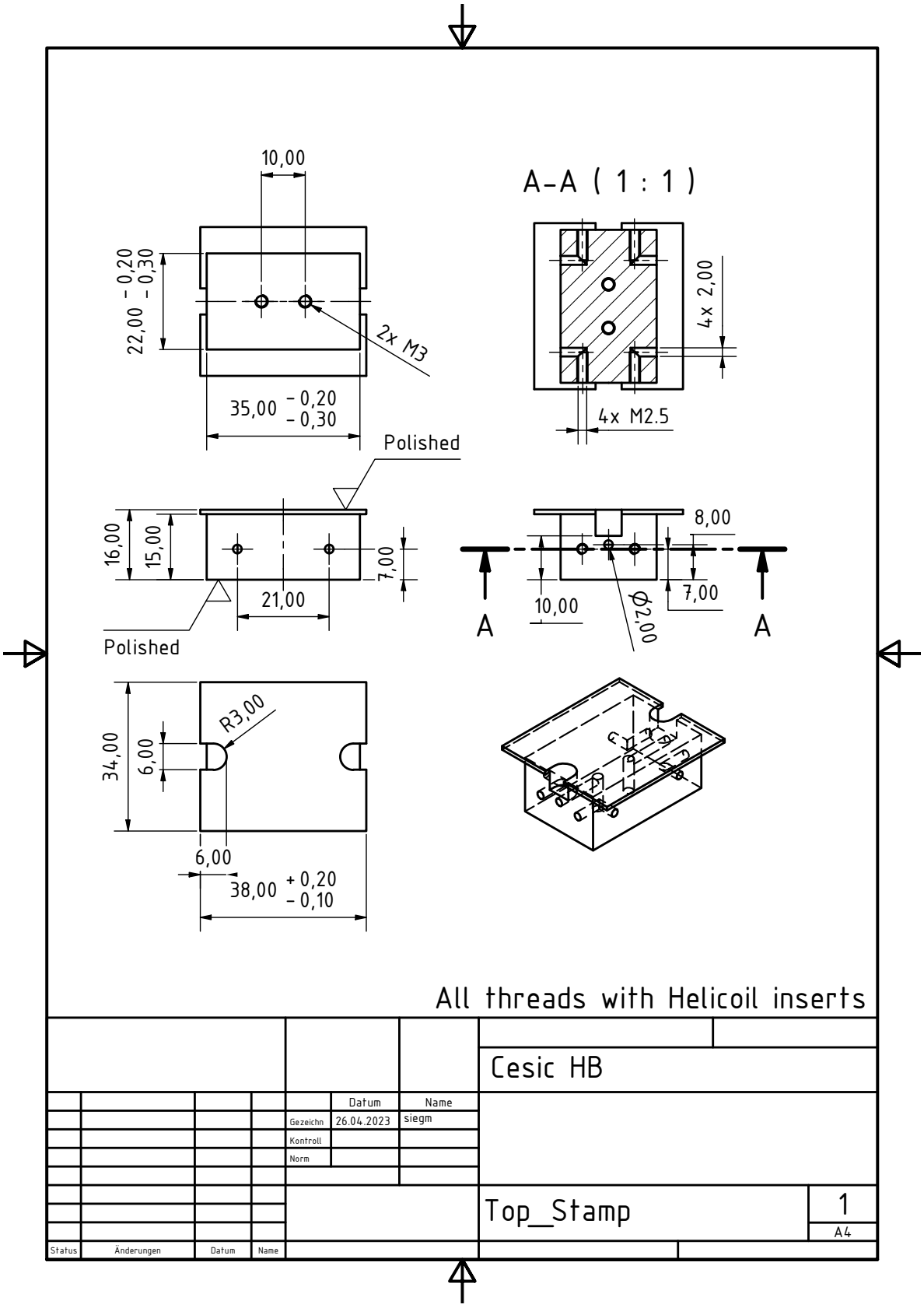

Figure E.2: Detector module mechanical drawing - Cesic interposer

E.2.1 *Copper Cooling Structure - Hollow Part*

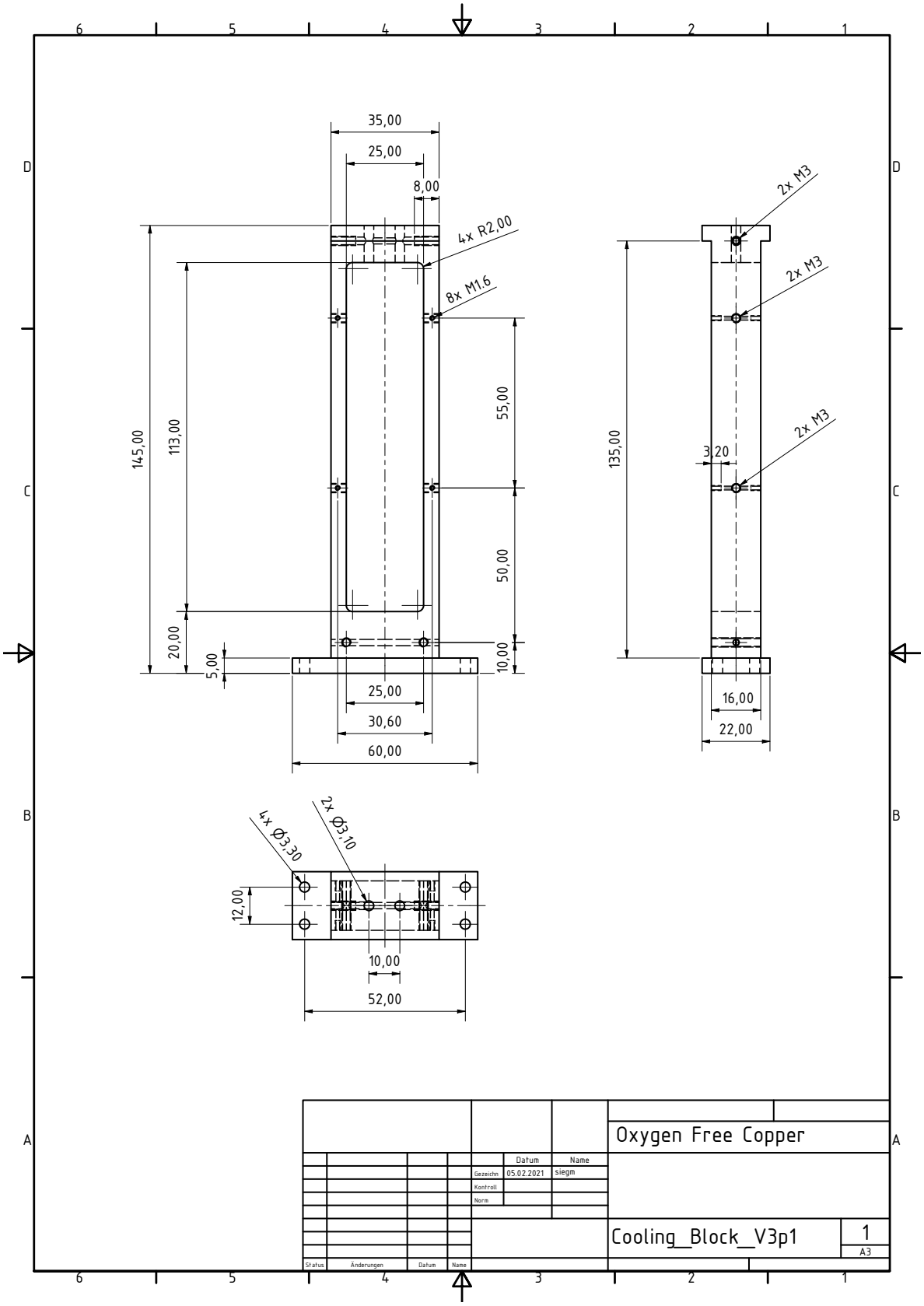

Figure E.3: Detector module mechanical drawing - Copper cooling structure hollow part

E.2.2 *Copper Cooling Structure - Cover part*

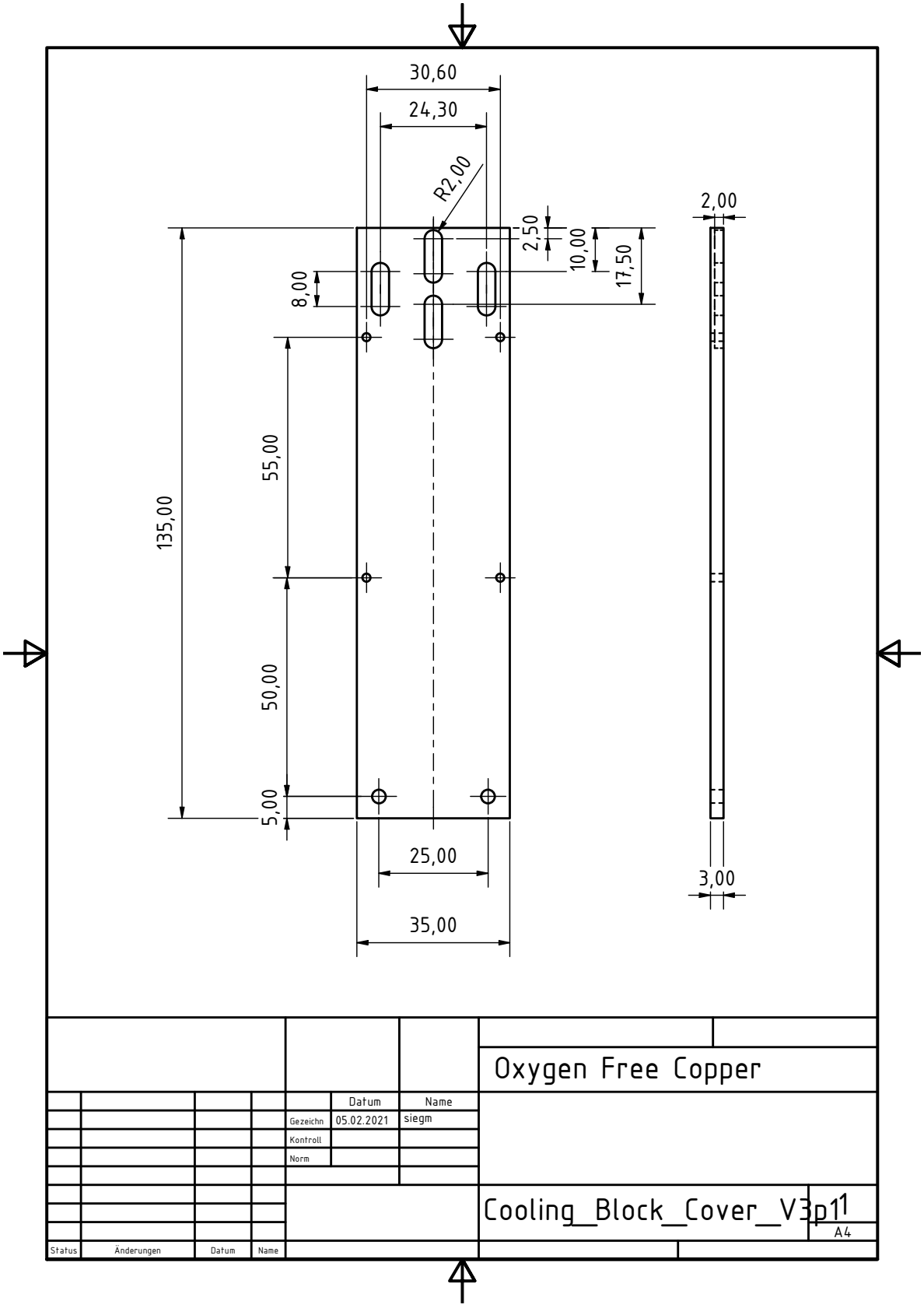

Figure E.4: Detector module mechanical drawing - Copper cooling structure cover part

E.2.3 *PEEK Base Plate - Mechanical Drawing*

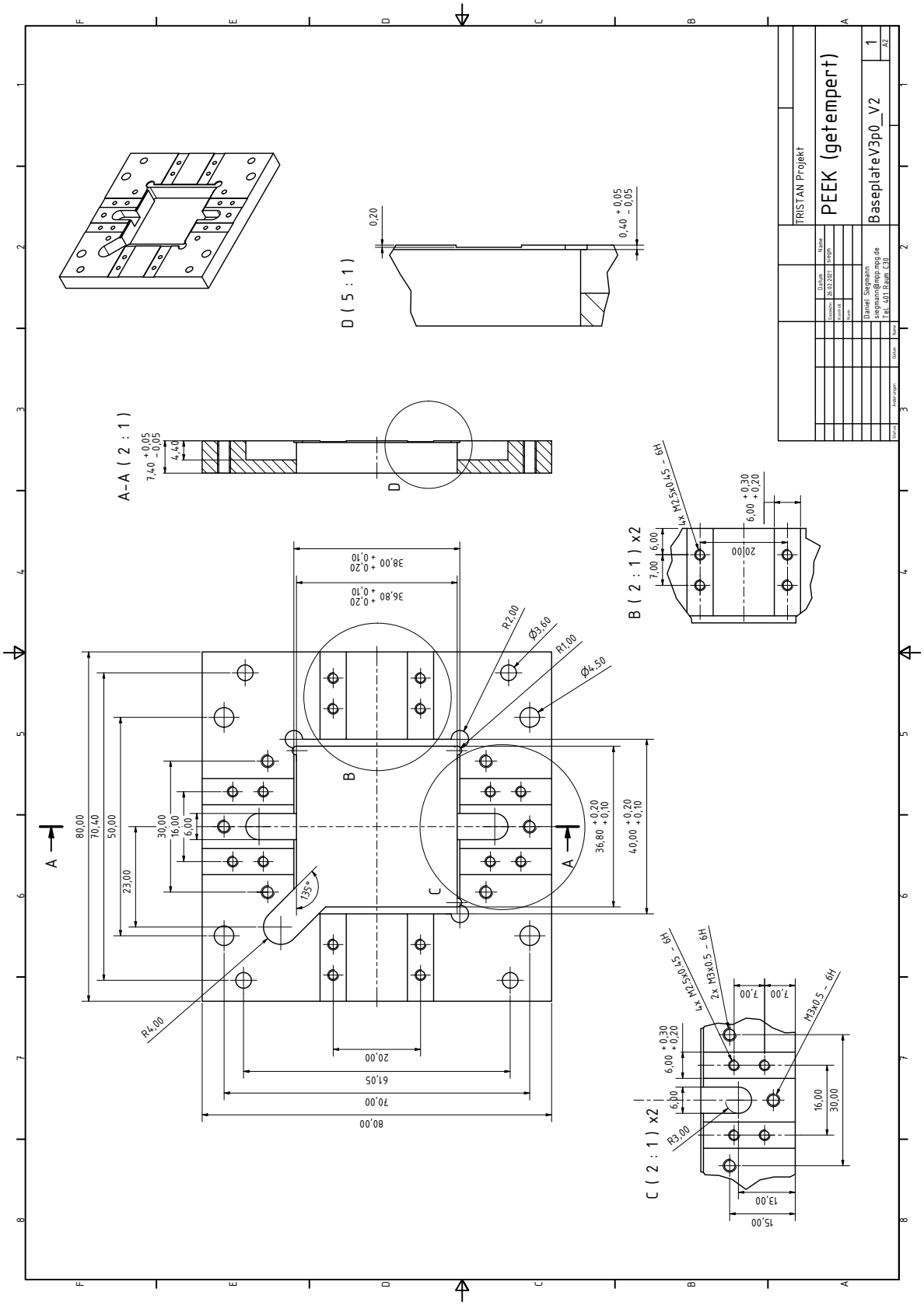

Figure E.5: Assembly mechanical drawing - PEEK base plate

E.2.4 *Perforated Fortal STS Aluminum Plate - Mechanical Drawing*

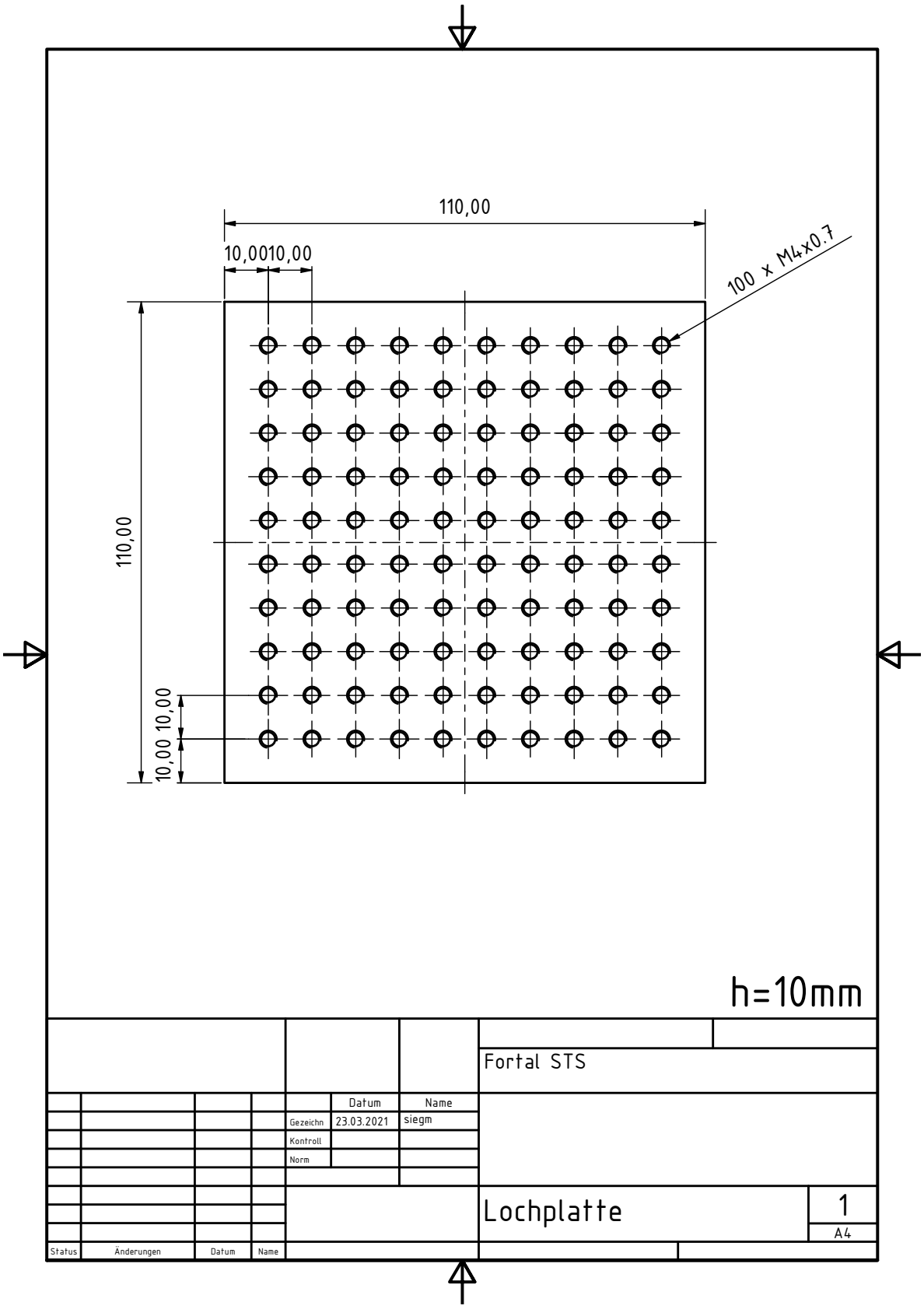

Figure E.6: Assembly mechanical drawing - Perforated Fortal STS aluminum plate

E.2.5 *Various Assembly Helper Parts - Mechanical Drawing*

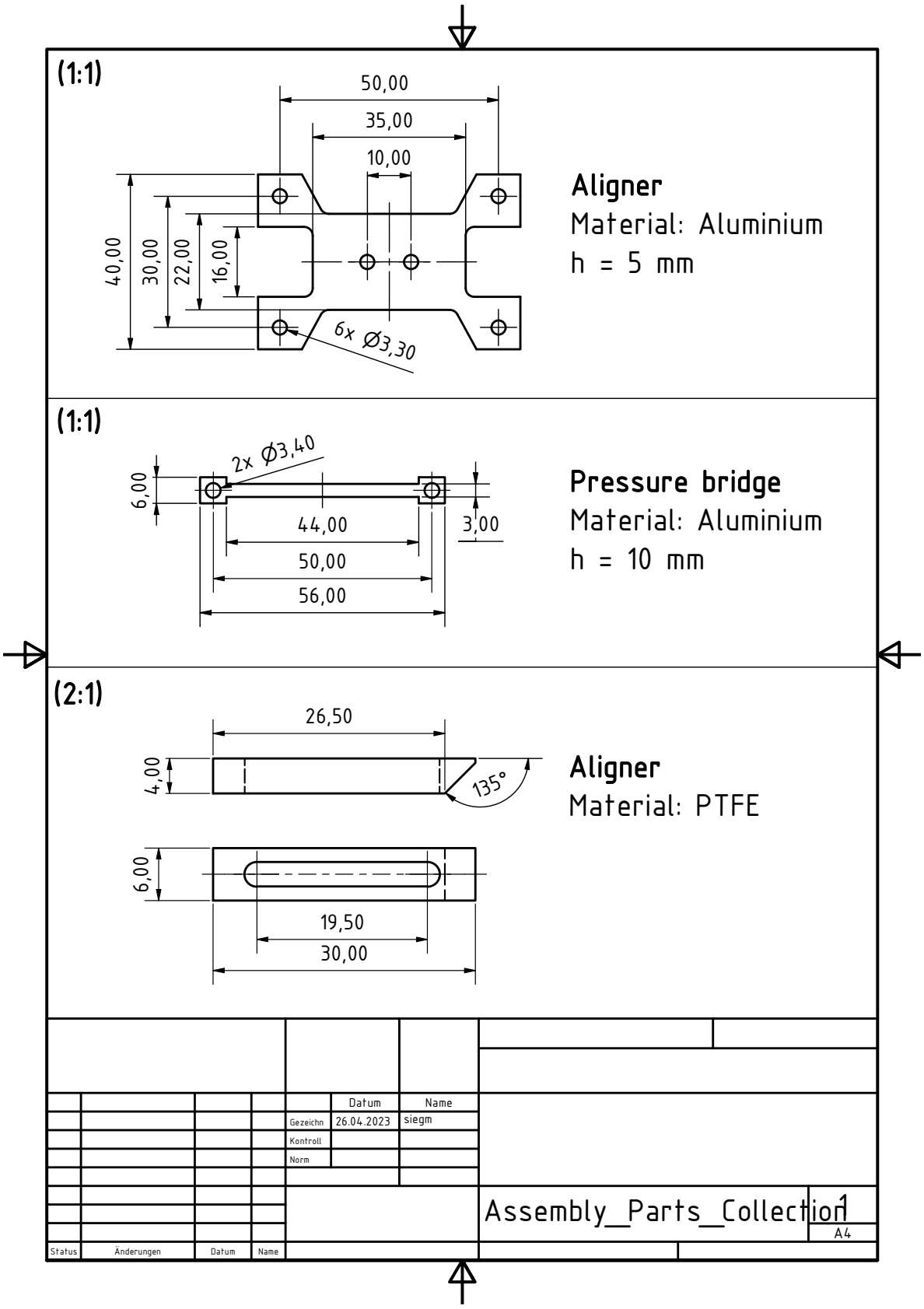

Figure E.7: Assembly mechanical drawing - Various assembly helper parts

E.2.6 *Protection Jaw - Mechanical Drawing*

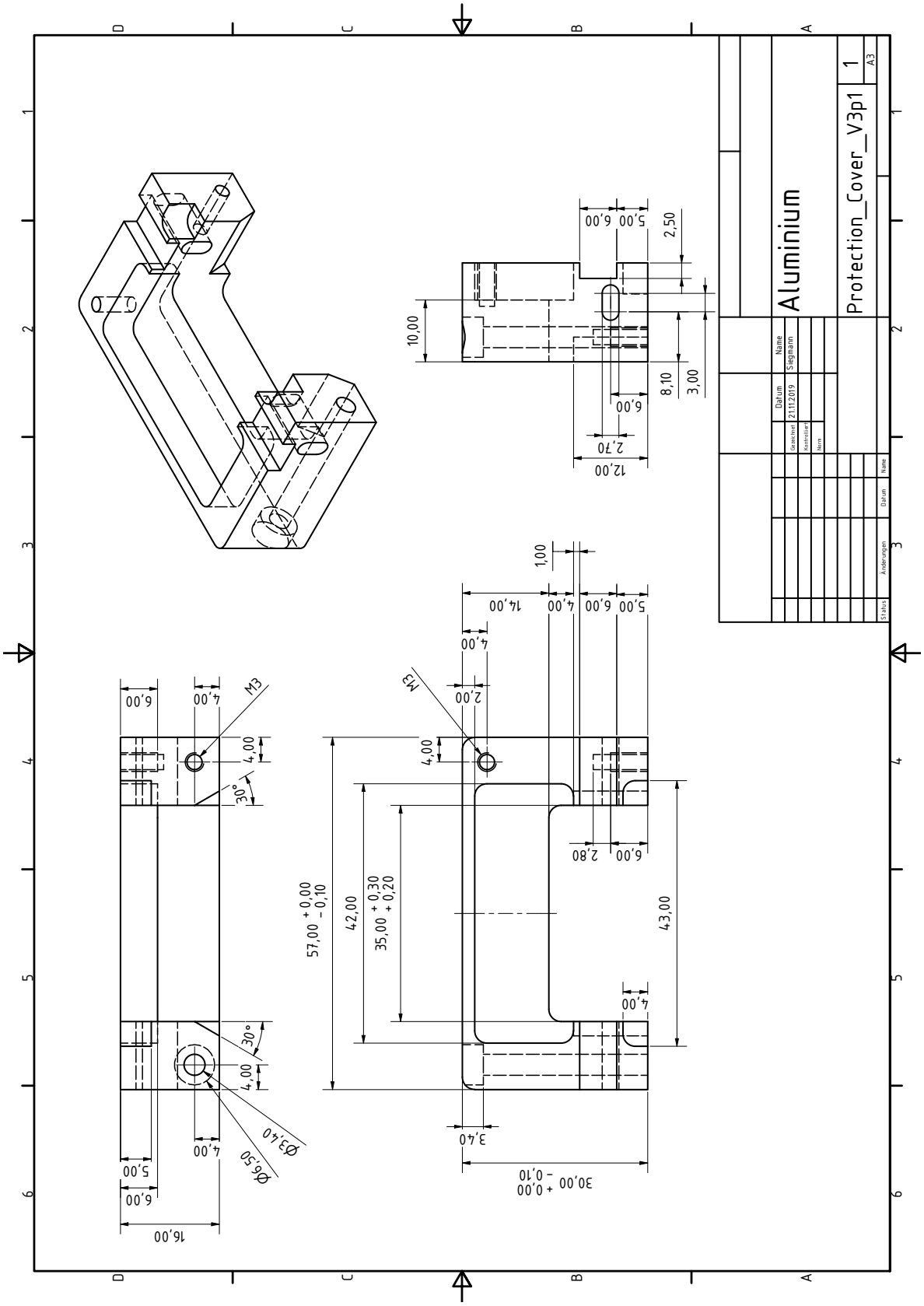

Figure E.8: Assembly mechanical drawing - Protection jaw

E.2.7 *Protection Hat - Mechanical Drawing*

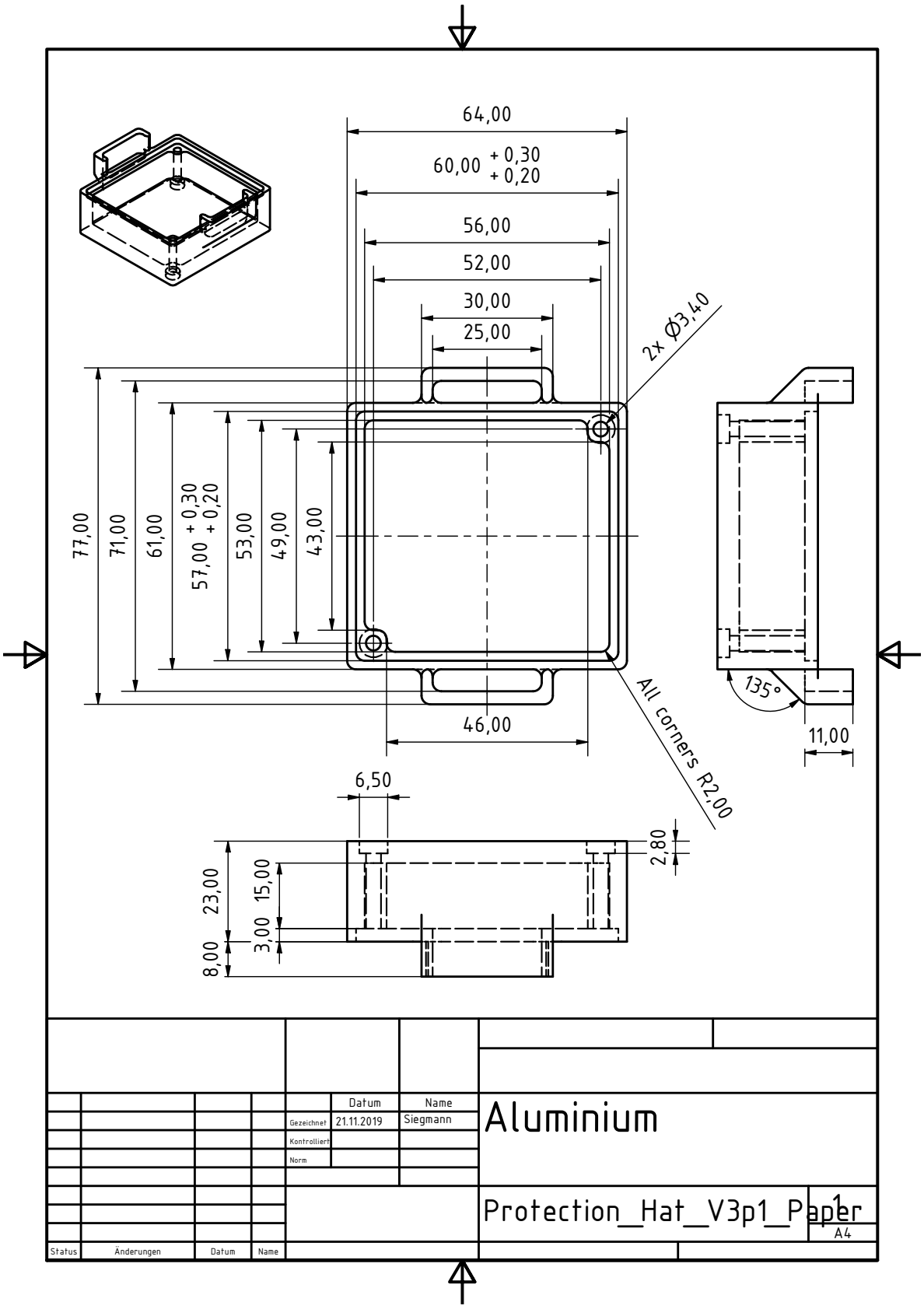

Figure E.9: Assembly mechanical drawing - Protection hat

LIST OF ACRONYMS

ADC analog-to-digital converter
ASIC application-specific integrated circuit
Au gold
BC back contact
BF back frame
BAO baryonic acoustic oscillations
BBN Big Bang nucleosynthesis
CAD computer aided design
CAEN VX2740B 64 channel digital signal processor with 16 bit resolution at 125 MS/s
CC charge current
CCD charge-coupled device
CCE charge collection efficiency
ΛCDM lambda cold dark matter
CKM Cabibbo-Kobayashi-Maskawa
CMB cosmic microwave background
CνB cosmic neutrino background
CP Charge-Parity
CPS cryogenic pumping section
CSA charge sensitive amplifier
CTE coefficient of thermal expansion
CTRL control
Cu copper
DAQ data acquisition system
DONUT Direct Observation of Nu Tau
DPS differential pumping section
$2\nu\beta\beta$-decay double β-decay
$0\nu\beta\beta$-decay neutrinoless double β-decay
DPP digital pulse processing
DR drain
EC electron capture
EMCS earth magnetic field compensation system
ENC equivalent noise charge
eV electron volt
FB feedback
Fe iron
FET field-effect transistor
FPC flexible printed circuit
FPD focal plane detector
FPGA field programmable array
FWHM full width half maximum
HDM hot dark matter
HOPG highly-oriented pyrolitic graphite
HLL Semiconductor laboratory of the Max Planck Society

HUNTER heavy unseen neutrinos from total energy-momentum reconstruction
ID identification number
IGR inner guard ring
I-U curve current-voltage curve
IIR infinite impulse response
IO inverted neutrino mass ordering
nJFET n-channel junction gate field-effect transistor
KATRIN Karlsruhe Tritium Neutrino
LDO low-dropout regulator
LEP large electron-positron collider
LFCS low field compensation system
lsb least significant bit
M33 Messier 33
MAC-E magnetic adiabatic collimation with electrostatic
νMSM neutrino minimal Standard Model
MoS Monitor Spectrometer
MPP Max Planck Institute for Physics
MSW Mikheyev-Smirnow-Wolfenstein
NC neutral current
NO normal neutrino mass ordering
OS outer substrate
PAE post acceleration electrode
PCB printed circuit board
PEEK polyether ether ketone
PET polyethylene terephthalate
PIN detector positive-intrinsic-negative detector
PMNS Pontecorvo-Maki-Nakagawa-Sakata
ppm parts per million
PTFE polytetrafluoroethylene
Res reset
ROI region of interest
RTN random telegraph noise
R1 inner most ring
RX outer most ring
SC source
SDD silicon drift detector
SDS source and detector section
SM Standard Model of particle physics
SNO Sudbury Neutrino Observatory
SO source
STS source and transport section
WGTS windowless gaseous tritium source
S0-47-3 detector front made form wafer chip SDD33.2 W01-G07
S0-47-4 detector front made form wafer chip SDD33.2 W07-G07
S0-166-1 detector front made from wafer chip SDD33.2 W01-F.06 (code name D.Va)
S0-166-2 detector front made from wafer chip SDD33.2 W08-F.11 (code name Mercy)
S0-166-3 detector front made from wafer chip SDD33.2 W07-B.06 (code name Echo)
S0-166-4 detector front made from wafer chip SDD33.3 W04-F.06 (code name Winston)
S0-166-5 detector front made from wafer chip SDD33.3 W05-F.06 (code name Brigitte)
S0-166-6 detector front made from wafer chip SDD33.3 W05-B.06 (code name Kiriko)

LIST OF FIGURES

LIST OF TABLES

BIBLIOGRAPHY

[1] R. L. Workman et al. "Review of Particle Physics." In: *Progress of Theoretical and Experimental Physics* 2022.8 (2022). DOI: 10.1093/ptep/ptac097 (cit. on pp. 1, 3, 5, 9, 11, 12, 22).

[2] Marco Drewes. "Sterile Neutrinos - Auf dem Weg zu neuen Ufern." In: *Physik Journal* 2 (2019). URL: https://pro-physik.de/zeitschriften/download/19194 (cit. on pp. 1, 3–5, 15–18).

[3] Alexander Merle. *Sterile neutrino dark matter*. Version: 20170301. /IOP release 3]. San Rafael, CA and Bristol: Morgan & Claypool Publishers and IOP Publishing, 2017. ISBN: 978-1-6817-4481-0. DOI: 10.1088/978-1-6817-4481-0. URL: http://iopscience.iop.org/book/978-1-6817-4481-0 (cit. on pp. 1, 3, 14–17).

[4] Basudeb Dasgupta and Joachim Kopp. "Sterile neutrinos." In: *Physics Reports* 928 (2021), ISSN: 03701573. DOI: 10.1016/j.physrep.2021.06.002 (cit. on pp. 1, 3, 15–18, 29).

[5] M. Aker et al. "The design, construction, and commissioning of the KATRIN experiment." In: *Journal of Instrumentation* 16.08 (2021), DOI: 10.1088/1748-0221/16/08/T08015 (cit. on pp. 1, 21, 23, 25–28).

[6] S. Mertens et al. "Sensitivity of next-generation tritium beta-decay experiments for keV-scale sterile neutrinos." In: *Journal of Cosmology and Astroparticle Physics* 2015.02 (2015), DOI: 10.1088/1475-7516/2015/02/020 (cit. on pp. 1, 29, 109, 121).

[7] TRISTAN group. "Conceptual Design Report: KATRIN with TRISTAN modules." In: (2022). URL: https://api.semanticscholar.org/CorpusID:248068381 (cit. on pp. 1, 21, 30, 54, 66, 116).

[8] Daniel Siegmann et al. "Development of a silicon drift detector array to search for keV-scale sterile neutrinos with the KATRIN experiment." In: *Journal of Physics G: Nuclear and Particle Physics* (2024). ISSN: 0954-3899. DOI: 10.1088/1361-6471/ad4bf8 (cit. on pp. 2, 73, 74, 88, 103, 106, 107, 110, 114, 120, 134, 141, 142).

[9] E. Corbelli and P. Salucci. "The extended rotation curve and the dark matter halo of M33." In: *Monthly Notices of the Royal Astronomical Society* 311.2 (2000), ISSN: 0035-8711. DOI: 10.1046/j.1365-8711.2000.03075.x (cit. on p. 4).

[10] Kai Zuber. *Neutrino Physics*. Boca Raton: CRC Press, 2020. ISBN: 9781315195612. DOI: 10.1201/9781315195612 (cit. on pp. 4–7, 11, 13, 14).

[11] J. Lesgourgues and S. Pastor. "Massive neutrinos and cosmology." In: *Physics Reports* 429.6 (2006), ISSN: 03701573. DOI: 10.1016/j.physrep.2006.04.001 (cit. on p. 5).

[12] M. Aker et al. "Direct neutrino-mass measurement based on 259 days of KATRIN data." In: (2024). Pre print. arXiv: 2406.13516 (cit. on pp. 5, 14, 23, 28).

[13] Lothar Oberauer and Judith Oberauer. *Neutrinophysik*. Berlin, Heidelberg: Springer Berlin Heidelberg, 2019. ISBN: 978-3-662-59334-9. DOI: 10.1007/978-3-662-59335-6 (cit. on p. 5).

[14] J Chadwick. "Intensitätsverteilung im magnetischen Spectrum der β-Strahlen von radium B + C." In: *Verhandl. Dtsc. Phys. Ges.* 16 (1914), URL: https://cds.cern.ch/record/262756 (cit. on p. 5).

[15] W. Pauli. "Dear radioactive ladies and gentlemen." In: *Phys. Today* 31N9 (1930), DOI: 10.1063/1.2995181 (cit. on p. 5).

[16] E. Fermi. "Versuch einer Theorie der β-Strahlen. I." In: *Zeitschrift fr Physik* 88.3-4 (1934), ISSN: 1434-6001. DOI: 10.1007/BF01351864 (cit. on pp. 6, 22).

[17] C. L. Cowan et al. "Detection of the Free Neutrino: a Confirmation." In: *Science (New York, N.Y.)* 124.3212 (1956), ISSN: 0036-8075. DOI: 10.1126/science.124.3212.103 (cit. on p. 6).

[18] George W. Rodeback and James S. Allen. "Neutrino Recoils Following the Capture of Orbital Electrons in A37." In: *Physical Review* 86.4 (1952), ISSN: 0031-899X. DOI: 10.1103/PhysRev.86.446 (cit. on p. 7).

[19] Arthur H. Snell and Frances Pleasonton. "Spectrometry of Recoils from Neutrino Emission in Argon-37." In: *Physical Review* 97.1 (1955), ISSN: 0031-899X. DOI: 10.1103/PhysRev.97.246 (cit. on p. 7).

[20] G. Danby et al. "Observation of High-Energy Neutrino Reactions and the Existence of Two Kinds of Neutrinos." In: *Physical Review Letters* 9.1 (1962), ISSN: 0031-9007. DOI: 10.1103/PhysRevLett.9.36 (cit. on p. 7).

[21] M. L. Perl et al. "Evidence for Anomalous Lepton Production in e+−e− Annihilation." In: *Physical Review Letters* 35.22 (1975), ISSN: 0031-9007. DOI: 10.1103/PhysRevLett.35.1489 (cit. on p. 7).

[22] K. Kodama et al. "Observation of tau neutrino interactions." In: *Physics Letters B* 504.3 (2001), ISSN: 03702693. DOI: 10.1016/S0370-2693(01)00307-0 (cit. on p. 7).

[23] "Precision electroweak measurements on the Z resonance." In: *Physics Reports* 427.5-6 (2006), ISSN: 03701573. DOI: 10.1016/j.physrep.2005.12.006 (cit. on pp. 7, 8).

[24] David J. Griffiths. *Introduction to elementary particles*. Weinheim: Wiley, 2007. ISBN: 0471603864 (cit. on p. 8).

[25] C. S. Wu et al. "Experimental Test of Parity Conservation in Beta Decay." In: *Physical Review* 105.4 (1957), ISSN: 0031-899X. DOI: 10.1103/PhysRev.105.1413 (cit. on p. 8).

[26] Richard L. Garwin, Leon M. Lederman, and Marcel Weinrich. "Observations of the Failure of Conservation of Parity and Charge Conjugation in Meson Decays: the Magnetic Moment of the Free Muon." In: *Physical Review* 105.4 (1957), ISSN: 0031-899X. DOI: 10.1103/PhysRev.105.1415 (cit. on p. 9).

[27] M. Goldhaber, L. Grodzins, and A. W. Sunyar. "Helicity of Neutrinos." In: *Physical Review* 109.3 (1958), ISSN: 0031-899X. DOI: 10.1103/PhysRev.109.1015 (cit. on p. 9).

[28] Aldo Ianni. "Solar neutrinos and the solar model." In: *Physics of the Dark Universe* 4 (2014), ISSN: 22126864. DOI: 10.1016/j.dark.2014.06.002 (cit. on p. 9).

[29] Raymond Davis, Don S. Harmer, and Kenneth C. Hoffman. "Search for Neutrinos from the Sun." In: *Physical Review Letters* 20.21 (1968), ISSN: 0031-9007. DOI: 10.1103/PhysRevLett.20.1205 (cit. on p. 9).

[30] Bruce T. Cleveland et al. "Measurement of the Solar Electron Neutrino Flux with the Homestake Chlorine Detector." In: *The Astrophysical Journal* 496.1 (1998), ISSN: 0004-637X. DOI: 10.1086/305343 (cit. on p. 9).

[31] Y. Fukuda et al. "Evidence for Oscillation of Atmospheric Neutrinos." In: *Physical Review Letters* 81.8 (1998), ISSN: 0031-9007. DOI: 10.1103/PhysRevLett.81.1562 (cit. on p. 9).

[32] V. Gribov and B. Pontecorvo. "Neutrino astronomy and lepton charge." In: *Physics Letters B* 28.7 (1969), ISSN: 03702693. DOI: 10.1016/0370-2693(69)90525-5 (cit. on p. 9).

[33] J. Boger et al. "The Sudbury Neutrino Observatory." In: *Nuclear Instruments and Methods in Physics Research Section A: Accelerators, Spectrometers, Detectors and Associated Equipment* 449.1-2 (2000), ISSN: 01689002. DOI: 10.1016/S0168-9002(99)01469-2 (cit. on p. 9).

[34] B. Aharmim et al. "Determination of the ν_e and total B8 solar neutrino fluxes using the Sudbury Neutrino Observatory Phase I data set." In: *Physical Review C* 75.4 (2007). ISSN: 0556-2813. DOI: 10.1103/PhysRevC.75.045502 (cit. on p. 10).

[35] R. Adhikari et al. "A White Paper on keV sterile neutrino Dark Matter." In: *Journal of Cosmology and Astroparticle Physics* 2017.01 (2017), DOI: 10.1088/1475-7516/2017/01/025 (cit. on pp. 10, 18).

[36] Ivan Esteban et al. "The fate of hints: updated global analysis of three-flavor neutrino oscillations." In: *Journal of High Energy Physics* 2020.9 (2020). DOI: 10.1007/JHEP09(2020)178 (cit. on p. 11).

[37] M. Agostini et al. "Final Results of GERDA on the Search for Neutrinoless Double-β Decay." In: *Physical Review Letters* 125.25 (2020), ISSN: 0031-9007. DOI: 10.1103/PhysRevLett.125.252502 (cit. on p. 12).

[38] S. Abe et al. "Search for the Majorana Nature of Neutrinos in the Inverted Mass Ordering Region with KamLAND-Zen." In: *Physical Review Letters* 130.5 (2023), ISSN: 0031-9007. DOI: 10.1103/PhysRevLett.130.051801 (cit. on p. 12).

[39] A. Boyarsky et al. "Masses of active neutrinos in the νMSM from x-ray astronomy." In: *Journal of Experimental and Theoretical Physics Letters* 83.4 (2006), ISSN: 0021-3640. DOI: 10.1134/S0021364006040011 (cit. on p. 15).

[40] S. Dodelson and L. M. Widrow. "Sterile neutrinos as dark matter." In: *Physical Review Letters* 72.1 (1994), ISSN: 0031-9007. DOI: 10.1103/PhysRevLett.72.17 (cit. on pp. 16, 17).

[41] Xiangdong Shi and George M. Fuller. "New Dark Matter Candidate: Nonthermal Sterile Neutrinos." In: *Physical Review Letters* 82.14 (1999), ISSN: 0031-9007. DOI: 10.1103/PhysRevLett.82.2832 (cit. on p. 17).

[42] Joshua W. Foster et al. "Deep Search for Decaying Dark Matter with XMM-Newton Blank-Sky Observations." In: *Physical Review Letters* 127.5 (2021), ISSN: 0031-9007. DOI: 10.1103/PhysRevLett.127.051101 (cit. on pp. 17, 18).

[43] Brandon M. Roach et al. "Long-exposure NuSTAR constraints on decaying dark matter in the Galactic halo." In: *Physical Review D* 107.2 (2023). ISSN: 2470-0010. DOI: 10.1103/PhysRevD.107.023009 (cit. on pp. 17, 18).

[44] Kenny C. Y. Ng et al. "Improved limits on sterile neutrino dark matter using full-sky Fermi Gamma-ray Burst Monitor data." In: *Physical Review D* 92.4 (2015). ISSN: 2470-0010. DOI: 10.1103/PhysRevD.92.043503 (cit. on pp. 17, 18).

[45] Kenny C. Y. Ng et al. "New constraints on sterile neutrino dark matter from NuSTAR M31 observations." In: *Physical Review D* 99.8 (2019). ISSN: 2470-0010. DOI: 10.1103/PhysRevD.99.083005 (cit. on pp. 17, 18).

[46] Brandon M. Roach et al. "NuSTAR tests of sterile-neutrino dark matter: New Galactic bulge observations and combined impact." In: *Physical Review D* 101.10 (2020). ISSN: 2470-0010. DOI: 10.1103/PhysRevD.101.103011 (cit. on pp. 17, 18).

[47] Martin Descher. "Differential spectrum modeling and sensitivity for keV sterile neutrino search at KATRIN." PhD thesis. 2023 (cit. on pp. 17, 19, 29–31, 54).

[48] Scott Tremaine and James E. Gunn. "Dynamical Role of Light Neutral Leptons in Cosmology." In: *Physical Review Letters* 42.6 (1979), ISSN: 0031-9007. DOI: 10.1103/PhysRevLett.42.407 (cit. on p. 17).

[49] Dominic Sicilian et al. "Probing the Milky Way's Dark Matter Halo for the 3.5 keV Line." In: *The Astrophysical Journal* 905.2 (2020), ISSN: 0004-637X. DOI: 10.3847/1538-4357/abbee9 (cit. on p. 18).

[50] Esra Bulbul et al. "DETECTION OF AN UNIDENTIFIED EMISSION LINE IN THE STACKED X-RAY SPECTRUM OF GALAXY CLUSTERS." In: *The Astrophysical Journal* 789.1 (2014), ISSN: 0004-637X. DOI: 10.1088/0004-637X/789/1/13 (cit. on p. 18).

[51] Christopher Dessert, Nicholas L. Rodd, and Benjamin R. Safdi. "The dark matter interpretation of the 3.5-keV line is inconsistent with blank-sky observations." In: *Science (New York, N.Y.)* 367.6485 (2020), ISSN: 0036-8075. DOI: 10.1126/science.aaw3772 (cit. on p. 18).

[52] J. N. Abdurashitov et al. "First measurements in search for keV sterile neutrino in tritium beta-decay in the Troitsk nu-mass experiment." In: *Journal of Experimental and Theoretical Physics Letters* 105.12 (2017), ISSN: 0021-3640. DOI: 10.1134/S0021364017120013 (cit. on p. 19).

[53] E. Holzschuh et al. "Search for heavy neutrinos in the β-spectrum of Ni." In: *Physics Letters B* 451.1-2 (1999), ISSN: 03702693. DOI: 10.1016/S0370-2693(99)00200-2 (cit. on p. 19).

[54] E. Holzschuh et al. "The β-spectrum of 35S and search for the admixture of heavy neutrinos." In: *Physics Letters B* 482.1-3 (2000), ISSN: 03702693. DOI: 10.1016/S0370-2693(00)00476-7 (cit. on p. 19).

[55] K. G. Leach and S. Friedrich. "The BeEST Experiment: Searching for Beyond Standard Model Neutrinos Using ^{7}Be Decay in STJs." In: *Journal of Low Temperature Physics* 209.5-6 (2022), ISSN: 0022-2291. DOI: 10.1007/s10909-022-02759-z (cit. on p. 19).

[56] M. Aker et al. "Search for keV-scale sterile neutrinos with the first KATRIN data." In: *The European Physical Journal C* 83.8 (2023). ISSN: 1434-6044. DOI: 10.1140/epjc/s10052-023-11818-y (cit. on pp. 19, 29).

[57] G. B. Kim. "MAGNETO-ν: Searching for keV sterile neutrino dark matter in 241Pu beta decay." In: Presentation at the UCLA Dark Matter 2023 conference, 2023 (cit. on p. 19).

[58] C. J. Martoff et al. "HUNTER: precision massive-neutrino search based on a laser cooled atomic source." In: *Quantum Science and Technology* 6.2 (2021), DOI: 10.1088/2058-9565/abdb9b (cit. on p. 19).

[59] Cristina Benso et al. "Prospects for finding sterile neutrino dark matter at KATRIN." In: *Physical Review D* 100.11 (2019). ISSN: 2470-0010. DOI: 10.1103/PhysRevD.100.115035 (cit. on p. 19).

[60] KATRIN Collaboration. *KATRIN design report 2004*. 2005. DOI: 10.5445/IR/270060419 (cit. on pp. 21, 25, 26, 137).

[61] Susanne Mertens et al. "A novel detector system for KATRIN to search for keV-scale sterile neutrinos." In: *Journal of Physics G: Nuclear and Particle Physics* 46.6 (2019), ISSN: 0954-3899. DOI: 10.1088/1361-6471/ab12fe (cit. on pp. 21, 48, 63).

[62] E. W. Otten and C. Weinheimer. "Neutrino mass limit from tritium beta decay." In: *Reports on Progress in Physics* 71.8 (2008), ISSN: 0034-4885. DOI: 10.1088/0034-4885/71/8/086201 (cit. on pp. 21, 22, 24).

[63] Tim Benjamin Brunst. "First generation prototype detectors for the TRISTAN project." en. PhD thesis. Technical University of Munich, 2020, URL: https://mediatum.ub.tum.de/1540377 (cit. on pp. 22, 48).

[64] V. M. Lobashev and P. E. Spivak. "A method for measuring the electron antineutrino rest mass." In: *Nuclear Instruments and Methods in Physics Research Section A: Accelerators, Spectrometers, Detectors and Associated Equipment* 240.2 (1985), ISSN: 01689002. DOI: 10.1016/0168-9002(85)90640-0 (cit. on p. 23).

[65] A. Picard et al. "A solenoid retarding spectrometer with high resolution and transmission for keV electrons." In: *Nuclear Instruments and Methods in Physics Research Section B: Beam Interactions with Materials and Atoms* 63.3 (1992), ISSN: 0168583X. DOI: 10.1016/0168-583X(92)95119-C (cit. on p. 23).

[66] Martin Slezak. "Monitoring of the energy scale in the KATRIN neutrino experiment." PhD thesis. Czech Academy of Sciences, 2015. URL: https://cds.cern.ch/record/2243754 (cit. on pp. 23, 113, 115, 123, 138).

[67] Laura Kuckert et al. "Modelling of gas dynamical properties of the Katrin tritium source and implications for the neutrino mass measurement." In: *Vacuum* 158 (2018), ISSN: 0042207X. DOI: 10.1016/j.vacuum.2018.09.036 (cit. on p. 26).

[68] K. Valerius. "The wire electrode system for the KATRIN main spectrometer." In: *Progress in Particle and Nuclear Physics* 64.2 (2010), ISSN: 01466410. DOI: 10.1016/j.ppnp.2009.12.032 (cit. on p. 27).

[69] Th Thümmler, R. Marx, and Ch Weinheimer. "Precision high voltage divider for the KATRIN experiment." In: *New Journal of Physics* 11.10 (2009), DOI: 10.1088/1367-2630/11/10/103007 (cit. on p. 27).

[70] J. F. Amsbaugh et al. "Focal-plane detector system for the KATRIN experiment." In: *Nuclear Instruments and Methods in Physics Research Section A: Accelerators, Spectrometers, Detectors and Associated Equipment* 778 (2015), ISSN: 01689002. DOI: 10.1016/j.nima.2014.12.116 (cit. on p. 28).

[71] M. Aker et al. "Analysis methods for the first KATRIN neutrino-mass measurement." In: *Physical Review D* 104.1 (2021). ISSN: 2470-0010. DOI: 10.1103/PhysRevD.104.012005 (cit. on p. 28).

[72] M. Aker et al. "Improved eV-scale sterile-neutrino constraints from the second KATRIN measurement campaign." In: *Physical Review D* 105.7 (2022). ISSN: 2470-0010. DOI: 10.1103/PhysRevD.105.072004 (cit. on p. 29).

[73] Marc Korzeczek. "Sterile neutrino search with KATRIN - modeling and design-criteria of a novel detector system." PhD thesis. 2020. DOI: 10.5445/IR/1000120634 (cit. on pp. 30, 54, 58).

[74] P. Voigt. "Transmission properties of the KATRIN main spectrometer (when operated) for a keV-scale sterile neutrino search." Master's Thesis. Technical University of Munich, 2023 (cit. on p. 31).

[75] B. G. Lowe and R. A. Sareen. *Semiconductor X-ray detectors*. Series in Sensors. Boca Raton, Fla.: CRC Press, 2014. ISBN: 9781466554009 (cit. on pp. 33, 36, 43–45, 179).

[76] Frank Mattias Hartmann. *Evolution of silicon sensor technology in particle physics*. Second edition. Vol. Volume 275. Physics. Cham: Springer, 2017. ISBN: 978-3-319-64436-3. DOI: 10.1007/978-3-319-64436-3 (cit. on pp. 33–38).

[77] Alexander Chao et al. *Pixel Detectors*. Berlin, Heidelberg: Springer Berlin Heidelberg, 2006. ISBN: 978-3-540-28332-4. DOI: 10.1007/3-540-28333-1 (cit. on pp. 33, 34, 37).

[78] Gerhard Lutz. *Semiconductor Radiation Detectors*. Berlin, Heidelberg: Springer Berlin Heidelberg, 2007. ISBN: 978-3-540-71678-5. DOI: 10.1007/978-3-540-71679-2 (cit. on pp. 33, 44, 56).

[79] R. C. Alig, S. Bloom, and C. W. Struck. "Scattering by ionization and phonon emission in semiconductors." In: *Physical Review B* 22.12 (1980), ISSN: 1098-0121. DOI: 10.1103/PhysRevB.22.5565 (cit. on pp. 33, 35, 43).

[80] Thomas Middelmann et al. "Thermal expansion coefficient of single-crystal silicon from 7 K to 293 K." In: *Physical Review B* 92.17 (2015). ISSN: 1098-0121. DOI: 10.1103/PhysRevB.92.174113 (cit. on pp. 35, 56).

[81] *Table de Radionucleides Fe-55*. 2005. URL: http://www.lnhb.fr/nuclides/Fe-55_tables.pdf (cit. on pp. 34, 91).

[82] D. Siegmann. "Investigation of the Detector Response to Electrons of the TRISTAN Prototype Detectors." Master's Thesis. Technical University of Munich, 2019 (cit. on pp. 36, 40, 48, 129, 145).

[83] W. Shockley and W. T. Read. "Statistics of the Recombinations of Holes and Electrons." In: *Physical Review* 87.5 (1952), ISSN: 0031-899X. DOI: 10.1103/PhysRev.87.835 (cit. on p. 37).

[84] Emilio Gatti and Pavel Rehak. "Semiconductor drift chamber — An application of a novel charge transport scheme." In: *Nuclear Instruments and Methods in Physics Research* 225.3 (1984), ISSN: 01675087. DOI: 10.1016/0167-5087(84)90113-3 (cit. on pp. 38, 39).

[85] Peter Lechner et al. "Silicon drift detectors for high resolution room temperature X-ray spectroscopy." In: *Nuclear Instruments and Methods in Physics Research Section A: Accelerators, Spectrometers, Detectors and Associated Equipment* 377.2-3 (1996), ISSN: 01689002. DOI: 10.1016/0168-9002(96)00210-0 (cit. on p. 39).

[86] P. Lechner, A. Pahlke, and H. Soltau. "Novel high-resolution silicon drift detectors." In: *X-Ray Spectrometry* 33.4 (2004), ISSN: 0049-8246. DOI: 10.1002/xrs.717 (cit. on p. 39).

[87] Christian Forstner. "Characterization of a TRISTAN Silicon Drift Detector Array with a Laser System." Master thesis. Technical University of Munich, 2023. URL: https://www.ph.nat.tum.de/fileadmin/w00bya/neutrinos/Thesis/Master/TRISTAN_Forstner_Christian_23.pdf (cit. on pp. 41, 63, 98, 118).

[88] Paolo Trigilio et al. "ETTORE: a 12-Channel Front-End ASIC for SDDs with Integrated JFET." In: *2018 IEEE Nuclear Science Symposium and Medical Imaging Conference Proceedings (NSS/MIC)*. IEEE, 2018, ISBN: 978-1-5386-8494-8. DOI: 10.1109/NSSMIC.2018.8824675 (cit. on pp. 41, 42, 64, 66).

[89] Matteo Gugiatti. "Development of a large-Matrix SDD-based radiation detector for beta-decay spectroscopy in neutrino physics." PhD Thesis. 2022 (cit. on pp. 41, 42, 47, 61, 63–66, 76, 77, 81, 164, 189–191).

[90] Glenn F. Knoll. *Radiation detection and measurement*. 2. ed., 9. [print.] New York, NY: Wiley, 1989. ISBN: 0471815047 (cit. on p. 41).

[91] U. Fano. "Ionization Yield of Radiations. II. The Fluctuations of the Number of Ions." In: *Physical Review* 72.1 (1947), ISSN: 0031-899X. DOI: 10.1103/PhysRev.72.26 (cit. on p. 43).

[92] Tobias Eggert. "Die spektrale Antwort von Silizium-Röntgendetektoren." PhD thesis. 2004. URL: https://mediatum.ub.tum.de/?id=603022 (cit. on pp. 44–46, 49).

[93] H. Nyquist. "Thermal Agitation of Electric Charge in Conductors." In: *Physical Review* 32.1 (1928), ISSN: 0031-899X. DOI: 10.1103/PhysRev.32.110 (cit. on p. 44).

[94] K. Kandiah, M. O. Deighton, and F. B. Whiting. "A physical model for random telegraph signal currents in semiconductor devices." In: *Journal of Applied Physics* 66.2 (1989), ISSN: 0021-8979. DOI: 10.1063/1.343523 (cit. on p. 45).

[95] Helmuth Spieler. *Semiconductor detector systems*. Repr. Vol. 12. Oxford science publications. Oxford: Oxford Univ. Press, 2012. ISBN: 9780198527848 (cit. on p. 45).

[96] A. Nava et al. "A Geant4-based model for the TRISTAN detector." In: *Journal of Physics: Conference Series* 2156.1 (2021), ISSN: 1742-6588. DOI: 10.1088/1742-6596/2156/1/012177 (cit. on pp. 46, 48, 129).

[97] Stephen Seltzer. *X-ray Form Factor, Attenuation and Scattering Tables, NIST Standard Reference Database 66*. 1995. DOI: 10.18434/T4HS32 (cit. on pp. 47, 119).

[98] S. Agostinelli et al. "Geant4—a simulation toolkit." In: *Nuclear Instruments and Methods in Physics Research Section A: Accelerators, Spectrometers, Detectors and Associated Equipment* 506.3 (2003), ISSN: 01689002. DOI: 10.1016/S0168-9002(03)01368-8 (cit. on p. 47).

[99] R. Hartmann et al. "Ultrathin entrance windows for silicon drift detectors." In: *Nuclear Instruments and Methods in Physics Research Section A: Accelerators, Spectrometers, Detectors and Associated Equipment* 387.1-2 (1997), ISSN: 01689002. DOI: 10.1016/S0168-9002(96)01000-5 (cit. on p. 48).

[100] Albert C. Thompson et al. *X-ray Data Booklet*. Lawrence Berkeley National Laboratory, University of California, 2009. URL: https://cxro.lbl.gov//PDF/X-Ray-Data-Booklet.pdf (cit. on pp. 48, 49, 93, 117, 119).

[101] Daniela Spreng. "Electron Backscattering on Silicon Drift Detectors and Its Impact on a Sterile Neutrino Search with KATRIN." Master's Thesis. 2023. URL: https://www.ph.nat.tum.de/fileadmin/w00bya/neutrinos/Thesis/Master/TRISTAN_Spreng_Daniela_23.pdf (cit. on pp. 50, 63).

[102] *Cesic by ecm*. 2019. URL: https://www.cesic.de/en (cit. on pp. 53, 56).

[103] M. Aker et al. "Direct neutrino-mass measurement with sub-electronvolt sensitivity." In: *Nature Physics* 18.2 (2022), ISSN: 1745-2473. DOI: 10.1038/s41567-021-01463-1 (cit. on p. 54).

[104] Lars Ullmer. "Investigations on the vacuum compatibility of the first TRISTAN detector module." Bachelor's Thesis. 2020 (cit. on p. 54).

[105] R. Clarke. *Magnetic properties of materials*. 2008. URL: http://info.ee.surrey.ac.uk/Workshop/advice/coils/mu/ (cit. on p. 56).

[106] *Mechanical properties of copper*. URL: https://www.matweb.com/search/datasheet_print.aspx?matguid=9aebe83845c04c1db5126fada6f76f7e (cit. on p. 56).

[107] Y. Koyatsu, H. Miki, and F. Watanabe. "Measurements of outgassing rate from copper and copper alloy chambers." In: *Vacuum* 47.6-8 (1996), ISSN: 0042207X. DOI: 10.1016/0042-207X(96)00053-X (cit. on p. 56).

[108] *Mechanical properties of 316 stainless steel*. URL: https://www.matweb.com/search/datasheet.aspx?MatGUID=dfced4f11d63459e8ef8733d1c7c1ad2 (cit. on p. 56).

[109] Norman Wilson and Paul Bunch, eds. *Magnetic permeability of stainless steel for use in Accelerator beam transport system*. 1991 IEEE Particle Accelerator Conference (PAC 1991), 1991. URL: https://accelconf.web.cern.ch/p91/pdf/pac1991_2322.pdf (cit. on p. 56).

[110] *Technical Data Sheet EOP-TEK 920-FL*. 2021. URL: https://www.epotek.com/docs/en/Datasheet/920-FL.pdf (cit. on pp. 56, 72, 79, 172).

[111] Norbert Meidinger et al. "Development of the focal plane PNCCD camera system for the X-ray space telescope eROSITA." In: *Nuclear Instruments and Methods in Physics Research Section A: Accelerators, Spectrometers, Detectors and Associated Equipment* 624.2 (2010), ISSN: 01689002. DOI: 10.1016/j.nima.2010.03.126 (cit. on p. 56).

[112] L. Strüder et al. "A 36 cm2 large monolythic pn-charge coupled device x-ray detector for the European XMM satellite mission." In: *Review of Scientific Instruments* 68.11 (1997), ISSN: 0034-6748. DOI: 10.1063/1.1148341 (cit. on p. 56).

[113] Lena Wunderl. "Characterization of the Electron Response of a TRISTAN Silicon Drift Detector in the KATRIN Monitor Spectrometer." Master's Thesis. 2022. URL: https://www.ph.nat.tum.de/fileadmin/w00bya/neutrinos/Thesis/Master/TRISTAN_Wunderl_Lena_22.pdf (cit. on pp. 63, 116).

[114] Stuart Turner, ed. *CAS - CERN Accelerator School : Vacuum Technology: Cleaning for vacuum service*. CERN Yellow Reports: School Proceedings. CERN, 1999. DOI: 10.5170/CERN-1999-005 (cit. on pp. 71, 77).

[115] *Data sheet of PTE foil*. URL: https://nx5412.your-storageshare.de/s/QDEyNx6TM7xNAiE (cit. on p. 72).

[116] Daniel Sigg. *Printed Circuit Boards for Ultra High Vacuum*. Tech. rep. Laser Interferometer Gravitational Wave Observatory - LIGO. URL: https://dcc.ligo.org/public/0027/T060280/000/T060280-00.pdf (cit. on p. 76).

[117] Mareike Held. *Cleaning procedure for vacuum components*. URL: https://iap-katrin-wiki.iap.kit.edu/katrin/images/0/0e/Reinigungsanweisungen_Mareike_Held.pdf (cit. on p. 77).

[118] Marco Carminati et al. "The TRISTAN 166-pixel detector: Preliminary results with a planar setup." In: *Nuclear Instruments and Methods in Physics Research Section A: Accelerators, Spectrometers, Detectors and Associated Equipment* 1049 (2023), ISSN: 01689002. DOI: 10.1016/j.nima.2023.168046 (cit. on p. 77).

[119] CAEN. *V2740 64 Channel 16 bit 125 MS/s Digitizer*. URL: https://www.caen.it/products/v2740/ (cit. on p. 88).

[120] Valentin T. Jordanov and Glenn F. Knoll. "Digital synthesis of pulse shapes in real time for high resolution radiation spectroscopy." In: *Nuclear Instruments and Methods in Physics Research Section A: Accelerators, Spectrometers, Detectors and Associated Equipment* 345.2 (1994), ISSN: 01689002. DOI: 10.1016/0168-9002(94)91011-1 (cit. on p. 90).

[121] *NIST Traceable Calibration Standards - Gamma Disc Sources*. URL: https://www.drct.com/dss/sources/gammasources.htm (cit. on p. 91).

[122] S. Pommé, H. Stroh, and R. van Ammel. "The 55Fe half-life measured with a pressurised proportional counter." In: *Applied radiation and isotopes : including data, instrumentation and methods for use in agriculture, industry and medicine* 148 (2019), DOI: 10.1016/j.apradiso.2019.01.008 (cit. on pp. 91, 108).

[123] *Table de Radionucleides Am-241*. 2005. URL: http://www.lnhb.fr/nuclides/Am-241_tables.pdf (cit. on p. 92).

[124] Daniela Spreng. "Energy Calibration of the TRISTAN Silicon Drift Detectors." Bachelor's Thesis. Technical University of Munich, 2020. URL: https://www.ph.nat.tum.de/fileadmin/w00bya/neutrinos/Thesis/Bachelor/TRISTAN_Spreng_Daniela_20.pdf (cit. on pp. 92, 93, 105, 106).

[125] Christina Bruch. "Characterisation of a 166-Pixel TRISTAN Detector Module in the KATRIN Monitor Spectrometer." Master thesis. Technical University of Munich, 2023 (cit. on pp. 98, 100, 121, 135, 136).

[126] S. S. Wilks. "The Large-Sample Distribution of the Likelihood Ratio for Testing Composite Hypotheses." In: *The Annals of Mathematical Statistics* 9.1 (1938), ISSN: 0003-4851. DOI: 10.1214/aoms/1177732360 (cit. on p. 108).

[127] E. W. Otten. "The Mainz neutrino mass experiment." In: *Progress in Particle and Nuclear Physics* 32 (1994), ISSN: 01466410. DOI: 10.1016/0146-6410(94)90016-7 (cit. on p. 113).

[128] Johannes David Goullon. "Installation and commissioning of the monitor spectrometer of KATRIN." Diplomarbeit. Karlsruher Instituts für Technologie, 2010. URL: https://cds.cern.ch/record/1525716/files/CERN-THESIS-2010-288.pdf (cit. on p. 113).

[129] Daniel Furse et al. "Kassiopeia: a modern, extensible C++ particle tracking package." In: *New Journal of Physics* 19.5 (2017), DOI: 10.1088/1367-2630/aa6950 (cit. on pp. 115, 138).

[130] Béla Kári et al. *Medical Imaging - Single rate, pile-up, dead time and random rate*. 2019. URL: http://oftankonyv.reak.bme.hu/tiki-index.php?page=Single+rate%2C+pile-up%2C+dead+time+and+random+rate (cit. on p. 121).

[131] Korbinian Urban. "Development of a detector and readout system for keV sterile neutrino search at KATRIN." To be published. PhD Thesis. 2024 (cit. on pp. 121, 143).

[132] Gábor L. Molnár, ed. *Proceedings of the 9th International Symposium on Capture Gamma-Ray Spectroscopy and Related Topics: Budapest, Hungary ; 8 - 12 October 1996*. Budapest u.a.: Springer, 1997. ISBN: 963-7775-55-2. URL: https://permalink.obvsg.at/AC05971837 (cit. on pp. 122, 123).

[133] M. Zbořil et al. "Ultra-stable implanted 83 Rb/ 83 m Kr electron sources for the energy scale monitoring in the KATRIN experiment." In: *Journal of Instrumentation* 8.03 (2013), DOI: 10.1088/1748-0221/8/03/P03009 (cit. on p. 123).

[134] D. Vénos et al. "Properties of 83 mKr conversion electrons and their use in the KATRIN experiment." In: *Journal of Instrumentation* 13.02 (2018), DOI: 10.1088/1748-0221/13/02/T02012 (cit. on pp. 123, 124, 188).

[135] K. Altenmüller et al. "Muon-induced background in the KATRIN main spectrometer." In: *Astroparticle Physics* 108 (2019), ISSN: 09276505. DOI: 10.1016/j.astropartphys.2019.01.003 (cit. on pp. 136, 137).

[136] M. Furman and M. Pivi. "Probabilistic model for the simulation of secondary electron emission." In: *Physical Review Special Topics - Accelerators and Beams* 5.12 (2002). DOI: 10.1103/PhysRevSTAB.5.124404 (cit. on p. 136).

[137] Burton L. Henke, Jerel A. Smith, and David T. Attwood. "0.1–10-keV x-ray-induced electron emissions from solids—Models and secondary electron measurements." In: *Journal of Applied Physics* 48.5 (1977), ISSN: 0021-8979. DOI: 10.1063/1.323938 (cit. on p. 136).

[138] Ch Kraus et al. "Final results from phase II of the Mainz neutrino mass searchin tritium β decay." In: *The European Physical Journal C* 40.4 (2005), ISSN: 1434-6044. DOI: 10.1140/epjc/s2005-02139-7 (cit. on p. 137).

[139] R. G. Duggleby and H. Kaplan. "A competitive labeling method for the determination of the chemical properties of solitary functional groups in proteins." In: *Biochemistry* 14.23 (1975), ISSN: 0006-2960. DOI: 10.1021/bi00694a023 (cit. on p. 143).

[140] K. Urban et al. "A thermionic electron gun to characterize silicon drift detectors with electrons." In: *Journal of Instrumentation* 19.06 (2024), DOI: 10.1088/1748-0221/19/06/P06004 (cit. on p. 143).

[141] XGLab S.R.L. *DANTE: The Digital Pulse Processor for X-Ray Spectroscopy*. URL: https://www.xglab.it/products/dante/ (cit. on p. 197).

ACKNOWLEDGMENTS

I want to thank all the people who contributed in so many different ways to this thesis. Without their assistance, encouragement, and sometimes patience, this work would not have been possible. Your contributions are sincerely appreciated!

Prof. Dr. Susanne Mertens It was and is a great pleasure working with you, and I am really happy that you have been my supervisor over all these years. I enjoyed my time in your working group and seeing how it developed over the years. I am glad that I could be part of it, and I always felt that you valued our opinions and ideas and took them seriously. This enabled me to follow my research interests, test different ideas, and gave me a lot of freedom and trust in my work. I am really grateful for all your support and guidance during my time as a PhD student.

Dr. Thibaut Houdy I enjoyed working with you and think we were very complimentary in our skills, which helped me greatly during my time as a PhD student and in my development as a person. I am thankful for your advice, and I miss the lively discussions about life on car rides and the various integration visits in Karlsruhe. Merci beaucoup!

Dr. Frank Edzards I appreciate all the time you took to discuss our research together and your excellent proofreading and presentation skills. I learned much from you and always valued your advice and our time together in the lab. Your energy and passion are catching, and you were inspiring during this work.

Dr. Tim Brunst Thank you for all the time together in the office, lab, and the various snowboarding sessions. I learned so many things from you and appreciated all the patience you had, especially at the beginning of my PhD, when I had a million questions. Your honest and warm manner supported me during my work and helped me a lot.

Christina Bruch I am grateful for all the time we spent together in the lab and the walks during the lunch breaks to get our heads free. The time during the integration in Karlsruhe was a blast. You always had my back, and I could trust you with everything. Thank you for everything, Christina (:

Dr. Peter Lechner I am thankful for all the discussions and know-how that you shared with me during the critical phases of the gluing and assembly procedure. Without your knowledge and patience in the lab, the assembly of the detector modules would not be possible.

Danilo Mießner Thank you for all the tests and brainstorming we performed to develop the gluing procedure. Without you, the assembly of the detector modules would not been possible. I always enjoyed our time together in the cleanroom and the discussions about life.

Dr. Dominic Hinz It was always a pleasure to come to Karlsruhe and work together with you on the Monitor Spectrometer. I enjoyed the welcoming and warm atmosphere you created every time I arrived there and your company during the installation and measurements.

Korbinian Urban Thank you for all the fruitful discussions about electronics and the fun times together in the office. Your way of explaining complex topics helped me a lot during my PhD, and I always enjoyed our time together at conferences or in the bouldering gym.

Daniela Spreng I appreciate all the constructive feedback and encouraging words you gave me on my work and during my time as a PhD. This work would not have been possible without your help during the assembly of the experimental setups and measurements.

Matthias Meier Thank you for all your moral support and the after-work discussion. The swinging atmosphere you created in our office helped during many brainstorming sessions.

Christoph Köhler I am grateful for the calming and welcoming atmosphere you created in our office. You made an atmosphere in which one feels at ease, both personally and locally.

Alessandro Schwemmer I wanted to thank you for all the nice days during various conferences. It was always a blast traveling with you and exploring new cities.

Florian Henkes Thank you for the short tennis soccer breaks during hard work days. They freed up my mind and helped me to keep my balance and focus.

Anthony Onillon I appreciated your support while writing the detector module paper and the constructive feedback for it and also in the bigger picture as a researcher.

Polimi group Thank you for all the good times during your visits to Munich and my visit to Milano. It was always a pleasure meeting you. This work would not have been possible without your expertise and cheerful nature.

EDM Chair Thank you for all the fun activities during and after work. I am grateful for the nice atmosphere you created and the many sports events, Christmas parties, and other activities we did together.

Ulrike Fahrendholz You were there during the easy times and the harder times, and I am grateful for all the support and encouragement you gave me.

Benedikt Berchtenbreiter Thank you for all the calming words when things were not working. You helped me keep my balance, and I am happy to have you as a friend.

My Family I want to thank you for your continuous and encouraging support, which allowed me to do what I enjoy.

Daniel Siegmann